UTS UNIVERSITY OF TECHNOLOGY SYDNEY

Investigation into Non-Flammable Electrolytes for Lithium and Zinc Secondary Batteries

by Pauline Jaumaux

Thesis submitted in fulfilment of the requirements for the degree of

Doctor of Philosophy

under the supervision of Prof. Guoxiu Wang, Asst. Prof. Dong Zhou and Dr. Bing Sun

University of Technology Sydney
Faculty of Science

August 2022

CERTIFICATE OF ORIGINAL AUTHORSHIP

I, Pauline Jaumaux declare that this thesis, is submitted in fulfilment of the requirements for the award of Doctor of Philosophy, in the Faculty of Science at the University of Technology Sydney.

This thesis is wholly my own work unless otherwise reference or acknowledged. In addition, I certify that all information sources and literature used are indicated in the thesis.

This document has not been submitted for qualifications at any other academic institution.

This research is supported by the Australian Government Research Training Program.

Production Note:
Signature removed prior to publication.

7-Aug-2022

ACKNOWLEDGMENTS

I am grateful for the continuous guidance and support that I have received from my supervisor, Professor Guoxiu Wang. I would like to thank my co-supervisors Asst. Prof. Dong Zhou and Dr. Bing Sun for their valuable help and advice during my PhD studies. Last but not least, I would like to recognize Dr. Yueping (Jane) Yao for her kind support and management of our laboratory.

I deeply thank my colleagues at the Centre for Clean Energy Technology in the University of Technology, Sydney. Dr. Jinqiang Zhang, Dr. Xin Guo, Dr. Liubing Dong, Dr. Weizhai Bao, Dr. Hao Tian, Dr. Xiaochun Gao, Dr. Kang Yan, Dr. Yi Chen, Dr. Fan Zhang, Dr. Xiao Tang, Dr. Shouqing Zhao, Dr. Tuhin Sahu, Shijian Wang, Javad Safaei and Yuhan Xie, and all the CCET members were available to support me in difficult times and their valuable collaborations were very helpful.

Furthermore, I acknowledge the support of the School of Mathematic and Physical Science administrative team, Elizabeth and Sorabh. I also would like to thank Ronald, Alex, Linda and Herbert, Mark and Kathie for their availability and essential training.

My PhD studies have been achieved thanks to the financial support from UTS scholarship and RMCRC project.

Finally, I am extremely grateful to my Nicolas, my family and my friends who supported me and believed in me through this journey.

List of publications

1. **Pauline Jaumaux,** Shijian Wang, Shuoqing Zhao, Bing Sun, and Guoxiu Wang, Solvation Structure Design via Molecular Crowding Effect for High Voltage Zinc Batteries. ***To be submitted.*** *Incorporated in this thesis as Chapter VI.*

2. **Pauline Jaumaux**[1], Xu Yang[1], Bao Zhang, Javad Safaei, Xiao Tang, Dong Zhou, Chunsheng Wang, and Guoxiu Wang, Localized Water-In-Salt Electrolyte for Aqueous Lithium-Ion Batteries. ***Angew. Chem. Int. Ed.***, 2021, 60, 19965-19973. DOI: 10.1002/anie.202107389. *Incorporated in this thesis as Chapter V*.

3. **Pauline Jaumaux**[1], Junru Wu[1], Devaraj Shanmukaraj[1], Yizhou Wang, Dong Zhou, Bing Sun, Feiyu Kang, Baohua Li, Michel Armand, and Guoxiu Wang, Non-Flammable Liquid and Quasi-Solid Electrolytes toward Highly-Safe Alkali Metal-Based Batteries. ***Adv. Funct. Mater.***, 2021, 31, 2008644. DOI: 10.1002/adfm.202008644

4. **Pauline Jaumaux**[1], Qi Liu[1], Dong Zhou, Xiaofu Xu, Tianyi Wang, Yizhou Wang, Feiyu Kang, Baohua Li, and Guoxiu Wang, Deep-eutectic-solvent-based self-healing polymer electrolyte for safe and long-life lithium-metal batteries. ***Angew. Chem. Int. Ed.***, 2020 59, 9134-9142. DOI: 10.1002/anie.202001793. *Incorporated in this thesis as Chapter IV*.

5. Jiahui Lu[1], **Pauline Jaumaux**[1], Tianyi Wang, Chengyin Wang and Guoxiu Wang, Recent Progress in Quasi-Solid and Solid Polymer Electrolytes for Multivalent Metal Ion Batteries. ***J. Mater. Chem. A***, 2021, 9, 24175-24194. DOI: 10.1039/D1TA06606D

6. Qi Liu[1], Yizhou Wang[1], Xu Yang, Dong Zhou, Xianshu Wang, **Pauline Jaumaux**, Feiyu Kang, Baohua Li, Xiulei Ji and Guoxiu Wang, Rechargeable anion-shuttle batteries for low-cost energy storage. ***Chem***., 2021, 7, 1993-2021. DOI: 10.1016/j.chempr.2021.02.004

7. Xiao Tang, Dong Zhou, Bao Zhang, Shijian Wang, Peng Li, Hao Liu, Xin Guo, **Pauline Jaumaux**, Xiaochun Gao, Yongzhu Fu, Chengyin Wang, Chunsheng Wang and Guoxiu Wang, A universal strategy towards high–energy aqueous multivalent–ion batteries. ***Nat. Commun.***, 2021, 12, 2857. DOI: 10.1038/s41467-021-23209-6

8. Tianyi Wang, Yanbin Li, Jinqiang Zhang, Kang Yan, **Pauline Jaumaux**, Jian Yang, Chengyin Wang, Devaraj Shanmukaraj, Bing Sun, Michel Armand, Yi Cui and Guoxiu Wang, Immunizing lithium metal anodes against dendrite growth using protein molecules to achieve high energy batteries. ***Nat. Commun.***, 2020, 11, 5429. DOI: 10.1038/s41467-020-19246-2

9. Jian Yang, Weizhai Bao, **Pauline Jaumaux**, Songtao Zhang, Chengyin Wang and Guoxiu Wang, MXene-based composites: synthesis and applications in rechargeable batteries and supercapacitors. ***Adv. Mater. Interfaces***, 2019, 6, 1802004. DOI: 10.1002/admi.201802004

10. Tuhin Subhra Sahu[1], Sinho Choi, **Pauline Jaumaux**, Jinqiang Zhang, Chengyin Wang, Dong Zhou and Guoxiu Wang, Squalene-derived sulfur-rich copolymer@ 3D graphene-carbon nanotube network cathode for high-performance lithium-sulfur batteries. ***Polyhedron***, 2019, 162, 147-154. DOI: 10.1016/j.poly.2019.01.068

TABLE OF CONTENT

LIST OF TABLES

LIST OF FIGURES

ABSTRACT

Greenhouse gas emission related to the burning of fossil fuels for energy production is the main driver responsible for the climate crisis our society is facing. To avert climate change, the transition toward renewable energy production is urgent. However, the intermittence of these energy sources restrict their implementation. Coupling sustainable energy sources with energy storage systems could solve this issue. Since its commercialisation, Lithium (Li) -ion batteries have been at the centre of the attention for high-energy storage systems. As the global energy demand keeps increasing, new battery requirements are expected such as higher energy density and improved safety, which cannot be met by the current commercial Li-ion batteries. The thermally instable liquid electrolyte (containing highly flammable and toxic solvents, and thermally instable Li salts) usually employed in Li-ion batteries causes serious safety concerns. Many fires and explosions incidents occurred in the past few decades due to over-heating Li-ion batteries. Herein, various non-flammable electrolytes such as deep-eutectic-solvents and aqueous electrolytes were engineered to answer safety, dendrite growth and cost issues in Li and zinc (Zn) –based batteries. A fluorinated self-healing deep eutectic solvent quasi-solid electrolyte allowed long cycling performance of a Li-metal battery (Li||lithium manganese oxide ($LiMn_2O_4$, LMO) by creating a robust protective layer on the Li anode meanwhile the gel matrix helped guiding the Li deposition, thereby reducing dendrite growth and maintaining high safety. Then, a localized highly concentrated aqueous quasi-solid electrolyte was designed for low-cost Li-ion aqueous batteries with high voltage LMO cathode. Finally, a molecular crowding strategy was employed to suppress dendrite growth and corrosion on Zn metal anode in hybrid Zn||LMO aqueous batteries. These electrolyte designs opened up fascinating ways to tailor electrolyte properties for high safety and low-cost next battery generation.

CHAPTER I: Introduction

The reduction of greenhouse gas emission is a priceless challenge to adverse climate change issue. As outlined during the *UN Climate Change Conference 26 (COP26)*, we need to secure global net zero by 2050 and keep warming temperature below 1.5 °C.[35] In term of energy production, the reduction of greenhouse gases emission can predominantly be achieved by transitioning away from fossil fuel to renewable energy sources (*e.g.*, solar, wind, *etc.*). Renewable energies come from intermittent energy sources that are weather dependant. Therefore, this energy transition also requires the development of energy storage systems suitable for large (*e.g.*, solar farms, wind farms) and smaller (*e.g.*, electrical vehicles) scale. Lithium (Li) –ion batteries undoubtedly dominate the global electrochemical energy storage market since their commercialisation in 1991. Subsequently, the scientific community kept studying different electrode materials and electrolytes to further improve the batteries' performances.[36] The energy density of Li-ion batteries based on graphite anode and Li intercalation cathode (*e.g.*, lithium cobalt oxide ($LiCoO_2$,LCO)) was enhanced by more than 2-folds over the past 30 years.[37] However, their energy density is now reaching a plateau meanwhile the expensive price, poor safety (*e.g.*, flammable, toxic electrolyte) and rare chemical elements (*e.g.*, cobalt, nickel) associated to their manufacturing remain serious shortcomings.

Several battery systems which can theoretically largely surpass the energy density and/or power density of the commercially available Li-ion batteries, are under intensive investigation as next battery generation (*e.g.*, Li-based batteries: Li metal, Li-sulphur, Li-oxygen; Sodium (Na)-based batteries; Zinc (Zn)-based batteries; *etc.*). For instance, replacing graphite by metal anodes could provide batteries with energy densities superior to 500 Wh kg^{-1}, which can meet the growing demands of high energy density batteries for electric vehicles or grid storage applications.[38] However, metal anodes are confronted to serious safety issues impeding their practical applications.[39] The uneven metal plating and stripping throughout cycling results in incontrollable dendrites growth. Dendrites are an accumulation of metal ion plated on top of each other creating a sharp spear shape, which can create short-circuits by penetrating the separator. Amongst all metal anodes, Li metal is particularly interesting owing to its ultrahigh specific capacity (3860 mAh g^{-1}) and lowest Li/Li^+ redox potential (-3.040 V *vs.*

standard hydrogen electrode).[40] However, Li metal is highly reactive with solvents and violently reacts with water/air triggering uncertainty about safety, thus an optimisation of the electrode and electrolyte is necessary to ensure safe operation. The decomposition of the electrolyte in the first cycles creates a protective layer on the Li anode called solid electrolyte interphase (SEI) layer.[41] The SEI layer formed on Li metal anodes lack of strength and flexibility and therefore cannot withstand the large volume change during the repeated Li plating and stripping processes. It is thought that Li ions preferentially defuse to defects, which are generated on the surface of the SEI layer, thereby creating dendrites. Furthermore, due to the fresh metal anode constantly exposed to the electrolyte in each cycle, dendrite growth contributes to the cyclic damage-reconstruction of the SEI, leading to continuous electrolyte consumption, low Coulombic efficiency and safety hazard.[42] Commercial rechargeable Li-ion batteries generally employ liquid electrolytes containing thermally unstable salts (*e.g.*, hexafluorophosphate salts) and highly flammable organic solvents (*e.g.*, carbonates and ethers), which have caused in the past dangerous accidents including explosion and fire.[43] Hence, combining Li metal batteries with highly flammable organic electrolytes could result in even more dramatic incidents, developing non-flammable and SEI-forming electrolytes are primordial to ensure safe Li metal battery operation. Non-flammable liquid electrolyte systems have attracted numerous interest in the scientific and industrial community. Novel safe electrolyte systems flourished over the past decade, including highly concentrated electrolytes[44], fluoride/phosphate solvent-based liquid electrolytes,[45] novel fire-retardant additives,[46] deep eutectic solvent (DES)-based electrolytes,[47] aqueous electrolytes, *etc.* Furthermore, quasi-solid electrolytes also gain extensive importance as gelling of the liquid electrolyte can alleviate leakage issues and therefore, improves the battery safety.[48]

Fundamentally, aqueous electrolytes present intrinsic non-flammability, non-toxicity, ease of manufacture and attractive price. However, aqueous electrolytes provide a narrow electrochemical stability window (*i.e.*, 1.23 V for pure water) preventing the utilisation of low potential anode materials and Li metal anodes whose reaction with water is extremely vigorous. Owing to its stability in aqueous electrolyte, Zn metal has lately enticed extensive curiosity. Zn metal inherits many benefits such as low redox potential (Zn/Zn^{2+}: -0.762 V *vs.* standard hydrogen electrode (SHE)), high theoretical specific capacity (820 mAh g^{-1}) and

ultrahigh volumetric energy density (5854 mAh cm^{-3}), inexpensive raw material and inherent safety owing to Zn compatibility with aqueous electrolytes.[24] The divalent feature of Zn atom implies electrochemical reactions transferring two electrons per metallic cations, therefore increasing the energy density of Zn-based batteries. Zn rechargeable batteries (Zn||manganese oxide (MnO_2)) were first introduced with an alkaline potassium hydroxide (KOH) aqueous solution in 1986 but suffered from low Coulombic efficiency and rapid capacity fading due to irreversible reactions at the electrodes.[49] It is only in 2012 that "Zn-ion batteries" were introduced. Kang *et al.* demonstrated the intercalation of Zn^{2+} cation in the MnO_2 cathode when a mild aqueous electrolyte based on Zn sulphate ($ZnSO_4$) or Zn nitrate ($Zn(NO_3)_2$) salts was employed.[50] Zn-ion batteries commonly employed a Zn metal anode, a manganese oxide cathode and an aqueous electrolyte. However, several bottlenecks still need to be overcome such as Zn dendrite growth, Zn oxide (ZnO) passivation layer on the anode resulting in substantial polarisation of the anode, sluggish Zn^{2+} insertion process in the cathode, irreversible degradation of the cathode material and corrosion of the Zn metal anode.[51] Furthermore, the volume expansion and the continuous consumption of the electrolyte associated to these side reactions further impede long cycling stability of Zn-based batteries.[52] Therefore, further investigations into aqueous electrolyte applied in Zn metal batteries are essential to meet commercial battery standard requirements.

As per the aforementioned challenges, my research objectives are (1) developing electrolyte designs (*e.g.*, deep eutectic solvents, aqueous electrolytes and quasi-solid electrolytes) to tackle the safety issue faced by organic-based electrolytes, (2) investigating novel solvation structures in aqueous electrolytes to improve the cycling performance and energy density of aqueous-based battery systems, and (3) applying these electrolytes in different battery systems (e.g., Li metal batteries, Li-ion batteries and hybrid Li/Zn batteries). My research focuses on non-flammable electrolytes for Li and Zn -based batteries and is organised as follow:

- *Chapter II* reviews the latest advancement regarding safe electrolytes for Li including Li metal batteries and Li-ion aqueous batteries, and Zn-based batteries. Non-flammable liquid and quasi-solid electrolytes are summarized for both Li and Zn -based batteries.

- *Chapter III* thoroughly details the methodology employed to synthesize, characterize and test the battery components and their electrochemical performances when employed in batteries.
- *Chapter IV* presents a self-healing deep eutectic solvent gel electrolyte for Li metal batteries. The as-prepare gel electrolyte was *in-situ* synthesised by thermally polymerising a homemade monomer and a cross-linker monomer in the optimised deep eutectic solvent -based electrolyte. The formation of dendrite growths were suppressed allowing long cycling and increased safety of Li||LMO batteries at both room and elevated temperatures meanwhile the non-flammability of the electrolyte was retained.
- In *Chapter V*, I designed a localized highly concentrated aqueous electrolyte for safe Li-ion batteries based on LMO cathode and Mo_6S_8 anode by *in-situ* polymerizing of tetraethylene glycol diacrylate (TEGDA) monomer in the liquid electrolyte. The as-prepared localized "water-in-salt" (LWIS) gel aqueous electrolyte displayed a 3 V-electrochemical stability window which is similar to "water-in-salt" electrolyte without flammability or liquid leakage hazard. The Mo_6S_8|LWIS gel electrolyte|LMO battery showed a high cycling stability with 98.53 % Coulombic efficiency at 1 C.
- In *Chapter VI*, Zn was employed as anode in aqueous Zn||LMO hybrid battery. Herein, a molecular crowding strategy was implemented to enlarge the electrochemical stability window of the aqueous electrolyte, which was then suitable to accommodate the high voltage cathode LMO and Zn anode. Such battery delivered a high working potential of 1.85 V and operated for more than 400 cycles with an average Coulombic efficiency close to 100 %.
- *Chapter VII* summarizes the achievements of my Ph.D. thesis as well as further research directions.

CHAPTER II: Literature review

2.1 Battery operation and nomenclature

Batteries are composed of three main components: (1) two electrodes (a cathode and an anode), (2) an electrolyte and (3) a separator (**Figure 2.1**). Electrochemical cells can store and deliver electricity due to a difference of potential between two oxidation-reduction (redox) couples. A redox couple includes a reducing agent that donates one or several electrons and an oxidizing agent that can receive the electron(s). The transfer of electrons corresponds to the electrochemical reactions called oxidation (gain of electrons) or reduction (loss of electrons). These electrochemical reactions inversely occur at each electrode of the battery, therefore creating an electron flow, which travels in the external circuit meanwhile ions migrate in the electrolyte. A brief description of each battery compound is presented as following:

(1) The electrodes are defined by the electrochemical reactions occurring at their surface, *i.e.* the cathode is where a reduction happens and the anode is where the oxidation take place. However, in battery field, the term cathode always designates the positive electrode (*i.e.*, redox couple with the higher potential) and anode the negative one (*i.e.*, redox couple with the lower potential).

(2) Electrolytes own an important role in the electrochemical device as they regulate the ionic transport between the pair of electrodes and dictate the chemistry at the electrode/electrolyte interface. The vast majority of electrolytes are composed of one or several metal salt(s) (*e.g.*, Li salts for Li-based batteries, Zn salts for Zn-based batteries, *etc.*) dissolved in a solvent or a mixture of solvents. Additives are commonly introduced in the solvent to enhance the electrolyte's stability (*e.g.*, electrochemical stability, thermal stability, *etc.*) or to ameliorate the compatibility with electrodes. As intermediate medium between the electrodes, the electrolyte composition and properties are crucial for achieving high battery performances. The ionic conductivity, oxidative and reductive decomposition potential of the solvent, thermal stability, non-reactivity towards electrode materials, low cost, eco-friendliness are amongst the characteristics to be considered when synthesizing electrolytes.[53]

(3) The separator, as its name indicates, aimed to prevent contact between the anode and the cathode electrodes, and thus to avoid short-circuiting of the battery. Separators must be non- electronically conductive, thin and inert in contact with the electrolyte and electrode materials but more importantly they must have a good wettability toward the electrolyte and good thermal stability.[54]

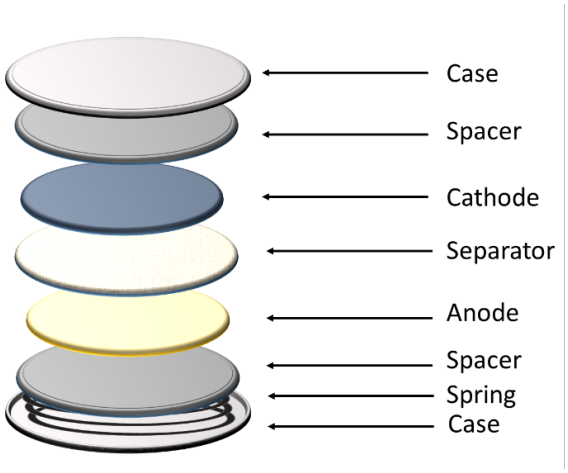

Figure 2.1. Schematic of a typical coin cell battery.

2.2 The development of batteries

Non-rechargeable batteries were first introduced mid-20th century. It was first observed in 1958 that lithium in a solution of lithium perchlorate ($LiClO_4$) dissolved in propylene carbonate (PC) could be electrodeposited.[55]. By late 1960's, non-rechargeable 3 V Li-ion batteries were already commercialised. In the meantime, the research community began to understand better the intercalation cathode mechanism leading to the emergence of rechargeable Li-ion batteries. In the 70's, Michel Armand proposed the idea of Li cations traveling back and forth between two intercalation electrodes with different potentials, commonly called the rocking chair mechanism.[56] Stanley Wittingham and co-worker discovered that layered titanium disulphide (TiS_2) cathode could chemically intercalate Li ions with a reasonable lattice expansion. They assemble a Li||TiS_2 battery, yet, some accidents such as explosions and fires due to the thermal runaway of the battery questioned the safety of these types of batteries. In order to solve the safety issue faced by Li metal batteries, two directions were adopted. The first one consisted in replacing the liquid electrolyte by solid electrolyte. Michel Armand's pioneering work on solid polymer electrolytes demonstrated the electrical properties of PEO-Li salt systems.[57] Solid-state electrolytes are regarded as a safe alternative to liquid

electrolyte for Li metal batteries owing to their ability to hinder dendrite growth. Although it is not the scope of this thesis, solid-state electrolytes are still attracting intensive interest to solve the safety issue faced by Li metal anode. The second direction concerned the anode, it was quickly understood that the replacement of Li anode by a less aggressive anode could also resolve the safety issue.[58] In 1976, Besenhard and Eichinger discovered that Li ions could reversibly intercalate and de-intercalate into and from graphite (C_6) anode.[59] However, the solvent co-intercalation induced the electrode structural collapse. In 1985, Akira Yoshino presented a petroleum coke (a less graphitized carbon issued from the residual petroleum fractionation) which could reversibly intercalate Li ions.[60] Regarding the electrolyte, Dahn and co-worker discovered that EC could form a stable SEI on graphitic anode preventing further electrolyte consumption and therefore reducing capacity fading.[41] In the meantime, John Goodenough and co-worker discovered three types of cathode materials that intercalated Li ions at high voltage >3.5 V: LCO[61], LMO[62] and polyanion oxide ($Li_xFe_2(XO_4)_3$, X=S, Mo, W, *etc.*)[63]. Asahi Kasei Corporation assembled a full cell battery based on the petroleum coke anode and LCO cathode, which Sony commercialised in 1991 making it the first lithium-ion battery on the market. Further research on the electrolyte enabled to increase the voltage and the energy density to 4.2 V and 400 Wh L^{-1}, respectively. In 1993, a novel electrolyte composed of lithium hexafluorophosphate ($LiPF_6$) salt dissolved in a mixture EC: dimethyl carbonate (DMC) was proposed by Guyomard and Tarascon.[64] This combination of a cyclic and a linear carbonate solvent provided the electrolyte with high anodic stability, high solvation of lithium salts and low viscosity which promoted improved ionic transport.[65] This new electrolyte type (*i.e.*, EC + one or several linear carbonate) set the direction of research for the state-of-the-art Li-ion electrolytes. Nowadays, these organic electrolytes remain widely used by battery manufacturers. To illustrate the importance of Li-ion battery research, in 2019 the Nobel Prize in Chemistry has been awarded to John B. Goodenough, M. Stanley Whittingham and Akira Yoshino for their extensive understanding and contribution to the development of Lithium-ion batteries.[66]

In the recent years, the research community endeavours to increase the energy density of batteries by investigating new electrochemical mechanisms. For instance, substituting intercalation electrode materials with conversion electrodes materials (*e.g.*, Li-sulphur batteries, *etc.*) or employing metal anodes based on plating and stripping processes (*e.g.*, Li

metal, Zn metal, *etc.*) have attracted extensive interest for next rechargeable battery technologies (**Figure 2.2**)

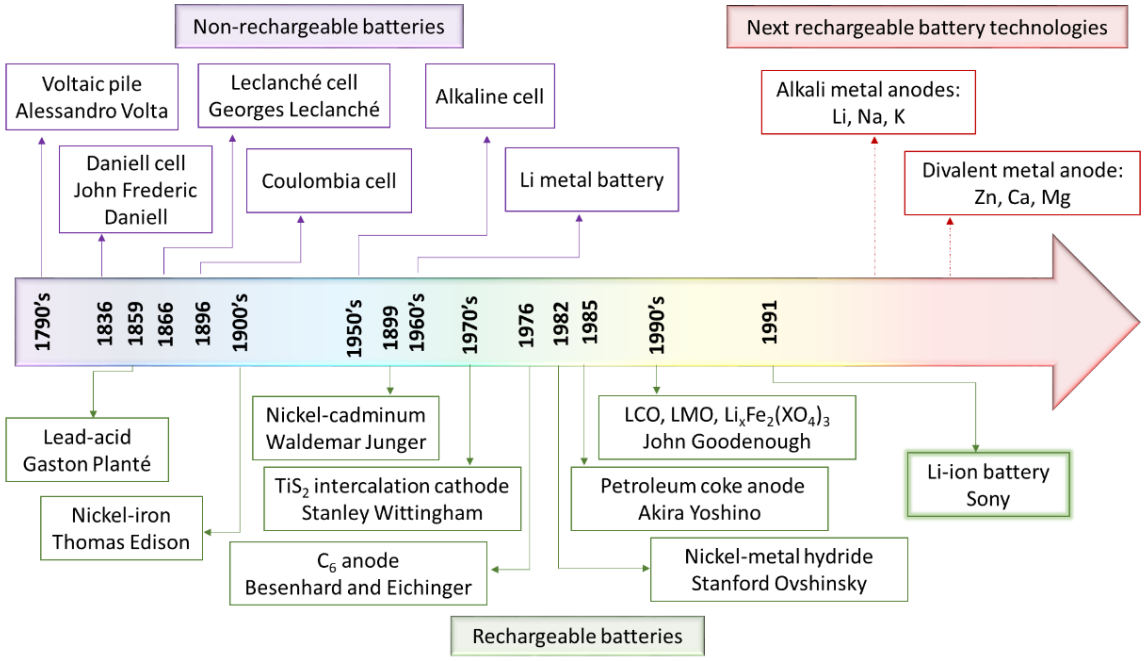

Figure 2.2. Battery development timeline. (K: potassium, Ca: calcium, Mg: magnesium)

2.3 Safety issue

The current commercial Li-ion batteries are generally employing toxic and flammable electrolytes based on organic solvents such as carbonates and ethers, and thermally unstable $LiPF_6$ salt. These electrolyte designs cannot ensure high safety as seen multiple times when batteries triggered fires or explosions. The thermal runaway mechanism of rechargeable Li-based batteries have been explored to understand how Li batteries can be at the origin of serious accidents.[43, 48, 67] Briefly, the stress caused by a mechanical, thermal or electrical abuse on the rechargeable battery result in an increase of the internal temperature, then, a succession of exothermic reactions leads to battery failure, fire or explosion. First, around 100 °C the SEI starts breaking and deteriorates thereby exposing fresh anode material and releasing flammable gases. Secondly, the decomposition of the electrolyte on the freshly exposed anode generates flammable hydrocarbon gases such as ethylene or ethane. Thirdly, around 130 °C, the separator made of polyethylene/polypropylene begins to decompose, thus short-circuits are likely to occur. This leads to a further increase of the internal temperature. Finally, when the temperature reaches 180 °C, the cathode material

deteriorates releasing even more gases that are flammable. The abnormally high internal pressure and temperature result in dangerous incidents such as explosion or fire of the battery. Such accidents is even more hazardous when thermally instable Li salts are employed in the electrolyte. For instance, Li salts based on hexafluorophosphate (PF_6^-) anions decompose into phosphorous pentafluoride species (PF_5) which are highly reactive with organic solvents and may produce extremely toxic gas (*e.g.*, hydrogen fluoride).[68]

Increasing the energy density of rechargeable batteries by replacing the electrodes with high voltage redox couples inevitably results in more dramatic consequences in case of an incident. Similarly, batteries relying on metal anodes (*e.g.*, Li metal, Zn metal) are prone to dendrite growth and early short-circuits, which also increase the safety issue. Therefore, developing non-flammable electrolytes goes hand in hand with developing the next battery generation. To measure the flammability of an electrolyte, several tests have been adopted as detailed below.[45b] Although these methods are yet to be normalized, the result enables sufficient information on the flammability of the electrolyte.

(1) Direct ignition test, where the sample is exposed an ignition source and the combustion is observed. This is a qualitative technique easy to perform with liquid and quasi-solid samples.

(2) Horizontal burning test consist of introducing the sample in a wick and measuring the flame propagation after ignition. This method is suitable for quantitative measure of the flame-retardant ability of liquid, quasi-solid and solid sample.

(3) Limited oxygen index (LOI) is based on measuring the oxygen needed to burn the sample of a specific mass during 60 s. LOI requires extra equipment to measure the oxygen concentration.

(4) Self-extinguishing time (SET) measures the sample flammability by recording the time of burning versus the mass of the sample (s g^{-1}). When SET < 6 s g^{-1}, the sample is non-flammable; when SET is between 6 and 20 s g^{-1}, the sample is flame retardant; and, when the SET > 20 s g^{-1}, the sample is flammable.[69]

Regarding Zn-based batteries, Zn metal was firstly introduced as anode in commercial primary batteries, however in the nineties, they lost attraction to the more energy density efficient and rechargeable Li-ion batteries. Over the past decade, Zn rechargeable batteries gained intensive attention as beyond Li-ion energy storage systems owing to the metal abundance

in the earth crust, making it a cheap alternative to the more expensive Li metal anode. Although, Zn batteries suffer from low operation voltage due to the low potential Zn intercalation cathode material generally employed (*e.g.*, MnO_2). An interesting approach to face this issue involve replacing Zn intercalation cathode by Li intercalation cathode material. For instance, LMO can be employed as cathode material in Zn/Li hybrid batteries. Such battery design requires the development of hybrid electrolytes containing Zn and Li salts. Theoretically, during the charging process, Zn ion are stripped from the Zn anode meanwhile Li ions intercalate in the Li intercalation cathode. During the discharge process, the reverse reactions occur: Zn ions are plated on the Zn anode while Li ions are extracted from the cathode.

2.4 Non-flammable liquid electrolytes

2.4.1 Non-flammable organic electrolytes

The thermal run-away comes from the increase in the internal temperature and pressure in the battery. The decomposition of organic solvent produces free radicals (*e.g.*, H•) which in turn can react with gases or trace water in the electrolyte to produces other free radicals (*e.g.*, R•, H•, O• and OH•), thereby maintaining the combustion reaction (**Equations 2.1-2.4**). Therefore, the flammability of organic electrolytes can be alleviated or retarded by either scavenging free radicals, or employing more thermally stable solvents.[45b, 70]

$RH \rightarrow R\bullet + H\bullet$ (**2.1**)

$R\bullet + O_2 \rightarrow ROO\bullet$ (**2.2**)

$H\bullet + O_2 \rightarrow HO + O\bullet$ (**2.3**)

$O\bullet + H_2 \rightarrow HO\bullet + H\bullet$ (**2.4**)

2.4.1.1 Hydrogen radical scavenging

Phosphate-based solvents are employed as fire inhibiter owing to their hydrogen radical scavenging properties. When the internal temperature increases in the battery, the phosphate species decompose into free radicals. Subsequently, these radicals recombines with free radicals already present in the electrolyte issued from the decomposition of the organic solvent.[45b] Therefore, the reaction chain is stopped and the flammability of the electrolyte is retarded or even suppressed. Phosphate solvents such as alkyl phosphates (*e.g.*,

trimethyl phosphate (TMP)[71], triethyl phosphate (TEP)[72], *etc.*) are fireproof, inexpensive and non-toxic, which make them of a great interest for electrolyte solvents. However, they are generally chemically instable against anodes, thereby preventing the direct application of this type of solvent in batteries.

To overcome this challenge, several electrolyte designs have been investigated. SEI-forming additives such as fluoroethylene carbonate (FEC) and vinylene carbonate (VC) have been introduced in small amount (*e.g.*, 2 %) into 1.0 M lithium bis(trifluoromethane sulfonyl)imide (LiTFSI) in TEP and applied in Li metal batteries with lithium iron phosphate ($LiFePO_4$, LFP), lithium titanium oxide ($Li_4Ti_5O_{12}$, LTO) and lithium nickel manganese cobalt oxide ($LiNi_xMn_yCo_zO_2$, NMC) cathodes.[72] The presence of FEC or VC enabled to create a protective film on the anode, thereby improving the cycling performance of the batteries while TEP solvent provides non-flammability. Fluorinated diluents such as 1,1,2,2-tetrafluoroethyl 2,2,3,3,-tetrafluoropropyl ether (HFE) were employed as co-solvent. For instance, Takada *et al.* introduced HFE into concentrated lithium bis(fluorosulfonyl)amide (LiFSA) /TMP electrolyte.[73] The as-prepared electrolyte retained non-flammability and passivation ability meanwhile the viscosity was decreased in comparison with the non-diluted electrolyte.

Another approach consisted in modifying the structure of the phosphate solvent molecule by substituting some carbon (C) atoms with fluoride (F) atoms, which enabled to stabilise further the electrolyte. Zheng *et al.* synthesised a fluorinated cyclic phosphate solvent (**Figure 2.3**a).[1] The cyclic carbonate species contributed to the formation of a stable SEI meanwhile the organic phosphates could trap hydrogen radicals, thus preventing combustion.

Finally, increasing the salt concentration can improve the electrochemical performance of the electrolyte by trapping the solvent molecules. In super-concentrated electrolytes, the formation of contact ion-pairs (anions coordinating to one Li^+) and aggregate clusters (anions coordinating with two or more Li^+) due to the scarcity of free solvent molecules, results in advantageous properties such as reduction of side reactions. Shi *et al.* presented a 5 M lithium bis(fluorosulfonyl)imide (LiFSI) in TMP which showed compatibility with graphite anode and remained non-flammable.[71] Furthermore, the corrosion of aluminium (Al) current collector was suppressed owing to the scarcity of free solvent molecules. Recently, Zheng *et al.* demonstrated that the key to stable electrolyte/electrode interface was the molar salt to

solvent ratio.[74] In their study, the ideal molar salt to solvent ratio was equal to 1: 2. By employing LiFSI-TEP (1: 2) electrolyte, the non-flammable battery delivered electrochemical performance comparable to that based on carbonate electrolyte.

Although phosphate-based solvents, co-solvents and additives are the primary fire-retardant chemicals employed in electrolyte design, other radical scavenger compounds have been identified. Han *et al.* provided a detailed review on scavenging additives for electrolytes based on $LiPF_6$ lithium salts and carbonate solvents.[75] They highlighted different mechanisms and chemical compounds to scavenge PF_5, hydrogen fluoride (HF), water (H_2O), therefore inhibiting the flammability of organic carbonate-based electrolytes.

2.4.1.3 Thermal stability

Employing thermal stable solvents can also limit flammability as the decomposition of the solvent is delayed. Fluorinated solvents present higher thermal stability owing to the numerous carbon-fluorine (C-F) bonds, which have a high binding energy (*e.g.*, C-F binding energy = 105.4 kcal mol^{-1}, carbon-hydrogen (C-H) binding energy = 98.8 kcal mol^{-1}).[76] Therefore, the breakage of the C-F bonds requires superior energy (*i.e.*, higher internal temperature) than for C-H bonds.[77] Moreover, less hydrogen atoms are present in the fluorinated electrolyte structure, thus less H• free radicals are likely to be formed. In addition, fluorinated solvents such as FEC are known to form a protective SEI layer on Li metal[78], graphite[79] and other anode materials.[80] In Li-ion or Li metal batteries, some decomposition product of fluorinated solvent have been highlighted as highly beneficial for anode stability and dendrite suppression. Amongst them, lithium fluoride (LiF) is thought to improve the robustness of the SEI owing to its high mechanical strength (*i.e.*, shear modulus of ~65 GPa *vs.* 4.9 GPa for Li metal).[81] However, fluorinated solvents generally present lower Li salt dissociation and higher viscosity than carbonate or ether -based solvents.[77] To overcome this issue, fluorinated solvents are often employed as co-solvent or additives. For instance, by introducing fluorinated ether (1,1,2,2-tetrafluoroethyl-2,2,3,3-tetrafluoropropyl ether (TTE) and FEC into carbonate-based electrolyte, Hagos *et al.* optimized 1 M $LiPF_6$ in FEC/TTE/ethyl methyl carbonate (EMC) electrolyte (in the volume ratio 3: 5: 2).[82] Such electrolytes displayed non-flammability and high oxidative stability up to 5.3 V. A non-flammable all fluorinated electrolyte was designed in which 1 M $LiPF_6$ was dissolved in a mixture of FEC, 3,3,3-fluoroethylmethyl carbonate and 1,1,2,2-tetrafluoroethyl-2',2',2'-trifluoroethyl ether

(FEC: FEMC: HFE, 2: 6: 2 by weight).[83] Such optimised electrolyte enable high cycling stability of a 5 V battery based on $LiCoCP_4$ cathode and Li metal anode.

Other organic non-flammable solvents have been investigated due to their high thermal stability including nitriles, sulfones and organosilicons. Nitrile-based solvents such as adiponitrile (ADN) and acetonitrile (AN), present high oxidation potentials (*e.g.*, 6 V for an electrolyte composed of 1 M LiTFSI salt dissolved in ADN) and large temperature range operation (*e.g.*, between -30 °C to 180 °C for 1 M LiTFSI salt dissolved in ADN).[84] However, nitrile species suffer from poor cathodic stability and are unable to protect anode materials due to their inability to form stable SEI layers. In particular, Li metal catalyses the polymerization of nitriles which contribute to spontaneous side reactions.[85] Therefore, salt concentration and additives have been tailored to stabilise the electrolyte/anode interface and improve cycling performance of the batteries. A super-concentrated electrolyte based on 3.5 M LiFSI in 1,3-bis(cyanopropyl)tetramethyl disiloxane solvent was explored.[85] As previously explained, free solvent molecules are depleted in super-concentrated electrolytes, therefore the reactivity of nitrile groups of disiloxane with Li metal is alleviated. In addition, two additives were investigated: 0.5 wt% lithium difluoro(oxalato)borate (LiDFOB) and 5 wt% of FEC were introduced in the electrolytes to further improve the electrochemical performance.

Sulfone-based solvents present high electrochemical and thermal stability, which contributes to low flammability. Alvarado *et al.* developed a single sulfone-based electrolyte containing 3.0 m LiFSI lithium salt and tetramethylene sulfone solvent, thereby creating a concentrated electrolyte.[86] Although no SEI-forming additives were introduced in the electrolyte, a SEI and cathode electrolyte interphase (CEI) protective layers were observed on the anode and cathode, respectively. Similar to super-concentrated electrolytes, the reduction of FSI^- anions drove the SEI/CEI formation. Therefore, the full cell displayed extended thermal and electrochemical stability as well as non-flammability. In order to improve the formation of protective layers on the electrodes, several groups investigated fluorinated sulfone compounds. Su *et al.* investigated the oxidative stability of several fluorinated sulfone electrolyte for high voltage Li ion batteries.[87] Although trifluoromethyl ethyl sulfone (FMES) and trilfuoromethyl propyl sulfone (FMPS) displayed the highest oxidative stability, these fluorinated sulfones have a poor non-flammability feature.[2] Recently, a new class of

fluorinated sulfone was designed by studying the position of the F atom (**Figure 2.3**b).[2] In comparison with α-fluorinated sulfones such as FMES and FMPS, β-fluorinated sulfones (*e.g.*, 1,1,2,2-tetrafluoro-3-(methylsulfonyl)propane, TFPMS) have a slightly smaller oxidative stability but lower reduction potential which make them compatible with graphite anode.[88] Furthermore, it was observed that TFPMS retained non-flammability. The best cycling performance of graphite||NMC622 full battery was obtained by mixing TFPMS with another fluorinated carbonate solvent such as FEC and difluoroethylene carbonate (DFEC) owing to the contribution of the fluorinate carbonate to stabilise the electrodes.[2] Finally, super-concentrated and localized super-concentrated sulfone based electrolyte were also investigated.[89] By introducing a non-solvating fluorinated ether TTE in a super-concentrated LiFSI-tetramethylsilane (TMS) electrolyte, the side reactions between TMS solvent and Li metal were alleviated. Therefore, a Li||$LiNi_{0.5}Mn_{1.5}O_4$ (LNMO) battery could achieve high cycling performance even at sub-zero temperature. To perform well, the batteries were preconditioned by cycling for 2 cycles at C/10 and then at C/3 for the charge and discharge processes.

Although fewer studies on organosilicon-based solvents are available, this family of solvent (*e.g.*, silane and siloxane) possesses high thermal resistance, low flammability and eco-friendliness, which are attributes to consider for electrolyte designs. Organosilicon solvents as co-solvents were introduced in carbonate-based electrolytes to improve safety. Yan *et al.* designed an organosilicon ($CN(CH_2)_2Si(CH_3)(OCH_2CH_2OCH_3)_2$, BNS) which was mixed in 20 vol% with 1 M $LiPF_6$ in EC/EMC/DEC commercial electrolyte.[68] The presence of BNS molecules in the electrolyte enabled the graphite||NCM battery to improve safety performance during nail penetration test. Amine *et al.* highlighted that siloxane solvents in concentrated electrolytes can eliminate the solvation-ion-exchange process happening in Li-sulphur batteries.[90] When the concentrated siloxane-based electrolyte (*i.e.*, 5.0 M LiTFSI in siloxane) is employed in Li-sulphur batteries, the charging/discharging mechanism involves a one-step solid-solid lithiation meanwhile Li stripping/plating was extremely stable. Increasing the salt concentration not only enhance safety but also contribute to the improvement of the cycling performance due to the scarcity of free solvent molecules.

2.4.1.4 Salt selection and concentration

As mention previously, electrolytes containing $LiPF_6$ lithium salts are more prone to safety hazard due to the decomposition of PF_6^- anions into PF_5 and toxic gases at relatively low temperature (*i.e.*, between 100 and 200 °C depending on the experimental conditions), and its exothermic reaction with organic solvent.[91] Replacing $LiPF_6$ by a more thermally stable lithium salts such LiTFSI, LiFSI, lithium tetrafluoroborate ($LiBF_4$) which possess higher decomposition temperature have been investigated to improve safety.

In addition, fabricating highly concentrated electrolytes can suppress flammability by reducing the solvent molecules activity.[92] In 2006, Henderson's group investigated the phase diagrams of several glyme-Li salt mixture in order to elucidate the molecular interactions occurring in such systems.[93] They provided a correlation between the Li solvation variation and the ionic association strength of the Li salt. Later on, concentrated glyme-cyclic imide lithium salt mixtures were employed in lithium batteries.[94] These early discoveries opened up a new approach to the development of concentrated electrolytes for Li battery systems. In highly concentrated electrolyte, the number of solvent molecules present in the electrolyte is insufficient to entirely solvate the ions. Therefore, interionic attraction increases creating ion-pairs and ion-aggregates where anions enter the first solvation sheath of cations. The alteration of the molecular arrangement in super-concentrated electrolytes affects numerous properties such as ionic conductivity and viscosity, electrochemical stability, and interfacial properties.[95] Furthermore, the number of free solvent molecules is close to zero, thus the reactivity and volatility of the solvent is minimized meanwhile the formation of SEI layers is driven by anionic decomposition in opposition to the solvent-driven SEI layer formation in dilute electrolytes.[44] Shiga *et al.* designed a self-extinguishing super-concentrated electrolyte based on tris(trifluoroethyl) phosphate (TFEP) solvent and LiFSA salt.[96] The synergetic effect of the super-concentrated electrolyte and fluorinated alkyl phosphates enabled a safe operation of graphite||$LiNi_{0.8}Co_{0.15}Al_{0.05}O_2$ batteries with a charge-discharge current ranging from 0.02–1.0 mA cm^{-2} with a cut-off for the graphite disk of 0.03–1.8 V.

Although highly concentrated electrolytes benefit from large electrochemical stability, high thermal stability and SEI forming properties, the large amount of expensive salt necessary for their fabrication increases consequently the price of the electrolyte. Moreover, high viscosity and lower ionic conductivity are also issues to resolve before practical application. In order to

overcome the latter issues, diluents or counter-solvents, which are miscible with the solvent but non-solvating toward Li salts, were introduced in highly concentrated electrolytes. In such electrolytes, commonly called localized highly concentrated electrolytes, the solvation structure of highly concentrated electrolytes is preserved locally meanwhile the cost is dramatically reduced. It is noted that the non-flammability of the electrolytes depends on the diluent and/or solvent properties and their ratios.[73] Wu *et al.* presented a localized concentrated electrolyte based on 1.2 M LiFSI + TEP/ bis(2,2,2-triflfluoroethyl) ether (BTFE) + 0.01 M 2-fluoropyridine.[3] Although BTFE is highly flammable, when mixed in the non-flammable concentrated electrolyte, the as-prepared localized super concentrated electrolyte retained non-flammability (**Figure 2.3**c). Piao *et al.* introduced TTE as diluent into the LiFSI/DMC electrolyte (DMC: TTE, 1: 1 by mol).[97] The introduction of TTE solvent into the carbonate-based electrolyte favoured the interaction between Li^+ and FSI^- leading to a LiF-rich SEI layer formation on the anode, meanwhile preventing flammability. Various diluents were investigated experimentally and theoretically, amongst them fluorinated ethers and fluorinated phosphates are attracting wide interests.[98]

Although non-flammable organic electrolytes includes many different electrolyte designs, their toxicity and cost remain superior to deep eutectic solvents and aqueous electrolytes. During my Ph.D. thesis, I chose to focus my attention only on the two latter electrolyte families. Therefore, I will only develop deep eutectic solvents and aqueous electrolytes in the following parts.

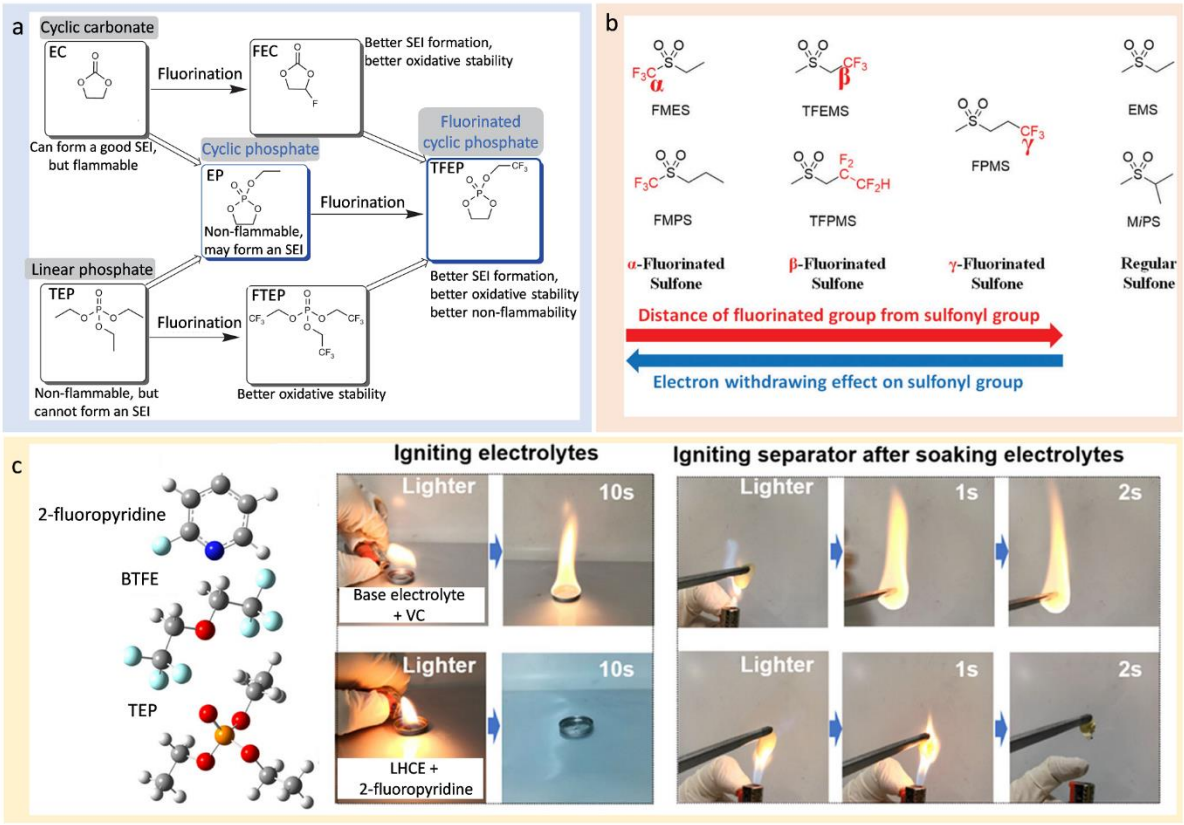

Figure 2.3. (**a**) Route design of fluorinated cyclic phosphate TFEP. Reproduced with permission.[1] Copyright 2020, Springer Nature. (**b**) Sulfones with fluorinated group in different position. Reproduced with permission.[2] Copyright 2021, Royal Society of Chemistry. (**c**) Flammability test of base electrolyte + VC and localized highly concentrated electrolyte (LHCE) + 2-fluoropyridine. Reproduced with permission.[3] Copyright 2021, American Chemical Society.

2.4.2 Ionic liquids and deep eutectic solvent electrolytes

2.4.2.1 Ionic liquids (ILs)

ILs are entirely composed of anionic and cationic species, which are defined as molten salts. They usually exhibit specific properties such as low melting point (< 100 °C), non-volatility, non-flammability and high thermal stability, thereby endowing high safety.[99] The physicochemical and electrochemical properties are intimately dictated by the anion-cation interactions, which can be adjusted by controlling the ILs composition.[100] Generally, IL-based electrolytes for battery applications are composed of a neat IL (organic cations and inorganic or organic anions), which is mixed with metallic salts (*e.g.*, Li salts, Zn salts, *etc.*). There are different types of ionic liquids: hydrophilic, hydrophobic, ionic, zwitterionic, *etc.* Depending

on the battery system, specific electrolyte properties would be more adequate. For instance, hydrophobic ILs for Li-ion batteries, while hydrophilic ILs for Zn batteries might be more suitable. Furthermore, the synthesis of ILs are significantly more eco-friendly than commercially available carbonate-based electrolytes. Developing "Green Chemistry" for energy storage is fundamental to reduce the carbon footprint of battery manufacturing.[101]

- Ionic liquid for lithium-based batteries

ILs employed as electrolytes for Li-batteries gain enormous interest recently, especially for Li metal batteries and high voltage cathode materials for which the electrolyte must display high safety and large electrochemical stability window. Numerous metallic salts were investigated in IL-based electrolytes, it was understood that the metal anion plays a major role in improving the ionic conductivity. For instance, Moreno *et al.* investigated the influence of the anions on the ILs electrochemical properties.[102] The N-butyl-N-ethylpyrrolidinium bis (fluorosulfonyl)imide/lithium bis(fluorosulfonyl)imide (PYR_{24}FSI-LiFSI) electrolyte displayed superior ionic transport and electrochemical stability than N-butyl-N-ethylpyrrolidinium-bis(trifluoromethanesulfonyl)imide (PYR_{24}TFSI-LiTFSI). It was suggested that the steric hindrance of the FSI anions contributed to high ionic conductivity and low viscosity. Although the deep understanding of the relation between ionic conductivity and viscosity with the ILs chemical structure still remains a great challenge. Additionally to high ionic conductivity, a large electrochemical stability of the electrolyte is primordial to build high energy density batteries. The oxidation and reduction of the anions and cations, respectively, are responsible for the electrochemical stability of ILs.[103] The commonly employed neat ILs based on pyrrolidinium and imidazolium cations, exhibit a cathodic limit between -2.0 to -3.0 V *vs.* Ag/AgCl, meanwhile the anodic limit depends on the anions. However, introducing Li salts in the ILs usually results in a widening of the electrolyte stability window.[104]

To enhance further the electrochemical stability of ILs, especially towards Li metal anode, various work investigated the electrode/electrolyte interface chemistry. The formation of an SEI layer in the initial cycling of Li metal batteries is primordial to attain long cycling performance with high Li plating/stripping efficiency.[105] Several strategies have been explored such as increasing the Li salt concentration and introducing a co-solvent. Similarly to organic highly concentrated and aqueous "water-in-salt" electrolytes, increasing the Li salt

concentration in ILs have divers benefits such as improve cycling performance, resistant SEI layer formation, and wide electrochemical stability window. Wang *et al.* presented a IL-based localized highly concentrated electrolyte for Li metal batteries by mixing LiFSI as Li salt, N-methyl-N-propyl-piperidinium bis(fluorosulfonyl)imide ($[PP_{13}][FSI]$) as IL and HFE as diluent.[106] HFE is non-flammable and contributes to lower the viscosity while increasing the ionic conductivity of the IL-based electrolyte. The investigation of the Li^+ solvation structure informed that HFE molecules promote more FSI anions to participate in the Li^+ solvation sheath. Therefore, the resulting SEI formed on the anode displayed high content of inorganic species, which are recognised to contribute to robust protective layer. Owing to the superior physico-chemical properties of the electrolyte and the strong SEI layer, the as-prepared electrolyte hindered the growth of dendrites during cycling even at high current density (10 mA cm^{-2}), meanwhile Li||LFP full cells exhibited a capacity retention of 87 % after 1000 cycles at 5 C. Introducing a co-solvent constitutes another approach to improve the electrochemical performance of IL-based electrolytes. Recently, Pal *et al.* introduced 20 wt% of DME into 3.2 m LiFSI N-propyl-N-methylpyrrolidinium bis(fluorosulfonyl)imide (C_3mpyrFSI) IL to control the interphase Li metal| IL electrolyte.[107] The XPS analyses of the SEI on the anode after cycling showed that the presence of DME perturbs the FSI decomposition mechanism. It seems that the SEI presented high content of Li, resulting in a more homogenous Li ion flux, and oligomeric product (ROxLi), which increased the SEI flexibility. Furthermore, this electrolyte stabilised the high voltage cathode NMC811 and NMC622, leading to outstanding cycling performance of high energy density batteries at high current density.

Tuning the electrolyte compositions by introducing different concentration of Li salts and co-solvents is widely accepted as method to improve the battery cycling performance. However, understanding the interfacial chemistry at the electrode| electrolyte is necessary to optimise and control the SEI formation mechanism. It was shown that increasing the Li salt concentration in ILs can significantly enhance rate capability owing to the increase in Li transference number.[108] Interestingly, the 3.2 m LiFSI in $[C_3$mpyr$][FSI]$ IL allowed the formation of a LiF-rich SEI layer at high current density (20 mA cm^{-2}) without formation of dendrite, while at low current density of 1 mA cm^{-2} the surface of the anode showed dendritic morphology with the absence of high fluorinated content.[109] More recently, it was found that with the 3.2 m LiFSI in $[C_3$mpyr$][FSI]$-DME (mass ratio 80-20) electrolyte, the current

density of 6.0 mA cm^{-2} at 1.0 mAh cm^{-2} is optimal to supply Li^+ cations from the bulk electrolyte to the electric double layer, thereby leading to a stable SEI composed of mixed organic and inorganic compounds.[105] The preconditioning protocol of Li batteries depends on the electrolyte composition, therefore, uncovering the ideal preconditioning for each electrolyte is critical to achieve high cycling performance.

- Ionic liquid for zinc-based batteries

The Zn chemistry has been recently investigated, especially a smooth Zn electrodeposition for corrosion resistance was demonstrated with various ILs.[110] For battery operation, efficient Zn plating and Zn stripping is essential for high reversibility. ILs such as alkoxyl-ammonium, imidazolium and pyrrolidinium –based ILs were employed as electrolytes for Zn-ion batteries.[111] Simons *et al.* studied two different ionic liquid-based electrolytes: (1) 1-ethyl-3-methylimidazolium dicyanamide (C_2mim-dca) and (2) N-butyl-N-methylpyrrolidinium dicyanamide (C_4mpyr-dca), both containing 3 wt% H_2O and 9 mol% $Zn(dca)_2$. When applied in Zn symmetric cells, the former IL could sustain over 90 cycles at 0.1 mA cm^{-2}, while the latter suffered from poor plating and stripping, achieving only 15 cycles at 0.05 mA cm^{-2}.[112] It was observed that the deposition overpotential between the two electrolyte varied, which may have resulted from electrode/electrolyte interfacial disparities. The structure of the ILs and Zn salts, and their interactions dictate the Zn plating and stripping mechanism. It was suggested that the anions of the ILs influence the Zn plating and stripping, whereas the cations may play a role in the Zn deposition.[113]

Several liquids (*e.g.*, H_2O, DMSO)[114] and solids (*e.g.*, $Ni(TfO)_2$[115], 2-methylimidazole[116]) additives were introduced in ILs to ameliorate the Zn batteries performances. For instance, a small amount of water was present in the electrolytes to facilitate Zn^{2+} mass transport and decrease the viscosity of the electrolyte. At a molecular level, the Zn cation coordinate either with water molecules or with IL anions to form complex anions. The hydrated complexes usually present higher diffusion rate, which leads to enhance redox kinetics and decrease the overpotential.[114] However, introducing water molecules reduces the electrochemical stability window of the electrolyte and can facilitate corrosion reactions, which are the main limiting issues in aqueous Zn-battery systems. Liu *et al.* studied the Zn dendrite growth in 1-butyl-1-methylpyrrolidinium trifluoromethylsulfonate ($[Py_{1,4}]TfO$) containing $Zn(TfO)_2$.[115]

They found out that the addition of $Ni(TfO)_2$ could inhibited dendrite growth by forming a thin Zn-Ni alloy on the surface as well as a SEI layer, attesting of the superior Zn metal stability in the ILs containing the additive. Engineering ILs to increase Zn plating and stripping reversibility, and suppress dendrite growth by the means of electrolyte additives seems a promising approach.

- *Poly(ionic liquids)*

Poly(ionic liquids) (PILs) are synthesised by the polymerisation of IL monomers. Usually, PILs are categorised as follow: (1) polycation in which cations are covalently bonded to the polymer, (2) poly(zwitterion) in which both cations and anions are covalently bonded to the polymer and (3) polyanion where the anion is covalently bonded to the polymer.[117] PILs present other advantages than ILs such as enhanced safety, flexibility, high metal cation transference number, *etc*.

Wang *et al.* studied several Li salt concentrations in a composite electrolyte polymer.[118] The PIL composite electrolyte, incorporated into PVDF fibers, was composed of LiFSI in C_3mpyrFSI IL mixed with poly(diallyldimethylammonium) bis(trifluoromethanesulfonyl)imide (PDADMA NTf_2,) 60: 40 in weight ratio). It was observed that when the Li salt concentration increased, the diffusivity decreased whereas the Li transference number increased. Owing to the Li transference number, the Li batteries assembled with Li metal anode and high voltage cathodes such as NMC and NCA cycled successfully with high areal capacity of 1.1 mAh cm^{-2}. PILs can also be prepared by *in-situ* polymerisation, which can be beneficial to improve the electrolyte/electrode contact. Huang *et al.* polymerized 1-vinyl-3-dodecylimidazolium bis(trifluoromethanesulfonyl) imide (VDIM-TFSI) inside a porous membrane (PVDF-HFP).[119] Furthermore, the mobility of TFSI anions from the PILs was impeded by cross-linking the as-prepared quasi-solid electrolyte with PEGDMA, thereby Li cation transference number was enhanced. The optimised PIL electrolytes cycled well in Li symmetric cells (*i.e.*, over 1000 h at 0.1 mA cm^{-2}) and in full Li||LFP batteries (*i.e.*, 100 cycles at 0.1 C).

ILs trapped in polymer matrix have also been employed in Zn –based batteries, for instance as thin protective film on Zn metal anode. Such quasi-solid IL electrolytes differ from PILs because none of the anions or cations ILs are part of the polymer backbone. Lee *et al.* employed a hydrophobic IL (1-butyl-1-methylpyrrolidinium bis(trifluoromethylsulfonyl)imide

(BMPTFSI)) mixed with $Zn(TFSI)_2$ and a UV-polymerised thiol-ene polymer (trimethylolpropane tris(3-mercaptopropionate) (TMPMP) and trimethylolpropane triacrylate (TMPTA)).[120] The as-prepared precursor solution was UV-polymerised on the Zn anode, and subsequently Zn-ion full cells (protected Zn anode||MnO_2) were assembled with aqueous electrolytes. The protective film answers two characteristics, ILs must not be soluble in water, and ILs must dissociate the Zn salts. It was demonstrated with NMR analyses that the anions in the ILs play a crucial role in the hydrophobicity of ILs. BMPTFSI not only is immiscible with water, but also dissolves $Zn(TFSI)_2$. This approach enabled to suppress the side reactions due to water molecules on the Zn anode, meanwhile improving the interface electrolyte/electrode.

2.4.2.2 Deep eutectic solvents (DESs)

DESs have recently attracted intensive interest from the research community as low-cost alternative to ionic liquids as they share many similarities. DESs consist in a eutectic mixture of at least two chemical compounds, one hydrogen bond donor and one hydrogen bond acceptor. Due to the charge delocalization occurring through hydrogen bonding, the mixture forms a liquid with a melting temperature largely inferior to that of each chemical taken separately.[121] The lower melting point of DESs results from intimate interactions such as hydrogen bonds, Lewis acid-base and Van der Waals interactions which contribute to decreasing the lattice energy of the mixture.[122] The first DES was discovered by Abbott *et al.* by mixing choline chloride (hydrogen bond acceptor) with urea (hydrogen bond donor).[123] DESs employed as electrolytes in Li-based batteries generally contain Li salt as Lewis acid (*e.g.*, LiTFSI, lithium nitrate ($LiNO_3$), *etc.*) mixed with as Lewis base (*e.g.*, urea, acetamide, *etc.*).[47] For instance, the eutectic mixture of LiTFSI (melting point: 234 °C) and N-methylacetamide (NMAc, melting point: 28 °C) in molar ratio 1: 4 formed a liquid electrolyte stable at extremely low temperature (up to -70 °C) (**Figure 2.4**a).[4] DESs recently gain extensive interest as electrolyte in batteries due to their low cost, non-flammability, reduced toxicity, solvent-free and electrochemical stability.

- Deep eutectic solvents for lithium-based batteries

In the past decade, various DESs electrolyte compositions were investigated. Boisset *et al.* studied the physical and electrochemical properties of three DESs based on LiTFSI: NMAc

(molar ratio 1: 4), $LiNO_3$: NMAc (molar ratio 1: 4) and $LiPF_6$: NMAc (molar ratio 1: 4).[4] LiTFSI/NMAc DES electrolytes exhibited high ionic conductivity (1.35 mS cm^{-1} at 25 °C), low viscosity (78.38 mPa s) and low melting point (-72 °C). The polarity of amide functional groups favours the destruction of the ionic bond between Li^+ and its anion; thereby amides can easily dissociate Li salts and create DESs (**Figure 2.4**a).

To improve further the electrochemical stability against electrodes (*e.g.*, Li metal anode) and physical properties (*e.g.*, viscosity) of DES electrolytes, several approaches were explored such as introducing co-solvents and co-salts. Our group synthesized a LiTFSI: NMAc (molar ratio 1: 4) DES electrolyte.[47] By introducing 10 wt% FEC in the DESs, a Li||LMO full cell achieved more than 200 cycles with high Coulombic efficiency. The high electrochemical performance ensues from the formation of an F-rich SEI formation on the anode and CEI on the cathode as explained into more details in *Chapter IV*. Similarly, Dinh *et al.* introduced 10 wt% EC in LiTFSI: trifluoroacetamide (molar ratio 1: 4) DESs to improve the cycling performance of Li||LMO batteries.[124] However, it was observed that introducing 20 wt% of EC in the DES resulted in poorer cycling performance of Li||LMO batteries (*i.e.*, DES + 10 wt% EC: discharge capacity of 104 with 84 % efficiency, vs. DES + 20 wt% EC: discharge capacity of 50 with 62 % efficiency). Other strategies were investigated, for instance a dual-anion DES (D-DES) electrolyte was created with succinonitrile (SN) and two lithium salts, namely lithium difluoro(oxalato)borate (LiDFOB) and LiTFSI.[5] The high concentration in Li salt leading to the intimate interaction with SN molecules restrained side reactions between the electrolyte and Li metal anode. Furthermore, LiDFOB created an SEI layer on the Li anode, leading to dendrite free deposition (**Figure 2.4**b). The cathode was also protected owing to the decomposition of LiTFSI and LiDFOB salts, thereby creating a CEI layer. The Li|D-DES|LCO battery delivered outstanding electrochemical performance (*i.e.*, capacity retention over 70 % for 500 cycles with a high charging voltage of 4.7 V) and safety.

Some DESs electrolytes synthesised in atmospheric conditions demonstrated that the presence of trace amount water in the DESs had a mild effect on the electrochemical performance of LTO||LFP batteries.[4] Besides, the presence of water could be beneficial to reduce viscosity and improve ionic transport, as well as decrease the cost of the electrolyte (*e.g.*, utilisation of hydrated Li salts, synthesis without inert gases, *etc.*). Jiang *et al.* designed a DES electrolyte for aqueous Li-ion batteries based on methylsulfonylmethane (MSM):

$LiClO_4$: H_2O (molar ratio 1.8: 1: z, z > 0.3).[30a] Although the introduction of water reduced the electrochemical stability window of the electrolyte, it remained satisfying to support good operation of LTO||LMO electrode couples. The as-assemble battery cycled for more than 1000 cycles with a capacity retention of 72.2 %. More recently, an aqueous DES was synthesized by mixing 5 M $LiClO_4 \cdot 3H_2O$ with urea in the mol ratio of 1: 2.[125] Owing to the depletion of water molecules, the as-prepared electrolyte exhibited an electrochemical stability window of 3.2 V and the corrosion of Al current collectors was suppressed. The aqueous DES was applied in LTO||LMO commercial-grade pouch cell of 12 Ah delivering an energy density of 65 Wh kg^{-1} based on the whole battery.

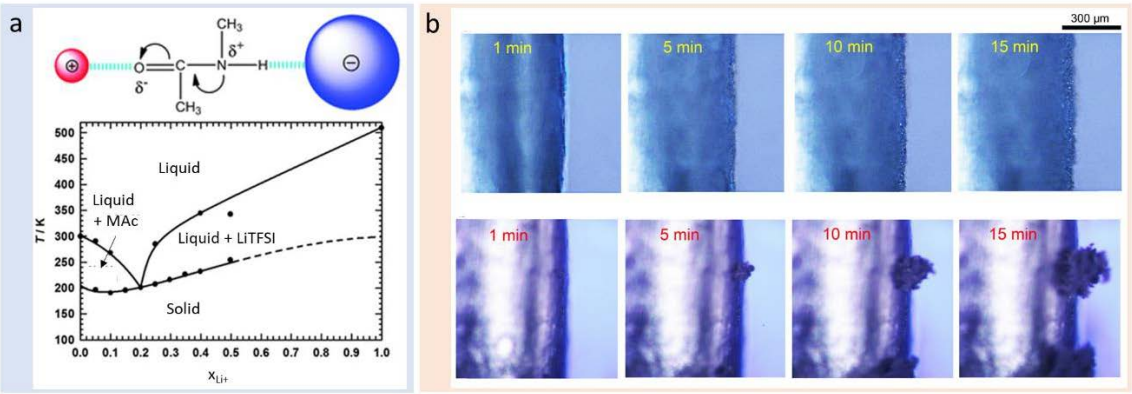

Figure 2.4. (**a**) Schematic representation of the cation–NMAc–anion system (top) and solid–liquid equilibrium of the NMAc–LiTFSI binary mixture as a function of the salt mole fraction, x_{Li+} describing a typical DES thermal behaviour (bottom). Reproduced with permission.[4] Copyright 2013, The Royal Society of Chemistry (**b**) Deposition morphology of lithium metal foils using an *in-situ* optical microscope in Li||Li cells with different electrolytes: D-DES (top) and 1 M $LiPF_6$-EC/DMC (bottom) under a current density of 5 mA cm^{-2} (plating time: 1, 5, 10, and 15 min). Reproduced with permission.[5] Copyright 2020, American Chemical Society.

- Deep eutectic solvent electrolytes for zinc-based batteries

Alike Li salts, Zn salts can form DES electrolytes when coupled with an electron donor compound such as acetamide or urea. In 2019, Kao-ian *et al.* presented a DES-based electrolyte for Zn-ion batteries. The 0.3 M $ZnCl_2$ in choline chloride-urea (1: 2 mol ratio) was employed in a Zn||ɣ-MnO_2 battery.[31] This electrolyte provided a large electrochemical stability window while remaining non-flammable. The Zn anode retained a dendrite-free morphology and demonstrated efficient Zn plating-stripping process. However, the low

Coulombic efficiency (≈ 85 %) and the capacity fading of the Zn||γ-MnO_2 full cell impeded long cycling performance. This could be due to the high viscosity of the 0.3 M $ZnCl_2$ in choline chloride-urea electrolyte and the sluggish Zn^{2+} intercalation in the cathode material. By introducing an hydrated ($Zn(ClO_4)_2 \cdot 6H_2O$) Zn salt with succinonitrile, Yang *et al.* formed a hydrated eutectic electrolyte, which they applied in Zn-organic battery.[6] When formulating a DES, the Zn salt selection and the salt to solvent ratio is primordial to obtain a homogenous liquid (**Figure 2.5**a) with low viscosity, high ionic conductivity (**Figure 2.5**b) and large electrochemical stability window (**Figure 2.5**c). Both water and succinonitrile molecules participated in the Zn^{2+} primary solvation sheath. Succinonitrile contributed to forming $[Zn(OH_2)_x(SN)_y]^{2+}$ cations hydration-deficient complexes (**Figure 2.5**d), while the water molecules in the hydrated eutectic structure guaranteed the reversible reactions of the organic cathode. The synergic effect of H_2O and succinonitrile allowed dendrite-free Zn plating and stripping on the Zn anode with an average Coulombic efficiency of 98.4 % and high performance of the organic cathode with negligible dissolution. Inspired by "water-in-salt" electrolytes, Shi *et al.* developed a "water-in-deep eutectic solvent" electrolyte based on $ZnCl_2$-acetamide-H_2O in the molar ratio 1: 3: 1.[126] The water molecules available in the aqueous DESs regulated the Zn^{2+} solvation sheath and thus diminished the Zn^{2+} desolvation energy barrier which benefit smooth plating on the Zn anode. When employed in a Zn||phenazine full battery, the aqueous Zn battery cycled for more than 10 000 cycles with a capacity retention of 85.7 %. Zn-ion batteries usually operates at low voltage (*i.e.*, 1.2-1.5 V) due to the narrow voltage window of the aqueous electrolyte, therefore developing novel high voltage cathode materials would enhance their average working voltage and energy density.

To increase the operational voltage of Zn-ion batteries, one strategy consists in replacing the Zn intercalation cathode (*e.g.*, MnO_2) by a high voltage Li intercalation cathode (*e.g.*, LMO), thereby designing Zn/Li hybrid batteries. Increasing the cathode voltage may result in poorer battery performance with low Coulombic efficiency if the voltage stability window of the electrolyte is not suitable. Therefore, such battery design requires an electrolyte with a wide electrochemical stability window, which contain a mixture Li and Zn salts. Zhao *et al.* developed a "water-in-deep eutectic solvent" electrolyte for Zn||LMO batteries.[7] The DES, a mixture of water, urea, LiTFSI and zinc bis(trifluoromethanesulfonyl)imide ($ZnTFSI_2$)

inherited the advantages of aqueous electrolytes (*e.g.*, low viscosity) and DESs (*e.g.*, low solvent content, about 30 mol% H_2O). The small amount of water molecules in the electrolyte were coordinated through H-bonds with the DES's internal interaction network. Therefore, side reactions such as dendrites growth and water evolution were suppressed. The Zn||LMO pouch cells delivered outstanding performances even at low rate with more than 90 % retention after 300 cycles at 0.1 C (**Figure 2.5**e-f). Similarly, N,N-dimethylacetamide (DMA) was introduced in a concentrated solution of 2.5 m zinc nitrate ($Zn(NO_3)_2$) + 13 m $LiNO_3$ electrolyte.[127] The low permittivity of DMA molecules weakened the Li^+ and Zn^{2+} solvation sheath, therefore the Zn anode displayed a dendrite-free surface after operating in Zn||LMO batteries for 200 cycles at 1 C.

For both Li and Zn –based batteries, DESs electrolytes enabled safe battery operation along with improved cycling performances owing to electrolyte engineering (*e.g.*, electrolyte additives, hydrated salts, *etc.*)

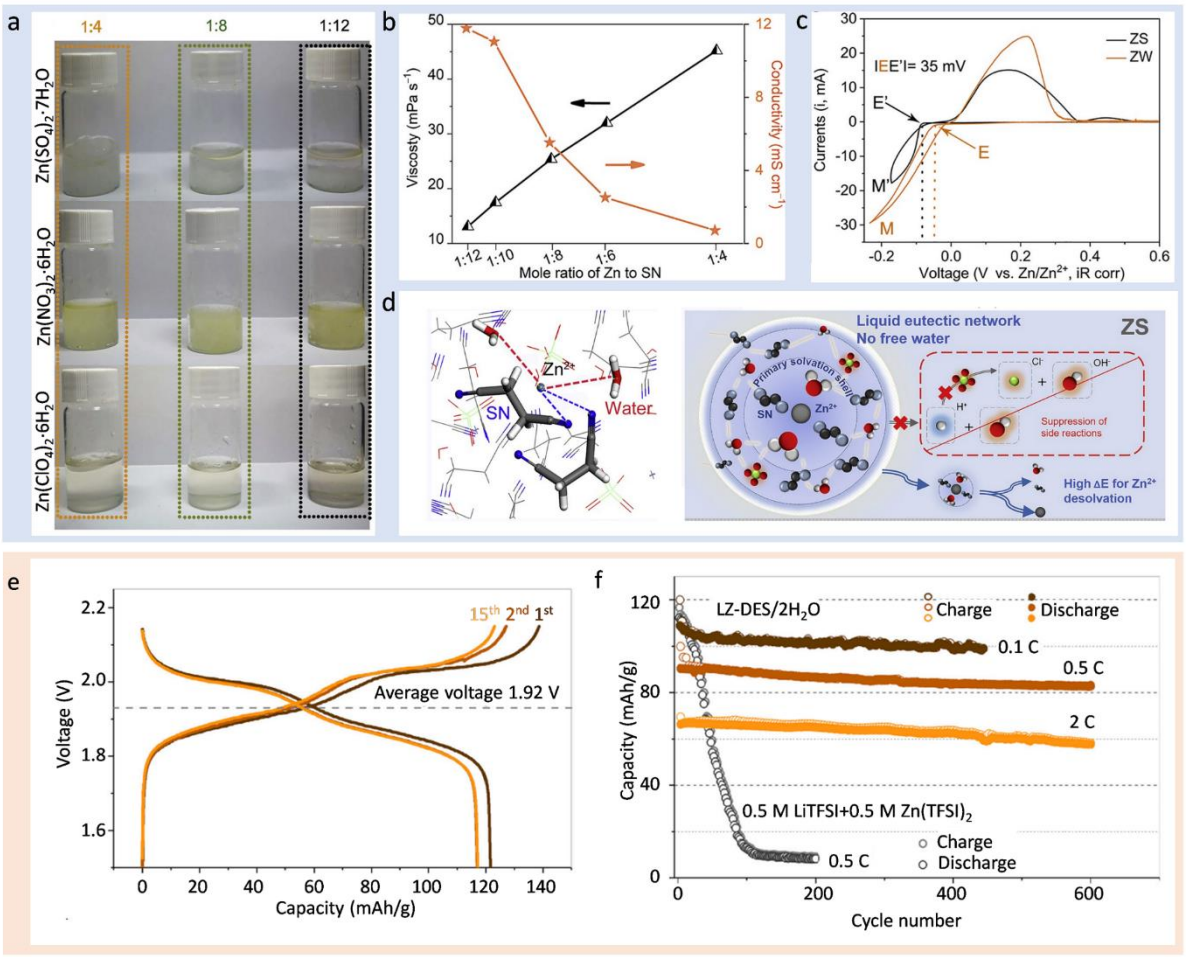

Figure 2.5. (**a**) The solubility of $ZnSO_4 \cdot 7H_2O$, $Zn(NO_3)_2 \cdot 6H_2O$, and $Zn(ClO_4)_2 \cdot 6H_2O$ in SN (the Zn salt/SN molar ratios are 1:4, 1:8, and 1:12 from left to right) (**b**) Viscosity and ionic conductivity of the $Zn(ClO_4)_2 \cdot 6H_2O$/SN eutectic solutions (the molar ratios of $Zn(ClO_4)_2 \cdot 6H_2O$/SN are 1:4, 1:6, 1:8, 1:10, and 1:12) (**c**) CV curves of Zn plating/stripping using stainless steel as the working electrode and Zn as the reference and counter electrodes in ZS ($Zn(ClO_4)_2 \cdot 6H_2O$/SN molar ratio of 1:8) and ZW ($Zn(ClO_4)_2 \cdot 6H_2O/H_2O$ molar ratio of 1:8) at scan rate of 1.0 mV s^{-1}. (**d**) Representative Zn^{2+}-solvation structure in the $Zn(ClO_4)_2 \cdot 6H_2O$/SN molar ratio of 1:8 electrolyte (left) Schematic diagrams of Zn^{2+} solvation structure and corresponding interfacial reactions in $Zn(ClO_4)_2 \cdot 6H_2O$/SN molar ratio of 1:8 (right). Reproduced with permission.[6] Copyright 2021, Elsevier B.V. (**e**) Charge-discharge profiles (0.06 C based on LMO) of Zn/LMO cell in LiTFSI-$ZnTFSI_2$-DES-$2H_2O$ electrolyte (**f**) Cycling performance of the Zn||LMO cell in LiTFSI-$ZnTFSI_2$-DES-$2H_2O$ under various rates, in comparison with those in 0.5 M LiTFSI + 0.5 M $ZnTFSI_2$. Reproduced with permission.[7] Copyright 2019, Elsevier B.V.

- Eutectogels

Quasi-solid DES electrolytes, also named eutectogels (ETGs), emerged recently as safer alternative to liquid electrolytes. Generally, eutectogels are synthesised by introducing a gelling agent in the DES electrolyte such as monomers or polymers (covalent network), or low-molecular weight gelators (self-assembled gel with no-covalent interactions).[128] Joos *et al.* introduced a DES electrolyte based on LiTFSI and NMAc into a silica matrix (**Figure 2.6**a).[8] The liquid DES is compatible with an acidic sol-gel process, which attests of the possible ease and cost efficient formulation of eutectogel electrolytes. The as-prepared eutectogel electrolyte demonstrated a thermal stability up to 130 °C, an electrochemical stability window of 3.7 V (1.1−4.8 V *vs.* Li/Li^+) and a high ionic conductivity at room temperature (1.46×10^{-3} S cm^{-1}). These properties well suited the operation of Li||LFP cells, which delivered a stable and reversible specific capacity of 105 mAh g^{-1} at 0.1 C over 100 cycles.

Endowing eutectogels with specific properties such as self-healing[47], improved flexiblility[9], *etc.*, promotes the development of extremely safe batteries. Li *et al.* proposed a cheap and safe eutectogel membrane by immobilized LiTFSI: NMAc DES liquid electrolyte in poly(vinylidene fluoride-hexafluoro propylene) polymer (PVDF-HFP).[129] The Li|eutectogel

membrane|LFP batteries not only delivered a discharge capacity of 133.9 mAh g^{-1} at 0.1 C after 100 cycles, but also exhibited extreme safety as proven by flammability and abuse tests such as folding, cutting and nail penetration. Logan *et al.* reported a UV-cured eutectogel electrolytes for LTO||LMO batteries.[9] The LiTFSI: NMAc DES was mixed in an optimised monomer mixture comprising 2-hydroxyethyl acrylate (HEA) and polyethylene glycol methyl ether acrylate (MPEGA). Acrylate-based polymers generally display robust mechanical properties. The as-prepared eutectogel exhibited flexibility and transparency (**Figure 2.6**b). As shown on **Figure 2.6**c, the eutectogel self-extinguishing time was sharply decreased as comparison with the liquid DES and commercial electrolyte (*i.e.*, <5 s g^{-1} for the eutectogel, ≈22 g s^{-1} for liquid DES and ≈40 g s^{-1} for 1 M $LiPF_6$ in EC/DMC).

Quasi-solid electrolytes represent an interesting strategy to improve cycling performance owing to ion confinement, dendrite growth suppression on metal anode and decrease of solvent activity. Meanwhile, extra functionality such as flexibility, self-healing, thermal resistance, *etc.* can also be provided. Furthermore, the techniques to synthesis such electrolytes can generally be adapted to different battery systems by changing the metal salt.

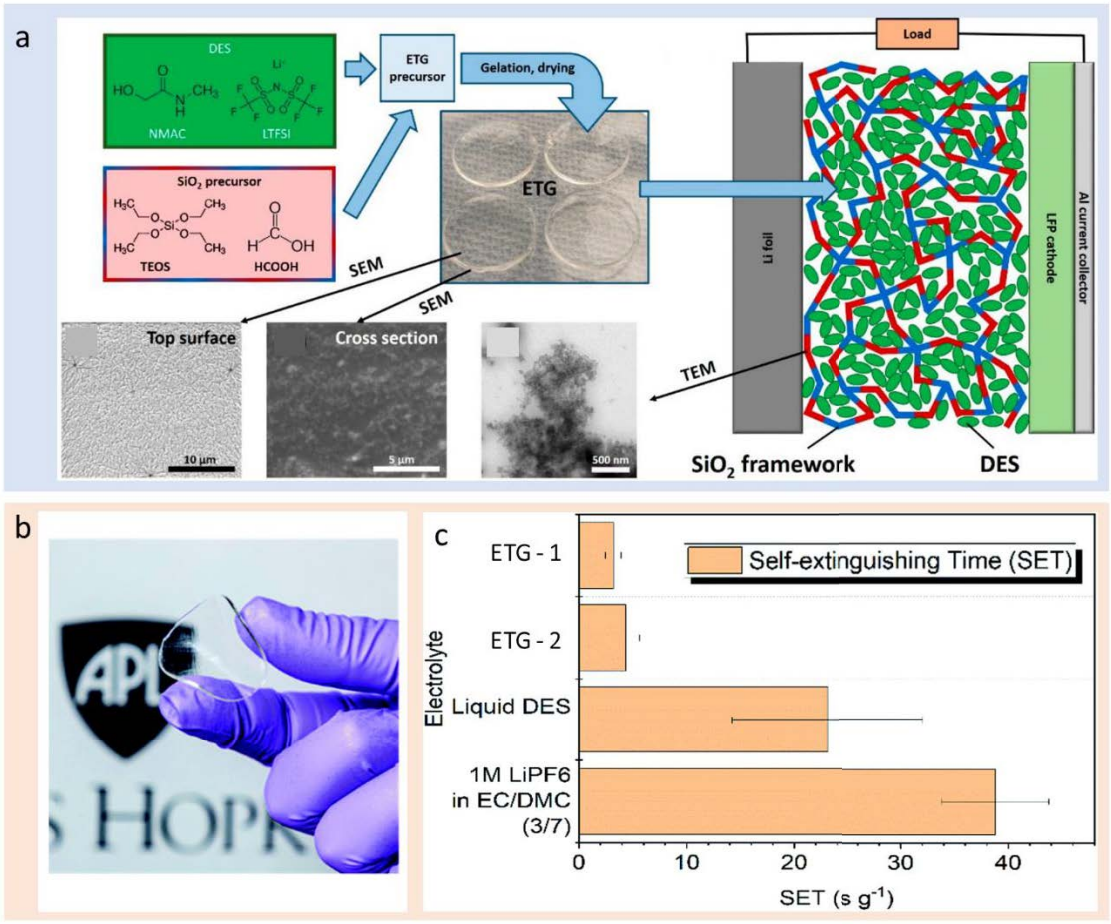

Figure 2.6. (**a**) Synthesis route for the ETGs and optical photograph of 4 ETG membranes (12 mm diameter) (top left); structural schematic of a Li||LFP cell with the ETG as electrolyte (right); SEM images of the surface and cross-section of an ETG membrane (bottom left); and TEM image of the silica framework after extraction of the DES (bottom middle). Reproduced with permission.[8] Copyright 2018, American Chemical Society. (**b**) Optical image of a UV-cured ETG and (**c**) self-extinguishing time for the liquid DES, a standard organic electrolyte control, and two ETGs. Reproduced with permission.[9] Copyright 2020, The Royal Society of Chemistry.

2.4.3 Aqueous electrolytes

Aqueous electrolytes present many benefits such as high ionic conductivity, low viscosity, good electrode and separator wetting ability, inexpensive, non-flammability and eco-friendliness.[48] However, their applications in rechargeable batteries remains challenging due to (1) narrow electrochemical window (*i.e.*, 1.23 V), (2) proton co-intercalation, (3) dissolution of electrode materials and (4) corrosion reactions. In order to achieve reversible charge and

discharge cycles and avoid side reactions, the electrode couple working potential must sit within the electrochemical stability window of the electrolyte (**Figure 2.7**a). Therefore, the narrow electrochemical stability window dictated by hydrogen evolution reaction (HER) and oxygen evolution reaction (OER) (**Equations 2.5** and **2.6**, respectively) dramatically limit the energy density of aqueous batteries (**Figure 2.7**b).[10]

$$H_2O = O_2 + 4H^+ + 4e^- \quad (\mathbf{2.5})$$

$$2H^+ + 2e^- = H_2 \quad (\mathbf{2.6})$$

As a result, reducing the activity of the water molecules is primordial to avoid HER/OER, widen the electrochemical stability of aqueous electrolytes and ultimately develop high energy density aqueous batteries.

2.4.3.1 Aqueous lithium-based batteries

Recently, aqueous electrolytes have attracted intensive interest from the research community. In 2015, Wang's group enlarged the electrochemical stability window of aqueous electrolyte to 3.0 V by introducing a large amount of LiTFSI in water, thereby creating a "water-in-salt" electrolyte.[130] For the first time, "water-in-salt" electrolyte based on 21 m LiTFSI dissolved in water allowed a 2.3 V Mo_6S_8||LMO full cell to achieve reversible charge-discharge cycling with high Coulombic efficiency.[130] More importantly, a SEI was observed in aqueous electrolyte. Previously, it has been demonstrated that SEI layers could not be formed in dilute aqueous electrolytes due to the continuous dissolution of SEI chemical species. In highly concentrated electrolytes, researchers usually employed molality (mol $kg^{-1}_{solvent}$, unit = m), which is based on mass and not on volume, thereby alleviating confusion due to volume change when adding large quantities of salt in the solvent. It was demonstrated that the increase of the salt concentration in "water-in-salt" electrolytes diminished the amount of free water and altered the working potential of electrode materials (*i.e.*, Nernst shift) (**Figure 2.7**c).[11, 130] This breakthrough spurred extensive research on aqueous electrolyte design with the aim of further enlarging the electrochemical stability window and achieving high energy density aqueous batteries.[12]

- Solid electrolyte interphase in aqueous electrolytes

Solid electrolyte interphases (SEIs) play a crucial role in stabilizing electrode materials beyond their thermodynamic limits.[20] In the first cycles, the metal salts and solvents are reduced, thus forming a protective layer on the anode that prevent electrolyte decomposition in the following cycles. Since the "water-in-salt" discovery, several research groups endeavour to characterise and understand the SEI formation mechanism in aqueous electrolytes. Suo *et al.* demonstrated that the SEI formation results from two possible reduction reactions: (1) reduction of anion complexes such as $Li_2(TFSI)^+$ leading to SEI layers containing LiF species and (2) reduction of dissolved gases (*i.e.*, O_2, CO_2) dissolved in the electrolyte providing lithium carbonate (Li_2CO_3) and lithium oxide (Li_2O) compounds (**Figure 2.7**d).[12] The reductions of dissolved gases and anion complexes occur around the same potentials (*i.e.*, ≈2.9 V) according to the below equations (**Equations 2.8-2.12**) whose potentials are above the HER reduction potential in "water-in-salt" electrolyte:[131]

$$4\,Li^+ + O_2 + 4\,e^- \rightarrow 2\,Li_2O \quad (\mathbf{2.8})$$

$$Li_2O + CO_2 + 4\,e^- \rightarrow 2\,Li_2CO_3 \quad (\mathbf{2.9})$$

$$Li_2O + H_2O \rightarrow LiOH \quad (\mathbf{2.10})$$

$$Li_2CO_3 + H_2O \leftrightarrow 2\,LiOH + CO_2 \quad (\mathbf{2.11})$$

$$LiTFSI + e^- \rightarrow LiF + TFSI^- \quad (\mathbf{2.12})$$

Moreover, these reduction products are non-soluble owing to the scarcity of water molecules. Differently, Dubouis *et al.* demonstrated that in the first cycles, hydroxides generated by the reduction of water molecules can chemically catalyse the reduction of TFSI anions, thereby assisting in the formation of a stable fluorinated SEI layer.[11] Yamada *et al.* revisited the formation of SEI layer in aqueous systems and highlighted three main remaining questions:[132]

- The role of the catalytic activity of the electrodes and current collectors.
- The cause of the shift of reduction potential of the anions. The positive shift could result of the strong interactions cation-anion-water in aggregates. Alternatively, the reduction of anions could be chemically catalysed by the decomposition of water molecules.
- As per the scarcity of free water molecules, their reduction mechanism may be altered as comparison with dilute electrolytes.

Therefore, additional *in-situ* characterizations are necessary to understand deeply the reactions happening at the electrode|electrolyte interface during the first charge and discharge cycles.

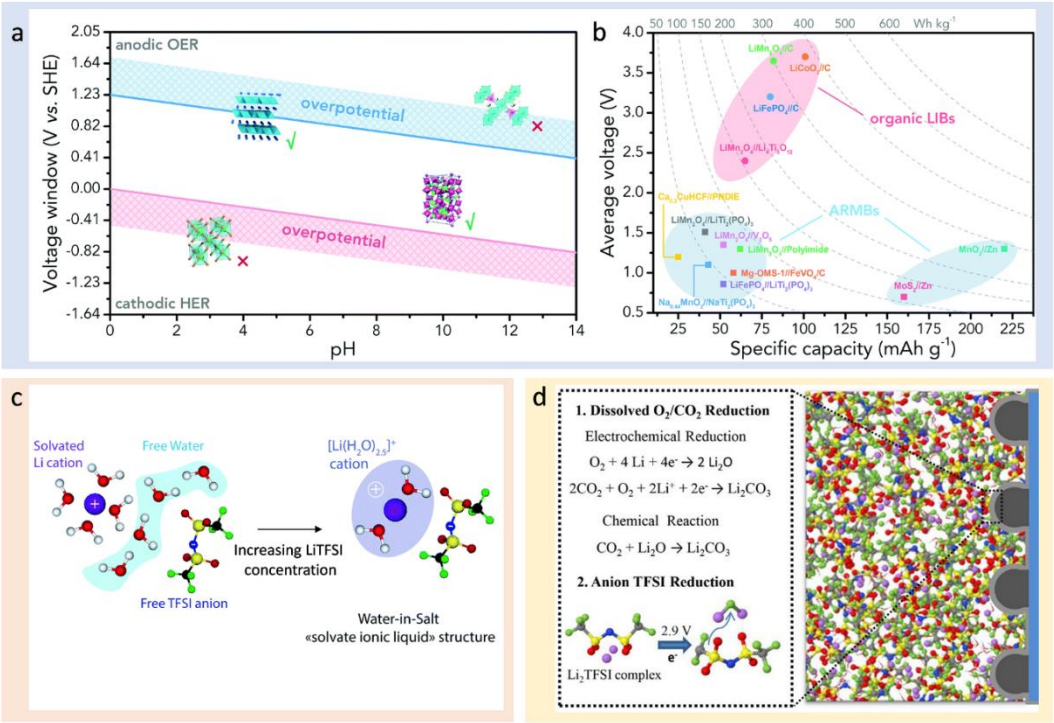

Figure 2.7. (**a**) Pourbaix diagram showing the voltage window of aqueous electrolytes depending on the pH. The electrodes materials should sit within the voltage stability window of aqueous electrolytes. (**b**) Energy comparison between typical aqueous rechargeable metal batteries (ARMBs) and conventional organic lithium-ion batteries (LIBs). Reproduced with permission.[10] Copyright 2020, The Royal Society of Chemistry. (**c**) schematic evolution of the solvation shell of Li^+ cations and $TFSI^-$ anions from diluted electrolytes (left) to "water-in-salt" electrolytes (right). Reproduced with permission.[11] Copyright 2018, The Royal Society of Chemistry. (**d**) SEI formation mechanisms in "water-in-salt" electrolytes. Reproduced with permission.[12] Copyright 2017, American Chemical Society.

- <u>High energy density aqueous Li-based batteries</u>

As explained previously, the limited energy density of aqueous battery impedes their practical applications. Owing to the enlargement of the voltage window of "water-in-salt" type electrolytes, novel electrode couples became suitable for aqueous systems. Sun *et al.* applied a "water-in-salt" electrolyte based on 21 m LiTFSI in H_2O in a TiS_2||LMO batteries, thereby

achieving an energy density of 78 Wh kg^{-1}.[133] Wang's group further increased Li salt concentration to 28 m by designing a "water-in-bisalt" electrolyte (*i.e.*, 21 m LiTFSI + 7 m LiOTf in H_2O).[134] The as-prepared electrolyte enabled carbon-coated titanium oxide (TiO_2)||LMO aqueous batteries to achieve high cycling stability and excellent Coulombic efficiency. By further dissolving 10 wt% Poly(vinyl alcohol) (PVA) in the "water-in-bisalt" electrolyte, a Li-sulphur (sulphur||LMO) battery delivered excellent cycling performance and could potentially achieve an energy density of 200 Wh kg^{-1}.[27] In the meantime, lithium titanium oxide ($Li_4Ti_5O_{12}$, LTO) anode with a low working potential (*i.e.*, ≈ 1.6 V *vs.* Li/Li^+) was also applied in aqueous lithium batteries. For instance, Yamada *et al.* designed a $Li(TFSI)_{0.7}$(bis(perfluoroethanesulfonyl)imide (BETI))$_{0.3}$·$2H_2O$ hydrate melt electrolyte, which provided a 2.7 V electrochemical stability window and therefore low voltage anode LTO became compatible.[135] In this electrolyte, all the water molecules participated in Li^+ solvation sheath, thereby suppressing HER and OER side reactions. More recently, it was discovered that introducing an asymmetric ammonium salt (Me_3EtN·TFSI) in water increases the solubility of LiTFSI by two-fold.[13] Therefore, a 63 m super concentrated aqueous electrolyte (42 m LiTFSI + 21 m Me_3EtN·TFSI in H_2O) presented a 3.25 V –wide electrochemical stability (**Figure 2.8**a), which supported a 2.5 V LTO||LMO aqueous battery (**Figure 2.8**b). The initial Coulombic efficiency of battery is about 95 % and increases to 99.5 % after 10 cycles, attesting of the high reversibility of this system. At 1 C, the LTO||LMO battery delivered a discharge capacity of 56 mAh g^{-1} based on both the cathode and anode mass, which corresponded to a high energy density of 145 Wh kg^{-1}.

Hybrid aqueous electrolytes were formulated by introducing a liquid co-solute into super-concentrated aqueous electrolytes, thereby benefiting from lower cost, expanded electrochemical stability and/or tailored stability toward the electrode couple. Wang *et al.* designed an aqueous/non-aqueous hybrid electrolyte in which a "water-in-salt" electrolyte (21 m LiTFSI in water) was mixed with a super-concentrated non-aqueous electrolyte (9.25 m LiTFSI in DMC) in the mass ratio 1: 1.[14] The synergic effect of high concentration and the presence of organic solvent molecules lead to the formation of a robust SEI layer mainly composed of LiF and Li_2CO_3 species, following the reduction of $Li^+(TFSI)_2$ and $Li^+{}_2$(DMC) clusters (**Figure 2.8**c). The as-prepared electrolyte exhibited a 4.1 V –wide electrochemical stability window, thereby supporting a 3.2 V LTO||LNMO battery. Similarly, an "ether-in-

water" electrolyte was formulated by introducing tetraethylene glycol dimethyl ether (TEGDME) into 15 m LiTFSI in water with a H_2O: TEGDME mass ratio = 1: 1).[136] The solvation sheath obtained in such electrolyte (*i.e.*, $Li_4(TEGDME)(H_2O)_7$) enabled the formation of a robust SEI layer driven by the reduction of $Li^+_2(TFSI^-)$ and $Li^+_4(TEGDME)$ species. Thus, the electrochemical stability of the hybrid electrolyte was widened to 4.2 V permitting a full aqueous Li-ion battery based on LTO anode and LMO cathode to deliver an energy density of 120 Wh kg^{-1} over 500 cycles.

As noted previously, fluorinated organic lithium salts are rather expensive. To reduce the cost of highly concentrated aqueous electrolytes, Xie *et al.* designed a molecular crowding strategy for dilute aqueous electrolytes.[15] The crowding agent must be soluble in water, have a good solvating ability toward lithium salts, and create numerous hydrogen bonds with H_2O molecules.[137] By introducing 96 % of polyethylene glycol (PEG 400) into a 2 m LiTFSI in H_2O electrolyte, the stability window was extended to 3.2 V owing to the depletion of free water molecules in the electrolyte. When applied in a LTO||LCO aqueous Li-ion batteries, this battery achieved more than 300 cycles at 1 C with high Coulombic efficiency, meanwhile no visible hydrogen/oxygen gas production was observable attesting of the inhibition of HER and OER side reactions (**Figure 2.8**d). The influence of the terminal group and chain length of the molecular crowding agent was later investigated.[16] When PEG 400 was replaced by polyethylene glycol dimethyl ether (PEGDME 450), the interaction PEGDME-PEGDME were weakened due to the end-of-chain terminal functional group (**Figure 2.8**e). Moreover, the ionic conductivity and viscosity of these molecular crowding agents are closely linked with their molecular mass (**Figure 2.8**e). Therefore, the ionic conductivity of the 2 m LiTFSI-94 % PEGDME-6 % H_2O electrolyte was 3-fold higher than 2 m LiTFSI-94 % PEG-6 % H_2O counterpart (**Figure 2.8**f). The LTO||LMO full cells demonstrated high cycling performance over 800 cycles at 5 C.

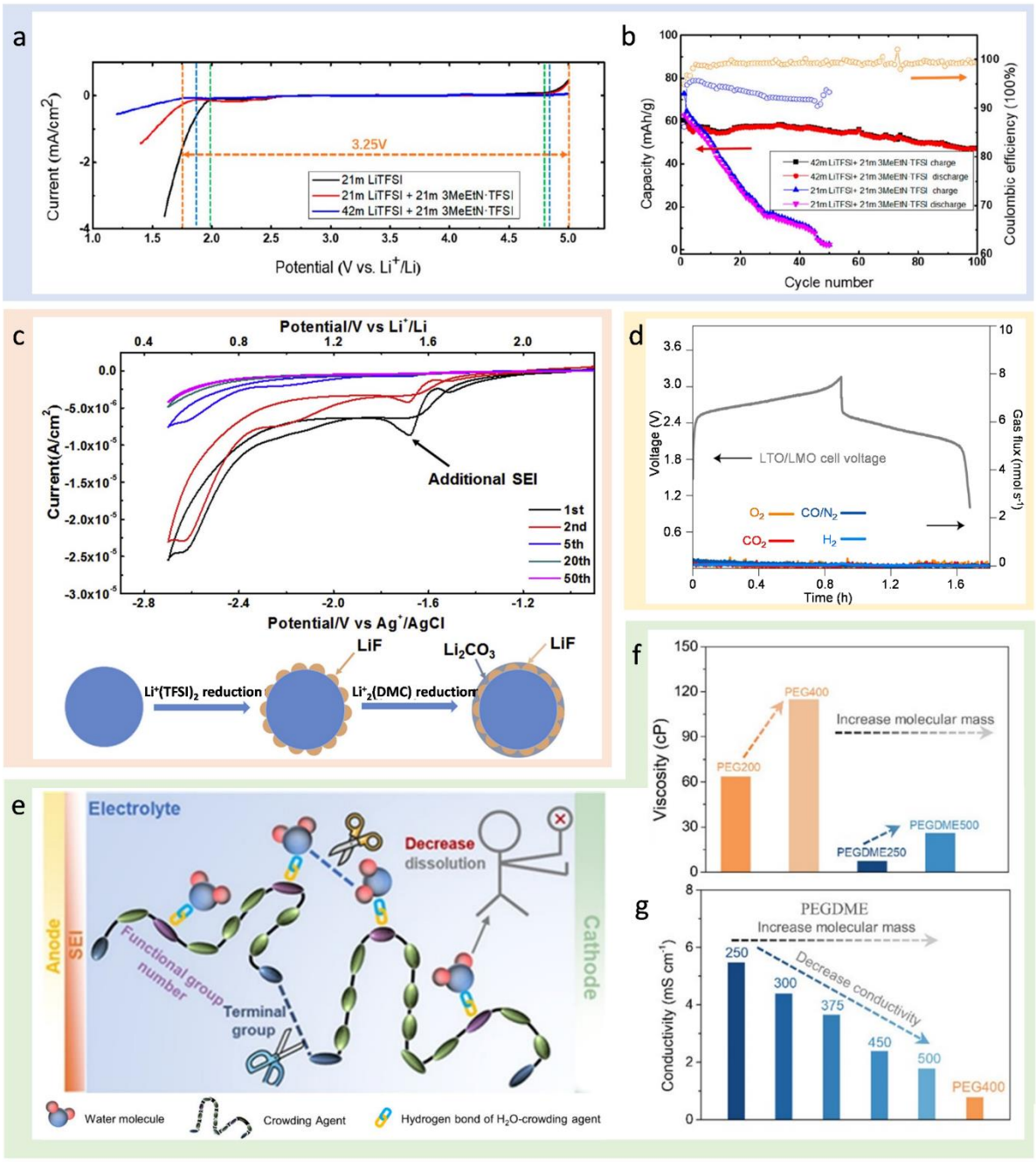

Figure 2.8. (**a**) Electrochemical windows of different aqueous electrolytes measured on stainless steel current collector at scanning rate of 5 mV s^{-1}. (**b**) Cycling stability and Coulombic efficiency of LTO||LMO full cell with the 42 m LiTFSI + 21 m Me_3EtN·TFSI aqueous electrolyte at the rate of 1 C. Reproduced with permission.[13] Copyright 2020, American Chemical Society. (**c**) Cyclic voltammetry of the aluminium electrode in aqueous/non-aqueous hybrid electrolyte using a three-electrode cell with activated carbon and Ag/AgCl as counter and reference electrodes, respectively, at a scan rate of 5 mV s^{-1} and schematic illustration of the anode SEI formation in aqueous/non-aqueous hybrid electrolyte. Reproduced with

permission.[14] Copyright 2018, Elsevier B.V. (**d**) On-Line Electrochemical Mass Spectrometry (OEMS) results of the LTO/LMO full cell conducted in 2 m LiTFSI–94%PEG–6%H_2O during tenth cycles at 1 C. Reproduced with permission.[15] Copyright 2020, Springer Nature Limited. (**e**) Schematic illustration of intermolecular interactions of H_2O–crowding agent, crowding agent–crowding agent, H_2O–H_2O. (**f**) Viscosity of pure PEG200, PEG400, PEGDME250, and PEGDME500. (**g**) Conductivity of 2 m LiTFSI-94%PEGDME(250,300,375,450,500)-6%H_2O and 2 m LiTFSI-94%PEG400-6%H_2O aqueous electrolytes. Reproduced with permission.[16] Copyright 2021, American Chemical Society.

- Electrode protection in aqueous electrolytes

Applying low potential anodes such as Li metal and graphite would dramatically enlarge the energy density of aqueous batteries. However, such anodes operate well-underneath the voltage stability of super-concentrated aqueous electrolytes (*e.g.*, Li: -3.04 V *vs.* SHE; graphite: ≈ -3.0 V *vs.* SHE). To overcome this challenge, Yang *et al.* engineered a novel protective layer on graphite and Li by coating a fluorinated interphase precursor (highly fluorinated ether: 1,1,2,2-tetrafluoroethyl-2',2',2'-trifluoroethyl ether, HFE) on the anodes (**Figure 2.9**a).[17] When mixed with 0.5 M LiTFSI and 10 wt% polyethylene oxide, HFE formed a gel precursor which demonstrated high stability with Li metal (**Figure 2.9**b). During the first cycle, this hydrophobic fluorinated gel repulsed water molecules from the anode surfaces, meanwhile its reduction products generated a fluorinated protective SEI layer rich in LiF and C-F species (**Figure 2.9**a). As proof of concept, after coating the anodes with HFE-gel, Li||$LiVPO_4F$, graphite||$LiVPO_4F$ and Li||LMO aqueous Li-ion batteries operated in "water-in-bisalt" electrolyte for 50 cycles with satisfying stability. Such strategy was further applied in aqueous Li-ion batteries based on halogen conversion-intercalation in graphite.[18] A $(LiBr)_{0.5}(LiCl)_{0.5}$-graphite composite cathode was paired with a HFE-protected graphite anode and a "water-in-bisalt" gel electrolyte (**Figure 2.9**c). Owing to the conversion-intercalation mechanism, such batteries delivered a high specific capacity of 243 mAh g^{-1} with an average potential of 4.2 V and an energy density of 460 Wh kg^{-1}.

Since high voltage transition metal cathode materials such as LMO and LCO suffers from transition metal dissolution into aqueous electrolytes, the formation of CEI layers were engineered by electrolyte optimization.[138] Additives were introduced into 21 m LiTFSI

"water-in-salt" electrolyte to improve the electrochemical compatibility of high voltage LCO cathode in aqueous electrolyte.[19] The electrochemical oxidation of tris(trimethylsilyl)borate (TMSB) additive provided a compact CEI layer on the surface of the high voltage LCO cathode (**Figure 2.9**d-e), thereby preventing Co dissolution and water evolution reactions. When coupled with Mo_6S_8 anode, the 2.5 V Mo_6S_8||high-voltage LCO battery demonstrated high cycling stability (1000 cycles with 0.0013 % capacity decay per cycle) and high energy density of 120 Wh kg^{-1}.

- Alternative to organic lithium salts

Although organic fluorinated lithium salts have been largely employed to fabricate "water-in-salt" electrolytes owing to their high solubility in water and SEI formation ability, they remain extremely costly. Non-fluorinated "water-in-salt" electrolytes benefit from lower cost and eco-friendliness while wide electrochemical stability window could also be achieved. For instance, Zheng *et al.* studied the $LiNO_3$ solvation structure in highly concentrated electrolyte.[139] It was demonstrated that a local structure of $(Li^+(H_2O)_2)_n$ polymer-like chains were responsible for the enlargement of the stability window. Similarly, a "water-in-ionomer" in which 50 % lithium polyacrylate (LiPAA) was dissolved in water demonstrated a 2.6 V electrochemical stability window and sustained a 2.1 V TiO_2||LMO battery with an initial specific energy of 124.2 Wh kg^{-1}.[140] Another approach consisted in employing an aqueous deep eutectic solvent electrolyte as detailed previously.[30a, 125] Recently, our group developed an inexpensive localized "water-in-salt" electrolyte based on inorganic $LiNO_3$ and a diol diluent (1,5-pentanediol, PD).[20] Similar to organic localized super-concentrated electrolytes, aqueous diluents must be miscible with water but non-solvating toward lithium salts. Therefore, the solvation structure of "water-in-salt" electrolytes remains unchanged after the introduction of the diluent (**Figure 2.9**f). A 12.5 m $LiNO_3$ in H_2O: PD demonstrated a 2.9 V electrochemical stability, which was further enlarged to 3.0 V with the *in-situ* polymerisation of tetraethylene dimethyl acrylate (TEGDMA) monomer (**Figure 2.9**g). When applied in Mo_6S_8||LMO aqueous Li-ion batteries, the cells achieved more than 250 cycles with high Coulombic efficiency. Such electrolyte demonstrated non-flammability, large electrochemical stability window and eco-friendliness. This work will be detailed in *Chapter V.*

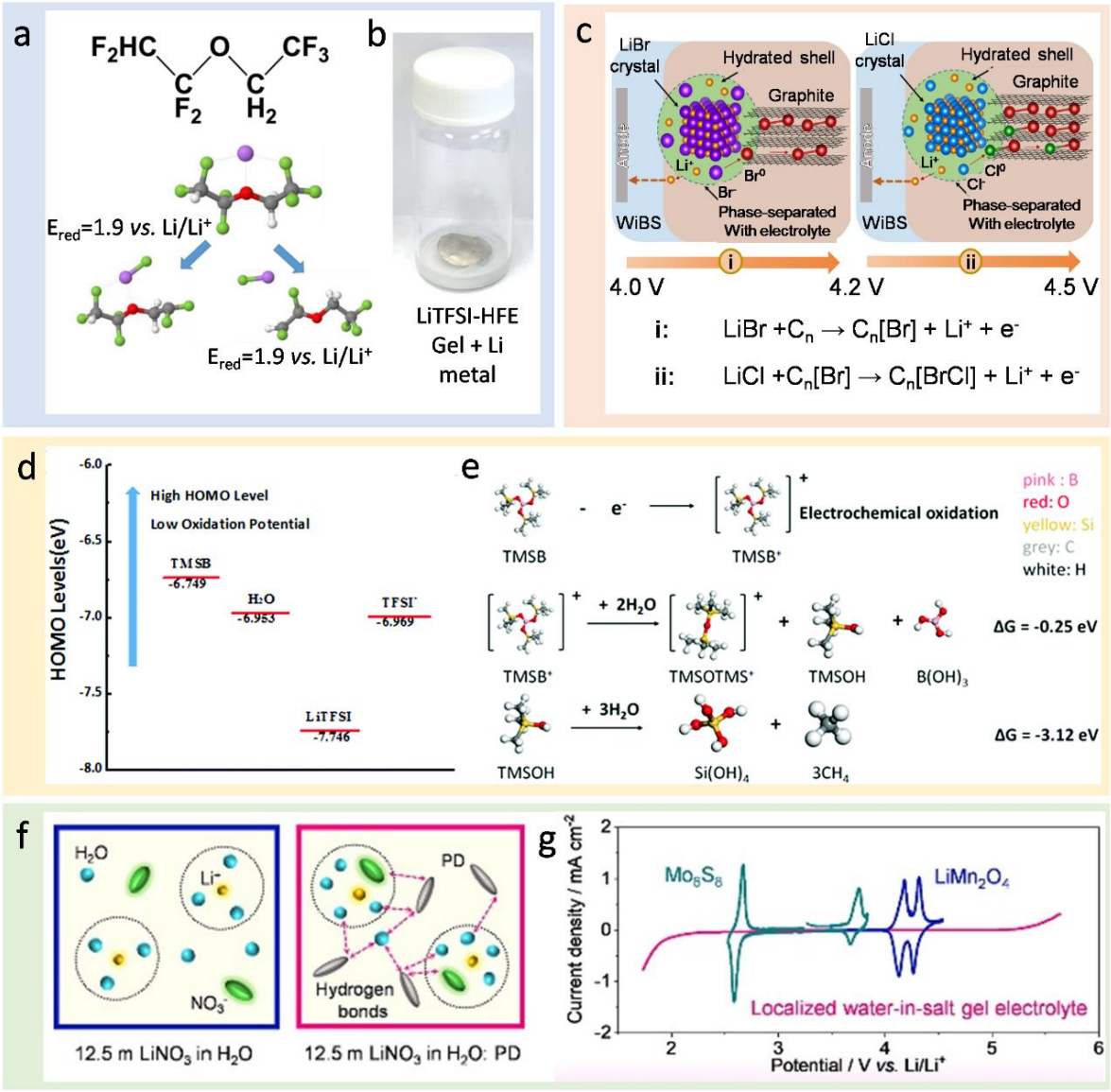

Figure 2.9. (**a**) The molecular structure of HFE (1,1,2,2-tetrafluoroethyl-2',2',2'-trifluoroethyl ether) and the reduction potentials of Li-HFE obtained with density functional theory (DFT) calculations. (**b**) The stability between Li metal and LiTFSI-HFE precursor gel. Reproduced with permission.[17] Copyright 2017, Elsevier B.V. (**c**) Schematic of the conversion–intercalation mechanism occurring in the $(LiBr)_{0.5}(LiCl)_{0.5}$-graphite composite cathode during its oxidation in "water-in-bisalt" aqueous-gel electrolyte. Reproduced with permission.[18] Copyright 2019, Springer Nature Limited. (**d**) Highest occupied molecular orbital (HOMO) levels of TMSB, H_2O, LiTFSI and $TFSI^-$. (**e**) Schematic of possible mechanisms for electrochemical oxidative decomposition of TMSB. Reproduced with permission.[19] Copyright 2016, The Royal Society of Chemistry. (**f**) Hypothetical diagrams of solvation structures for the electrolytes. (**g**) CV curves of the Mo_6S_8 and LMO electrodes at 0.1 mV s^{-1} obtained with the "localized water-in-

salt" gel electrolyte and the electrochemical window of "localized water-in-salt" gel electrolyte. Reproduced with permission.[20] Copyright 2021, John Wiley & Sons, Inc.

2.4.3.2 Aqueous electrolytes for zinc-based batteries

Over the past decade, Zn rechargeable batteries gained intensive attention as beyond Li-ion energy storage systems owing to the metal abundance in the earth crust, making it a cheap alternative to the more expensive Li metal anode. Benefiting from Zn metal compatibility with water, the inherently safe aqueous electrolytes have been a preferential choice for Zn-based batteries. However, the narrow electrochemical stability window of aqueous electrolytes and the thermodynamic instability of Zn metal in alkaline and mild aqueous electrolytes remain problematic.[141] To circumvent these drawbacks, many approaches have been investigated such as artificial Zn anode protection, structural design and electrolytes engineering.

- Highly concentrated aqueous electrolytes

Several dilute aqueous electrolytes have been reported for Zn-ion batteries employing inorganic zinc salts such as zinc sulphate ($ZnSO_4$), zinc nitrate ($Zn(NO_3)_2$), zinc chloride ($ZnCl_2$), zinc acetate ($Zn(CH_3COOH)_2$) or even zinc perchlorate ($Zn(ClO_4)_2$).[21] The common dilute aqueous electrolytes based on $ZnSO_4$ cannot provide long cycling performance when coupled with Zn anode and MnO_2 or VO_2 cathode due to the continuous formation of an insulating zinc hydroxide sulphate ($Zn_4SO_4(OH)_6{\cdot}nH_2O$) passivation layer on the anode and inability to suppress dendrite growth.[142] Recently, Wang *et al.* demonstrated that a simple 1 m $Zn(ClO_4)_2$ electrolyte could promote stable and reversible Zn plating-stripping processes (**Figure 2.10**a).[21] The inorganic $Zn(ClO_4)_2$ salt contributed to the formation of an insoluble chloride-containing protective layer which efficiently reduced the side reactions and improved the cycling performances. In comparison, when 1 m $ZnSO_4$ and 1 m $Zn(CH_3COOH)_2$ were employed as aqueous electrolytes, the batteries displayed poor efficiency due to continuous electrolyte consumption and formation of insulator by-products such as $Zn_4SO_4(OH)_6{\cdot}nH_2O$ and carboxyl-based species, respectively.

To improve the performance of such electrolytes, water-in-salt strategy have been adopted with the aim of reducing the water activity. Highly concentrated Zn salts can modify the solvation structure of Zn^{2+} cations and reduce the amount of free water molecules. Therefore, this electrolyte design diminishes side reactions such as corrosion of the metal anode and

water evolution. By increasing the salt concentration to 3 M $ZnSO_4$, a Zn||V_2O_5 battery achieved high cycling performance by allowing dual Zn^{2+} and H^+ co-insertion in the cathode.[143] As H^+ inserted in the cathode during discharging, OH^- would simultaneously contribute to the formation of $Zn_4SO_4(OH)_6{\cdot}5H_2O$ particles near the cathode. Meanwhile during charge, the reverse reactions occurred with $Zn_4SO_4(OH)_6{\cdot}5H_2O$ disappearing and Zn^{2+} and H^+ de-intercalating. A similar ready-to-dissolve phase ($Zn_5(OH)_8Cl_2{\cdot}H_2O$) was observed on the $Ca_{0.2}V_2O_5{\cdot}0.8H_2O$ cathode upon discharging in a 30 m $ZnCl_2$ electrolyte.[144] Since these phases are reversible and do not contribute to active material or electrolyte consumption, the batteries could deliver high cycling performance with low capacity fading. Lately, a 25 m $ZnCl_2$ mixed with 5 m ammonium chloride (NH_4Cl) "water-in-bisalt" electrolyte enable a Zn||$Na_3V_2(PO_4)_2O_{1.6}F_{1.4}$ to perform well.[145] Although the amount of free water molecules in such electrolyte is greatly reduced, some unbounded water molecules can still contribute to HER/OER. A hydrate-melt based on $ZnCl_2$ was proposed by Chen *et al.* in a Zn-air battery.[22] This electrolyte, in which all the water molecules participate in the Zn^{2+} hydration shells (**Figure 2.10**b), has shown to efficiently suppress dendrite growth on the Zn metal and improve the shelf life expectancy of the battery (**Figure 2.10**c). Furthermore, hydrate-melts benefit from superior thermal stability as comparison with super-concentrated aqueous electrolytes. Interestingly, Zhang *et al.* discovered that by investigating specific $ZnCl_2$ electrolyte concentrations the hydrogen bond network could be broken. The solid-liquid transition temperature of the 7.5 m to 10 m $ZnCl_2$ aqueous electrolyte was lowered, thereby suitable for battery applications.[146] Although the above electrolytes allowed superior cycling performance, $ZnCl_2$ salts remained corrosive and could not allow long cycling stability. Highly concentrated aqueous electrolytes were also investigated with organic Zn salts. Patil *et al.* demonstrated that increasing the concentration to 4 M $Zn(TFSI)_2$ improved the stability of the aqueous electrolyte toward Zn anode owing to a more positive corrosion potential and lower corrosion current than the conventional $ZnSO_4$ -based aqueous electrolyte.[147]

- Additives for aqueous electrolytes

Another approach consisted in introducing liquid[148] or solid[149] electrolyte additives to regulate the electrode/electrolyte interfacial chemistry. Song *et al.* introduced acetonitrile as co-solvent in a $Zn(TFSI)_2$ aqueous electrolyte enlarging the electrochemical stability window of the aqueous electrolyte.[150] The presence of acetonitrile molecules enabled to reduce

dendrite growth on the Zn anode and suppress the formation of the by-product $Zn(OH)_2$. Meanwhile, the larger electrochemical stability window and the limited free water molecules endowed the stability of MnO_2 cathode at high voltage. Saccharin was added as electrolyte additive to control the electrical double layer structure on the Zn anode.[151] Interestingly, saccharin derived anions are favourably adsorbed and decomposed on Zn anode, thereby excluding water molecules from the electrical double layer. Therefore, Zn plating and stripping processes demonstrated high reversibility. By introducing zinc dihydrogen phosphate ($Zn(H_2PO_4)_2$) salt into 1 M $ZnTFSI_2$ electrolyte, a robust SEI layer was formed on the Zn anode owing to the reaction of $Zn(H_2PO_4)_2$ salt with OH^- produced by HER in the first cycles (**Figure 2.10**d).[23] Furthermore, the SEI formation on Zn anode was also investigated when a fluorinated additive (trimethylethyl ammonium trifluoromethanesulfonate ($Me_3EtNOTF$)) was introduced with $ZnOTF_2$ –based electrolyte.[152] Similarly than in Li metal batteries, it was demonstrated that fluorinated species are beneficial to form a robust SEI layer on Zn anode.

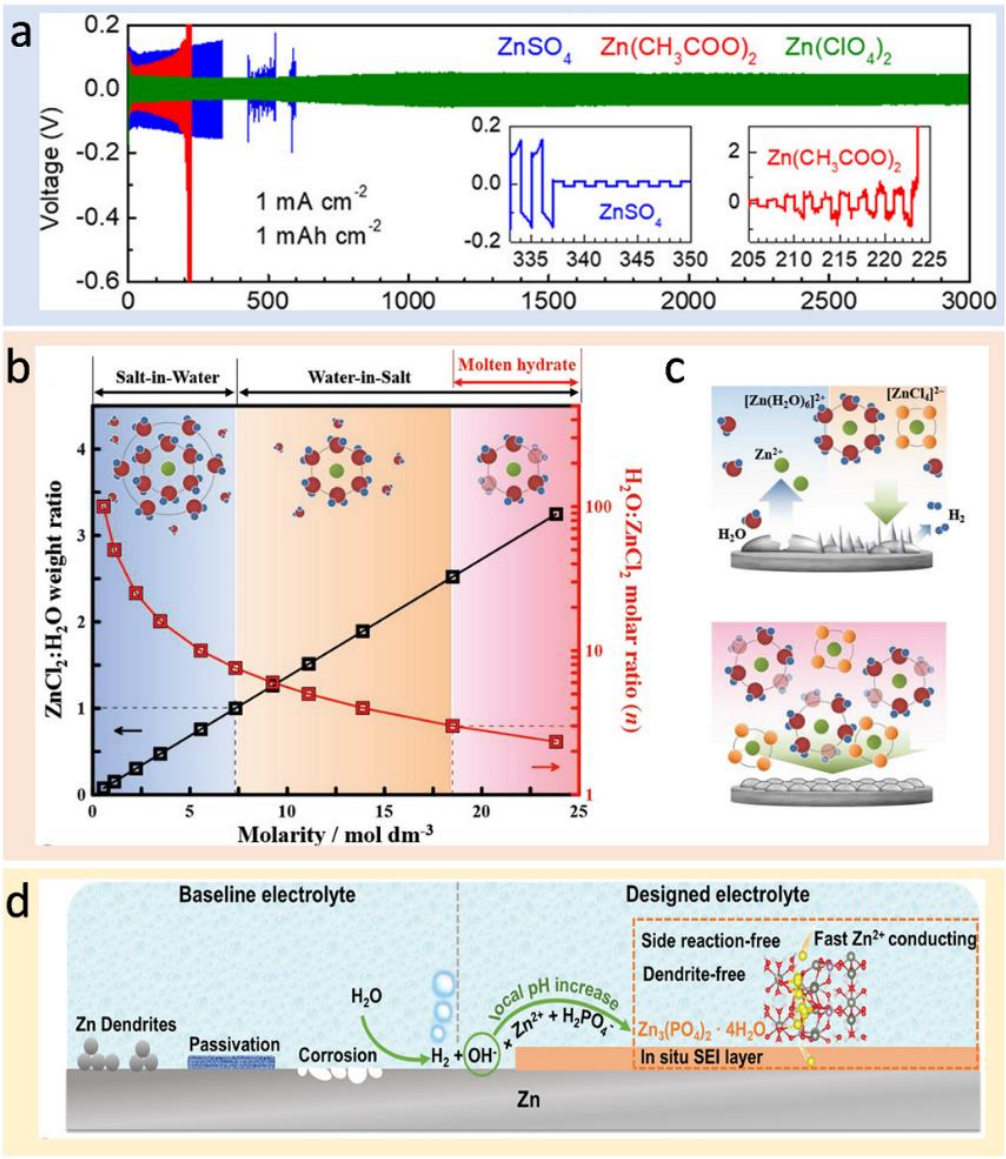

Figure 2.10. (**a**) Zn stripping/plating behaviour in symmetric cells at 1 mA cm^{-2} with $ZnSO_4$ (blue), $Zn(CH_3COO)_2$ (red), and $Zn(ClO_4)_2$ (green) electrolytes. Reproduced with permission.[21] Copyright 2019, American Chemical Society. (**b**) Molarity of the $ZnCl_2$–H_2O binary system as functions of the weight ratio of $ZnCl_2$ to H_2O and the molar ratio of H_2O to $ZnCl_2$ (n). The prospective hydration shells around Zn are shown as inset and (**c**) Schematic illustration of Zn deposition in conventional electrolytes (top) and in a molten hydrate electrolytes (bottom). Reproduced with permission.[22] Copyright 2019, John Wiley & Sons, Inc. (**d**) Schematic illustration of Zn surface evolution in baseline electrolyte and the SEI formation mechanism in the as-prepared electrolyte. Reproduced with permission.[23] Copyright 2021, John Wiley & Sons, Inc.

- Hybrid zinc-lithium batteries

As cited above, Zn-ion batteries suffer from low average voltage and sluggish kinetics of Zn^{2+} insertion in the cathode host.[142] Coupling Zn metal anode with a lithium intercalation cathode is an attractive approach to fabricate high average voltage batteries with improved reaction kinetics while maintaining high safety. Alike Zn-ion batteries, the practical application of Zn-Li hybrid batteries still faces several issues (*e.g.*, side reactions, dendrite growth, capacity fading, *etc.*). Recently, electrolyte engineering such as employing highly concentrated electrolytes and introducing electrolyte additives have demonstrated promising result to overcome these issues.

As previously explained, the discovery of "water-in-salt" electrolytes have opened up new research directions to enlarge further the electrochemical stability window of aqueous electrolytes, thereby reducing water evolution and increasing reversibility of aqueous –based batteries. Wang *et al.* synthesised a 20 m LiTFSI + 1 m $Zn(TFSI)_2$ highly-concentrated aqueous electrolyte which was applied in a hybrid Zn-LMO battery.[24] The high concentration of TFSI anions altered the solvation sheath structure of Zn^{2+} in the electrolyte where close ion pairs $(Zn\text{-}TFSI)^+$ became predominant, replacing the usual $(Zn\text{-}(H_2O)_6)^{2+}$ complex solvation structure (**Figure 2.11**a-b). The super-concentrated electrolyte enabled nearly 100 % Coulombic efficiency attesting of the dendrite free plating/stripping reversible processes. When applied in a Zn||LMO battery, the system delivered an energy density of 180 Wh kg^{-1} while maintaining 80 % capacity over 4000 cycles. The pH of aqueous electrolytes in Zn-based batteries dictates the zinc species electrochemical stability. With this in mind, Yu *et al.* introduced ammonia in a 1 M $Zn(CH_3COO)_2$ + 4 M $LiCH_3COO$ until adjusting the pH of the electrolyte to 11.[153] By designing this mildly alkaline aqueous electrolyte, the H^+ co-insertion into LCO cathode was alleviated meanwhile zinc ligand cations $(Zn(NH_3)_4^{2+}$ were formed, therefore the Zn||LCO hybrid batteries provided high voltage and high cycling stability.

Another approach consists in protecting the Zn anode by incorporating additives in the dilute aqueous electrolyte. Jin *et al.* stabilised the Zn anode by adding 0.5 wt% polyethylene oxide (PEO) in a dilute Zn-Li hybrid aqueous electrolyte (1 M $ZnSO_4$ + 1 M lithium sulphate (Li_2SO_4)).[25] As schematically drawn on **Figure 2.11**c, the long PEO chains hinder Zn^{2+} cation transfer kinetics along the anode and regulate the Zn^{2+} cation concentration near the Zn

anode, therefore promoting smooth Zn plating, which was confirmed with SEM (**Figure 2.11**d). Moreover, the adsorbed PEO chains on the anode inhibited HER leading to a decrease of electrolyte consumption as well as the formation of by-products (*e.g.*, ZnO). Therefore the plating and stripping Coulombic efficiency in half-cells reached over 99.5 % with high stable cycling of over 3000 h. Hao *et al.* reported a cheap electrolyte additive, sodium dodecyl benzene sulfonate, to improve the electrochemical performances of hybrid Zn||LFP aqueous batteries.[154] Sodium dodecyl benzene sulfonate is a well-known surfactant. When applied in Zn||LFP rechargeable batteries, the surfactant improved the wettability of LFP cathode and ameliorated the Zn plating and stripping processes. It was demonstrated that dendrite growths were suppressed owing to the passivation film formed by the adsorption of the surfactant molecules on the Zn anode.

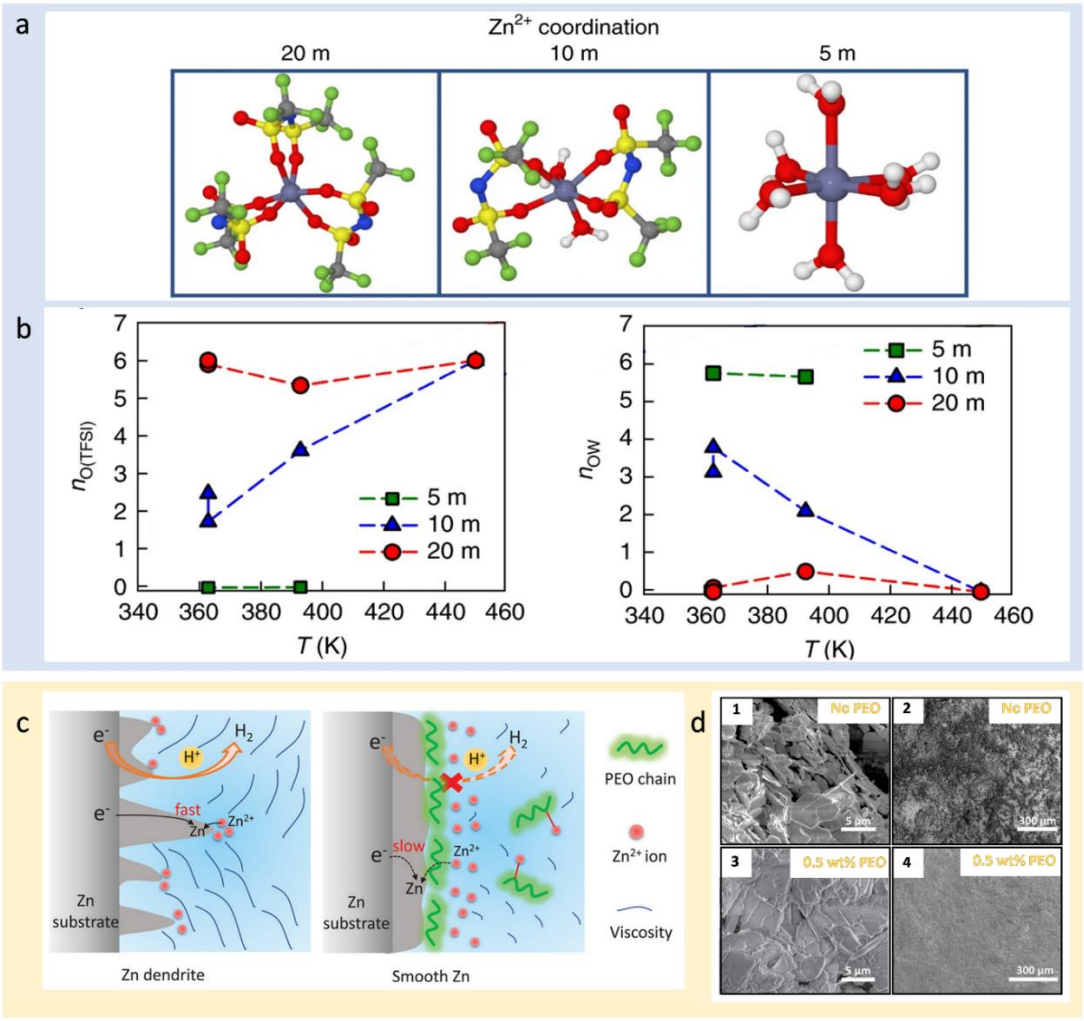

Figure 2.11. (**a**) Representative Zn^{2+}-solvation structures in the electrolytes with 1 m $Zn(TFSI)_2$ and three concentrations of LiTFSI (5 m, 10 m and 20 m).(**b**) Zn^{2+}–O(TFSI) (left) and Zn^{2+}–

O(water) (right) coordination numbers for aqueous electrolytes with 1 m $Zn(TFSI)_2$ and three concentrations of LiTFSI (5 m, 10 m and 20 m). Reproduced with permission.[24] Copyright 2018, Springer Nature Limited (**c**) Schematics of electrochemical Zn deposition mechanism without (left panel) and with (right panel) PEO polymer molecules. (**d**) SEM images of Zn anodes after 200 cycles (1,2) without PEO polymer and (2,3) with 0.5 wt% PEO polymer in 1 m $ZnSO_4$ aqueous electrolytes. Reproduced with permission.[25] Copyright 2020, Elsevier B.V.

2.5 Quasi-solid electrolytes

Quasi-solid electrolytes are constructed with a polymer matrix whose pores are filled with liquid electrolyte. The liquid phase in quasi-solid electrolytes provides high ionic conductivity and good electrode/electrolyte interfacial contact, meanwhile the polymer matrix ensures high mechanical properties. In the recent years, gel electrolytes have been largely investigated to enhance the electrode/electrolyte interface stability and the safety of batteries by preventing leakage, and to optimise the electrolyte physical properties (*e.g.*, thermal stability, self-healing, flexibility, *etc.*). Generally, quasi-solid electrolytes can be separated according to two fabrication methods: chemical polymerisation or physical polymerisation.

2.5.1 Chemical electrolyte polymerisation

The chemical electrolyte polymerisation consists in introducing monomers, cross-linkers and initiators in the liquid electrolyte to create a precursor solution. Subsequently, the polymerisation reaction is initiated by applying an external force, depending on the type of initiator (*e.g.*, heat-sensitive, light sensitive, electrochemical sensitive, *etc.*). In general, quasi-solid electrolytes are synthesised *via* addition polymerisation process, which follow three steps:

(1) Initiation. The initiators are decomposed into radicals which can open the carbon-carbon double bond (C=C) on monomers. Then, the monomers can react with other open monomers, thereby creating polymer chains.

(2) Propagation. The continuous addition of monomer units to the polymer chains is called the propagation.

(3) Termination. The termination process occurs when a free radical reacts with the activated end of the polymer chain or if two polymer chains combine.

In battery applications, precursor solutions are finely tuned to achieve specific properties. For instance, to enhance the electrode|electrolyte contact, the polymerisation may be *in-situ* initiated by impregnating the separator with the precursor solution. Another approach consists in developing quasi-solid electrolytes with high mechanical strength as electrolyte membrane, thereby playing the role of electrolyte and separator. Furthermore, introducing cross-linker monomers in the precursor solution results in quasi-solid electrolytes with high thermal stability owing to the strong chemical bonding between the polymer chains.[155]

Our group developed a deep eutectic solvent-based self-healing polymer electrolyte by a thermal-initiated *in-situ* polymerisation.[47] The strong crosslinking bonds in the polymer matrix not only retained the liquid electrolyte but also provided Li^+ channels, thereby preventing dendrite growth on the metal anode. Moreover, the as-prepared polymer demonstrated self-healing abilities owing to the formation of hydrogen bonds between polymer chains, as further detailed in *Chapter IV*. Another approach to create ionic channels consisted in employing polyzwitterion species which are charged polymers with anionic and cationic groups. A poly [2-(methacryloyloxy) ethyl] dimethyl-(3-sulfopropyl) polyzwitterionic hydrogel electrolyte employed in Zn-ion batteries exhibited a high ionic conductivity of 3.2 x 10^{-2} S cm^{-1} with a Zn^{2+} transference number of 0.656.[26] Furthermore, the hydrophilic charged group in the polymer immobilized the water molecules and therefore inhibited side reactions such as dendrite growth and Zn corrosion (**Figure 2.12**a). Finally, this hydrogel also demonstrated high mechanical properties such as stretching, twisting and self-healing owing to the crosslinking network of the polymer matrix (**Figure 2.12**b). The full Zn||MnO_2 or Zn||VS_2 could sustain cutting which attest of the high safety provided with this electrolyte.

Radiation-initiated polymerisation is also a rapid polymerisation process widely used in quasi-solid electrolyte design. Wu *et al.* synthesized a self-standing nanocomposite polymer electrolyte by UV curing a cross-linked polyurethane acrylate monomer and forming *in-situ* TiO_2 nanoparticles.[156] The as-prepared gel electrolyte enabled excellent safe operation of Li metal batteries with dendrite-free morphologies. Such polymerisation technique has also been employed to fabricate protective films on metal anodes. For instance, an ionic liquid

skinny gel was spin-coated and directly UV-polymerised on the surface of Zn anode.[120] The hydrophobic polymer repulsed water molecules from the Zn anode while allowing Zn plating and stripping processes. Our group design a UV-initiated aqueous quasi-solid electrolyte for Mo_6S_8||LMO batteries (*Chapter V*). The gelling of the liquid electrolyte enabled to enlarge further the electrochemical stability window of the quasi-solid electrolyte owing to the blockage of water molecules through hydrogen bonds with the polymer chains.

Numerous pathways to initiate an additive polymerisation have been explored. However, thermally and UV –cured gel electrolytes are the most commonly employed techniques in quasi-solid electrolyte designs owing to their simplicity, inexpensive and fast processes.

2.5.2 Physical electrolyte polymerisation

The physical polymer electrolytes can be prepared either by dissolving or by swelling a solid polymer in the liquid electrolyte. This technique requires little equipment, therefore is inexpensive and is easily scalable. Depending on the end-of-product utilisation, the gel electrolyte properties can be optimised by carefully selecting the nature of the polymer.

PVA has been largely employed in aqueous electrolytes to further enlarge the electrochemical stability window of "water-in-salt" electrolytes.[17-18, 27] Furthermore, when employed in a sulphur||LMO aqueous battery, PVA matrix prevented polysulphide species dissolution; thereby the batteries achieved high reversibility with small capacity decay as comparison with the liquid "water-in-bisalt" aqueous electrolyte (**Figure 2.12**c).[27] In addition to the enhancement of cycling performance (suppression of dendrite growth and side reactions), mechanical properties (stretchability and flexibility), thermal stability (low and high temperature) and safety, more exotic properties can be integrated to the hydrogel such as self-healing. The self-healing mechanism rest on large amount of hydrogen bonds that can be broken/re-formed between polymer chains.[157] Huang *et al.* presented a self-healing hydrogel electrolyte based on PVA polymer and $Zn(TFSI)_2$ zinc salt.[158] When this electrolyte was applied in Zn||PANI-based cathode, the battery exhibited high performance even after being cut/healed several times.

A wide temperature range where gel electrolytes can operate is essential for battery commercialisation. Several research groups explored anti-freezing hydrogel using highly

concentrated electrolytes[159] or glycerol[160] as anti-freezing agent to decrease the water freezing point. Anti-freezing agents disturb the water arrangement at low temperature and diminish water evaporation at high temperature owing to hydrogen bonds. Zhao *et al.* explored a quasi-solid electrolyte with cooling recovery ability involving a temperature dependant sol-gel transition process of the thermoreversible polymer.[28] At room temperature the gel electrolyte was solid, then, by simply cooling down the battery, the electrolyte became liquid (**Figure 2.12**d). This feature enabled the battery to repair the electrode/electrolyte contact damages due to mechanical abuses (*e.g.*, bending, twisting, *etc.*). This quasi-solid electrolyte was formed through physical entanglements of poly(ethylene oxide)-poly(propylene oxide)-poly(ethylene oxide) (PEO-PPO-PEO, Pluronic) polymer dissolved in 0.25 M $ZnSO_4$ and 0.25 M Li_2SO_4. The Zn|Pluronic-based gel electrolyte|LMO battery displayed a healing efficiency superior than 98 % attesting of the capability of the cooling-recovery concept. Yang *et al.* addressed high temperature issues by the mean of a hydroscopic hydrogel electrolyte based on polyacrylamide or PVA applied in a unsealed battery design.[161] Simply, when the battery exceed normal operational temperature the water in the hydrogel will naturally evaporate resulting in a sharp decrease of ionic conductivity and therefore shutdown of the battery. As the temperature of the battery cools down, the hydroscopic electrolyte will naturally absorb water from the ambient air and therefore the battery will recover its functionality. This approach is particularly interesting for safe battery applications.

In metal-based batteries, physical polymerisation is also a common strategy to improve the plating/stripping performance of the battery due to the ionic regulation provided by the gel network, which guide the cations and prevent dendrite growth. Tang *et al.* employed a simple and effective method to synthesis a bio-based alginate zinc polymer electrolyte by directly dissolving sodium alginate in deionized water and subsequently initiating a Zn ions crosslinking reaction with 2 M $ZnSO_4$ and 0.2 M manganese sulphate ($MnSO_4$).[162] The carboxylate groups on the alginate polymer chains forms channels for Zn^{2+} cations migration. This ion confinement arrangement enable dendrite-free Zn anode and minimised side reactions of the aqueous alginate-zinc gel electrolyte in Zn||MnO_2 batteries, meanwhile retaining high ionic conductivity (1.83 x 10^{-2} S cm^{-1}). However, such bio-sourced polymer usually lack of mechanical properties.

2.5.3 Hybrid polymer electrolytes

Gel electrolytes obtained by physical polymerisation may suffer from low mechanical strength and low thermal stability. By combining chemical and physical polymerisations, such gel electrolytes can benefit from both advantages.

Chan *et al.* synthesised a single-ion conducting double network hydrogel electrolyte based on co-polymerisation of iota carrageen and acrylamide, therefore combining both physical and chemical polymerisation.[163] Iota carrageen backbones provided control on the anionic species and water molecules by immobilizing them within the hierarchical porous network while acrylamide improved structural and mechanical properties of the hydrogel. Owing to the ionic channels created by the hydrogel matrix, this electrolyte demonstrated high ionic conductivity of 2.15 x 10^{-3} S cm^{-1} with a zinc transference number of 0.93 meanwhile the gel electrolyte could withstand a stretchability of 300 % strain.

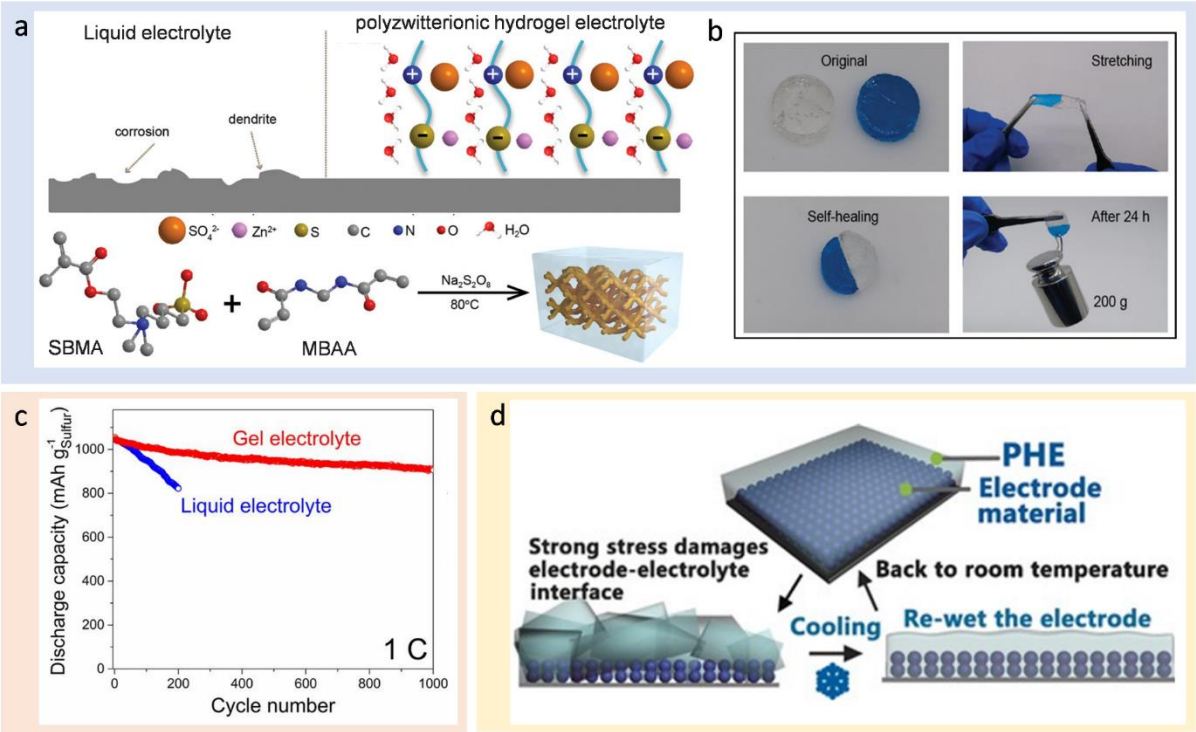

Figure 2.12. (**a**) Schematic illustration of the morphologies of Zn metal anode with liquid electrolyte and polyzwitterionic hydrogel electrolyte during Zn plating and schematic illustration of the formation of polyzwitterionic hydrogel electrolyte (SBMA: [2-(methacryloyloxy) ethyl] dimethyl-(3-sulfopropyl) monomer; MBAA: N,N'-methylenebisacrylamide). (**b**) Stretching and self-healing behaviour of the hydrogel electrolyte with and without blue colorant. Reproduced with permission.[26] Copyright 2020,

John Wiley & Sons, Inc. (**c**) Cycling performance of aqueous sulphur||$LiMn_2O_4$ full cells with liquid and gel electrolytes at 1C rate. Reproduced with permission.[27] Copyright 2017, National Academy of Sciences. (**d**) The cooling-recovery function by incorporation of a thermoreversible Pluronic hydrogel electrolyte (PHE). Reproduced with permission.[28] Copyright 2017, John Wiley & Sons, Inc.

2.6 Summary

This literature chapter introduced some general background on battery operations and their development with the point of view of safety. Li-ion batteries widely employed in portable devices were developed about 30 years ago. Although the astonishing improvement of the electrode materials and electrolytes allowed to dramatically increase the energy density of Li-ion batteries with high safety since their first commercialisation in 1991, the high energy density required for electric vehicles and large grid energy storage surpasses the theoretical energy density achievable by Li-ion batteries based on graphitic anode.[48] Therefore, other battery technologies are attracting extensive interest as next battery generation such as metal-based batteries (e.g., Li metal) and multivalent-based batteries (e.g., Zn).

Organic electrolytes, which are common in Li-based batteries, usually present high flammability due to the decomposition of the electrolyte at high temperature, which leads to the thermal runaway of the battery. However, battery safety remains primordial for commercialisation. Accordingly, diverse non-flammable liquid electrolytes were explored and are summarized below, their advantages and disadvantages are also presented in **Figure 2.13**.

(1) Non-flammable organic electrolytes. Introducing fire-retardant additives such as phosphate-based compounds, which are able to scavenge hydrogen radicals; selecting thermally stable Li salts (e.g., LiTFSI, LiFSI, etc.); and employing high concentrated electrolytes thereby reducing the solvent molecule reactivity are the most common methods to enhance the safety of organic electrolytes. The fire-retardant effect versus the cost of the electrolyte should be judiciously balanced by optimising the electrolyte composition.

(2) Ionic liquids and DESs. Ionic liquids and DESs present non-flammability and are considered as a much safer electrolyte alternative, especially for Li metal batteries.

However, the former faces cost issues while the later lacks of electrochemical stability towards high-voltage cathode materials.

(3) Aqueous electrolytes. Employing water as solvent inherently provide non-flammability. Although many progresses have been made to improve the electrochemical stability window of aqueous electrolytes, the energy density of Li-ion batteries still remains limited. Other battery technologies such as Zn-ion batteries are predominately coupled with aqueous electrolytes owing to the compatibility of Zn anode with water solvent.

Furthermore, the gelling of the liquid electrolytes to create quasi-solid electrolytes provides leak-proof safety. The gelling of the electrolyte occurs through physical or chemical polymerisation. The former rely on the dissolution of a polymer in the liquid electrolyte, while the latter is prepared by introducing monomers and initiator in the electrolyte, which is subsequently *in-situ* polymerised. Therefore, quasi-solid electrolytes may be tailored by careful selection of the polymer/monomer (*e.g.*, self-healing, flexibility, *etc.*).

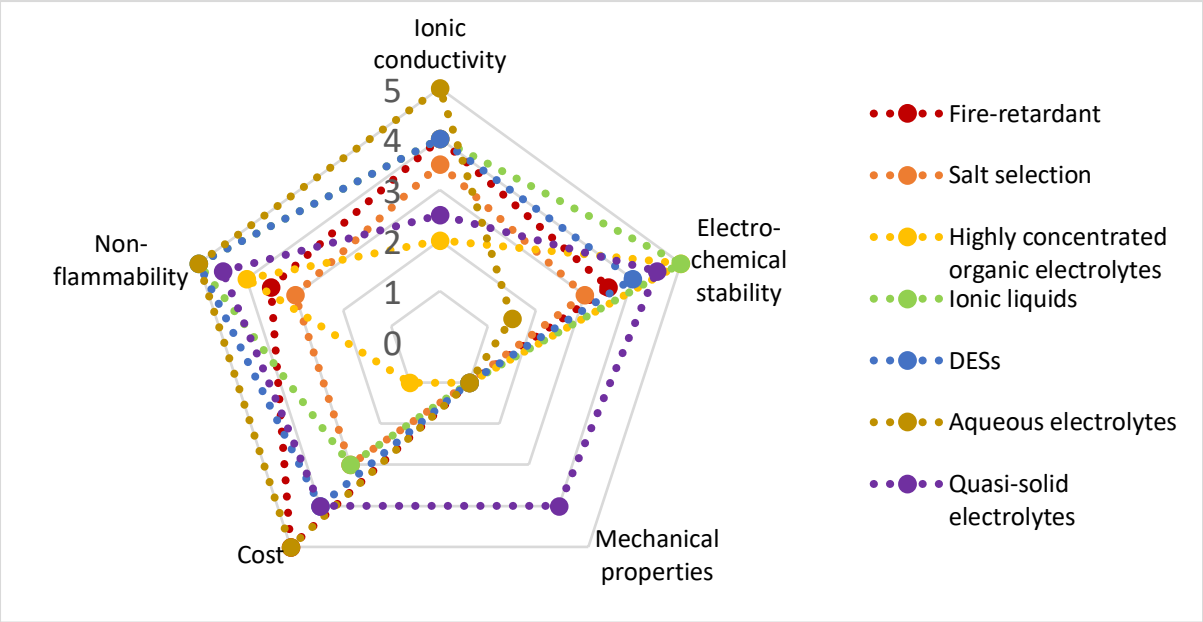

Figure 2.13. Summary of different non-flammable systems.

Chapter III: Methodology

3.1 General approach

Figure 3.1 schematically represents the methodology employed during this Ph.D. thesis. The electrolytes were first prepared and systematically characterized with physical, electrochemical and chemical analyses. Then, electrode materials were selected and several type of batteries were assembled to investigate the battery cycling performances. Finally, post-mortem analysis were carried out on the electrodes and separator materials. **Table 3.1** summarize the chemical compounds employed during experiments.

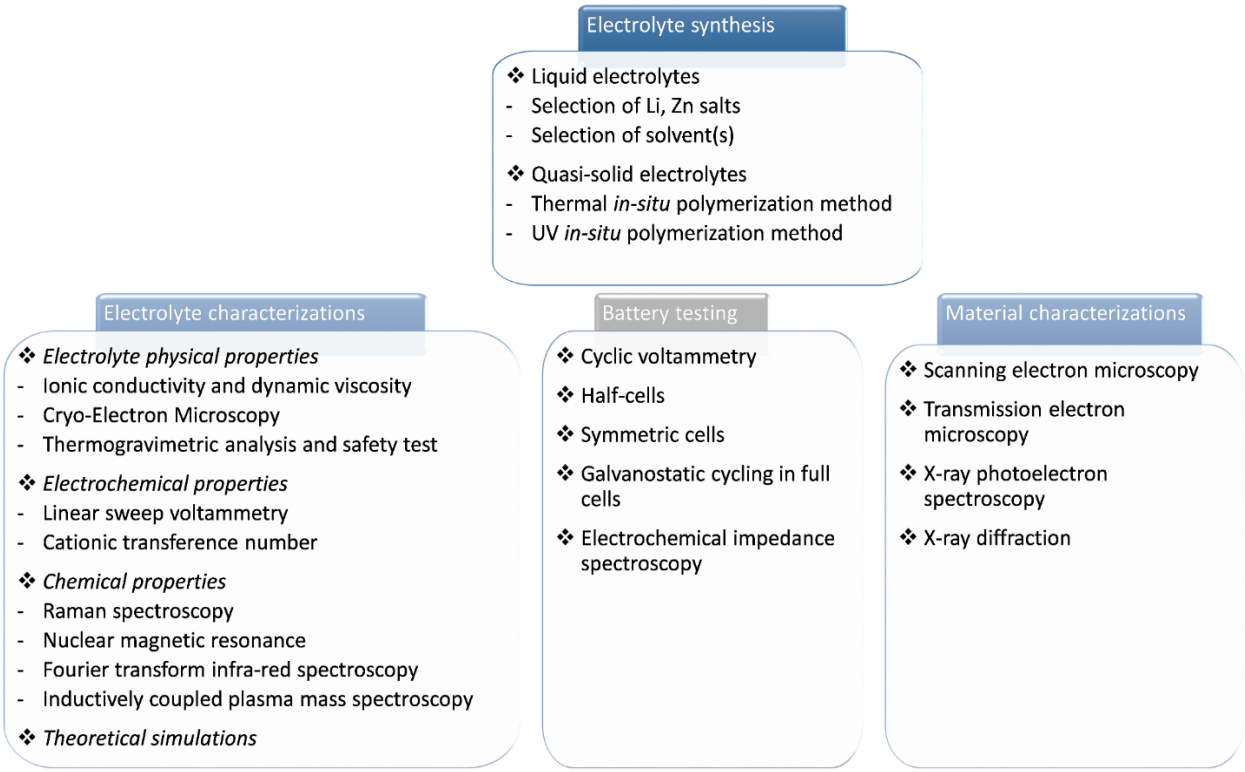

Figure 3.1. Summary of the methodology employed in this Ph.D. thesis.

Table 3.1: Chemical compounds employed during experiments.

Chemical name	Chemical formula	Purity	Supplier
Lithium bis(trifuoromethane sulfonyl)imide (LiTFSI)	$LiC_2F_6NO_4S_2$	99.95 %	DuoDuo Chem

Electrolyte preparation	Lithium hexafluorophosphate	$LiPF_6$	99.95 %	DuoDuo Chem
	Lithium nitrate	$LiNO_3$	99.99 %	Sigma-Aldrich
	Lithium trifluoromethanesulfonate (LiOTf)	CF_3SO_3Li	99.995 %	Sigma-Aldrich
	Zinc trifluoromethanesulfonate ($Zn(OTf)_2$)	$(CF_3SO_3)_2Zn$	98 %	Sigma-Aldrich
	N-methylacetamide (NMAc)	C_3H_7NO	99 %	Sigma-Aldrich
	N-methylformamide (NMF)	C_2H_5NO	99 %	Sigma-Aldrich
	Fluoroethylene carbonate (FEC)	$C_3H_3FO_3$	99 %	DuoDuo Chem
	Dimethyl sulfoxide (DMSO)	$(CH_3)_2SO$	99.9 %	Sigma-Aldrich
	Diethylene carbonate (DEC)	$(C_2H_5O)_2CO$	99 %	Sigma-Aldrich
	Propylene carbonate (PC)	$C_4H_6O_3$	99 %	Sigma-Aldrich
	Ethylene carbonate (EC)	$C_3H_4O_3$	99 %	Sigma-Aldrich
	Tetraethylene glycol dimethyle ether (TEGDME)	$C_{10}H_{22}O_5$	99 %	Sigma-Aldrich
	1,5-pentanediol	$C_5H_{12}O_2$	96 %	Sigma-Aldrich
	2-Amino-4-hydroxy-6-methylpyrimidine	$C_5H_7N_3O$	98 %	Sigma-Aldrich
	2-isocyanatoethyl methacrylate	$C_7H_9NO_3$	98 %	Sigma-Aldrich
	Pentaerythritol tetraacrylate (PETEA)	$C_{17}H_{20}O_8$	-	Sigma-Aldrich
	2,2′-azobis(2-methylpropionitrile) (AIBN)	$C_8H_{12}N_4$	-	Sigma-Aldrich
	Tetraethylene glycol diacrylate (TEGDA)	$C_{14}H_{22}O_7$	Technical grade	Sigma-Aldrich
	2-hydroxy-2-methylpropiophenone (HMPP)	$C_{10}H_{12}O_2$	97 %	Sigma-Aldrich
	Li metal chips	Li	99.999 %	DuoDuo Chem

Electrode preparation	Zn metal foil	Zn	99.95 %	Sigma-Aldrich
	Lithium manganese oxide (LMO)	$LiMn_2O_4$	-	Shanshan Co, Ltd
	Carbon black	C	100 %	Sigma-Aldrich
	Polyvinylidene fluoride (PVDF)	$-(C_2H_2F_2)_n-$	-	Sigma-Aldrich
	Polytetrafluoroethylene (PTFE)	$-(C_2F_4)_n-$	60 % solution	Sigma-Aldrich
	N-methyl-2-pyrrolidone (NMP)	C_5H_9NO	99.5 %	Sigma-Aldrich
	Potassium chloride	KCl	99 %	Sigma-Aldrich
	Molybdenum disulfide	MoS_2	98 %	Sigma-Aldrich
	Copper(II) sulfide	CuS	99 %	Sigma-Aldrich
	Molybdenum	Mo	99.9 %	Sigma-Aldrich
Separator	Glass fibre			Whatman GF/A

3.2 Electrolyte syntheses

3.2.1 Liquid electrolytes

Generally, electrolytes are synthesised by directly dissolving the metal salts (*e.g.*, Li salts or Zn salts) in the solvent (*e.g.*, water for aqueous electrolytes). The concentration of metal salt in the electrolyte is expressed either in molarity referred as "M" (*i.e.*, mole of salt dissolved in one litre of solvent, mol L^{-1}) or in molality referred as "m" (*i.e.*, mole of salt dissolved in one kilo of solvent, mol $kg^{-1}_{solvent}$). In dilute electrolyte, molarity is predominantly employed because the volume change resulting from the introduction of salt in the electrolyte is negligible. In highly concentrated electrolytes, the large amount of salt introduced in the solvent considerably changes the volume of the electrolyte therefore, molality is preferred.

When preparing super-concentrated electrolytes, determining the salt solubility at room temperature is essential to avoid crystallisation of the electrolyte. To prepare super-concentrated electrolytes, a maximum amount of salt is dissolved in the solvent by stirring the solution at 40 ℃ for several hours, then the electrolyte is slowly cooled down to room temperature and remains in liquid state. It is noted that the salt solubility increases with temperature.

Deep eutectic solvents (DESs) are a mixture of at least two chemical compounds, one is a hydrogen bond donor, and the second one is a hydrogen bond acceptor. When these compounds are mixed together in their eutectic ratio, the resulting mixture presents a melting point significantly lower than that of each chemical taken separately. Therefore, finding the correct ratio between the components is primordial to obtain a deep eutectic solvent electrolyte. Subsequently, the binary blend is stirred at 40-60 °C to well homogenise the mixture, then upon cooling down, the as-prepared DES remains in a liquid state.

3.2.2 Quasi-solid electrolytes

The transition from liquid to quasi-solid electrolytes is effectuated by adding a gelling agent. The gelling agent can either be a monomer, which is *in-situ* polymerised or a polymer, which is directly dissolved, in the liquid electrolyte at high temperature (*i.e.*, chemical or physical polymerisation). Here after, only *in-situ* polymerisation is introduced since I have focused my work on chemical polymerisation processes.

Briefly, an *in-situ* polymerisation consists in introducing monomers directly into the liquid electrolyte to prepare a precursor solution. Subsequently, the *in-situ* polymerisation is triggered within the precursor solution. Therefore, *in-situ* polymerisation is beneficial for intimate electrode/electrolyte contact and good separator wetting. A range of monomers is commercially available, yet to obtain specific properties (*e.g.*, high flexibility, self-healing, *etc.*), one may need to synthesise the monomer itself. In this thesis, I have employed thermal and UV-sensitive initiators, which will be details in *Chapter IV* and *Chapter V*, respectively.

3.3 Electrolyte characterisations

3.3.1 Electrolyte physical properties

As electrolytes are the medium that carries chemical charges between the electrodes, their chemical, electrochemical and physical properties are key for superior electrode|electrolyte stability and high battery cycling performance. Usually, electrolytes must present specific properties such as high ionic conductivity; good compatibility with electrodes, current collectors and battery case; low viscosity along with good separator and electrode wettability; non-flammability; *etc.*

3.3.1.1 Ionic conductivity

The ionic conductivity is calculated from the bulk resistance (R_b) of the electrolyte obtained with EIS analysis (**Equation 3.1** and **Figure 3.2**). As shown in **Figure 3.2**, the testing set-up was composed of a heating bath to control the temperature, a testing electrode linked to EIS electrochemical station and the electrolyte sample. The ionic conductivity of a sample at a specific temperature was calculated according to the following equation.

$$\sigma = \frac{l}{R_b \times d} \qquad (3.1)$$

With σ the ionic conductivity (in S cm^{-1}), l the distance separating the two electrodes (in cm), d the surface area of the electrodes (cm^{-2}) and R_b the bulk resistance of the electrolyte (in Ω).

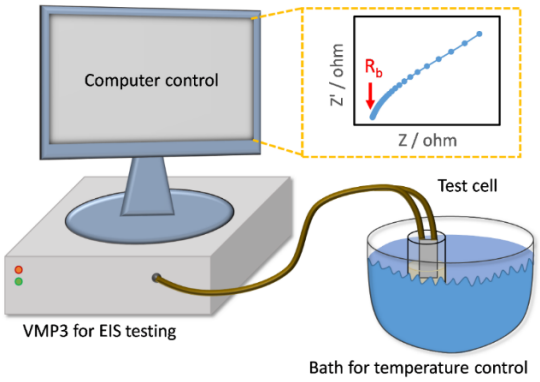

Figure 3.2. Typical experimental set-up to determine the ionic conductivity at various temperature and EIS spectra to determine the bulk resistance of the electrolyte.

The ionic conductivity is closely related to the temperature. By using a water bath, the ionic conductivity of the electrolytes was measured for multiple temperature ranging from 4 °C to

80 °C. Generally, the Arrhenius equation (**Equation 3.2**) or the Vogel–Fulcher–Tammann (VTF) equation (**Equation 3.3**) can accurately describe the relation between ionic conductivity and temperature.

$$\sigma = \sigma_0 \times \exp(-\frac{E_a}{k_B \times T}) \quad (\mathbf{3.2})$$

With σ the ionic conductivity, σ_0 the pre-exponential factor, E_a the activation energy, k_B the Boltzmann constant and T the absolute temperature. By plotting, log σ *vs.* 1/T a straight line is obtained from which the activation energy and the pre-exponential factor can be determined.

$$\sigma = \sigma_0 T^{-\frac{1}{2}} \exp\left(-\frac{E_a}{\mathrm{R}(T-T_0)}\right) \quad (\mathbf{3.3})$$

where σ_o is the pre-exponential factor, E_a is the activation energy, T_o is the effective glass transition temperature, and R is the ideal gas constant.

3.3.1.2 Dynamic viscosity

Dynamic viscosity measurements were effectuated with a cone and plate viscometer. The sample is located in the space between the plate and the cone, then the plate rotates at a known angular speed while the cone is fixed. With this system, the viscosity is calculated from the shear stress obtained from the torque and the shear rate acquired from the angular velocity.

3.3.1.3 Cryo-Electron Microscopy

Cryo-electron microscopy (Cryo-EM) is carried out to investigate samples at cryogenic temperature, generally cooled down with liquid nitrogen. This technique was employed to observe the gel electrolyte structure in *Chapter IV*.

3.3.1.4 Thermogravimetric analysis

Thermogravimetric analysis (TGA) is effectuated by measuring the weight of a sample while slowly rising the temperature in the furnace. Volatile elements evaporate at different temperature. Therefore, the mass loss as a function of the temperature corresponds to certain elements, which can be identified and quantified.

3.3.1.5 Safety test

The safety of the electrolytes was tested by flammability and volatility tests. The flammability test consisted in exposing the electrolyte to an open flame for several seconds. The volatility of the electrolyte was measured in ambient conditions by recording the weight of the sample.

3.3.2 Electrolyte electrochemical properties

3.3.2.1 Linear sweep voltammetry

Linear sweep voltammetry (LSV) is an electrochemical technique employed to measure the electrochemical stability window of the electrolytes. In linear sweep voltammetry, a fixed potential range is scanned at a certain scan rate (mV s^{-1}) while the current response is recorded. The electrochemical stability of the electrolyte can be tested in two different cell set-up, namely the three-electrode system or the two-electrode system.

- Three-electrode system is based on three electrodes (**Figure 3.3**): the *reference electrode* with a fix potential (*e.g.*, Ag/AgCl reference electrode) which control the potential at the working electrode, the *working electrode* where the desired potential is applied (*e.g.*, titanium foil, stainless steel foil, *etc.*) and the *counter electrode* which passes the current needed (*e.g.*, platinum wire).
- Two-electrode system considers the reference and the counter electrode as one electrode while the positive electrode is the working electrode.

Depending on the electrolyte, one or the other system may be more appropriate. The three-electrode system requires a large amount of electrolyte (few mL) and is suitable for any electrolytes, while the two-electrode system is usually fabricated in coin cell with Li or Zn metal anode as reference and counter electrode. Therefore, the electrolyte must be stable against the metal anode and less than 100 µL is necessary.

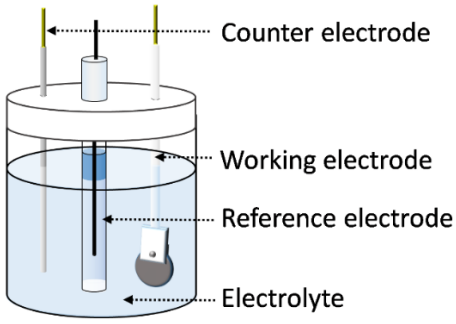

Figure 3.3. Three-electrode system arrangement.

3.3.2.2 Cationic transference number

The cationic transference number (t^+) is a characterisation commonly used for quasi-solid and solid-state electrolytes. It informs on the electrical mobility of the cation and its contribution to the total current carried in the electrolyte. Ionic species travel at different speed in the electrolyte depending on their charge, size, *etc.*, therefore the fraction of current they carried also varies according to the ionic species and electrolyte. The transference number is usually calculated according to Bruce and Vincent method by applying a small constant potential between non-blocking electrodes until a steady current is reached.[164] Subsequently, the transference number is calculated from the **Equation 3.3**:

$$t^+ = \frac{I_{ss} \times (\Delta V - I_0 R_0)}{I_0 \times (\Delta V - I_{ss} R_{ss})} \qquad (\mathbf{3.3})$$

With I_{ss} the steady-state current, I_0 the initial current, ΔV the applied potential, and R_{ss} and R_0 the electrode resistances after and before the polarization (obtained with EIS measurement), respectively.

3.3.3 Electrolyte chemical properties

Raman spectroscopy, Nuclear Magnetic Resonance (NMR) and Fourier Transform Infra-Red (FT-IR) analyses inform on the chemical structure of the electrolytes.

3.3.3.1 Raman spectroscopy

Raman spectroscopy consists on focusing a laser light on the sample and observing the shift in the wavelength from the scattered radiation, which provides information on the chemical and molecular interaction or structure of the sample. In this study, Raman spectroscopy

permitted to understand the molecular structure and interaction between ionic species and solvent molecules.

3.3.3.2 Nuclear magnetic resonance

H-Nuclear magnetic resonance is based on placing the sample in a strong magnetic field, then the H atoms become polarized. Subsequently, the resonant frequencies are measured and transformed into NMR spectra. Several atoms can be observed by NMR such as hydrogen or oxygen, however only hydrogen atoms were relevant in my experiments.

3.3.3.3 Fourier transform infra-red spectroscopy

Fourier transform infra-red (FT-IR) analysis measures the wavelengths which are absorbed by a material in the infra-red area. FT-IR is used to recognise chemical groups present in a molecule by identifying the corresponding absorption peaks to the chemical groups. This method was applied to verify the successful polymerisation of the liquid electrolytes into quasi-solid electrolytes. The spectra obtained for the polymer matrix was compared with that of monomers, in case of a complete polymerisation the C=C double bonds would disappear in the spectrum of the polymer matrix (*Chapter IV*). FT-IR further informed on the solvation structure in aqueous electrolytes (*Chapter V and VI*).

3.3.3.4 Inductively coupled plasma mass spectroscopy

Inductively coupled plasma mass spectroscopy (ICP-MS) is an analytical analysis to quantify the amount of a chemical element in a sample. The sample is first ionized into atoms, which are detected. This technique is extremely precise and requires several preparation steps (*e.g.*, preparation of the standards, calibration, *etc.*). In my research, ICP-MS was employed to analyse the amount of transition metal species (manganese) which had dissolved from the cathode into the electrolyte during cycling (*Chapter IV and VI*).

3.3.4 Theoretical properties

Numerical simulations theoretically confirmed the experimental results and further highlighted the effect of the gel electrolyte on the Li plating and stripping processes as detailed in *Chapter IV*.

Molecular dynamic (MD) simulations enabled to understand further the solvation structure of the electrolyte and the interaction between solvent and ionic species (*Chapter V and VI*). In this PhD thesis, several open source code were employed such as Packmol[165], LAMMPS[166] and NAMD[167] for molecular calculation and VMD[168] for molecular visualisation.

3.4 Battery testing

3.4.1 Battery assembly

All the batteries were assembled and tested in coin cells (as per **Figure 2.1**). Two type of coin cells were investigated depending on the electrochemical testing required.

(1) Half-cells.

Half-cells are employed to study the performance of one electrode at a time. Half-cells are composed of a reference/counter electrode (*e.g.*, Li metal, copper (Cu) metal or Zn metal) and a working electrode, the electrode of interest. The two electrodes are separated by a separator filled with electrolyte. To remove the oxide layer on Cu metal, the Cu foils were first washed with 1 M hydrochloric acid (HCl). Subsequently, they were rinsed with DI water and dry at 100 °C in a vacuum oven before storing in the glovebox.

(2) Full cells.

Full cells consist of an anode (*e.g.*, Li metal, Mo_6S_8, Zn metal) and a cathode (*e.g.*, LMO) which are separated by a separator (*e.g.*, glass fibre) filled with electrolyte.

The electrode materials were fabricated according to two methods depending on the current collector. In the case of aluminium and titanium foil current collectors, the slurry was obtained by mixing the active material (LMO), binder (polyvinylidene fluoride, PVDF) and carbon back in the mass ratio 80: 10: 10 with anhydrous N-methyl-2-pyrrolidone (NMP) solvent. The slurry was manually coated on the current collector and subsequently dried overnight in a vacuum oven at 70 °C. The as-prepared electrodes had a mass loading of about 1.5 mg cm^{-2}. For stainless steel mesh current collectors, the active material (LMO or Mo_6S_8) was mixed with polytetrafluoroethylene (PTFE) and carbon black in the mass ratio 80: 10: 10. Then, the mixture was pressed on the mesh current collector. After that, the electrodes were

dried overnight in a vacuum oven at 70 °C. The mass loading of these electrodes was about 3 mg cm^{-2}.

3.4.2 Electrochemical testing

Several electrochemical tests were effectuated to investigate the electrochemical reactions occurring at the electrodes such as cyclic voltammetry (CV), symmetric cells, galvanostatic cycling and electrochemical impedance spectroscopy (EIS).

Cyclic voltammetry (CV) analysis is an electrochemical technique that measures the current response of an electrochemical system as a function of an applied potential (*i.e.*, scan rate measured in mV s^{-1}). The current will fluctuated when the redox potential is approached (redox peaks) which correspond to the redox reactions occurring at the working electrode. The reversibility of each reaction is observed by comparing the reduction and oxidation peaks as well as the peak potential/intensity changes over several cycles. Depending on the electrolyte, the CV test cell is either a two-electrode (*i.e.*, half-cell) or a three-electrode system.

In metal anode–based batteries (*e.g.*, Li or Zn), symmetric cells were employed to analyse the metal plating and stripping process reversibility. To do so, a constant current is applied to the cell meanwhile the voltage is recorded over a determined period. Half-cells (*i.e.*, Cu as anode and Li or Zn as cathode) were assembled to measure the plating and stripping Coulombic efficiency. In half-cell, a plating process occurs for a chosen period of time, then, the stripping process begins and stops when the cell voltage reaches the cut-off potential attesting that all the deposited metal have been stripped off. For my experiments, I choose 0.5 V as cut-off potential, which prevented electrolyte degradation.

Galvanostatic charge-discharge is usually employed to test the cycling efficiency of full cells. Briefly, a constant current density is applied between a certain voltage window. The specific capacities of the electrodes can be calculated from the **Equation 3.4**.

$$Q = I \times t \qquad (\mathbf{3.4})$$

with Q the specific capacity in mAh g^{-1}, I the current density in mA g^{-1} and t the charge/discharge time in hours. In practice, the current density is calculated based on the

theoretical specific capacity of the electrode and cycling rate considered (*i.e.*, 1 C corresponds to 1 h charge and 1 h discharge cycle). Long cycling performances were obtained by cycling the full cells for more than 150 cycles. Rate performances were acquired by cycling the full cells while increasing the cycling rate (*e.g.*, 0.2 C to 2 C). Specific charge and discharge capacities were recorded during galvanostatic cycling, while the Coulombic efficiency was calculated by dividing the discharge capacity by the charge capacity.

Electrochemical impedance spectroscopy (EIS) is an electrochemical technique that quantify the resistance and diffusion processes in an electrochemical cell. The EIS spectra is obtained by imposing a small amplitude alternating current over a wide range of frequencies on the electrochemical cell, meanwhile the resulting impedance is measured. The bulk resistance (R_b) equals the resistance of the electrolyte, the separator and the electrodes. In the high frequency area, the semi-circle usually correspond to the resistance of the SEI layer. The semi-circle in the medium frequency range is related to the resistance of the charge transfer at the electrode/electrolyte interface. The linear line at low frequency range corresponds to the Warburg impedance created by the diffusion process. EIS was tested in full cells before and after galvanostatic charge-discharge cycling, the difference in the EIS spectra provided precious information on the electrochemical mechanism.

3.5 Material analyses

3.5.1 Field emission scanning electron microscopy

Field emission scanning electron microscopy (FE-SEM) is an electron microscope that creates an image of the surface of the sample. The sample is scanned by a focused electron beam, therefore producing various scattered electrons, which can provide information on the morphology and composition of the surface of the sample. Here, FE-SEM was employed to observe the metal deposition on the anode (*e.g.*, Li deposit or Zn deposit) and to characterize dendrite growth. Top section and cross section images were obtained to compare the morphology of the deposition in different samples.

3.5.2 Transmission electron microscopy

Transmission electron microscope (TEM) is an electron microscope where an electron beam is transmitted through the sample generating high-magnified images. The resolution being much higher than FE-SEM images, TEM analysis enabled to observe the SEI or CEI layer formed on the anode and on the cathode, respectively.

3.5.3 X-ray photoelectron spectroscopy

X-ray photoelectron spectroscopy (XPS) is a quantitative spectroscopic technique that analyses the surface chemistry of a sample (*e.g.*, chemical state, element bonding and elemental composition). Briefly, a beam of X-rays irradiates the surface sample meanwhile the number of ejected electrons and kinetic energies are measured, thereby the binding energies are obtained.

For XPS depth profiling, XPS is paired with ion-beam etching in order to analyse the sample across the surface. This is a very powerful instrument to understand the formation of SEI layer as the identity and quantity of the chemical compounds in the SEI can be identified.

3.5.4 X-ray diffraction

X-ray diffraction (XRD) is an analytical technique used to characterize crystalline material. The sample placed under X-rays produces constructive interferences when the conditions satisfy Bragg's Law (**Equation 3.5**) or else destructive interferences.

$$n\lambda = 2d \sin\theta \qquad \textbf{(3.5)}$$

where n is the diffraction order, λ is the wavelength of the X-ray, d the spacing of the crystal lattice and θ the angle between the incident ray and the scatter plane.

By analysing the sample at various incident angle, several crystallographic planes can be identified. This technique was employed to confirm the purity of cathode and anode active materials and analyse electrode surface after cycling (*Chapter IV and VI*).

Furthermore, by adapting the sample cell, *in-situ* XRD can inform on the spacing between crystallographic planes during charge and discharge processes of the battery, thereby revealing reversibility and phase changes in the material (*Chapter VI*).

3.6 Summary

Many different electrochemical, analytical and theoretical analyses were employed in the realisation of this thesis. **Table 3.2** summarised the different instruments as well as the parameters adopted in the experiments.

Table 3.2. Experimental analyses and equipment

Test	**Equipment**	**Parameters**
Ionic conductivity	Bio-logic VMP3	Temperature: 4 to 90°C, from 100 kHz to 1 Hz, alternating current amplitude of 5 mV
Dynamic viscosity	Discovery HR-1 hybrid rheometer	Geometry 60mm, 2.008° cone plate, Peltier plate steel, at 25 °C
pH	FiveEasy Plus pH Meter FE28	Room temperature
Cryo-EM	Tecnai G^2 F30 TEM	300 kV
TGA	TGA TA Instruments SDT 2960	Room temperature to 300 °C, heating rate 10 °C min^{-1} under nitrogen atmosphere
LSV	Bio-logic VMP3	Scanning rate of 10 mV s^{-1}
CV	Bio-logic VMP3	Scanning rate 0.1 mV s^{-1}
Galvanostatic cycling	NEWARE LAND 2001 A Battery tester	1 C
EIS	Bio-logic VMP3	Frequency range: 10 mHz to 100 kHz, disturbance amplitude of 5 mV
Cationic transference number	Bio-logic VMP3	Polarization potential (10 mV), Li||Li symmetric cells
Raman spectroscopy	Renishaw inVia	785 nm laser
NMR spectroscopy	Agilent 500 MHz	H-NMR
ICP-MS	Nexion300	GF membrane separators via immersing into 3 mol L^{-1} HCl
Numerical simulation	COMSOL Multiphysics®	-
MD simulation	NAMD, VMD, Packmol, LAMMPS	-
FE-SEM	Zeiss EVO LS15 SEM	10 kV
TEM	Tecnai G^2 F30 TEM	300 kV
XPS	PHI 5000 VersaProbe II	Monochromatic Al Kα X-ray source at 1486.6 eV
XRD	Bruker D8 Discover	10 2θ - 90 2θ, increment 0.02 2θ, at room temperature

CHAPTER IV: Deep Eutectic Solvent-Based Self-Healing Polymer Electrolyte for Safe and Long-Life Lithium Metal Batteries

4.1 Introduction

Lithium (Li)-ion batteries have been widely used in modern society to power portable electronic devices.[169] However, the energy density of the state-of-the-art Li ion batteries employing graphite anodes has almost reached their theoretical upper limit (~250 Wh kg^{-1}).[170] To further increase the energy density to 500 Wh kg^{-1} for fulfilling the application requirements of long-range electric vehicles, new battery configurations are urgently needed.[38] Among alternative anode materials, metallic Li anodes have attracted worldwide attention due to their ultrahigh specific capacity (3860 mAh g^{-1}) and lowest redox potential (-3.040 V *vs.* SHE).[171] However, several troublesome obstacles have impeded the practical application of Li metal anodes in rechargeable batteries. Currently, liquid electrolytes with highly flammable solvents (such as carbonates and ethers) are widely applied in Li metal batteries, which causes great safety concerns such as fire, explosion and toxic electrolyte leakage.[40] More importantly, Li metal with high reactivity spontaneously reacts with the solvents and Li salts in these electrolytes, thus forming a passive solid electrolyte interface (SEI) on the anode surface.[172] Generally, the strength of SEI cannot withstand the volume change in the repeated Li plating-stripping processes, which generates defects on the SEI.[173] Li ions prefer to diffuse to these defects where the local current density is concentrated during the subsequent deposition, thus leading to Li dendrite growth.[174] Li dendrites can penetrate through the separator, and trigger serious safety issues (*e.g.*, short circuits and thermal runaway).[175] Furthermore, dendrites with a large surface area of fresh Li results in a continuous damage-reconstruction of the SEI upon cycling, which decreases the Coulombic efficiency of Li metal batteries.[176] Moreover, when applying lithium transition metal oxides as cathode materials in Li metal batteries, the cathodic transition metal ions generally suffer from pronounced dissolution into liquid electrolytes, and subsequently cause negative effects on the Li metal anode. This is even more severe at elevated temperature, and aggravates capacity fading of Li metal batteries.[138]

In recent years, extensive efforts have been devoted to developing non-flammable electrolyte systems for Li metal batteries. These include all-solid-state and quasi-solid

electrolytes,[177] all-fluorinated-based electrolytes,[83] ionic liquid-based electrolytes,[178] and deep eutectic solvent (DES) electrolytes, *etc.* Among them, the DES electrolytes are of particular interest owing to their numerous advantages such as low vapour pressure, non-flammability, biodegradability, low cost, and ease of preparation.[179] Fundamentally, DESs are eutectic mixtures of Lewis or Brønsted acids and bases. The melting points of DESs are lower than those of each individual component due to the intermolecular hydrogen bonds, thus enabling them to remain in liquid state at room temperature.[180] The DESs applied as electrolytes for Li metal batteries are generally prepared by spontaneous liquefaction when mixing Li salts (*e.g.*, lithium bis(trifluoromethanesulfonyl)imide (LiTFSI)[4]) with hydrogen bond donors (low cost solid organics such as urea[30b] and amides[181]), which is attractive for large-scale battery applications. However, DES electrolytes still face safety risks of electrolyte leakage due to their liquid nature. More seriously, the poor compatibility between DES electrolytes and Li metal, and the high solubility of cathodic transition metal ions in DESs result in low reversible capacity and poor cycle life of Li metal batteries. At present, there are only a few reports about DES electrolyte for Li metal batteries.[8, 30b]

In this work, we report on a new type of DES-based self-healing polymer (DSP) electrolyte for stable Li metal batteries. This DSP electrolyte was synthesized *in-situ* by thermally polymerizing 2-(3-(6-methyl-4-oxo-1,4-dihydropyrimidin-2-yl)ureido)ethyl methacrylate (UPyMA) and pentaerythritol tetraacrylate (PETEA) monomers in the presence of an DES-based electrolyte, which contains LiTFSI and N-methylacetamide (NMAc) in an eutectic ratio, and fluoroethylene carbonate (FEC) as additive. The addition of FEC significantly improves the ionic conductivity and electrochemical stability of the DSP electrolyte. It simultaneously constructs robust fluorine (F)-rich SEI and cathode electrolyte interface (CEI) against Li dendrite growth on the anode and structural deterioration on the cathode, respectively. The self-healing UPyMA-PETEA copolymer matrix keeps the DSP electrolyte in a quasi-solid-state without the safety issues of electrolyte leakage, and maintains excellent electrode|electrolyte interfacial contacts during prolonged cycling. Moreover, the copolymer matrix not only efficiently regulates the Li ion flux that leads to a dendrite-free Li deposition on the anode, but also effectively suppresses transition metal ion dissolution from the lithium transition metal oxide cathode. The as-developed DSP electrolyte exhibits non-combustibility, high ionic conductivity (1.79×10^{-3} S cm^{-1} at 25 °C) and electrochemical stability (up to 4.5 V

vs. Li/Li^+), as well as stable interfacial properties. When applied in Li metal||$LiMn_2O_4$ (LMO) batteries, the DSP electrolyte -based batteries deliver superior cycling performances at both room and elevated temperatures.

4.2 Experimental section

4.2.1 Synthesis of the UPyMA monomer

The monomer was synthesized as follows (**Figure 4.1**a).[182] Basically, 2-Amino-4-hydroxy-6-methylpyrimidine (1.0 g, 8 mmol, Sigma-Aldrich) was added into 25 mL dimethyl sulfoxide (DMSO, Sigma-Aldrich), and stirred for 10 min at 150 °C. Then 2-isocyanatoethyl methacrylate (1.32 g, 8.5 mmol, Sigma-Aldrich) was added into the flask, and white solid was precipitated when the solution cooled down to room temperature. The precipitate was collected and washed several times with methanol and acetone to remove the residual DMSO. Then the precipitate was dried under vacuum at 30 °C for 4 h, and the obtained white powder was collected. The ^1H nuclear magnetic resonance (NMR) spectrum with $CDCl_3$ as solvent via an Agilent 500MHz NMR spectrometer verified that the UPyMA monomer was successfully prepared (**Figure 4.1**c).

4.2.2 Preparation of the DSP electrolyte:

To prepare the DES electrolyte, lithium bis(tri-fuoromethanesulfonyl)imide (LiTFSI, DuoDuo Chem) and N-methyacetamide (NMAc, Sigma-Aldrich) was mixed in different molar ratios at 50 °C until a transparent solution was obtained. The DES + FEC electrolyte was prepared by adding 10 wt% of fluoroethylene carbonate (FEC, DuoDuo Chem) into the DES electrolyte (with a LiTFSI: NMAc molar ratio of 1: 4). The DSP electrolyte was prepared by *in-situ* polymerisation of a precursor solution. Firstly, 3 wt% UPyMA monomer was dissolved in the DES + FEC electrolyte, and subsequently the mixture was heated to 40 °C until it became transparent. After that, 1.5 wt% pentaerythritol tetraacrylate (PETEA) as cross-linker and 0.1 wt% 2,2'-azobis(2-methylpropionitrile) (AIBN) as initiator were added to the mixture and thus obtain the transparent precursor solution. The polymerisation was thermally initiated at 70 °C for 15 min to obtain the DSP electrolyte (**Figure 4.1**b). All above procedures were conducted in an argon-filled glove box (Universal 2440/750) with a moisture/oxygen concentration below 0.1 ppm.

The polymer matrix was separated from the DSP electrolyte by washing it with acetone. After that, the mixture was by centrifuged at 10,000 rpm for 15 min. Above procedures were repeated for three times, and then the write precipitate was vacuum-dried at 120 °C to obtain the separated UPyMA-PETEA copolymer matrix.

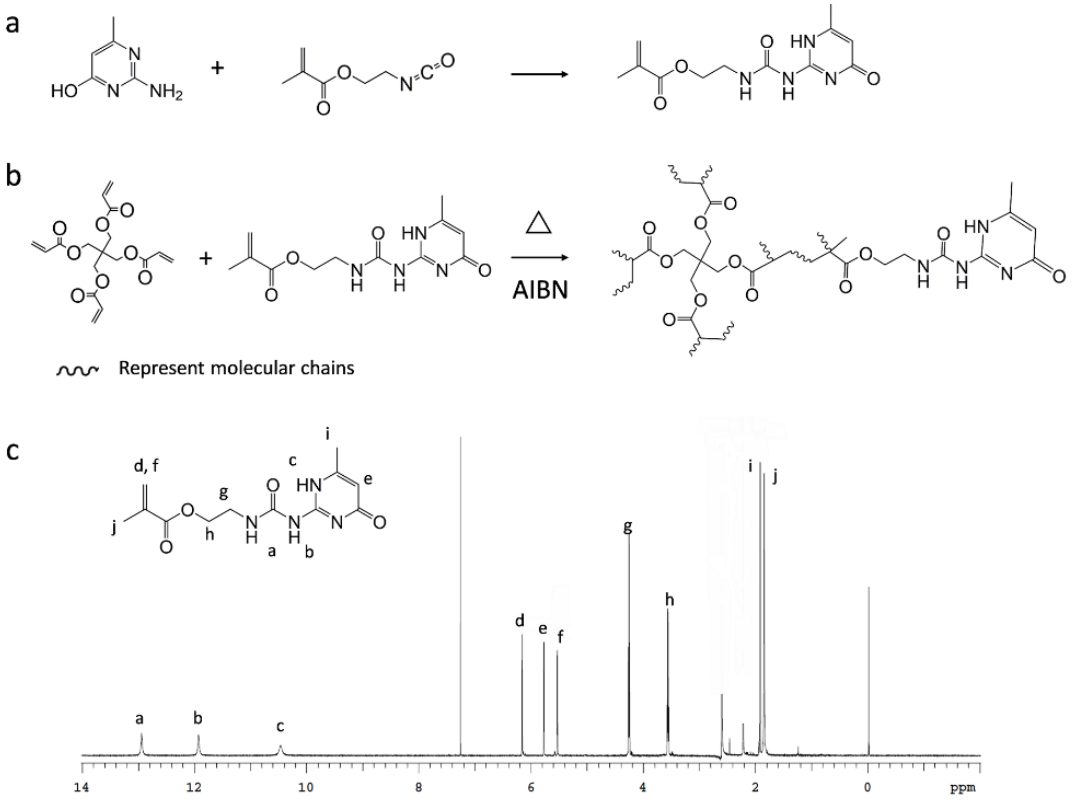

Figure 4.1. Synthesis route of (**a**) the UPyMA monomer and (**b**) the polymerisation process. (**c**) NMR spectra of the as-synthesised monomer.

4.2.3 Characterisation of the DSP electrolyte

The viscosity of the DES and DES + FEC electrolytes were measured with a Discovery HR-1 hybrid rheometer (geometry 60mm, 2.008° cone plate, Peltier plate steel) at 25 °C. The Fourier transform infrared (FT-IR) spectra of the UPyMA monomer, PETEA cross-linker and polymer matrix of DSP electrolyte were tested by a Nicolet Magna 6700 spectrometer at room temperature. Transmission electron microscopy (TEM) and Cryo-EM images were conducted by Tecnai G^2 F30 TEM instrument. The weight losses of DSP electrolyte and $LiPF_6$ in EC: DEC (1: 2 by volume) electrolytes were recorded in open air at room temperature (25 °C). Thermogravimetric analysis (TGA) was measured from room temperature to 300 °C with a heating rate of 10 °C min^{-1} under nitrogen atmosphere. For the flammability test, 1 g

electrolyte samples were applied on a piece of glass fiber (GF) membrane. After that, the combustion optical photographs were recorded after the electrolyte samples were exposed to the flame of matchstick for 5 s.

The ionic conductivity of the DSP electrolyte was evaluated from 4 °C to 90 °C via electrochemical impedance spectroscopy (EIS) on a VMP3 (Bio Logic Science Instruments) multichannel electrochemical station from 100 kHz to 1 Hz with an alternating current amplitude of 5 mV. The test cell was a small piece of DSP electrolyte sandwiched between the two stainless steel blocking electrodes. To reach thermal equilibrium, the cell was kept at each testing temperature for at least 20 min before the EIS measurement. The electrochemical stability of the DSP electrolyte was studied via linear sweep voltammetry (LSV) method, which was conducted in a two-electrode test cell with Li foil as both counter and reference electrode and stainless-steel blocking electrode as working electrode using the VMP3 multichannel electrochemical station. The voltage was increased from the open circuit voltage to 6.0 V *vs.* Li/Li^+ at a scanning rate of 10 mV s^{-1}. The lithium ion transference number (t_{Li}^+) of the DSP electrolyte was tested using the method proposed by Evans *et al.*[164, 183] The polarization currents (including the initial (I^o) and steady state (I^{ss}) current values) under a small polarization potential (10 mV) were recorded on a symmetric Li||Li testing cell. In the meantime, the initial and steady state values of the bulk resistances ($R_b{}^o$ and $R_b{}^{ss}$) and electrode|electrolyte interfacial resistances ($R_i{}^o$ and $R_i{}^{ss}$) were measured by EIS before and after the potentiostatic polarization. The t_{Li}^+ was then calculated according to the following equation

$$t_{Li}^+ = \frac{I^{ss}R_b^{ss}(\Delta V - I^0 R_i^0)}{I^0 R_b^0(\Delta V - I^{ss}R_i^{ss})} \quad \textbf{(4.1)}$$

The stability of the DES toward Li metal electrode was measured by galvanostatic cycling method. A symmetrical Li||Li cell was assembled and repeatedly charged and discharged at 0.2 mA cm^{-2} with a cut-off capacity of 0.4 mA h cm^{-2}. The corresponding EISs after 4 h and 160 h cycling were recorded on the VMP3 electrochemical station in a frequency range of 10 mHz to 100 kHz with a disturbance amplitude of 5 mV. Coulombic efficiencies of Li plating and stripping cycles were studied via a Li||Cu cell configuration. In each cycle, 0.4 mA h cm^{-2} of Li was plated on the Cu electrode at a current density of 0.2 mA cm^{-2}, and then stripped until

the potential reached 0.5 V *vs.* Li/Li$^+$. The Li deposition morphology was characterised by field emission scanning electron microscope (FE-SEM) after plating 1.5 mA h cm^{-2} Li on Cu substrate at 0.1 mA cm^{-2}. Before FE-SEM imaging, the Li anode was rinsed with DEC (Sigma-Aldrich) in argon-filled glove box, and then transferred in a FE-SEM instrument (Zeiss Supra 55VP). The depth profiling X-ray photoelectron spectroscopy (XPS) was carried out on a PHI 5000 VersaProbe II spectrometer using a monochromatic Al Kα X-ray source at 1486.6 eV.

4.2.4 Assembly and characterization of the quasi-solid-state Li metal batteries

The $LiMn_2O_4$ (LMO) cathode was prepared by a simple coating method. The LMO active material (Shanshan Co., Ltd), carbon black and polyvinylidene fluoride (PVDF) binder were grinded together in a mass ratio 80: 10: 10 in anhydrous N-methyl-2-pyrrolidone (NMP, Sigma-Aldrich). The slurry was then coated on an aluminium current collector and dried overnight at 70 °C. The mass loading of the cathode was ~1.5 mg cm^{-2}. Lithium chips (DuoDuo Chem) were used as anode and GF membranes (Whatman GF/A) were applied as the separator. The precursor solution containing 3 wt% UPyMA, 1.5 wt% PETEA and 0.1 wt% AIBN in DES + FEC electrolyte was injected into the GF membrane separator and filled into the cells. The assembled cells were aged for 3 h to guarantee that the electrolyte well-wetted the electrodes and the separator. Subsequently, the cells were heated for 30 min at 70 °C to ensure the complete polymerization of monomers. Cycling performances of the assembled cells were tested at various rates (1 C = 148 mA h g^{-1} based on the mass of LMO) between 3.0 and 4.4 V *vs.* Li/Li$^+$ on a Land 2001 A battery testing system at 25 °C. EISs of the Li||LMO cells after 1 and 100 cycles were tested on the VMP3 electrochemical station in a frequency range of 10 mHz to 100 kHz with a disturbance amplitude of 5 mV. High temperature tests were run in a constant temperature oven at 60 °C at 0.1 C. The amount of Mn ions dissolved in the electrolyte after cycling was determined by inductively coupled plasma mass spectroscopy (ICP-MS). The cells were disassembled after 10 cycles, and the Mn ions were eluted from the GF membrane separators via immersing into 3 mol L^{-1} HCl. Then the solutions were diluted 100 times with ultra-pure DI water (< 18 Ω) before running ICP-MS. Owing to the electrode composition (*i.e.*, active material: carbon additive: binder mass ratio 8: 1: 1) and the relatively low mass loading (≈ 2 mg cm^{-2}), the LMO particles stuck well together on the current collector.

Therefore, we can assume that the concentration of Mn^{2+} measured with ICP-MS solely comes from the Mn species dissolved in the electrolyte during cycling.

4.2.5 Numerical simulations

The electrodeposition module in COMSOL Multiphysics® software was applied as the Einstein relation (D = μkbT/q). The cell geometries in COMSOL Multiphysics® simulation were set as follows. The Li nuclei diameter was 200 nm. The distance between two electrodes was set as 50 μm. The overpotential of deposition was -200 mV *vs.* Li/Li^+ at the working electrode, meanwhile the Li^+ diffusion coefficient was set to be 1×10^{-5} cm^2 s^{-1}. The liquid electrolytes were confined in porous structures with different pore sizes: 1 μm in the case of glass fibre membrane, and 10 nm in the case of DSP electrolyte matrix. The surface charge was set as 10 eV on each fibre of the porous structures.

4.3 Discussion

Figure 4.2 schematically illustrates the optimization mechanism of the DSP electrolyte. In the Li metal||LMO cell with non-flammable DES electrolyte consisting of LiTFSI and NMAc in an eutectic ratio (**Figure 4.2**a, left panel), the thick and unstable SEI as a reductive product of the DES on the Li metal anode surface introduces severe Li dendrite growth during cycling. Moreover, the bivalent manganese ions (Mn^{2+}) largely dissolve into the DES from the LMO cathode, which causes structural failure of cathodic active material.[184] Meanwhile, the NMAc dramatically decomposes on the cathode surface during the charging process, which leads to the formation of a high-resistance CEI film. All these result in the poor electrochemical performances of Li metal|DES electrolyte|LMO cells (**Figure 4.2a**, right panel). In contrast, in the cell using DSP electrolyte (**Figure 4.2**b, left panel), the FEC additive can facilitate the formation of a thin and robust SEI film on the Li metal anode, protecting against dendrite growth. Meanwhile, the self-healing UPyMA-PETEA copolymer matrix not only maintains good electrode|electrolyte contacts during cycling without interfacial cracks, but also facilitates homogeneous Li ion flux distribution to enable uniform Li plating. As for the cathode, the copolymer matrix efficiently reduces the Mn dissolution from the cathode, and the FEC with high oxidative stability contributes to a thin and stable protective CEI on the LMO, guarding against interfacial side reactions. Such multifunctional DSP electrolyte is

expected to ensure an excellent cycling stability for both anode and cathode in Li metal||LMO batteries.

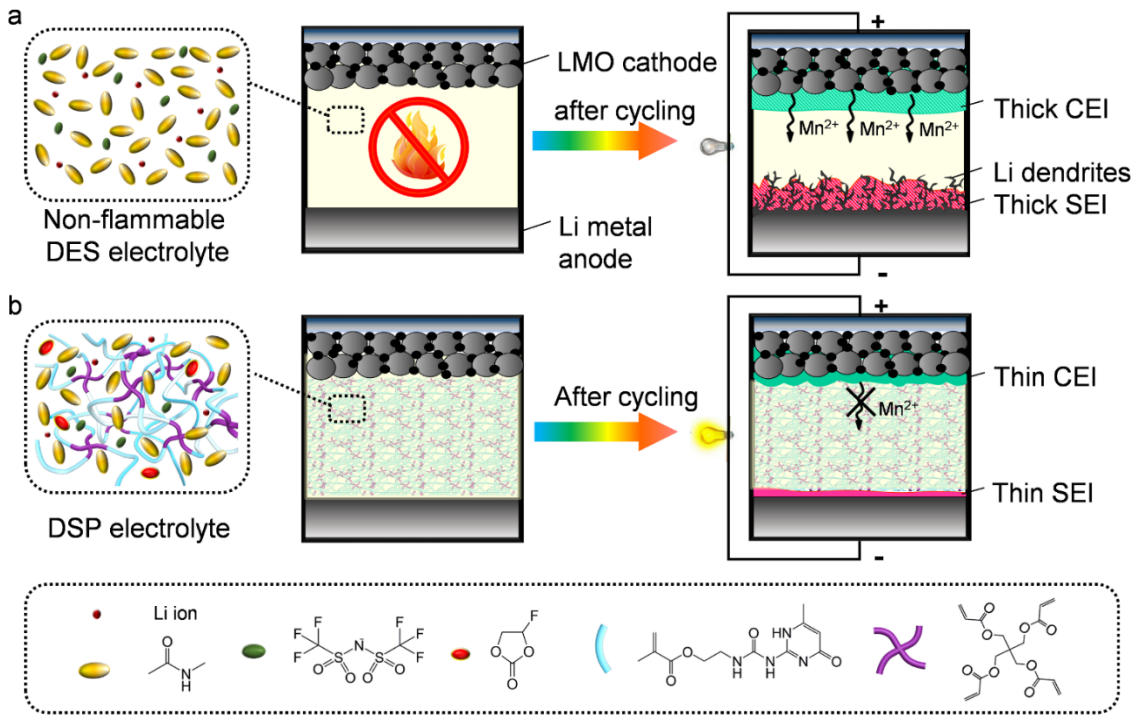

Figure 4.2. Schematic illustration of (**a**) the deep eutectic solvent (DES) and (**b**) DES-based self-healing polymer (DSP) electrolytes in Li||LMO.

4.3.1 Characterisation of the DSP electrolyte

Figure 4.3a shows the Raman spectra of DES electrolytes with different LiTFSI: NMAc molar ratios ranging from 1: 2 to 1: 50. With an increase in LiTFSI: NMAc ratio, the peak intensity of free $TFSI^-$ at ~742 cm^{-1} firstly rises due to the increased $TFSI^-$ concentration, and then decreases accompanying the appearance of a new peak related to $[Li(TFSI)^{2-}]$ ion clusters (~748 cm^{-1}).[185] The corresponding ionic conductivities at 25 °C are shown in **Figure 4.3**b. The ionic conductivity of DES gradually increases with the LiTFSI: NMAc ratio, owing to the increase of ion carrier concentration and then decreases due to ion cluster formation,[4] which is consistent with the Raman spectra. The ionic conductivity of DES reaches its maximum value (1.7×10^{-3} S cm^{-1}) at a ratio of 1: 5 (**Figure 4.3**b). However, the LiTFSI: NMAc ratio of 1: 4 is nearly the eutectic point and can maintain the DES in liquid state for a wider temperature range,[186] meanwhile its ionic conductivity (8.9×10^{-4} S cm^{-1}) is sufficient for battery application. Thus, the LiTFSI: NMAc ratio for the DES electrolyte was set to 1: 4 in this work.

When 10 wt% FEC is added into the DES electrolyte, a new peak at ~733 cm^{-1} appears in the Raman spectra (**Figure 4.3**a), which can be assigned to the coordinated FEC.[187] Moreover, assuming that the scattering cross sections of free $TFSI^-$ anion and $[Li(TFSI)^{2-}]$ ion clusters are similar, the percentage of free $TFSI^-$ in the electrolyte can be calculated based on the following equation:[188]

$$[Free\ TFSI^-] = \frac{A_f}{A_f + A_c} \times 100\ \% \qquad (\mathbf{4.2})$$

where A_f is the integrated intensity of the free $TFSI^-$ band, and A_c is the integrated intensity of the $[Li(TFSI)^{2-}]$ cluster band. The percentage of free $TFSI^-$ anion in the DES electrolyte with a LiTFSI: NMAc ratio of 1: 4 is 87.8 %. It increases to 89.3 % with the addition of FEC, suggesting that the FEC additive dissociates the $[Li(TFSI)^{2-}]$ ion clusters. Moreover, the introduction of FEC efficiently decreases the viscosity of DES electrolyte (from 73 to 37 × 10^{-3} Pa s, **Figure 4.4**a.). These lead to a high ionic conductivity (2.2 × 10^{-3} S cm^{-1} at 25 °C, **Figure 4.4**b) for the obtained DES + FEC electrolyte.

After dissolving UPyMA and PETEA monomers into the DES + FEC electrolyte, the as-prepared transparent precursor solution (**Figure 4.3**c, left) can be transformed into the DSP electrolyte as a translucent gel (**Figure 4.3**c, right) via *in-situ* polymerization. According to the Einstein-Stokes formula, the mesh size of the cross-linked gel is estimated to be around 10 nm.[189] Cryo-electron microscopy (Cryo-EM) images of the DSP electrolyte are displayed in **Figure 4.3**d. Although the meshes formed by polymer chains cannot be directly observed due to the limited resolution, the DSP electrolyte clearly presents a hierarchical porous structure with abundant pores ranging from 50 nm to 2 μm. This structure largely traps the DES + FEC electrolyte inside, which can be expected to enable a high ionic conductivity.

Fourier-transform infrared spectra (FTIR) were measured to verify the polymerisation of monomers in DSP electrolyte. As shown in **Figure 4.3**e, peaks at ~1156 cm^{-1} (C-O symmetrical stretching), ~1265 cm^{-1} (C-O antisymmetric stretching), ~1404 cm^{-1} and ~1460 cm^{-1} (CH_2 bending), and ~1735 cm^{-1} (C=O stretching) appear in the spectrum of the PETEA monomer. Meanwhile, the peaks at ~1647 cm^{-1} and ~1510 cm^{-1} in the UPyMA monomer are assigned to the stretching of N=C and N-H bonds, respectively.[190] It is seen that the C=C vibration peak

at about 1635 cm^{-1} in the monomers almost disappears in the spectrum of polymer matrix,[191] which verifies a high conversion of UPyMA and PETEA monomers to form DSP electrolyte.

The thermal safety of electrolytes is crucial for Li metal batteries. It is seen that our DSP electrolyte blend cannot be ignited (**Figure 4.3**f, upper right panel), and it undergoes negligible weight loss at temperatures up to 100 °C (**Figure 4.4**c). In contrast, the conventional 1 M $LiPF_6$ in ethylene carbonate (EC): diethyl carbonate (DEC) (1: 2 by volume) liquid electrolyte is highly combustible (**Figure 4.3**f, upper left panel), and evaporates quickly even at room temperature due to the low boiling point of the carbonate solvents (**Figure 4.4**d). Such excellent thermal stability of the DSP electrolyte facilitates a safe operation of high-energy Li metal batteries. Furthermore, the DSP electrolyte could completely self-heal within 2 h at room temperature after a through cut (**Figure 4.3**f, lower panels). This is attributed to the intramolecular hydrogen bonding between the ester groups and urea groups in the UPyMA units of the polymer chain.[182] This endows DSP electrolyte-based batteries with an adaptable electrode|electrolyte interface stable against the repeated electrode volume change throughout cycling.

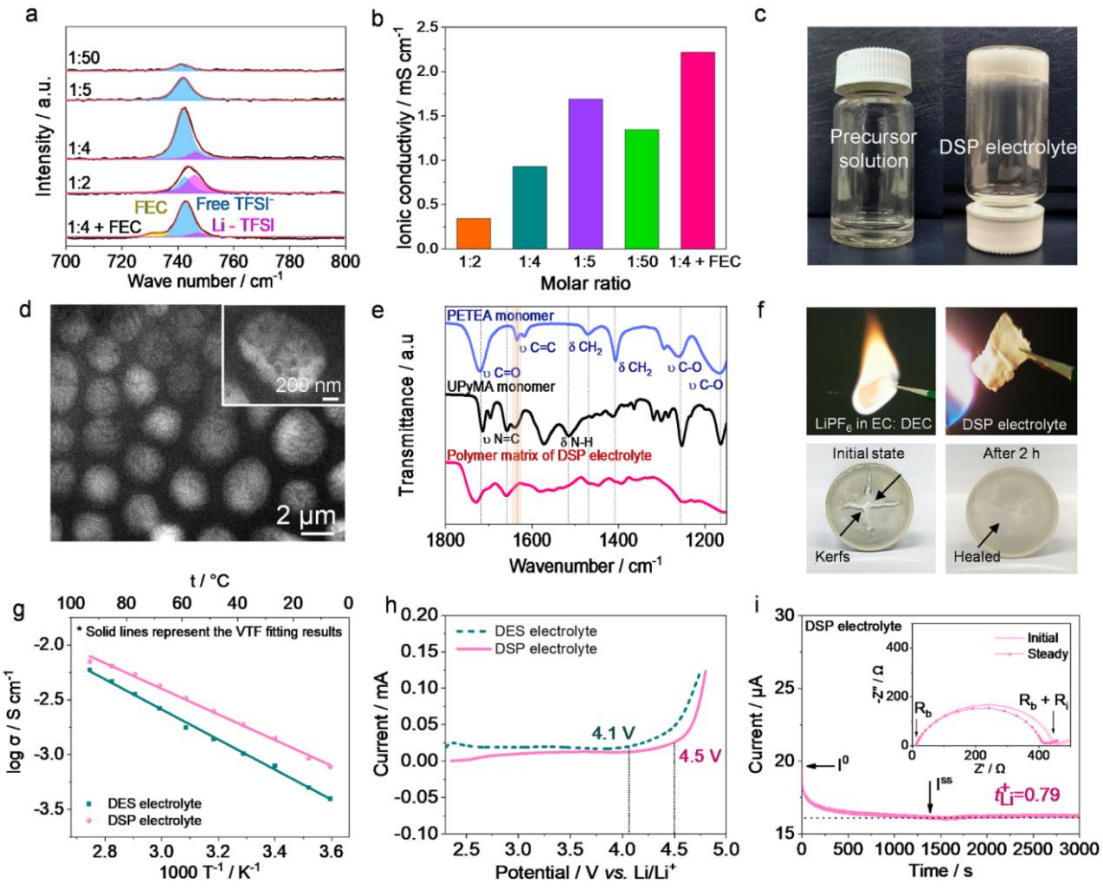

Figure 4.3. Characterization of the DSP electrolyte. (**a**) Raman spectra and (**b**) room temperature (25 °C) ionic conductivities of the DESs with different LiTFSI: NMAc molar ratios; (**c**) Optical images of the precursor solution (left) and DSP electrolyte (right); (**d**) Cryo-EM images of the DSP electrolyte; (**e**) FT-IR spectra of the PETEA monomer, UPyMA monomer and polymer matrix of DSP electrolyte; (**f**) Optical images of the 1 M $LiPF_6$ in EC: DEC electrolyte (upper left panel) and DSP electrolyte (upper right panel) under combustion test, and the self-healing process of DSP electrolyte after being cut (lower panels); (**g**) Ionic conductivities of DES and DSP electrolytes as a function of temperature. The plots represent the experimental data meanwhile the solid lines represent VTF fitting results; (**h**) LSVs of the DES and DSP electrolytes at a scan rate of 10 mV s^{-1} using stainless steel as working electrode, and Li as counter and reference electrodes; (**i**) The chronoamperometry profile of Li|DSP electrolyte|Li cells under a polarization voltage of 10 mV. The corresponding electrochemical impedance spectroscopy (EIS) spectra before and after polarization are shown in the inset.

Figure 4.3g and **Figure 4.4**b present the temperature dependencies of ionic conductivities for different samples (DES electrolyte, DES + FEC electrolyte and DSP electrolyte) in a temperature range from 0 °C to 90 °C. The plots of log σ vs. T^{-1} present a non-linear relationship for the three samples, which is well-described by the Vogel-Tamman-Fulcher (VTF) equation below:[192]

$$\sigma = \sigma_0 T^{-\frac{1}{2}} \exp\left(-\frac{E_a}{\mathrm{R}(T-T_0)}\right) \qquad (\mathbf{4.3})$$

where σ_o is the pre-exponential factor, E_a is the activation energy, T_o is the effective glass transition temperature, and R is the ideal gas constant. The fitting results and ionic conductivities at 25 °C are listed in **Table 4.1**. The ionic conductivity data were also fitted following the Arrhenius equation as reported in **Appendices 1-2**. Both fitting results display a similar trend with similar E_a values. As mentioned above, the addition of FEC increases the ionic conductivity of the DES electrolyte. After polymerisation, the DSP electrolyte maintains a high ionic conductivity of 1.79×10^{-3} S cm^{-1} at 25 °C. Furthermore, it is worth noting that the E_a value for the DSP electrolyte (4.91×10^{-2} eV) is quite close to that of the DES + FEC electrolyte (4.03×10^{-2} eV). This indicates that the ionic mobility inhibition caused by the crosslinking polymer matrix is negligible, considering E_a is the barrier for ionic conduction.

Such a high ionic conductivity is sufficient to meet the application requirements for Li metal batteries.

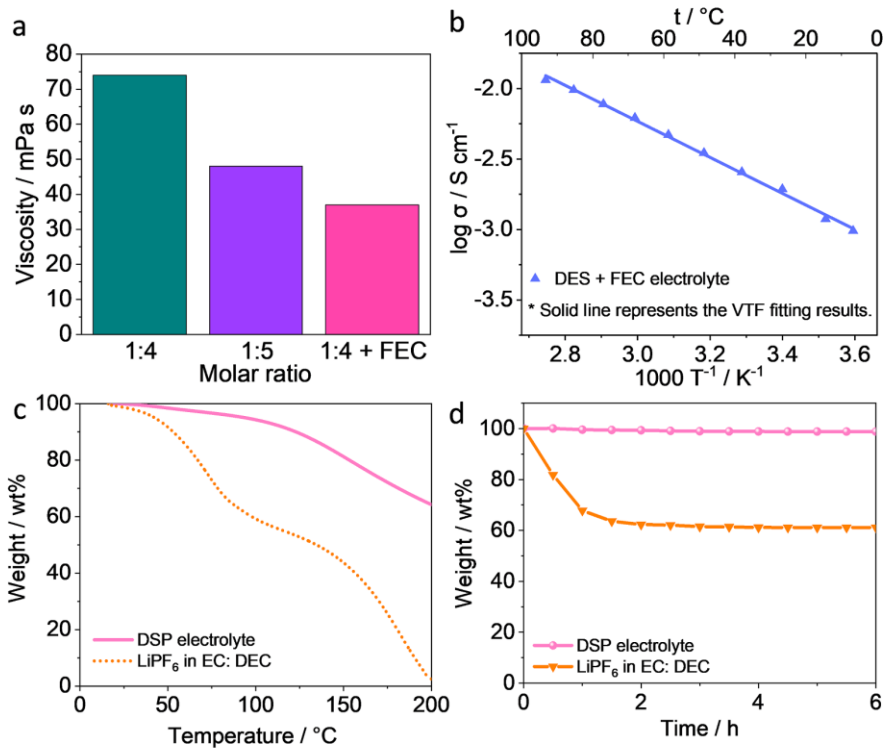

Figure 4.4. (**a**) Viscosity measurements of the DES electrolyte and DES + FEC electrolyte with different LiTFSI: NMAc molar ratios at 25 °C. (**b**) Ionic conductivity of the DES + FEC electrolyte as a function of temperature. The plot represents the experimental data while the solid line represents the VTF fitting value. (**c**) TGA thermograms of the DSP electrolyte and $LiPF_6$ in EC: DEC electrolyte; (**d**) The weight losses of the DSP electrolyte and $LiPF_6$ in EC: DEC (1:2 by volume) electrolyte during an aging of 6 h at room temperature (25 °C).

Table 4.1. The values of VTF fitting parameters in **Figure 4.3**g and **Figure 4.4**b

Sample	**σ at 25 °C** (**S cm^{-1}**)	**σ_o** (**S cm^{-1} K$^{-1/2}$**)	**E_a** (**eV**)	**T_o** (**K**)
DES electrolyte	8.91×10^{-4}	2.38 ± 0.027	2.92×10^{-1} ± 0.084	135.61 ± 0.084
DES + FEC electrolyte	2.24×10^{-3}	1.89 ± 0.024	4.03×10^{-2} ± 0.076	109.93 ± 0.076
DSP electrolyte	1.79×10^{-3}	1.74 ± 0.027	4.91×10^{-2} ± 0.084	121.02 ± 0.084

The electrochemical stabilities of electrolyte samples were tested by linear sweep voltammetry (LSV). As shown in **Figure 4.3**h, the DES electrolyte is stable up to 4.1 V vs. Li/Li^+. With the introduction of FEC and polymer matrix, the electrochemical stability of DES + FEC electrolyte and DSP electrolyte rise to 4.2 V (**Figure 4.5**a) and 4.5 V (**Figure 4.3**h) vs. Li/Li^+, respectively, mainly due to the high oxidative resistance of the FEC and polymer matrix.[191, 193] The lithium ion transference number (t_{Li}^+) is another core parameter for the electrolytes. As shown in **Figure 4.3**i, the t_{Li}^+ of the DSP electrolyte attains 0.79, which is much higher than the value for DES electrolyte (0.15, **Figure 4.5**a) and DES + FEC electrolyte (0.53, **Figure 4.5**b). Such high t_{Li}^+ of the DSP electrolyte is mainly owing to the fact that the polymer matrix can efficiently hamper the movement of the anions, thus benefiting low concentration polarization and enhanced rate performance for in Li metal batteries.[191]

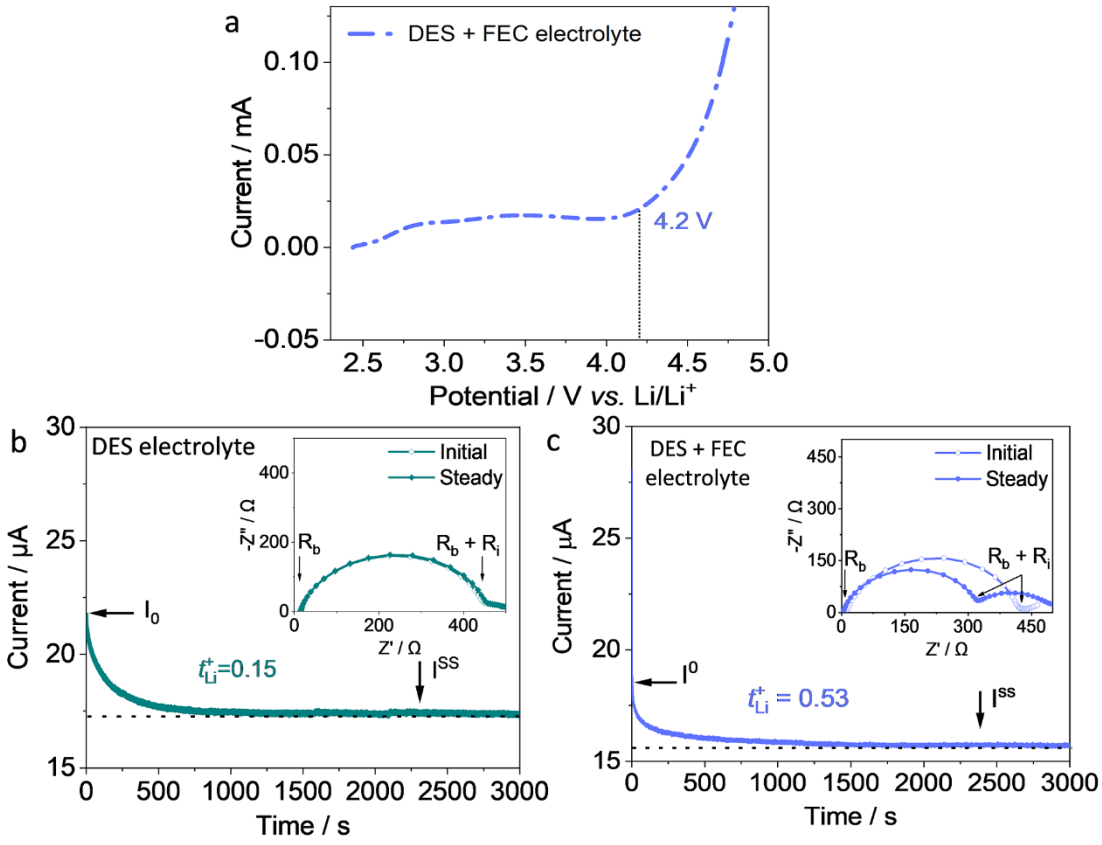

Figure 4.5. (**a**) LSV of the DES + FEC electrolyte at a scan rate of 10 mV s^{-1} using stainless steel as working electrode, and Li as counter and reference electrodes. The chronoamperometry profiles of (**b**) Li|DES electrolyte|Li and (**c**) Li|DES + FEC electrolyte|Li cells under a polarization voltage of 10 mV. The corresponding EISs before and after polarization are shown in the insets.

4.3.2 Lithium plating and stripping behaviour in the DSP electrolyte

The numerical simulation of the Li deposition process in DES was conducted using COMSOL Multiphysics® software, which was simulated on a Li substrate with nuclei size of 200 nm with an over-potential of -200 mV *vs.* Li/Li^+ for 0.5 s. For the DES + FEC electrolyte absorbed in a glass fibre membrane as separator (with pore size of 1 μm), an uneven current density distribution was observed. The current density is concentrated on the tops of Li nuclei. Thus, Li ions are preferentially deposited at these concentrated current "hot spots", accompanied with a severe concentration polarization in the electrolyte (**Figure 4.6**a). This concentrated Li ion flux favours dendritic growth.[172, 194] In contrast, when the electrolyte is changed to DSP electrolyte with a small mesh size (10 nm), the Li ion flux distributes much more homogeneously (**Figure 4.6**b), which contributes to dendrite-free Li deposition. This confirms that below a limiting current density, DSP electrolyte efficiently stabilizes the Li electrodeposition owing to its mesh size much smaller than the nucleation points.[195]

To investigate further the compatibility between DSP electrolyte and Li metal anode, the galvanostatic cycling of a symmetric Li||Li cell was assessed at 0.2 mA cm^{-2}. For the cell using DES electrolyte (the inset in **Figure 4.6**c), the voltage hysteresis increases sharply with the cycling time, owing to the continuously thickening SEI (as verified by the increase of the interfacial resistance, EIS, **Figure 4.7**). A severe voltage drop appears after 155 h, indicating a short-circuit caused by Li dendrite growth.[192] In contrast, the Li|DSP electrolyte|Li cell delivers a small and steady voltage hysteresis of ~25 mV vs. Li/Li+ over more than 600 h, which is much lower than the cell using DES + FEC electrolyte (~50 mV, **Figure 4.8**a). This confirms that the DSP electrolyte enables a uniform Li deposition on the anode (**Figure 4.7**).[174, 191] Although the DSP electrolyte effectively contribute to suppress the safety hazard, further investigation at higher current densities is necessary to fully appreciate the extend of dendrite inhibition.

Li||Cu half-cells were fabricated to evaluate the Coulombic efficiencies of Li plating-stripping in different electrolytes. The cell with DES electrolyte presents extremely low Coulombic efficiency (<30 %), and suffers from battery failure within 15 cycles (**Figure 4.6**d). This cell exhibits a huge voltage hysteresis of ~500 mV in the 10^{th} cycle (**Figure 4.6**e). With the addition of FEC, the Coulombic efficiency and cycling stability significantly increase (**Figures 4.8**b-c). As

for Li|DSP electrolyte|Cu cell, it is seen that the cell undergoes an activation process due to the formation of SEI.[196] Thereafter the Coulombic efficiency rapidly approaches over 98 % within only 10 cycles, and maintains 99.2 % after 100 cycles (**Figure 4.6**d). The corresponding voltage hysteresis is as low as ~46 mV upon cycling (the inset in **Figure 4.6**d-e), indicating a low battery polarization with a steady Li|DSP electrolyte interface.

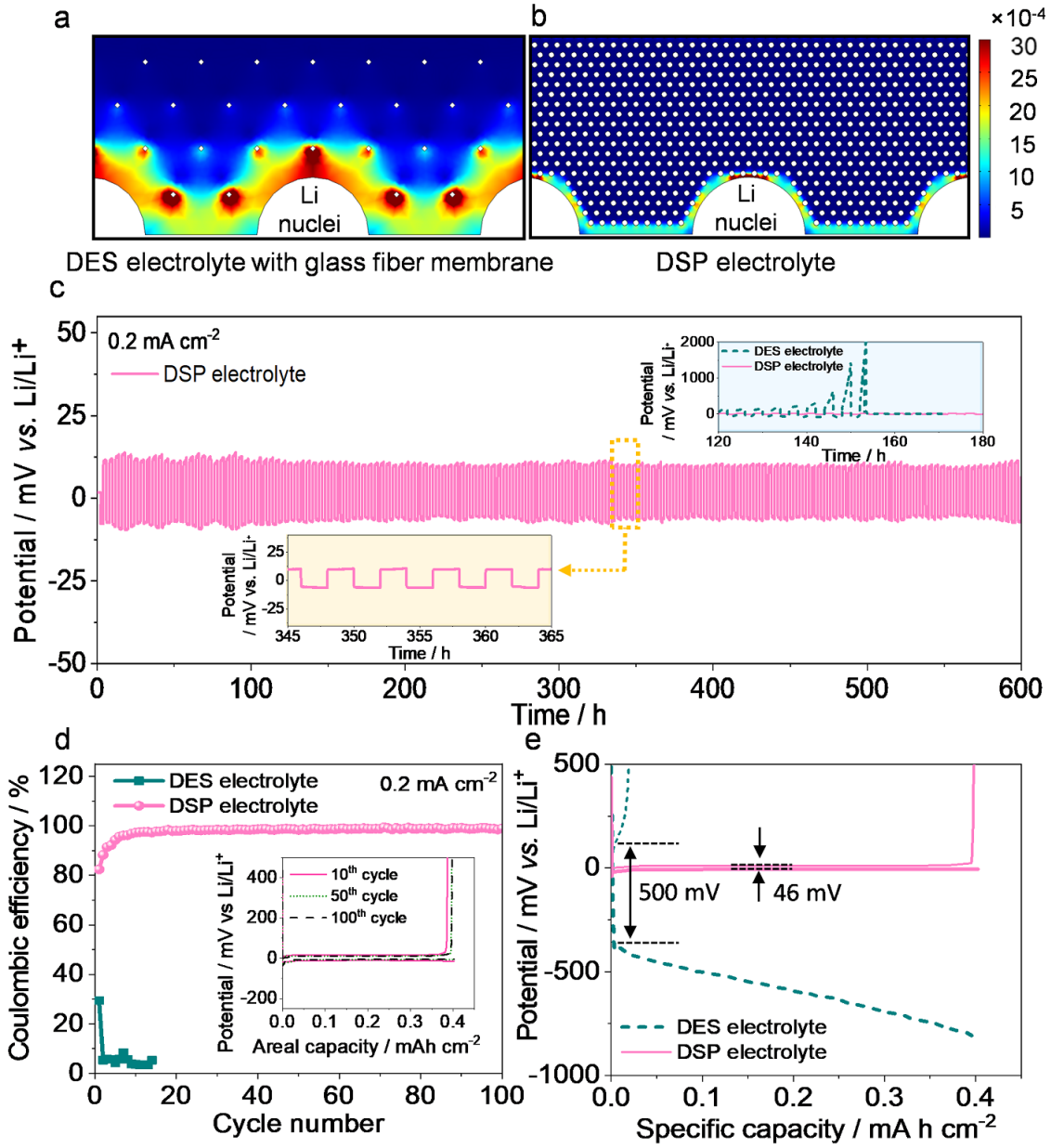

Figure 4.6. Li plating-stripping behaviour in DSP electrolyte. Numerical simulations of the Li ion flux distribution on the Li metal anode surfaces for (**a**) DES electrolyte with glass fibre membrane and (**b**) DSP electrolyte; (**c**) Voltage profiles of Li||Li symmetric cells using DES (cyan line in the upper inset) and DSP (pink lines) electrolytes at 0.2 mA cm^{-2} with a cut-off

capacity of 0.4 mAh cm^{-2}. The corresponding potential profiles of the Li|DSP electrolyte|Li cell during cycling are shown in the lower inset. (**d**) Coulombic efficiencies of Li plating-stripping in Li||Cu cells using the DES and DSP electrolytes at 0.2 mA cm^{-2} with a capacity limitation of 0.4 mAh cm^{-2}. The corresponding voltage profiles of the Li|DSP electrolyte|Cu cell in different cycles are shown in the inset. (**e**) The galvanostatic voltage profiles of Li|DES electrolyte|Cu (10^{th} cycle) and Li|DSP electrolyte|Cu (100^{th} cycle) cells at 0.2 mA cm^{-2}, respectively.

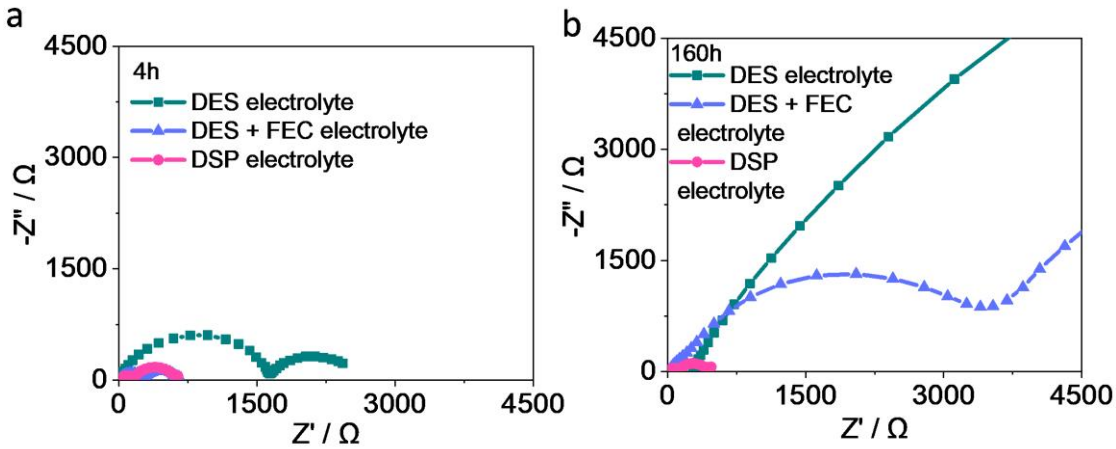

Figure 4.7. EIS spectra of a Li||Li symmetric cells using DES electrolyte, DES + FEC electrolyte or DSP electrolyte after cycling for (**a**) 4 h and (**b**) 160 h at 0.2 mA cm^{-2}, corresponding to **Figure 4.6**c.

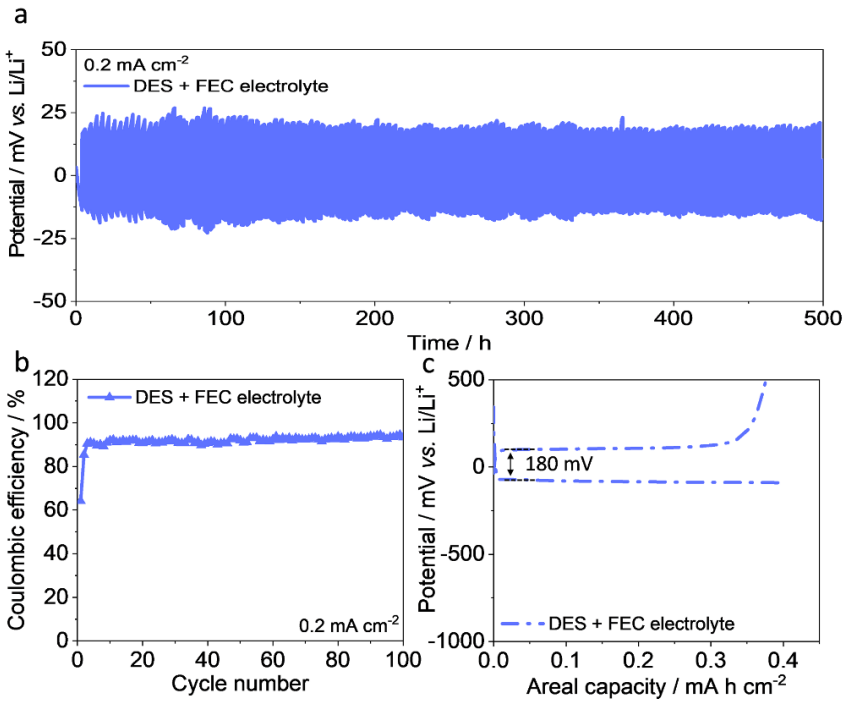

Figure 4.8. (**a**) Voltage profile of the Li||Li symmetric cells using DES + FEC electrolyte at 0.2 mA cm^{-2} with a cut-off capacity of 0.4 mAh cm^{-2}; (**b**) Coulombic efficiency of Li plating-stripping in Li||Cu cells using the DES + FEC electrolyte at 0.2 mA cm^{-2} with a capacity limitation of 0.4 mAh cm^{-2}; (**c**) The 10^{th} cycle galvanostatic voltage profiles of Li|DES + FEC electrolyte|Cu cell at 0.2 mA cm^{-2}.

Field emission scanning electron microscopy (FE-SEM) was conducted to observe the Li deposition morphologies in different electrolytes by plating 1.5 mAh cm^{-2} Li onto copper (Cu) substrates. As seen from **Figure 4.9**a, the Li plating in the Li|DES electrolyte|Cu cell presents a highly porous and loose morphology with massive dendrites and dead Li. Moreover, the thickness of the Li deposition layer is ~25 µm (the inset of **Figure 4.9**a), far exceeding the theoretical thickness value (*i.e.*, 7.3 µm). After addition of FEC, the surface of Li deposition becomes smoother while the thickness lessens (~16 µm, **Figure 4.9**b). In contrast, in the cell using DSP electrolyte, a dendrite-free plating structure with compactly aggregated bulks is observed (**Figure 4.9**c). The thickness of the Li layer deposited in DSP electrolyte is only ~11 µm (**Figure 4.9**c, inset), which is very close to the theoretically expected value. Such a dense Li deposition in DSP electrolyte can effectively mitigate the interfacial side reactions with electrolyte due to its low surface area, and thus results in the high Coulombic efficiency and good cycling stability (**Figure 4.6**d). Although the SEI can prevent the electrolyte

decomposition and favour suppression of dendrite at low current density, at high current density the SEI may not be as effective. We suggest that the batteries should be pre-cycled at low current densities to allow the SEI formation before increasing the cycling rate.

Depth profiling X-ray photoelectron spectroscopy (XPS) was employed to investigate the SEI composition on Li metal anodes from cycled Li||Li cells with different electrolytes. For Li metal cycled in DES electrolyte, three peaks appear at about 288.9, 286.6 and 284.8 eV in the C 1s spectrum, which are assigned to Li_2CO_3, LiCOOR ("R" represents alkyl groups) and other organic species (C-C, such as polyethylene oxide (PEO)) as the reaction products of the electrolyte with Li metal, respectively (**Figure 4.9**d).[32] Meanwhile, the Li 1s spectrum in **Figure 4.9**e exhibits four distinctive peaks at around 57.2, 55.3, 54.8 and 54.4 eV, corresponding to LiF, Li_2CO_3, LiCOOR and Li_2O, respectively.[194] These are consistent with the F 1s and O 1s spectra in **Figures 4.10-4.11**. It is seen that with increasing sputtering depth, the peak intensity of LiCOOR decreases rapidly while the intensities of Li_2CO_3 and LiF increase. This demonstrates that for the SEI layer formed in DES electrolyte, organic compounds such as LiCOOR concentrate in the outer layer of SEI (close to electrolyte), and inorganic molecules such as Li_2CO_3 and LiF mainly distribute in the inner layer of SEI (close to the Li metal; **Figure 4.9**h, left). Such a non-uniform SEI with a fragile multilayer structure is unstable during cycling, resulting in a fast Li and electrolyte depletion.[172] Furthermore, the peak intensity of LiCOOR drops with the introduction of FEC additive (**Figures 4.12**) and the self-healing polymer matrix (**Figures 4.9**e-f); while the intensity of LiF rises remarkably. LiF is known to possess ultra-high mechanical strength (*e.g.* a shear modulus of 54.2 GPa, the highest value among the common SEI components[197]), which provides the obtained F-rich SEI layer with high mechanical robustness against Li dendritic growth. Additionally, the LiCOOR and Li_2CO_3 peaks maintain almost constant intensities with increasing sputtering depth, demonstrating the monolithic feature of the SEI in the DSP electrolyte, and leading to homogenous Li stripping-plating (**Figure 4.9**h, right).[172] Beyond the effect of SEI, the DSP electrolyte polymer matrix also efficiently restricts the movement of Li ions towards the SEI surface defects via the interaction force with the polymer matrix.[177] This promotes a uniform Li ionic flux to facilitate dendrite-free Li deposition (**Figure 4.9**h, right). All these contribute to the highly reversible Li stripping-plating with long cycle life in the DSP electrolyte.

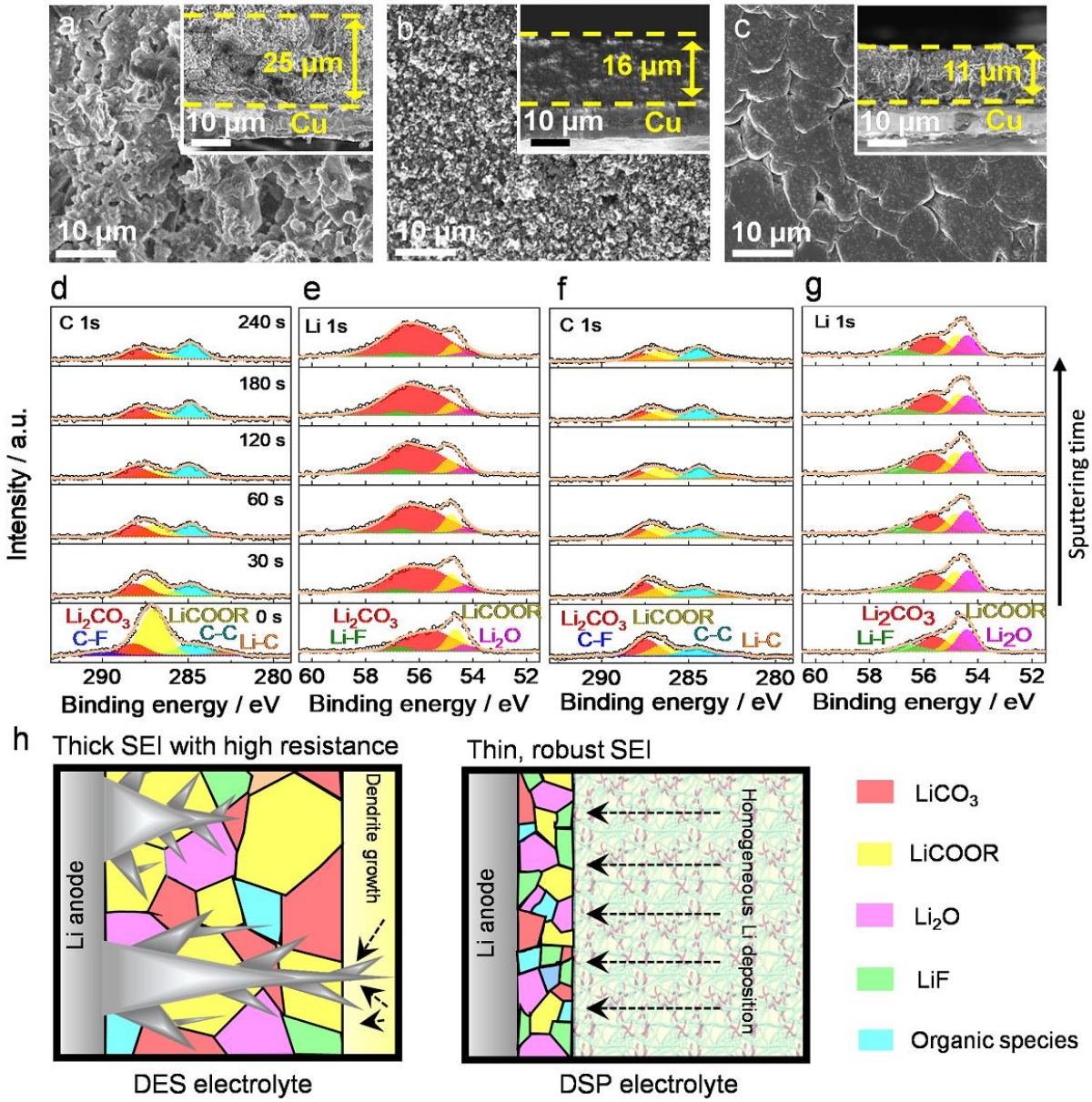

Figure 4.9. Characterization of Li deposition in DSP electrolyte. (**a, b, c**) Top and cross-sectional (shown in insets) FE-SEM images of Li deposition obtained by plating 1.5 mAh cm^{-2} Li on Cu substrate at 0.1 mA cm^{-2} in (**a**) Li|DES electrolyte|Cu, (**b**) Li|DES + FEC electrolyte|Cu and (**c**) Li|DSP electrolyte|Cu cells; (**d, f**) C 1s and (**e, g**) Li 1s depth profiling XPS spectra of Li metal anodes from Li||Li symmetric cells using (**d, e**) DES and (**f, g**) DSP electrolytes after 10 cycles; (**h**) Schematic illustrations of the SEI compositions on Li metal surfaces in DES electrolyte (left) and DSP electrolyte (right).

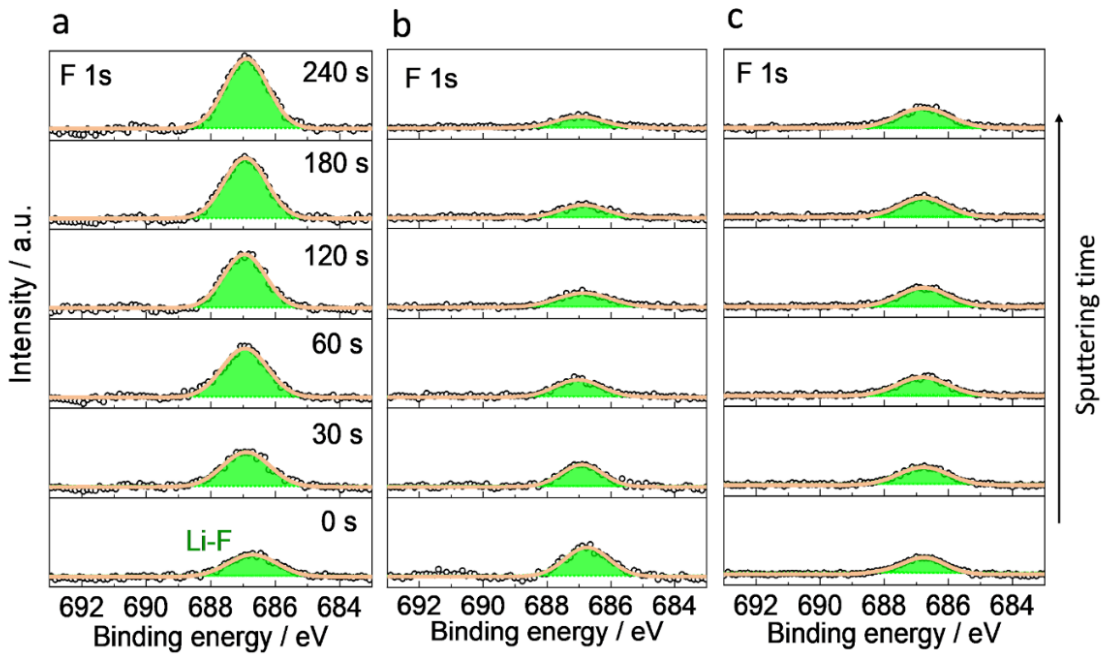

Figure 4.10. F 1s depth profiling XPS spectra of the Li metal anodes from Li||Li symmetric cells using (**a**) DES electrolyte, (**b**) DES + FEC electrolyte and (**c**) DSP electrolyte after 10 cycles. LiF: ~686.2 eV.[29]

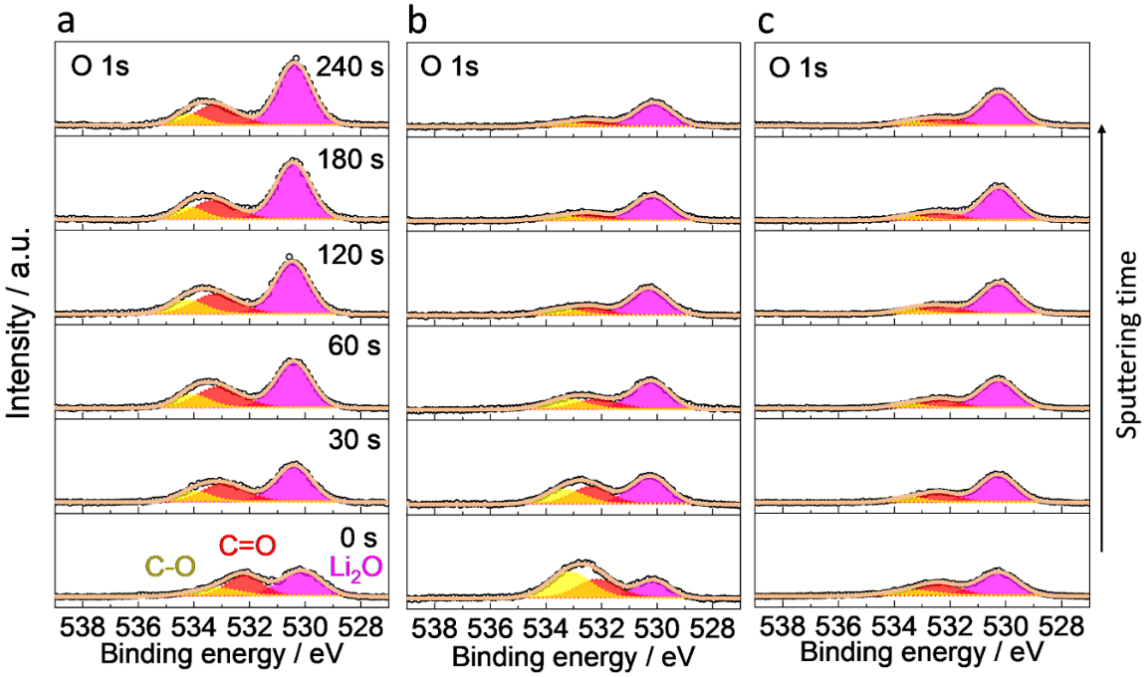

Figure 4.11. O 1s depth profiling XPS spectra of the Li metal anodes from Li||Li symmetric cells using (**a**) DES electrolyte, (**b**) DES + FEC electrolyte and (**c**) DSP electrolyte after 10 cycles. C-O: 533.1 eV; C=O: 532.1 eV; Li_2O: 530.2 eV.[29]

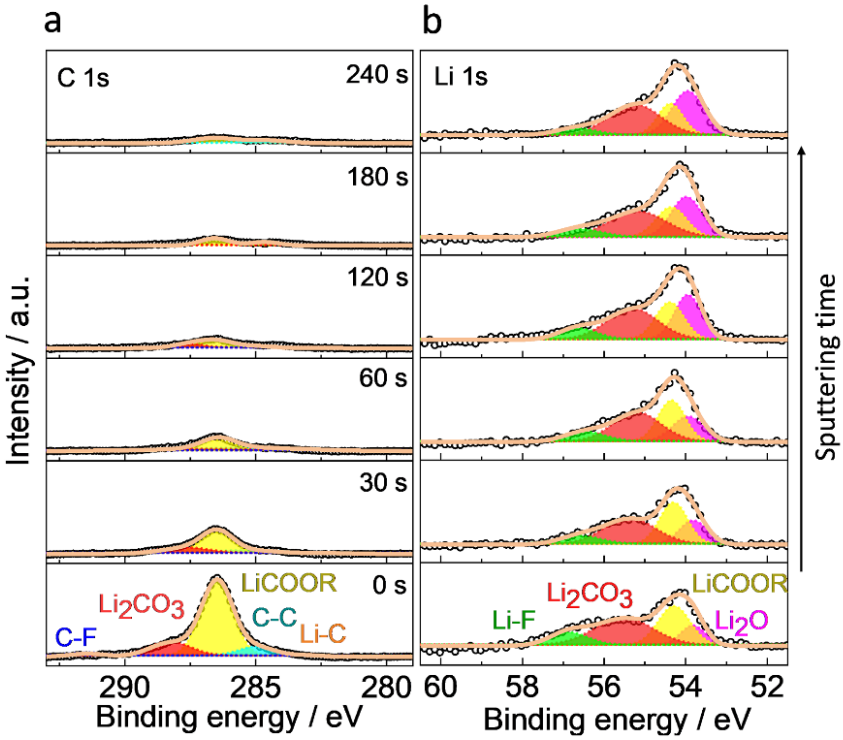

Figure 4.12. (**a**) C 1s and (**b**) Li 1s depth profiling XPS spectra of the Li metal anode from Li||Li symmetric cell using DES + FEC electrolyte after 10 cycles.

4.3.3 Electrochemical performances of DSP electrolyte in Li||LMO full batteries

Figures 4.13a-b show the rate performances of Li||LMO cells with different electrolytes at room temperature and corresponding discharge-charge curves. As shown in **Figure 4.13**a, the discharge-charge potential gaps of the Li|DSP electrolyte|LMO cell at various rates are obviously smaller than those in Li|DES electrolyte|LMO (**Figure 4.14**) and Li|DES + FEC electrolyte|LMO cells (**Figure 4.15**a), indicating an obvious reduced polarization. The Li|DSP electrolyte|LMO cell delivers high reversible specific capacities of 117.2, 116.7, 114.8, 110.9 and 104.3 mA h g^{-1} at 0.1, 0.2, 0.5, 1 and 2 C, respectively, which are much higher than the cells using DES electrolyte (**Figure 4.13**b, which cannot be cycled at current density higher than 0.5 C) and DES + FEC electrolyte (**Figure 4.15**b). The capacity retention of the Li|DSP electrolyte|LMO cell is calculated to be 98.6 % of the starting value when the current density was changed back to 0.1 C. This demonstrates that the battery system with DSP electrolyte is highly robust and reversible (**Figure 4.13**b) which is consistent with the CV results in **Figure 4.16**. The cycling performance of a Li|DSP electrolyte|LMO cell at 0.1 C is shown in **Figure**

4.13c. It exhibits a reversible capacity of 99.5 mA h g^{-1} after 200 cycles with a capacity retention of 86.1 %. In sharp contrast, the Li|DES electrolyte|LMO cell suffers from rapid capacity fading and presents a battery failure after 80 cycles. The reversible capacity for the Li|DES + FEC electrolyte|LMO cell is only 88.6 mA h g^{-1} after 200 cycles (**Figure 4.15**c).

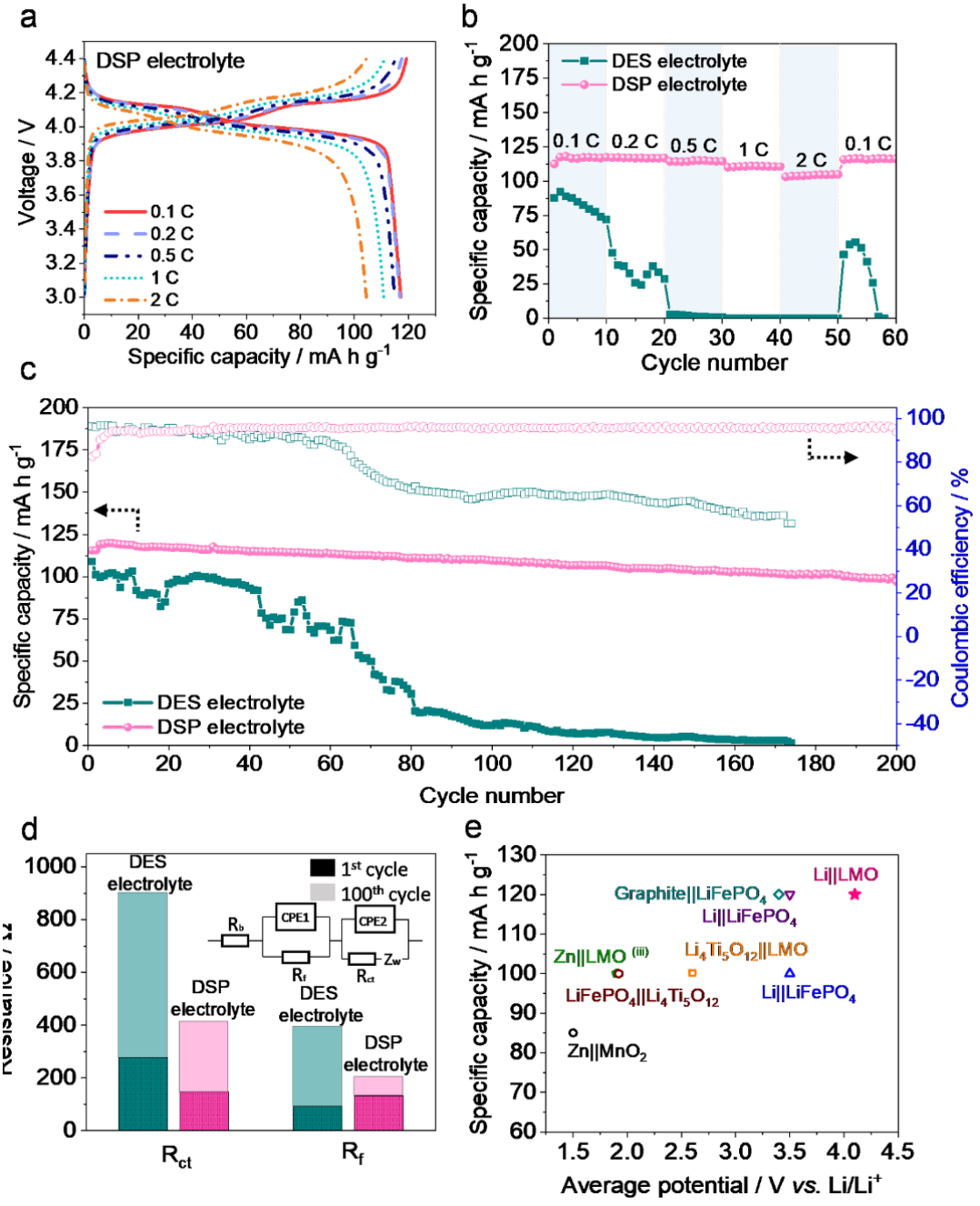

Figure 4.13. Electrochemical performances of a quasi-solid-state Li|DSP electrolyte|LMO cell at room temperature. (**a**) Typical charge-discharge profiles of Li|DSP electrolyte|LMO cell; (**b**) Rate performances and (**c**) cycling performances at 0.1 C of Li|DES electrolyte|LMO and Li|DSP electrolyte|LMO cells; (**d**) The evolution of interfacial resistances of Li||LMO cells with

different electrolytes after 1 and 100 cycles; (**e**) Comparison of average discharge potentials and specific capacities (based on the mass of cathode material only) for representative reported rechargeable batteries employing DES-based electrolytes (hollow symbols)[4, 7-8, 30-31] and this work (solid star).

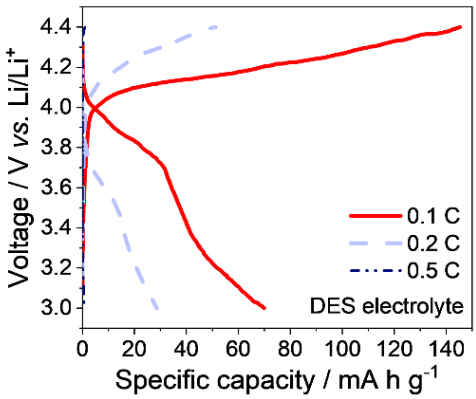

Figure 4.14. Typical charge-discharge profiles of the Li|DES electrolyte|LMO cell at different rates.

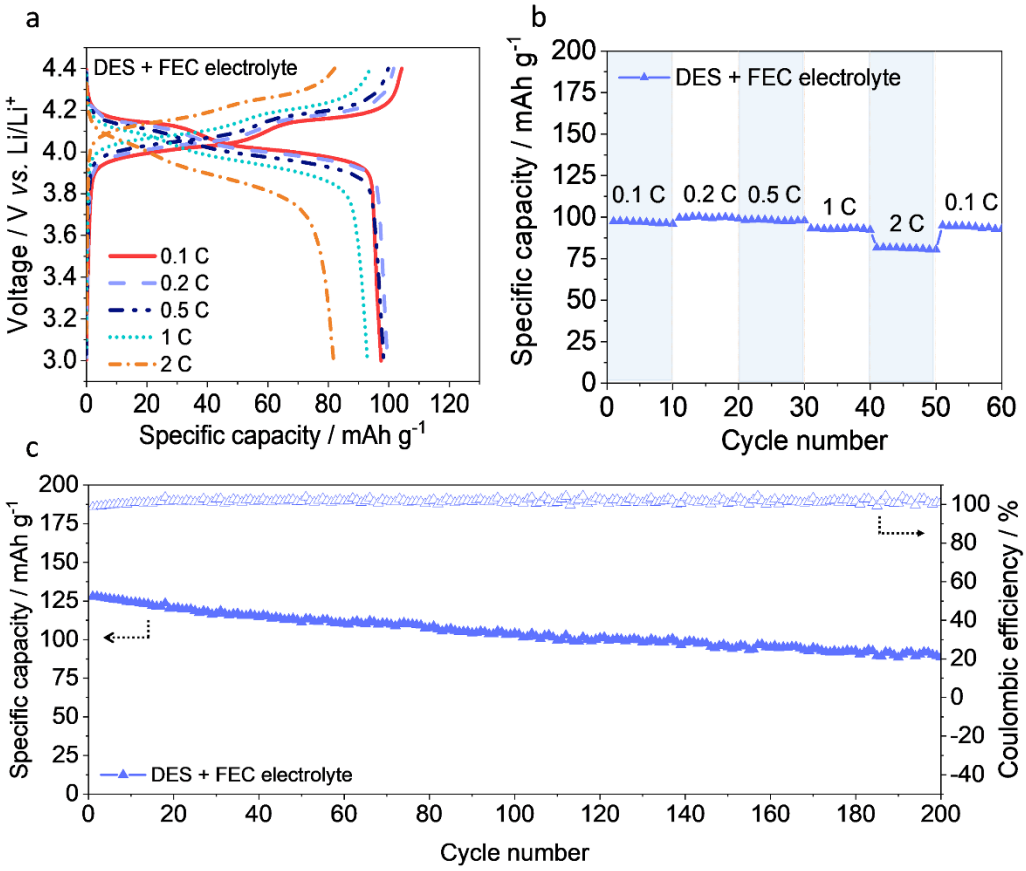

Figure 4.15. Electrochemical performances of the Li|DES + FEC electrolyte|LMO cell at room temperature. (**a**) Typical charge-discharge profiles of the Li|DES + FEC electrolyte|Li cell; (**b**)

Rate performances and (**c**) cycling performances at 0.1 C of the Li|DES + FEC electrolyte|LMO cell.

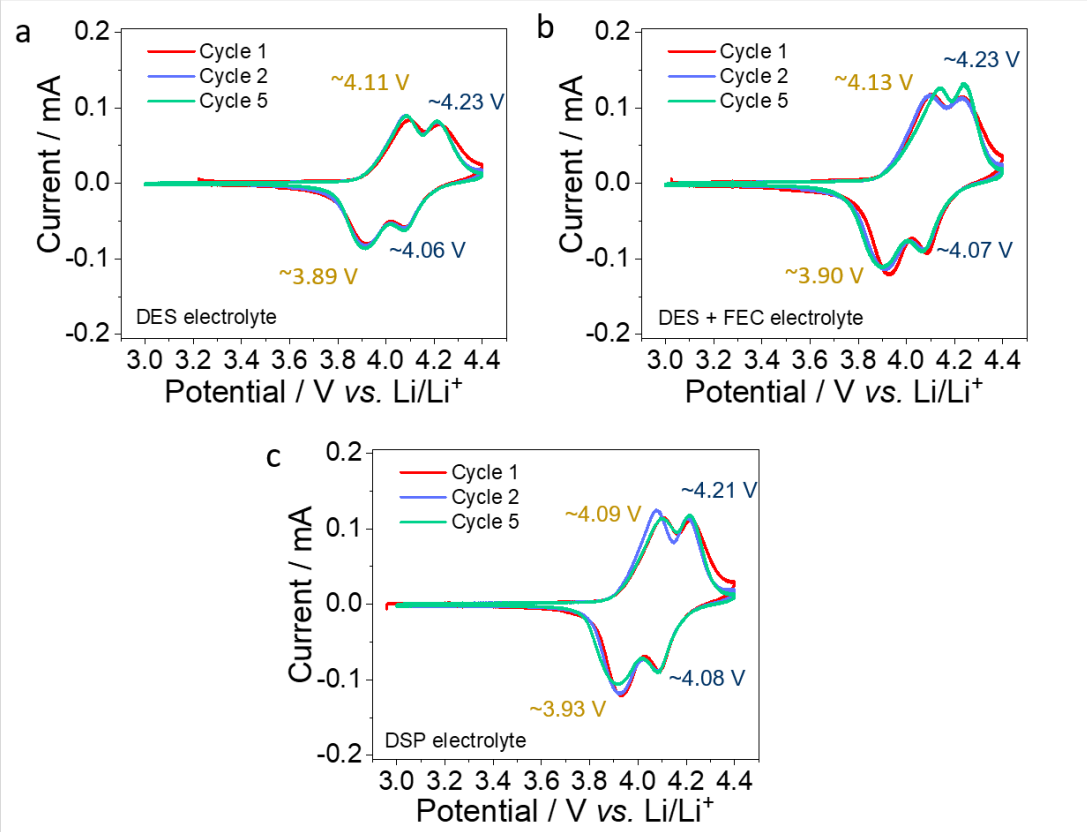

Figure 4.16. CVs of Li||LMO cells with (**a**) DES electrolyte, (**b**) DES + FEC electrolyte and (**c**) DSP electrolytes at a scan rate of 0.1 mV s^{-1}.

Figure 4.17 shows EIS results for the Li||LMO cells after different cycles at 0.1 C. The EIS spectra can be well-simulated via an equivalent circuit (**Figure 4.13**d) and the simulation results are summarized in **Table 4.2**. For the cell with DES electrolyte, the solid electrolyte interface resistance (R_f) sharply rises from 91.9 to 303.2 Ω and the charge transfer resistance (R_{ct}) remarkably increases from 277.5 to 624.5 Ω after 100 cycles, which can be interpreted as an unstable SEI film associated with dendrite growth on the Li metal anode as well as manganese dissolution from the LMO cathode. For comparison, after applying the FEC additive and gelating the electrolyte, the values of R_{ct} and R_f became much smaller, and remained steady with limited variation during 100 cycles (**Figure 4.13**d). This implies a stable Li metal|DSP electrolyte interface and an effective inhibition of manganese dissolution in the DSP electrolyte, which contribute to the significantly enhanced cycling performance (**Figure 4.13**c). The electrochemical performances (specific capacity and average output potential) of

the Li|DSP electrolyte|LMO cell in this work are better than that of previously reported on rechargeable batteries employing DES-based electrolytes. Therefore, the as-synthesised DSP electrolyte can be used for the development of safe and durable Li metal batteries with high energy density.

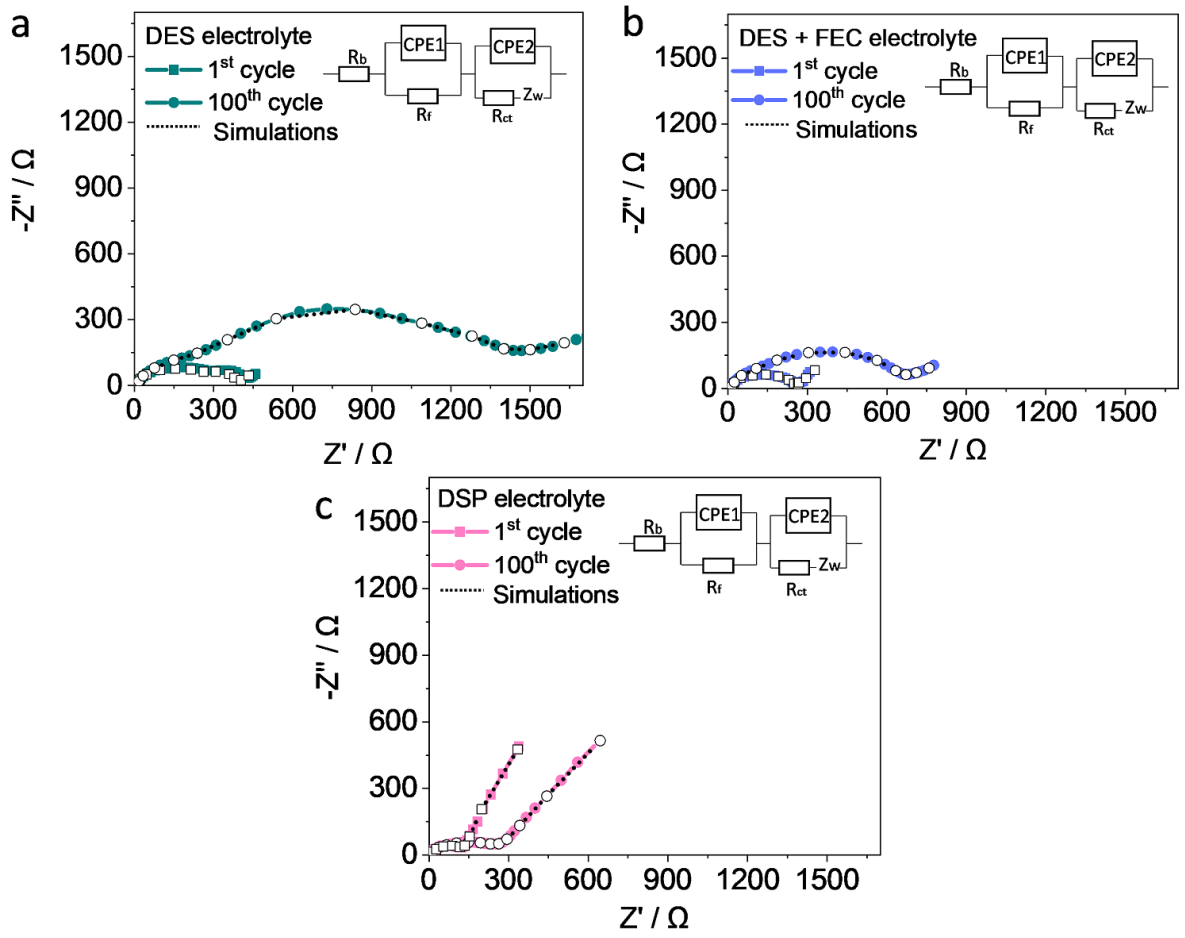

Figure 4.17. EISs of the Li||LMO cells using (**a**) DES electrolyte, (**b**) DES + FEC electrolyte and (**c**) DSP electrolyte after 1 and 100 cycles at 0.1 C.

Table 4.2. The EIS simulation results of the Li||LMO cells in the three electrolyte samples. The results are obtained from the three electrolyte samples after selected cycles corresponding to **Figure 4.17**.

Battery sample	**After 1 cycle**			**After 100 cycles**		
	R_b / Ω	**R_{ct} / Ω**	**R_f / Ω**	**R_b / Ω**	**R_{ct} / Ω**	**R_f / Ω**
Li|DES |LMO	6.5 ±0.012	277.5 ±0.015	91.93 ±0..009	6.9 ±0.010	624.5 ±0.017	303.2 ±0.012

Li|DES + FEC |LMO	10.1 ±0.015	163.8 ±0.011	68 ±0.012	9.4 ±0.014	394 ±0.011	192 ±0.013
Li|DSPE|LMO	1.8 ±0.011	146.1 ±0.016	133 ±0.012	5.2 ±0.012	268 ±0.014	71.2 ±0.011

Figure 4.18a and **Figure 4.19**a show the cycling performances of Li||LMO cells with different electrolytes at 60 °C. It is well-known that LMO cathodes suffer from disproportionation of trivalent manganese (Mn^{3+}) species during cycling:

$$2\,Mn^{3+} \rightarrow Mn^{2+} + Mn^{4+} \qquad (\mathbf{4.4})$$

The resulted Mn^{2+} ions are highly soluble in the electrolyte, which leads to rapid capacity fading. This dissolution issue becomes more severe at elevated temperature.[198] As a result, the Li||LMO cell with DES electrolyte exhibits an extremely short cycle life of only 11 cycles (**Figure 4.18**a). Meanwhile, the Li|DES + FEC electrolyte|LMO cell presents a capacity fading from 90 to 33 mAh g^{-1} during 50 cycles (**Figure 4.19**a). In contrast, the cell using DSP electrolyte successfully maintains a specific capacity of 81 mAh g^{-1} after 50 cycles at 0.1 C (**Figure 4.18**a). The concentrations of Mn in the electrolytes after 10 cycles at 60 °C were determined by inductively coupled plasma mass spectroscopy (ICP-MS). It is seen that the concentration of Mn dissolved in DSP electrolyte (0.20 ppm per mg of LMO, inset in **Figure 4.18**a) is significantly lower than that in the DES + FEC electrolyte (0.25 ppm, inset in **Figure 4.19**a) and DES electrolyte (2.31 ppm, inset in **Figure 4.18**a). Moreover, as further seen from the XPS spectrum of the cycled LMO electrode DES electrolyte, three peaks at around 641.1 eV, 642.2 eV and 643.9 eV appear in the Mn $2p_{3/2}$ spectrum, which can be assigned to Mn^{2+}, Mn^{3+} and Mn^{4+}, respectively (**Figure 4.18**b).[199] Intriguingly, the peak intensity of Mn^{2+} dramatically decreases with the introduction of FEC additive (**Figure 4.19**b) and UPyMA-PETEA polymer matrix (**Figure 4.18**c), which is well consistent with the ICP-MS results. Furthermore, the transmission electron microscopy (TEM) image of LMO cathode cycled in DES electrolyte at 60 °C shows that the electrode surface is covered by a thick CEI layer of ~12 nm (**Figure 4.18**d). The main components of this CEI layer are electrolyte decomposition products (*i.e.* organic species and LiF, **Figure 4.20**) due to the low electrochemical stability of the DES electrolyte. The electrode cycled in the DES + FEC electrolyte shows a reduced CEI

thickness of ~7 nm (**Figure 4.18**e). For the LMO electrode from the cell using DSP electrolyte, the CEI thickness further decreases to ~3 nm (**Figure 4.18**f). Meanwhile, the LiF content in the CEI obviously increases, which is associated with a decline in the content of organic species (**Figure 4.20**), resulting in an enhanced CEI robustness.[197] Such a thin and strong CEI layer together with the crosslinking polymer matrix of DSP electrolyte efficiently hinder manganese dissolution,[198] thus leading to improved cycling performance at elevated temperature as shown in **Figure 4.18**a.

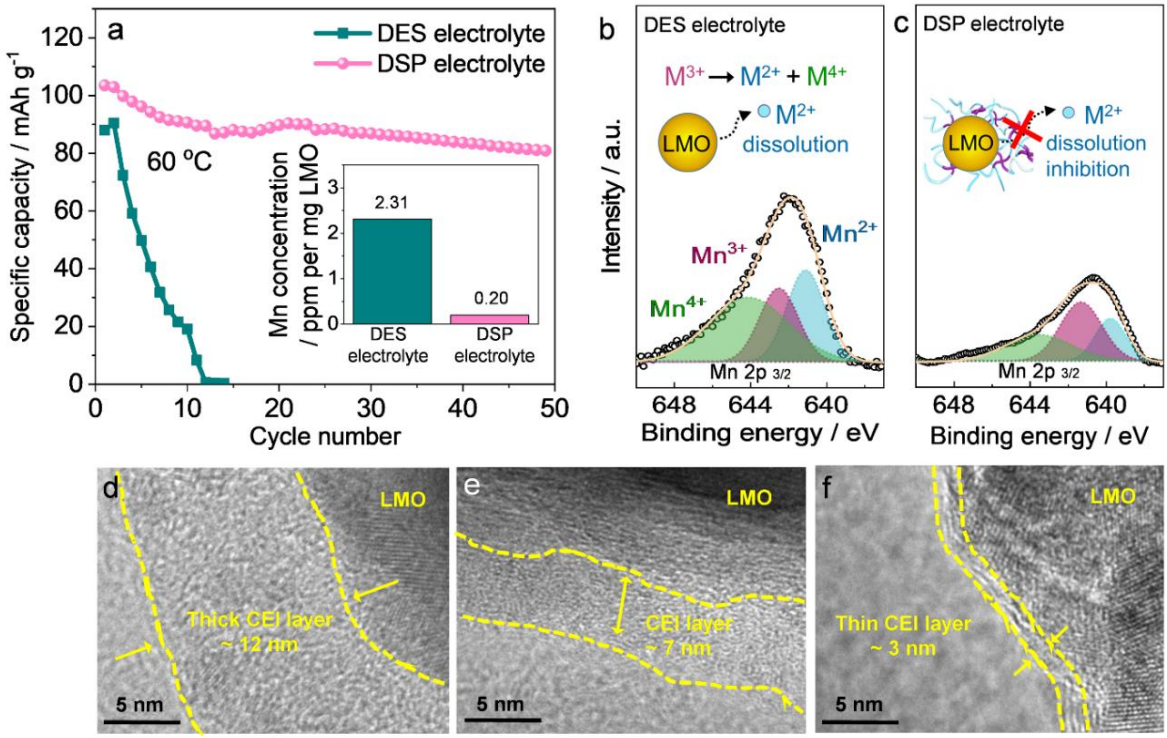

Figure 4.18. Characterization of Mn dissolution in a Li|DSP electrolyte|LMO cell at elevated temperature. (**a**) Cycling performances of Li|DES electrolyte|LMO and Li|DSP electrolyte|LMO cells at 0.1 C at 60 °C. The corresponding Mn amounts on the separators after 10 cycles are shown in inset. Mn $2p_{3/2}$ XPS spectra of LMO cathodes from cells with (**b**) DES and (**c**) DSP electrolytes after 10 cycles at 60 °C; TEM images of the LMO cathode surfaces from (**d**) Li|DES electrolyte|LMO, (**e**) Li|DES + FEC electrolyte|LMO and (**f**) Li|DSP electrolyte|LMO cells after 10 cycles at 60 °C.

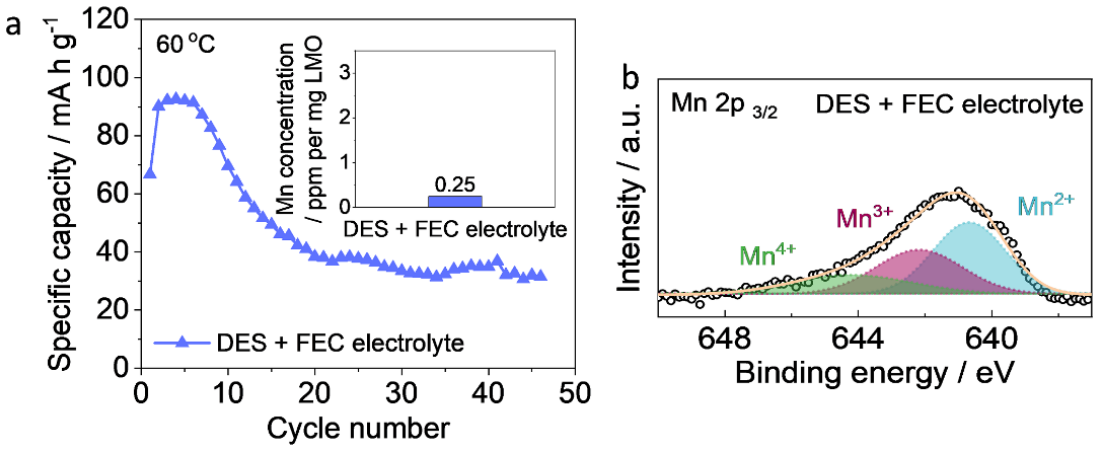

Figure 4.19. (**a**) Cycling performances of Li|DES + FEC electrolyte|LMO cell at 0.1 C at 60 °C, the corresponding Mn amounts on the separator after 10 cycles is shown in the inset. (**b**) Mn $2p_{3/2}$ XPS spectra of LMO cathode from the cell with DES + FEC electrolyte after 10 cycles at 60 °C.

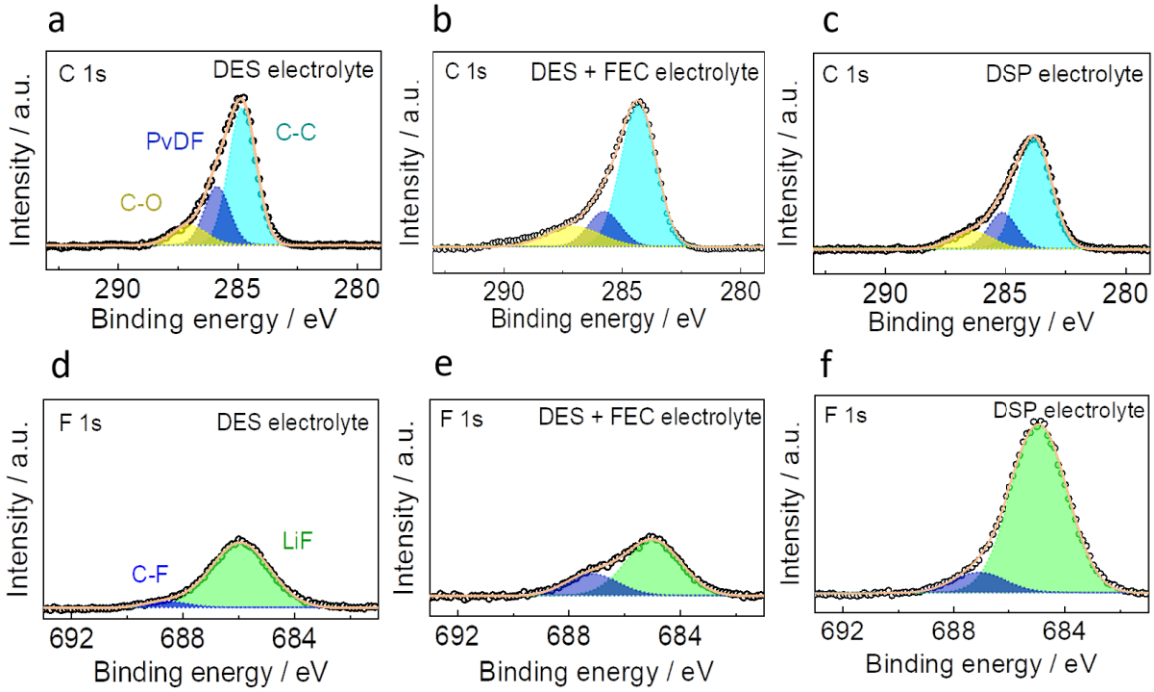

Figure 4.20. (**a-c**) C 1s and (**d-f**) F 1s XPS spectra of the LMO cathode from the cells using (**a, d**) DES electrolyte, (**b, e**) DES + FEC electrolyte and (**c, e**) DSP electrolyte after 10 cycles at 60 °C. C-O: 286.6 eV; PVDF: 286.1 eV; C-C: 284.8 eV[32]; C-F: 688.9 eV[33]; LiF: ~686.2 eV.[29]

4.4 Conclusion

In summary, we successfully developed a new type of DES-based self-healing polymer electrolyte that can dramatically enhance the safety and cyclability of Li metal||LMO batteries. This polymer electrolyte was synthesised by integrating an UPyMA-PETEA copolymer matrix with non-flammable DES + FEC electrolyte via a facile *in-situ* thermally-initiated polymerization. The FEC additive enables high ionic conductivity, enhanced oxidative stability, and effective formation of protective SEI on the Li anode and thin CEI on the LMO cathode against structural deterioration. Furthermore, the self-healing UPyMA-PETEA polymeric network keeps the DSP electrolyte in a safe quasi-solid state without electrolyte leakage and endows integrated electrode|electrolyte contacts. It also facilitates homogeneous Li plating onto the anode and suppresses manganese dissolution from the cathode. The as-developed DSP electrolyte simultaneously possesses non-flammability, high ionic conductivity (1.79×10^{-3} S cm^{-1} at 25 °C), superior electrochemical stability, and stable interfacial characteristics. These exceptional features ensure superior battery cycling performances at both room and elevated temperatures when applying the DSP electrolyte in Li||LMO batteries. These key findings provide a deep insight to inspire progresses in the development of highly safe and durable Li metal batteries. The electrolyte design strategy can also be extended to other high-energy density rechargeable metal batteries such as sodium batteries, magnesium batteries and zinc batteries.

CHAPTER V: "Localized Water-In-Salt" Electrolyte for Aqueous Lithium-Ion Batteries

5.1 Introduction on aqueous electrolytes

Rechargeable lithium (Li)-ion batteries have dominated the energy storage market from portable electronics to electric vehicles in the past two decades due to their high energy density and long cycle life.[18] However, the prevailing application of non-aqueous electrolytes based on flammable and toxic organic solvents (*e.g.* carbonates and ethers) in Li-ion batteries has triggered severe safety hazards, including fire, explosion and harmful leakage.[48] Replacing these non-aqueous electrolytes with aqueous electrolytes not only can efficiently eliminate the safety issues of Li-ion batteries, but also reduce the battery manufacturing costs due to the non-reliance on ultra-dry assembly facilities.[139] Nonetheless, the electrochemical stability window (<2 V) of traditional dilute aqueous electrolytes is too narrow to support high-energy electrochemical couples, which is a major bottleneck for the development of aqueous Li-ion batteries.[15, 200]

In 2015, "water-in-salt" (WIS) electrolytes were developed to unprecedentedly expand the electrochemical window of aqueous electrolytes, in which the dissolved Li salts far outnumber water molecules by both volume and mass.[130] A protective SEI was constructed on the anode surface in a 21 m LiTFSI aqueous electrolyte which exhibited a 3.0 V-wide stability window. Other organic Li salts, *e.g.* lithium bis(pentafluoroethanesulfonyl)imide[135], lithium trifluoromethane sulfonate[134] and lithium (trifluoromethanesulfonyl)(pentafluoroethanesulfonyl)imide[201], have been introduced to the WIS electrolytes to further improve the saturation limitation of salts and thus further widen the electrochemical window. In addition, a co-solvent (*e.g.* ether[136] and carbonate[14]) was also introduced into WIS electrolyte to promote the SEI formation. However, the super-high concentration of these toxic Li salts in WIS electrolytes raises new concerns of high cost, high viscosity, poor wettability toward electrodes, and environmental hazards.[202]

To overcome above intrinsic challenges of WIS electrolytes, herein, we (1) used inexpensive and eco-friendly inorganic Li salts to replace the toxic and costly organic Li salts, and (2) lowered the electrolyte salt concentration by diluting the WIS electrolytes with an inert

solvent (called a “diluent”) that dissolves the water but not the inorganic salt. Therefore, the diluent does not alter the salt solvation structure of WIS electrolytes forming a “localized water-in-salt (LWIS)” electrolytes. Since the organic diluent has a much wider electrochemical stability window than water-in-salt electrolyte, the LWIS are expected to preserve (or even enhance) the electrochemical stability of WIS electrolytes while reducing the salt concentration, decreasing the viscosity and improving the wettability. The salt/diluent configuration for LWIS electrolytes have not been reported to our best knowledge. To demonstrate the concept of LWIS, we used lithium nitrate ($LiNO_3$) as Li salt and 1,5-pentanediol (PD) as diluent. The application of PD not only significantly lowers the total Li salt concentration of WIS electrolyte, but also reduces the water reactivity in HER/OER via hydrogen-bonding interactions between PD with water molecules and NO_3^- anions, thus enabling an electrochemical stability window of ≈2.8 V (partly attributed to the formation of SEI on the anode surface). Furthermore, by *in-situ* polymerizing of tetraethylene glycol diacrylate (TEGDA) monomer in the LWIS electrolyte, the as-prepared aqueous gel electrolyte exhibited an enhanced electrolyte stability of ≈3.0 V without flammability or liquid leakage hazard. The as-developed Mo_6S_8|LWIS gel electrolyte|LMO battery showed a high cycling stability with 98.53 % Coulombic efficiency at 1C. The design principles for LWIS electrolytes reported in this work will boost the future development of high-energy and low-cost aqueous Li-ion batteries.

5.2 Experimental section

5.2.1 Synthesis of the LWIS gel electrolyte

All lithium salts (lithium bis(trifluoromethane sulfonyl) imide (LiTFSI, 99.95% trace metals basis, Sigma Aldrich) and lithium nitrate ($LiNO_3$, Sigma Aldrich), *etc.*), and solvents (diethyl carbonate (DEC, 99% Sigma Aldrich), fluoroethylene carbonate (FEC, 99% Sigma Aldrich), propylene carbonate (PC, 98% Sigma Aldrich), ethylene carbonate (EC, anhydrous 99% Sigma Aldrich), tetraethylene glycol dimethyl ether (TEGDME, 99% Sigma Aldrich), 1,5-pentanediol (PD, 96%, Sigma Aldrich)) were used as received without further purification. To prepare the LWIS gel electrolyte, a precursor solution consisting of 6 wt% tetra(ethylene glycol) diacrylate (TEGDA, technical grade, Sigma Aldrich) monomer and 0.5 wt% 2-hydroxy-2-methylpropiophenone (HMPP, 97 % Sigma Aldrich) photo-initiator dissolved in 12.5 m (*i.e.*

mol $kg^{-1}_{solvent}$) $LiNO_3$ in H_2O: PD (1: 1 by mass) electrolyte was exposed to ultraviolet (UV)-irradiation from a Hg UV lamp (with an irradiation peak intensity of ≈2000 mW cm^{-2}) for 15 min. The as-prepared gel electrolytes were directly applied in aqueous batteries without further treatments. We used water uptake (η) to quantitatively compare the porosity of electrodes with/without gel filling:[174]

$$\eta = \frac{W_t - W_0}{W_o} \times 100\ \% \quad \textbf{(5.1)}$$

Where W_o is the weight of the electrode and W_t is the weight after absorbing water. The water uptakes of pristine Mo_6S_8 and $LiMn_2O_4$ electrodes were 16.1 % and 11.6 %, respectively. In contrast, water uptakes of the Mo_6S_8 and $LiMn_2O_4$ electrodes form a disassembled cell after 1 cycle sharply reduced to 1.03 % and 0.80 %, demonstrating the pores of electrodes were well-filled by the gel electrolyte.

5.2.2 Electrolyte characterizations

The pH of the electrolytes was measured with a FiveEasy Plus pH Meter FE28 (METTLER TOLEDO) at room temperature. The viscosity of the electrolytes was measured with a Discovery HR-1 hybrid rheometer (geometry 60 mm, 2.008 ° cone plate, Peltier plate steel) at 25 °C. The solubilities were measured by gradually dissolving salts in water at 40 °C, and then recording the maximum concentration when the solution started to crystallize after cooling down to 25 °C. The electrochemical stability window of the electrolytes was studied via cyclic voltammetry (CV) method, which was run using the VMP3 (Bio Logic Science Instruments) multichannel electrochemical station. The experiment was carried in a three electrodes system with titanium (Ti) mesh as working electrode, platinum (Pt) wire as counter electrode and Ag/AgCl (Sigma Aldrich, Ag/AgCl (3M KCl) Reference Electrode) as reference electrode. The voltage range was -1.5 to 2.4 V *vs.* Ag/AgCl, and the scan rate was 0.1 mV s^{-1}. The electrochemical stability window was recorded from where the HER current density was lower than -0.5 mA cm^{-2} and OER was higher than 0.5 mA cm^{-2}. The Fourier transform infrared (FT-IR) spectra of the TEGDA monomer and polymer matrix of the LWIS electrolyte were obtained via a Nicolet Magna 6700 spectrometer at room temperature. To separate and purify the polymer matrix from the LWIS gel electrolyte, the gel electrolyte was mashed into pieces and washed with deionized water, followed by a vacuum drying at 120 ^oC overnight. The as-

obtained precipitates were dialyzed against deionized water for 3 days to further remove the residual ions and micromolecules. The precipitates were then vacuum-dried at 120 ^{o}C again to obtain the separated TEGDA-based polymer matrix. The Raman spectra were measured with a Renishaw Raman spectrometer system (Gloucestershire, UK). The ionic conductivity of the electrolytes was measured from 10 °C to 80 °C via electrochemical impedance spectroscopy (EIS) with on the VMP3 electrochemical station from 100 kHz to 1 Hz with an alternating current amplitude of 5 mV. The test cells were assembled by soaking two stainless steel blocking electrodes in electrolyte samples. To ensure thermal equilibrium, the cells were kept at each testing temperature for at least 30 min before each EIS measurement. For the combustion test, 1 g of electrolyte sample was poured into a dish, and then the optical photographs and videos were recorded after the samples were ignited. The weight losses of different electrolyte samples were measured by aging at 25 °C in the open air.

The Li ion transference number was determined by the Wagner's DC polarization method to determinate the ionic transference number:[203]

$$t_{ionic} = \frac{I_i - I_f}{I_i} \quad (\mathbf{5.2})$$

Where I_i is the initial current and I_f is the current of the steady-state when applying a potential of 1 V.

5.2.3 Assembly and Characterization of the aqueous full cells

Chevrel phase Mo_6S_8 was synthesized based on the previous report.[204] Lithium manganese oxide (LMO) was purchase from Shanshan Co., Ltd. Both electrodes were prepared by mixing the active material with carbon black and polytetrafluoroethylene (PTFE, Sigma Aldrich) in water with a mass ratio of 80: 10: 10. The slurry was coated onto a Ti mesh as current collector and dried overnight at 70 °C. The CVs of the Mo_6S_8 and LMO electrodes were recorded with Pt wire as counter electrode and Ag/AgCl as reference electrode at 0.1 mV s^{-1}. The Mo_6S_8 exhibited a specific capacity of 87.2 mAh g^{-1}, which was 71.5 % of the theoretical capacity; and the $LiMn_2O_4$ demonstrated a specific capacity of 106.1 mAh g^{-1}, which was 71.6 % of the theoretical capacity. To assemble the Mo_6S_8||LMO aqueous full cells, the mass loading of the anode was ≈2 mg cm^{-2} and the mass ratio of LMO: Mo_6S_8 in the electrodes was set as 1.5. The precursor solution of the LWIS gel electrolyte (*i.e.* 6 wt% TEGDA and 0.5 HMPP dissolved in

12.5 m $LiNO_3$ in H_2O: PD) was injected into the glass fibre membrane (Whatman GF/A) as separator and then exposed to UV light for 30 min to ensure a total polymerization. The electrolyte: Mo_6S_8 ratio in each cell was set at ≈60 μL mg^{-1} uniformly. To estimate the electrochemical performances, the cells were cycled at various rates (1 C = 122 mAh g^{-1} based on the mass of Mo_6S_8) between 0.5 to 2.3 V on a LAND 2001 A battery testing system at room temperature. The anodes were collected from the Mo_6S_8||LMO cells after 20 cycles at 1 C, washed with dimethoxyethane (DME) and subjected to transmission electron microscopy (TEM, Tecnai G2 F30) and X-ray photoelectron spectroscopy depth profiling (XPS, PHI 5000 VersaProbe II spectrometer with a monochromatic Al Kα X-ray source at 1486.6 eV) characterizations.

5.2.4 Numerical simulation

Molecular dynamics (MD) simulations were performed to investigate the structures of aqueous solutions/gel electrolyte. The MD simulations were run using LAMMPS[166]. The systems were setup initially by using PACKMOL[165] and Moltemplate (http://www.moltemplate.org/). Periodic boxes were used here. The properties of H_2O are assessed with SPC/E parameters. The force-fields parameters of Li^+ and NO_3^- were taken from previous report[205] with partial charges. The force-fields parameters of NO_3^-, PD and TEGDA polymer chains were taken from OPLS-AA parameters.[206] A Lennard–Jones (LJ) cut-off of 10 Å and a particle-particle particle-mesh solver[207] for long-range Coulombic interactions were also employed. Herein, the electronic continuum model was employed to improve effective short-range ion-ion interactions in aqueous solution.[208] The charge scaled factors were 0.75, 0.72 and 0.72 for 12.5 m $LiNO_3$ in H_2O, 12.5 m $LiNO_3$ in H_2O: PD and LWIS gel, respectively.

Velocity-Verlet algorithm was applied to integrate the equations of motion with a time step equalled to 1 fs. The simulation box needs to reach equilibrium before sampling. To reach equilibrium, we firstly performed a 1 ns (1,000, 000 steps) Langevin dynamics at 500 K to randomize the initial shape of the molecules. Then, a 10 ns NPT simulation (10,000,000 steps) was performed at 298 K to ensure that the equilibrium salt dissociation had been reached. Finally, the NVT runs were 20 ns long (20,000,000 steps) at 298K. The last 10 ns trajectory was used to obtain the structure of electrolyte. The hydrogen bonds were defined by a distance cut-off of 3.5 Å and an angle cut-off of 30°.

5.3 Discussion

5.3.1 Salt/diluent screening for a wide electrochemical stability window

According to the design concept of LWIS electrolytes, an ideal diluent should simultaneously possess: (1) high miscibility with water; (2) low Li salt solubility and (3) wider chemical and electrochemical stability with electrodes during the battery operation.[89, 209] We compared the miscibility of different solvents with water in a mass ratio 1: 1. As shown in **Figure 5.1**a, diethylene carbonate (DEC), fluoroethylene carbonate (FEC) and propylene carbonate (PC) formed bi-phasic mixtures with water, while tetraethylene glycol dimethyl ether (TEGDME) formed an emulsion in water. In contrast, ethylene carbonate (EC) and PD can be well-mixed with water without phase separation (**Figure 5.1**a), and offer wider electrochemical stability window (4.2 V) than WIS (3.0 V) as shown in **Figure 5.2**a, which is in the working voltage range of batteries.[210] Therefore, EC and PD can act as diluent candidates. Furthermore, the solubilities of LiTFSI as a representative organic Li salt and $LiNO_3$ as a representative inorganic Li salt in different solvents at 25 °C are also presented in **Figure 5.1**b. It should be noted that these solubility values represent the solubility limits of stable supersaturated solutions which were prepared by dissolving the Li salt at 40 °C and then cooling down to 25 °C. It is seen that LiTFSI delivers high solubility in both water (21 m) and organic diluents (*i.e.* 8.0 m in EC and 6.5 m in PD). For comparison, inorganic $LiNO_3$ salt is highly soluble in water (25 m), but has poor solubility in diluents (*i.e.* 0.87 m in EC and 0.75 m in PD). This solubility difference of inorganic Li salts makes them suitable candidates to develop LWIS electrolytes.[211] Moreover, we measured the solubilities of various inorganic Li salts, including lithium chloride (LiCl), lithium sulphate (Li_2SO_4), lithium phosphate (Li_3PO_4) and lithium acetate (LiAc), in water and PD diluent. As seen from **Figure 5.1**c, although all the inorganic Li salts exhibit low solubilities of <2 m in PD, the water solubility of $LiNO_3$ (25 m) far exceeds other Li salts (LiCl: 24.1 m; LiAc: 11.1 m; Li_2SO_4: 3.2 m; Li_3PO_4: 0.2 m). Consequently, $LiNO_3$ was chosen as the ideal Li salt to form a LWIS electrolyte. Although, $LiNO_3$ is an oxidizer, the as-prepared aqueous electrolyte remains non-flammable. The $LiNO_3$ -based aqueous electrolytes is weakly acidic with pH values comparable to LiTFSI-based electrolytes (**Figure 5.2**b).

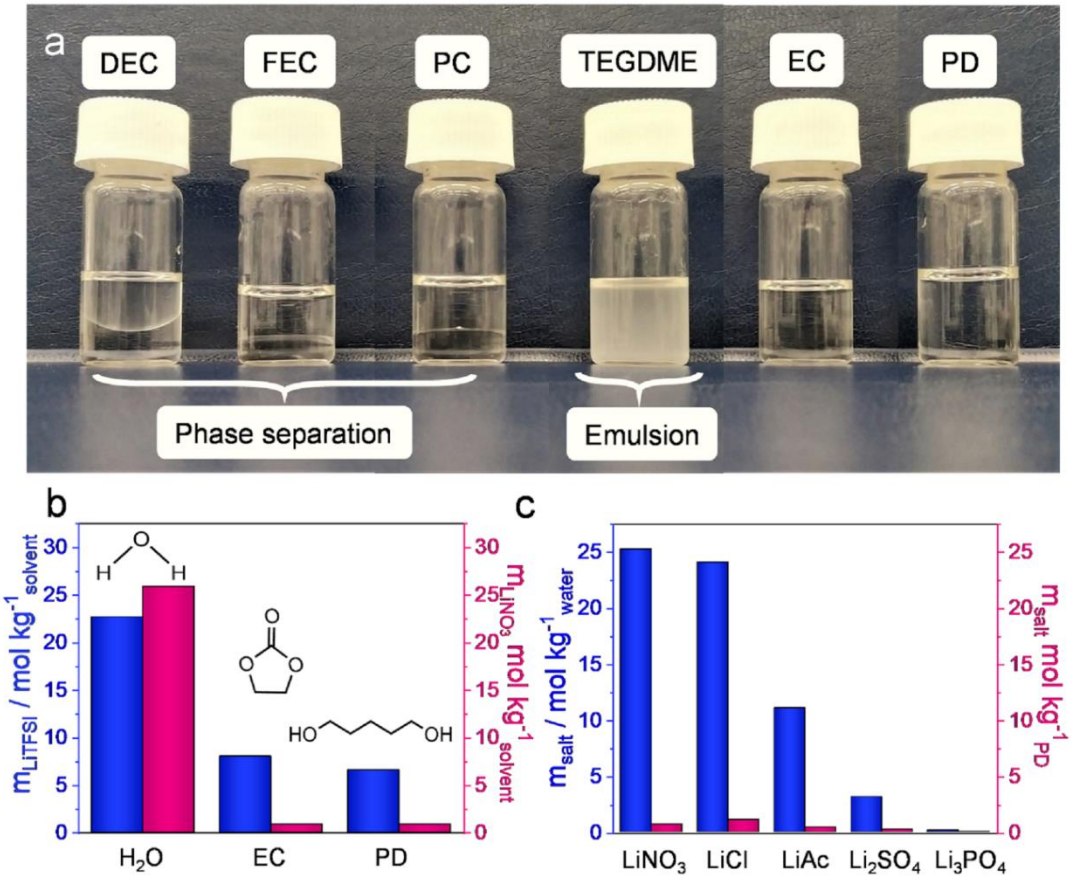

Figure 5.1. (**a**) Illustration of the miscibility of different solvents with water in a 1: 1 mass ratio. (**b**) Solubilities of LiTFSI (blue) and $LiNO_3$ (pink) in different solvents at 25 ℃. (**c**) Solubilities of different Li salts in water (blue) and PD (pink) at 25 ℃.

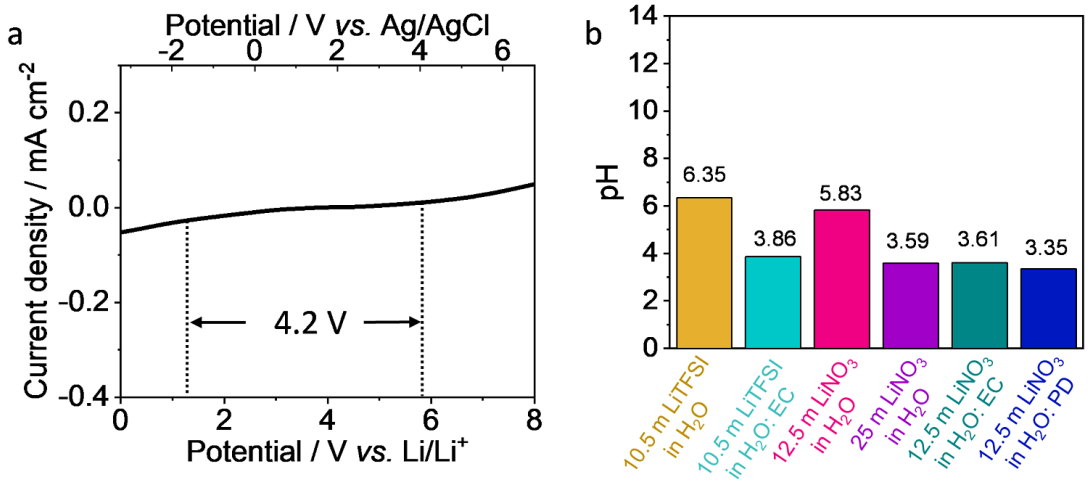

Figure 5.2. (**a**) Electrochemical stability window of 0.5 M LiTFSI in PD solution with Ti mesh as working electrode, Pt wire as counter electrode and Ag/AgCl as reference electrode at a scan rate of 0.1 mV s^{-1}. It is seen that PD possesses a wide electrochemical stability of 4.2 V. (**b**) pH values of different electrolytes.

The electrochemical stability windows of the $LiNO_3$-based LWIS and WIS electrolytes were evaluated by cyclic voltammetry (CV) in a three-electrode cell with titanium (Ti) mesh as working electrode, platinum (Pt) wire as counter electrode and Ag/AgCl as reference electrode. **Figure 5.3** shows the first and second CV curves of the 25 m $LiNO_3$ in H_2O WIS electrolyte, 12.5 m $LiNO_3$ in H_2O: PD (1: 1 by mass), LWIS electrolyte and LWIS gel electrolyte (prepared by *in-situ* polymerizing 6 wt% TEGDA monomer in 12.5 m $LiNO_3$ in H_2O: PD electrolyte). The electrochemical window values of LWIS and LWIS gel electrolytes from the 2nd CV cycle were obviously larger than those in the 1st cycle, while the electrochemical stability windows showed almost no change during cycling in the 12.5 m and 25 m $LiNO_3$ in H_2O electrolytes. This seems to be mainly due to the SEI formation that suppresses the hydrogen evolution reaction (HER) in two LWIS aqueous electrolytes,[17] which will be discussed in the following part. The impact of diluents (EC and PD) on electrochemical stability window of LWIS electrolytes was also investigated.

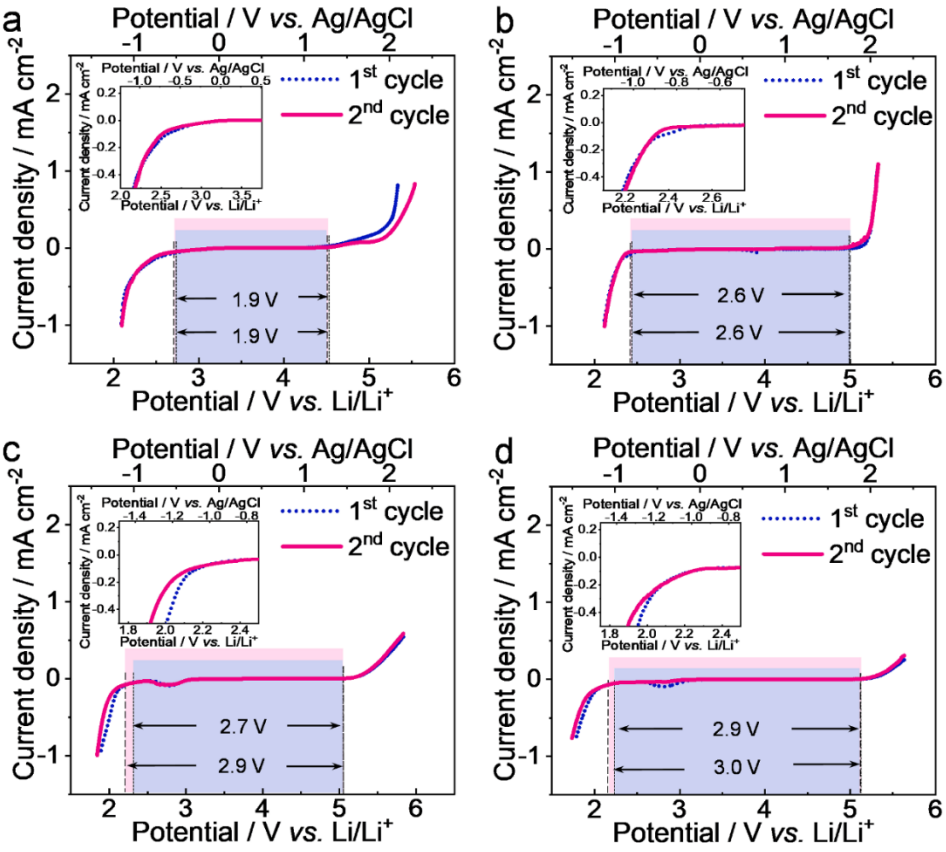

Figure 5.3. 1st and 2nd CV curves of the (**a**) 12.5 m $LiNO_3$ in H_2O electrolyte, (**b**) 25 m $LiNO_3$ in H_2O electrolyte, (**c**) 12.5 m $LiNO_3$ in H_2O: PD electrolyte and (**d**) LWIS gel electrolyte at 0.1 mV s^{-1}. The enlarged region related to HER are shown in insets.

Figure 5.4 and **Appendix 3** shows the 2nd linear polarization profiles of the electrolytes with and without dilute. The 10.5 m LiTFSI in H_2O electrolyte exhibited a stability window of 2.1 V (**Figure 5.4**a). In this electrolyte, Li ions are solvated by water molecules to form solvation sheaths, meanwhile anions are mostly excluded from these solvation sheaths (**Figure 5.4**e, left panel).[130, 212] After adding 50 wt% EC into the solvent, the solvation structure of the electrolyte did not dramatically change, except for the appearance of EC molecules with high solubility of LiTFSI in the solvation sheaths (**Figure 5.4**e, right panel).[14] The 10.5 m LiTFSI in H_2O: EC (1: 1 by mass) electrolyte delivered a stability window of 2.3 V (**Figure 5.4**a), which is still much lower than the 3.0 V-wide window of the saturated 21 m LiTFSI in H_2O electrolyte.[130] This is due to the huge amount of free water molecules outside of the solvation sheaths that trigger preferential hydrogen evolution. In sharp contrast, when EC was introduced in the 12.5 m $LiNO_3$ in H_2O electrolyte, the electrochemical window was dramatically widened from 1.9 V to 2.7 V (**Figure 5.4**b), which is very close to that of the saturated 25 m $LiNO_3$ in H_2O electrolyte (2.6 V, **Figure 5.5**a). This is because in the as-developed EC-based LWIS electrolyte (*i.e.* 12.5 m $LiNO_3$ in H_2O: EC, 1: 1 by mass), the EC molecules as diluent do not participate in the solvation sheaths due to the low $LiNO_3$ solubility in EC.[213] The increased $LiNO_3$: H_2O ratio in the EC-based LWIS electrolyte leads to an enlarged percentage of water molecules that are coordinated with Li^+, significantly decreasing the reactivity of water molecules in HER/OER. Furthermore, NO_3^- anions appear in the primary solvation sheaths of Li^+ to generate ion aggregates, reducing the water content in the primary solvation sheaths (**Figure 5.4**f, right panel). Likewise, the addition of PD diluent could form a LWIS electrolyte (*i.e.* 12.5 m $LiNO_3$ in H_2O: PD, 1: 1 by mass) with a similar solvation structure. However, as protic solvent, PD can form numerous hydrogen bonds between its hydroxyl groups and the water molecules as well as NO_3^- anions, forming polymer-like chains consisting with solvation sheaths (**Figure 5.4**g, right panel).[214] The reactivity of water solvent in HER/OER was thereby further reduced and the electrochemical stability window was extended to 2.9 V (**Figure 5.4**c and **Figure 5.5**b). For the LWIS gel electrolyte, the fluidity of electrolyte was eliminated meanwhile additional hydrogen bonds were formed between the polymer matrix and water molecules (**Figure 5.4**h, right panel), thus leading to a stability window as wide as 3.0 V (**Figure 5.4**d and **Figure 5.5**c). This high electrolyte stability is eligible to fulfil the requirements of the electrochemical redox couple of Mo_6S_8 anode and LMO

cathode. Therefore 12.5 m $LiNO_3$ in H_2O: PD gel electrolytes were selected for further investigation.

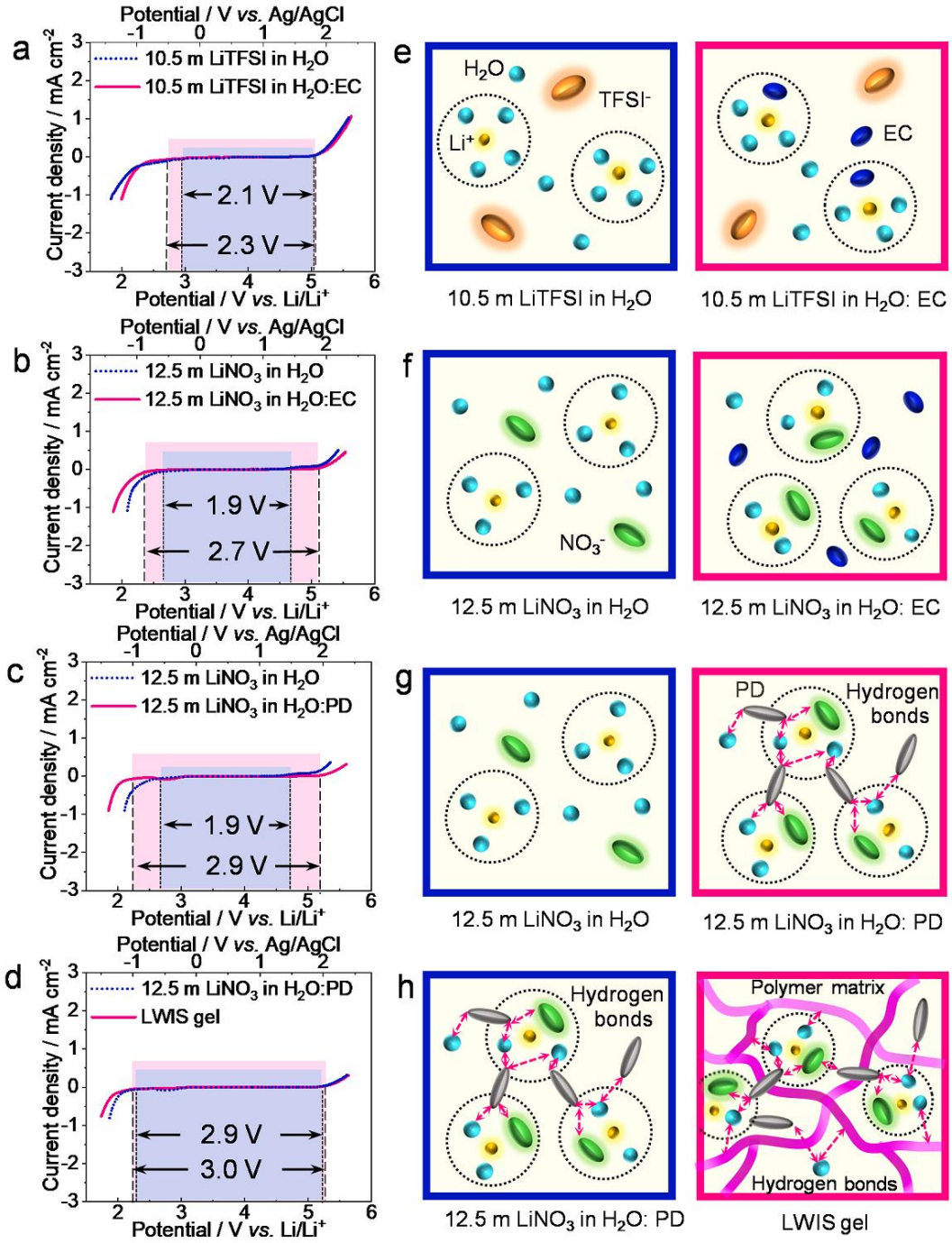

Figure 5.4. (**a-d**) 2nd CV curves of (**a**) 10.5 m LiTFSI in H_2O and 10.5 m LiTFSI in H_2O: EC, (**b**) 12.5 m $LiNO_3$ in H_2O and 12.5 m $LiNO_3$ in H_2O: EC, (**c**) 12.5 m $LiNO_3$ in H_2O and 12.5 m $LiNO_3$ in H_2O: PD, and (**d**) 12.5 m $LiNO_3$ in H_2O: PD and LWIS gel electrolyte couples at 0.1 mV s^{-1}. (**e-h**) The corresponding schematic hypothetical diagrams of solvation structures for the electrolytes.

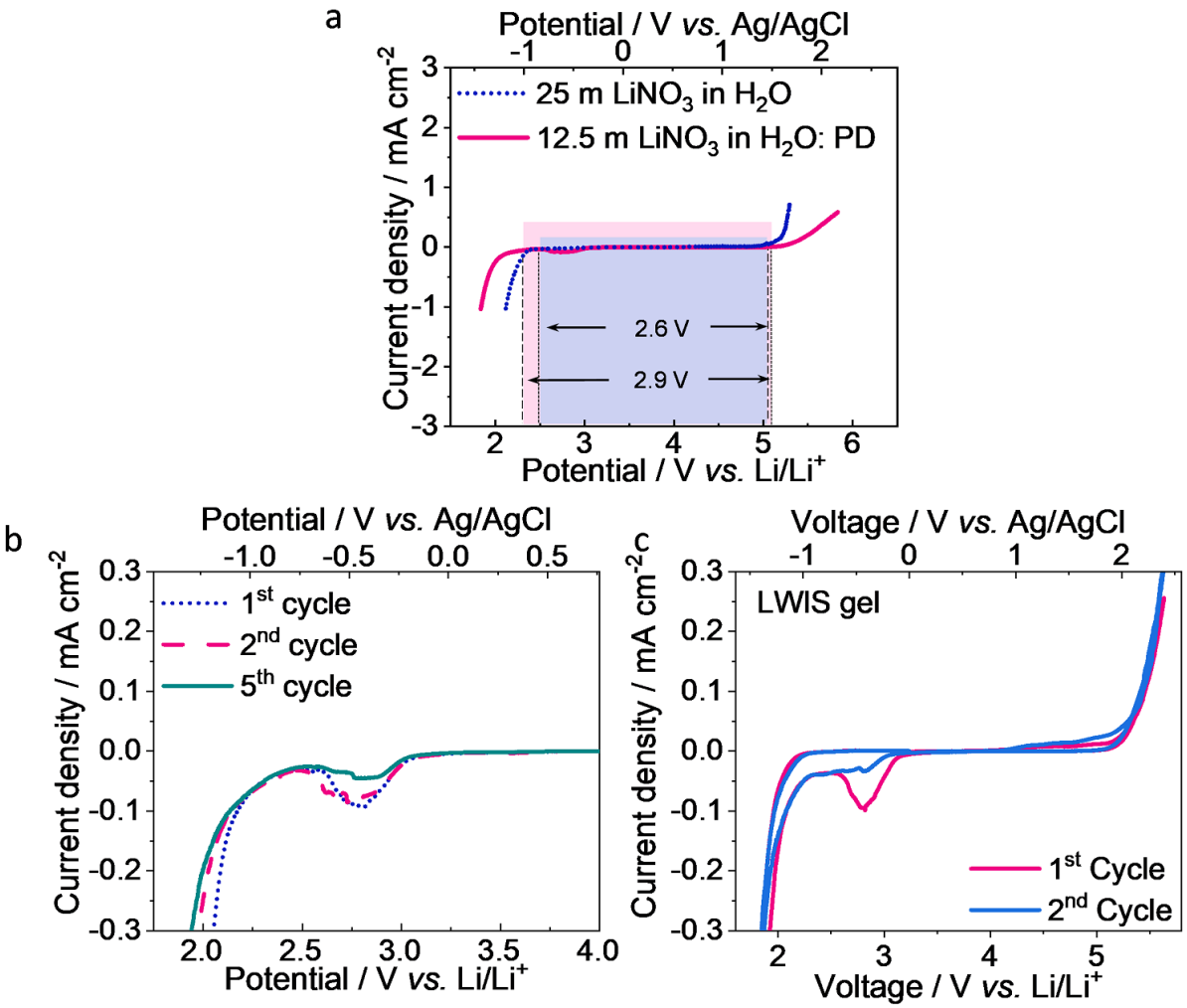

Figure 5.5. (**a**) 2nd CV curves of 25 m $LiNO_3$ in H_2O and 12.5 m $LiNO_3$ in H_2O: PD electrolytes at 0.1 mV s^{-1}. (**b**) Zoomed-in CV curves of the 12.5 m $LiNO_3$ in H_2O: PD electrolyte. The current peaks between 3 and 2.5 V *vs.* Li/Li^+ only appeared in the aqueous electrolytes that contain PD. Their intensities gradually decreased in the following cycles. We speculate this may be related to the reduction of PD-involved solvation shell. (**c**) 1st and 2nd CV curves of the LWIS gel electrolyte at 0.1 mV s^{-1}.

5.3.2 Solvation structure of 12.5 m $LiNO_3$ in H_2O: PD LWIS gel electrolytes

Molecular dynamic (MD) simulations were conducted to investigate the solvation structures of 12.5 m $LiNO_3$ in H_2O: PD LWIS gel electrolytes, and compared it with two baseline electrolytes (12.5 m $LiNO_3$ in H_2O and 12.5 m $LiNO_3$ in H_2O: PD). As shown in **Figure 5.6**a, in the 12.5 m $LiNO_3$ in H_2O electrolyte, Li ions are mainly solvated with 4 water molecules to

form a primary solvation sheath. Meanwhile, around 70 % of water molecules are coordinated with Li^+ ions, while others interact with each other via hydrogen bonds (**Figure 5.6**d). Such a huge amount of uncoordinated water molecules triggers significant HER reaction on the anode, which severely deteriorates the performance of the batteries.[215] Moreover, most NO_3^- ions are randomly distributed among the water molecules without any coordination with Li^+ ions (**Figure 5.6**a). When PD is introduced into the electrolyte, large amount of Li^+ ions prefer to partially share the primary water sheaths with the neighbouring Li^+ ions, and the Li^+ primary solvation shells are aggregated together to from polymer-like chain due to the hydrogen-bonding linkage of PD (**Figure 5.6**b). In such 12.5 m $LiNO_3$ in H_2O: PD LWIS electrolyte, the amount of water molecules coordinated with Li^+ dramatically increase to 94.3 %, leading to a sharp reduction of the reactivity in HER/OER for water molecules (**Figure 5.6**d). In particular, the number of NO_3^- anions observed in each Li^+ primary solvation sheath rises from 0.89 to 1.55 after the introduction of PD. This reduces the water number in each Li^+ primary solvation sheath, which further extends the electrochemical window (**Figure 5.5**a). When gelling the 12.5 m $LiNO_3$ in H_2O: PD electrolyte with TEGDA monomer, the Li^+-H_2O complexes delivers a long-range aggregation. It indicates that most water molecules are immobilized by localized concentrated $LiNO_3$ salt and the polymerized TEGDA matrix (**Figure 5.6**c). Furthermore, as shown in **Figure 5.6**d, the hydrogen bonds of 12.5 m $LiNO_3$ in H_2O solution are ≈1.2 per water molecule, which significantly increases to ≈1.25 and 1.35 with the addition of PD and polymer matrix, respectively. This is mainly due to the formation of hydrogen bonds between the water molecules and NO_3^- anions in the electrolyte and the hydroxyl groups in the PD (**Figure 5.7**) as well as the ether groups in the polymerized TEGDA. Such water/NO_3^--PD and water-polymerized TEGDA interactions can disturb the water hydrogen bond network and further decrease the reactivity of water solvent in HER/OER, thereby effectively inhibiting the electrolyte decomposition.[216]

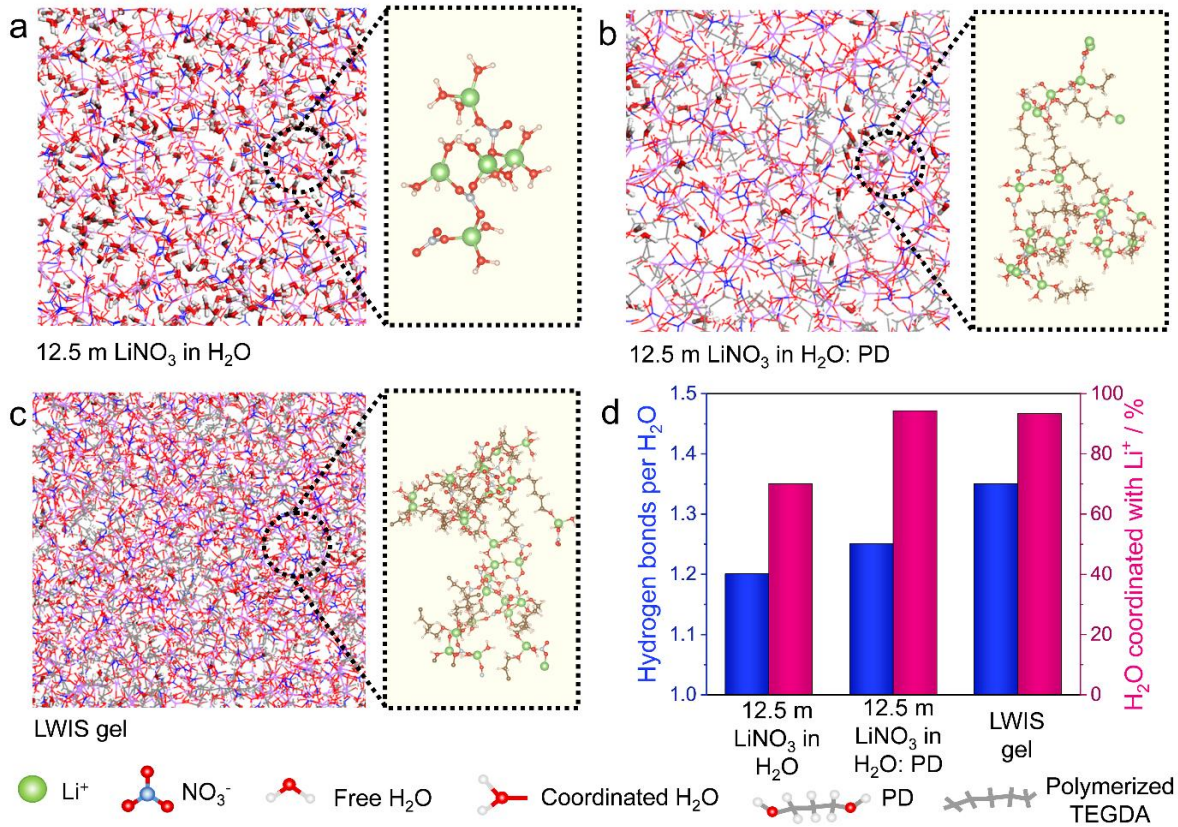

Figure 5.6. MD simulations of aqueous electrolytes. (**a-c**) Snapshots of the local structures of (**a**) 12.5 m $LiNO_3$ in H_2O, (**b**) 12.5 m $LiNO_3$ in H_2O: PD and (**c**) LWIS gel electrolytes obtained via MD simulation after 20 ns at 298 K. (**d**) The hydrogen bonds and the percentage of water molecules coordinated with Li^+ for three aqueous electrolyte samples at 20 ns.

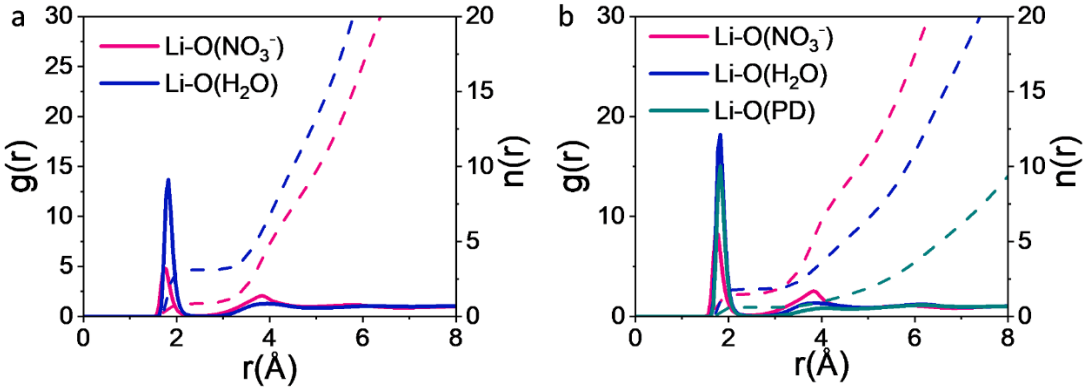

Figure 5.7. Radial distribution functions g(r) of Li-O(H_2O), Li-O(NO_3^-), and Li-O(PD) pairs calculated from MD simulation trajectories in (**a**) 12.5 m $LiNO_3$ in H_2O and (**b**) 12.5 m $LiNO_3$ in PD: H_2O electrolytes. A Li-O(PD) peak is identified at 1.85 Å in the 12.5 m $LiNO_3$ in PD: H_2O electrolyte, demonstrating the PD molecules can partially participate in the Li^+ solvation sheath and link them together via hydrogen bonding.

5.3.3 Characterization of the 12.5 m $LiNO_3$ in H_2O: PD LWIS gel electrolyte

Figure 5.8a exhibits the polymerization mechanism of TEGDA monomer in the LWIS electrolyte. The primary radicals derived from the ultraviolet light (UV)-irradiation of 2-hydroxy-2-methyl-1-phenyl-1-propanone (HMPP) photo-initiator attack the C=C bonds of the monomer to generate free radicals. Subsequently, a chain growth reaction occurs through sequentially adding TEGDA monomer to the radical ends on the initiated monomer. Finally, a three-dimensional polymerized TEGDA network is constructed in LWIS electrolyte, and a gel electrolyte is thereby *in-situ* obtained. As shown in the right panel of **Figure 5.8**a, the as-prepared LWIS gel electrolyte presents an appearance of a freestanding transparent film, which can maintain its integrity under the pressure of a 100 g weight (**Figure 5.9**). **Figure 5.8**b shows the Fourier-transform infrared (FT-IR) spectra of the TEGDA monomer and polymer matrix of LWIS gel electrolyte. The peaks at ≈1245 cm^{-1} (C–O antisymmetric stretching), ≈1450 cm^{-1} and ≈1390 cm^{-1} (CH_2 bending) and ≈1720 cm^{-1} (C=O stretching) appear in the spectrum of TEGDA monomer.[47] The absorption peak at ≈1615 cm^{-1} corresponding to stretching vibration of C=C bonds disappears after polymerization, confirming a successful *in-situ* gelation of the LWIS gel electrolyte. Raman spectroscopy was employed to detect the O–H stretching vibration in different electrolytes. As shown in **Figure 5.8**c, the O–H stretching vibration of pure water displays a broad band centered around 3320 cm^{-1}, which is attributed to the different hydrogen-bonding environment of water molecules.[139] The intensity of this band gradually shrinks in the spectra of 12.5 m $LiNO_3$ in H_2O and 12.5 m $LiNO_3$ in H_2O: PD electrolytes, indicating that the Li^+-H_2O coordination breaks the hydrogen-bonding structure of water. The LWIS gel electrolyte exhibits a small hump at ≈3480 cm^{-1} in the Raman spectrum, which demonstrates that the free water population is dramatically diminished in this quasi-solid electrolyte. This is well-consistent with the MD simulation results in **Figure 5.6**.

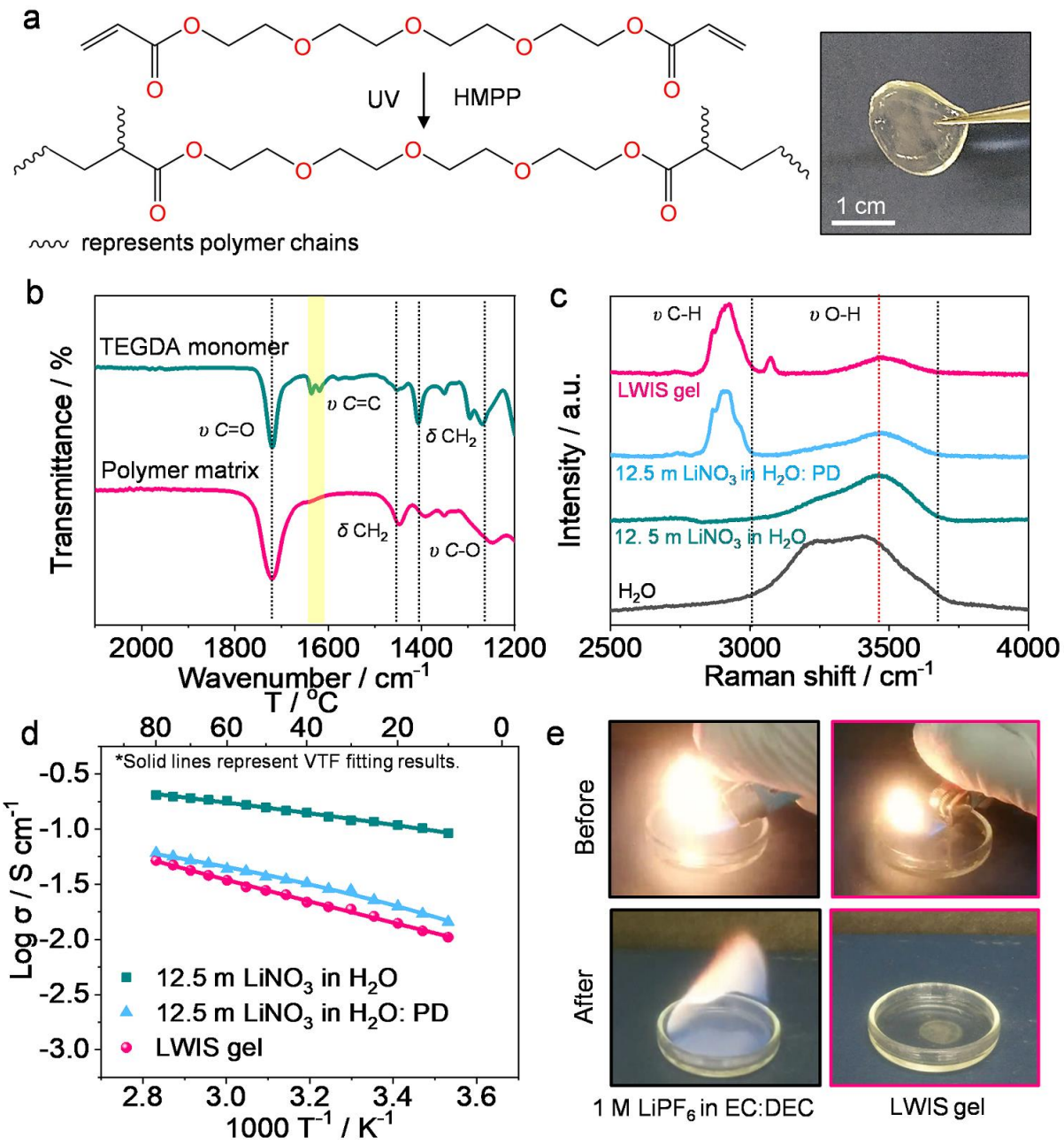

Figure 5.8. (**a**) *In-situ* polymerization mechanism of the TEGDA monomer in the presence of LWIS electrolyte. An optical image of an as-prepared LWIS gel electrolyte membrane is shown in the right panel. (**b**) FT-IR spectra of TEGDA monomer and the polymer matrix of LWIS gel electrolyte. (**c**) Raman spectra of pure water and 12.5 m $LiNO_3$ in H_2O, 12.5 m $LiNO_3$ in H_2O: PD and LWIS gel electrolytes. (**d**) Ionic conductivities of 12.5 m $LiNO_3$ in H_2O, 12.5 m $LiNO_3$ in H_2O: PD and LWIS gel electrolytes as a function of temperature. The discrete points represent the experimental data while the solid lines represent VTF fitting results. (**e**) Flammability tests of 1 M $LiPF_6$ in EC: DEC (left panels) and LWIS gel (right panels) electrolytes.

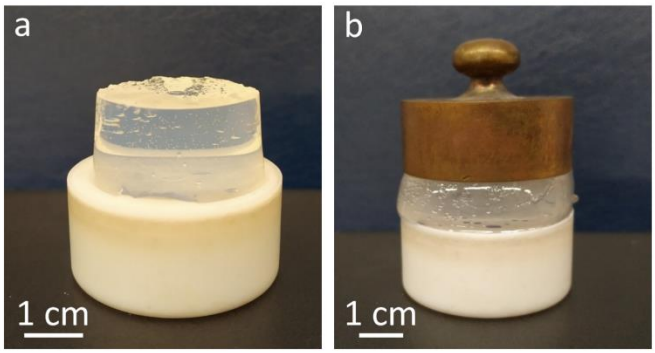

Figure 5.9. Pictures of the LWIS gel (**a**) at rest state and (**b**) under the pressure of a 100 g weight.

The ionic conductivities of the different electrolyte samples were measured by electrochemical impedance spectroscopy (EIS) in a temperature range from 10 °C to 80 °C. As shown in **Figure 5.8**d and **Figure 5.10**a, the plots of log σ versus T^{-1} present a non-linear Vogel Tamman-Fulcher (VTF) relationship as described by the following equation:[192]

$$\sigma = \sigma_0 T^{-\frac{1}{2}} exp(-\frac{E_a}{\mathrm{R}(T-T_0)}) \qquad (\mathbf{5.1})$$

where σ_o is a pre-exponential factor, T_o is the effective glass transition temperature, E_a is the activation energy and R is the ideal gas constant. The corresponding fitting values and ionic conductivities at 25 °C are listed in **Table 5.1**. The Arrhenius equation was additionally employed to fit the ionic conductivities as shown in **Appendices 4-5**. The 12.5 m $LiNO_3$ in H_2O baseline electrolyte has highest ionic conductivity of 1.16×10^{-1} S cm^{-1} at 25 ℃, which is two-time higher than that of 25 m $LiNO_3$ in H_2O WIS electrolyte (7.38×10^{-2} S cm^{-1}). The low ionic conductivity of WIS electrolyte is mainly due to its huge viscosity, which blocks ion transport (51 mPa s, **Figure 5.10**b). Moreover, the crystallization of $LiNO_3$-based WIS electrolyte starts at temperature below 25 ℃, which leads to a sharp decline in ionic conductivity (from 1.73×10^{-2} S cm^{-1} at 20 °C to 1.60×10^{-5} S cm^{-1} at 10 °C, **Figure 5.10**a). The viscosity and crystallization of $LiNO_3$-based WIS electrolyte strongly limits its practical application in batteries. After adding 50 % PD into 25 m $LiNO_3$ in H_2O electrolyte, the 12.5 m $LiNO_3$ in H_2O: PD LWIS electrolyte delivered a low viscosity (22 mPa s), which is comparable to that of the 12.5 m $LiNO_3$ in H_2O electrolyte (10 mPa s, **Figure 5.10**b). The electrolyte crystallization was successfully inhibited in the tested temperature range attributed to the addition of PD. This results in a relatively minimal ionic conductivity change from 1.99×10^{-2} S cm^{-1} at 20 °C to 1.44

× 10^{-2} S cm^{-1} at 10 °C (**Figure 5.8**d). After polymerization, the LWIS gel electrolyte still maintains an ionic conductivity of 1.62 × 10^{-2} S cm^{-1} at 25 °C with a low E_a value of 2.84 × 10^{-2} eV (**Figure 5.8**d). This conductivity value is much higher than most of the organic liquid/gel electrolytes, and is sufficient to meet the requirements of Li-ion batteries.[177]

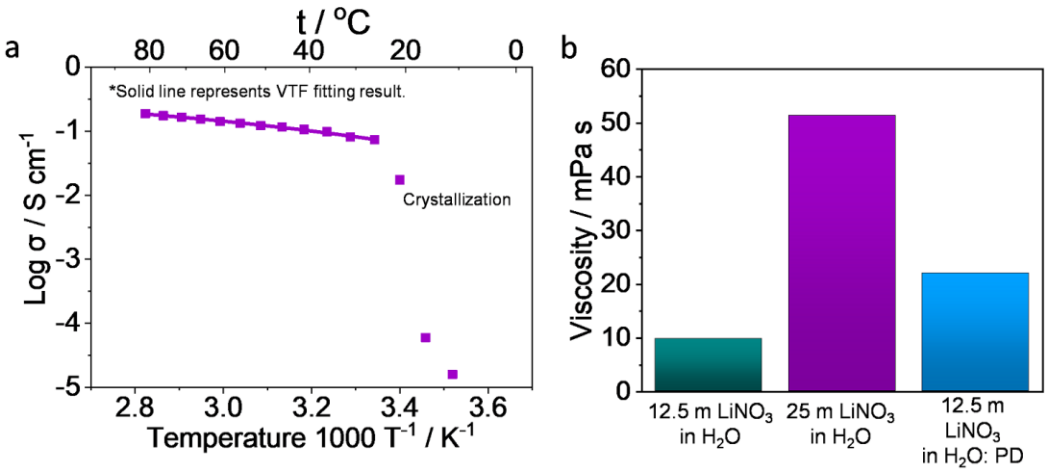

Figure 5.10. (**a**) Ionic conductivities of the 25 m $LiNO_3$ in H_2O electrolyte as a function of temperature. (**b**) Viscosities of the 12.5 m $LiNO_3$ in H_2O, 25 m $LiNO_3$ in H_2O and 12.5 m $LiNO_3$ in H_2O: PD electrolytes at 25 °C.

Table 5.1. VTF fitting parameters and ionic conductivities at 25 °C of different electrolyte samples.

Sample	σ at 25 °C (S cm^{-1})	σ_o (S cm^{-1} $K^{-1/2}$)	E_a (eV)	T_o (K)
25 m $LiNO_3$ in H_2O	0.0738	23.65 ± 0.021	3.15×10^{-2} ± 0.073	193.5 ± 0.073
12.5 m $LiNO_3$ in H_2O	0.116	47.7 ± 0.010	2.31×10^{-2} ± 0.033	92.4 ± 0.033
12.5 m $LiNO_3$ in H_2O:PD	0.0228	12.53 ± 0.025	2.65×10^{-2} ± 0.079	170.6 ± 0.079
LWIS gel	0.0162	0.21 ± 0.014	2.84×10^{-2} ± 0.044	177.5 ± 0.044

The LWIS gel electrolyte also exhibits improved electronic insulation (**Figure 5.11**). Moreover, the thermal safety of LWIS gel electrolyte and conventional 1 M $LiPF_6$ in ethylene carbonate (EC): diethyl carbonate (DEC) (1: 2 by vol) electrolyte was examined via combustion tests. The LWIS gel electrolyte could not be ignited by fire sources (**Figure 5.8**e, right panels) and the weight loss was negligible after aging in open air at 25 °C for 4 h (3 wt%, **Figure 5.12**). In

contrast, the 1 m $LiPF_6$ in EC: DEC liquid electrolyte was highly flammable (**Figure 5.8**e, left panels) and evaporated quickly at 25 ℃ (96 wt% after 4h, **Figure 5.12**) due to the low boiling points of the organic solvents. The superior thermal stability of the LWIS gel electrolyte facilitates safe operation of Li-ion batteries. Furthermore, the LWIS gel electrolyte can well-fill the pores of the electrodes and keep good interfacial contact with electrodes (**Figure 5.13** and **Table 5.2**).

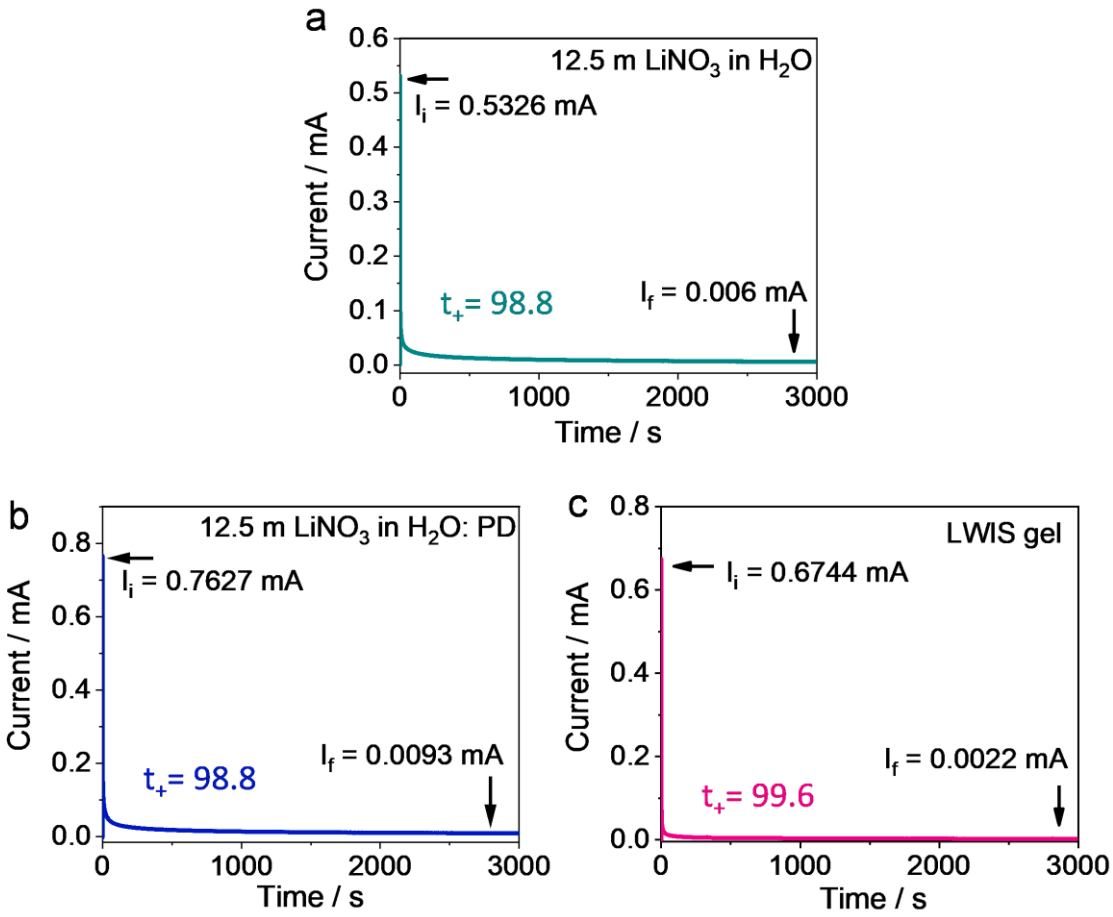

Figure 5.11. Chronoamperometry profile under a polarization of 1 V in (**a**) 12.5 m $LiNO_3$ in H_2O, (**b**) 12.5 m $LiNO_3$ in H_2O: PD and (**c**) LWIS gel electrolytes.

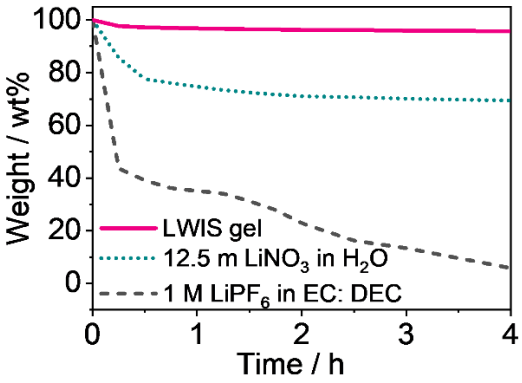

Figure 5.12. Weight losses of 1 M $LiPF_6$ in EC: DEC, 12.5 m $LiNO_3$ in H_2O and LWIS gel electrolytes along with aging time at 25 °C.

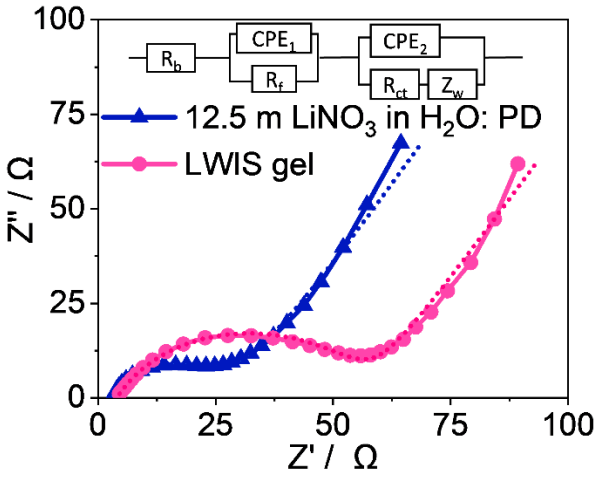

Figure 5.13. EIS spectra of Mo_6S_8||LMO cells with 12.5 m $LiNO_3$ in H_2O: PD electrolyte (blue) and LWIS gel electrolyte (pink) tested in a half-charged state in the initial cycle. Frequency range: 10^{-2} to 10^5 Hz; disturbance amplitude: 5 mV. The dot lines represent the fitting values from the equivalent circuit. The equivalent circuit is shown in inset.

Table 5.2. The bulk resistance (R_b), SEI resistance (R_f) and the charge transfer resistance (R_{ct}) fitting value obtained from the equivalent circuit.

Sample	**R_b (Ω)**	**R_f (Ω)**	**R_{ct} (Ω)**
12.5 m $LiNO_3$ in H_2O: PD	3.4 ± 0.045	5.1 ± 0.021	23.5 ± 0.010
LWIS gel	30.3 ± 0.023	7.6 ± 0.022	10.7 ± 0.011

5.3.4. Electrochemical performance of the Mo_6S_8||$LiMn_2O_4$ full cells using LWIS Gel electrolytes

LWIS gel-electrolytes and baseline electrolytes were compared in full cells with Mo_6S_8 anodes and LMO cathodes. CV curves of Mo_6S_8 anode and LMO cathode, and electrochemical stability window are displayed in **Figure 5.14**a. The Li intercalation/de-intercalation redox peaks at about 2.66 V and 3.68 V for Mo_6S_8 and the characteristic redox peaks of LMO at 4.15 and 4.29 V [130, 136] are within stability window of LWIS gel-electrolytes. However, the redox potential of the Mo_6S_8 anode is lower than the HER onset potential of pure water, 12.5 m $LiNO_3$ in H_2O and 12.5 m $LiNO_3$ in H_2O: PD electrolytes (≈2.77, 2.70, and 2.27 V *vs.* Li/Li^+, respectively, **Figure 5.14**b), which triggers water decomposition during the battery cycling and thus reduces the battery reversibility. In contrast, the LWIS gel electrolyte exhibits a 3.0 V-wide electrochemical window with a HER onset potential of 2.20 V *vs.* Li/Li^+, enabling the successful operation of the electrochemical redox couple of Mo_6S_8 anode and LMO cathode.

Mo_6S_8||LMO full cells with LWIS and LWIS gel electrolytes were cycled at 1 C (1 C = 122 mAh g^{-1}, based on the mass of the Mo_6S_8 anode) between 0.5 and 2.3 V (**Figure 5.14**c). In the cells using 12.5 m $LiNO_3$ in H_2O, a cut-off time set as 2 h was applied in the charge process to avoid continuous water decomposition. The cell suffered from severe HER at ≈2 V in the charging process (the inset of **Figure 5.14**c) due to 1.9 V stability window (**Figure 5.14**b), resulting in a low capacity of ≈25 mAh g^{-1} in the subsequent discharge (**Figure 5.15**a). When the salt concentration in the aqueous electrolyte was doubled to 25 m, the cell delivered an initial discharge capacity of 71 mAh g^{-1} with a Coulombic efficiency of 35 %. However, the water decomposition during cycling led to a crystallization of the aqueous electrolyte (see inset of **Figure 5.15**b), which triggered a rapid capacity fading (34 mAh g^{-1} after 10 cycles, **Figure 5.15**b). The 12.5 m $LiNO_3$ in H_2O: PD LWIS electrolyte exhibited an improved cycling performance, compared with the saturated electrolyte in the full cell due to the suppression of electrolyte crystallization (**Figure 5.15**c). The LWIS gel electrolyte with an expanded stability window matches well with the electrode couple. As shown in **Figure 5.14**d, the cell showed a high initial discharge capacity of 105 mAh g^{-1} in the voltage between 0.5 and 2.3 V. The Coulombic efficiency gradually increased to 97.80 % after 20 cycles, and maintained an average Coulombic efficiency of 98.53 % over 250 cycles at 1 C (excluding the initial 20

activation cycles, whose low Coulombic efficiency could be due to the breakdown/reconstruction of SEI, irreversible proton co–intercalation in acidic electrolyte, and other complicated side reactions in the initial cycles[14, 134]). The initial Coulombic efficiency was 66.15 % for the Mo_6S_8||LMO cell (**Figure 5.14**d). Considering the delithiation/lithiation Coulombic efficiency of the anode was calculated to be 74.71 % based on the CV curve of Mo_6S_8 without influence of HER (**Figure 5.14**a), around 8.56 % of the charge capacity (*i.e.* the difference in Coulombic efficiency) could be attributed to the HER in the first cycle.[217] The Mo_6S_8|LWIS gel electrolyte|LMO full cell delivered a capacity retention of 70.0 % after 250 cycles at 1 C, demonstrating an inhibited HER and stable electrolyte|electrode interfaces. The capacity fading could be due to the transition metal ion dissolution from cathode and other side reactions (*e.g.* the thickening of SEI) that consuming the limited Li inventory in the cathode.

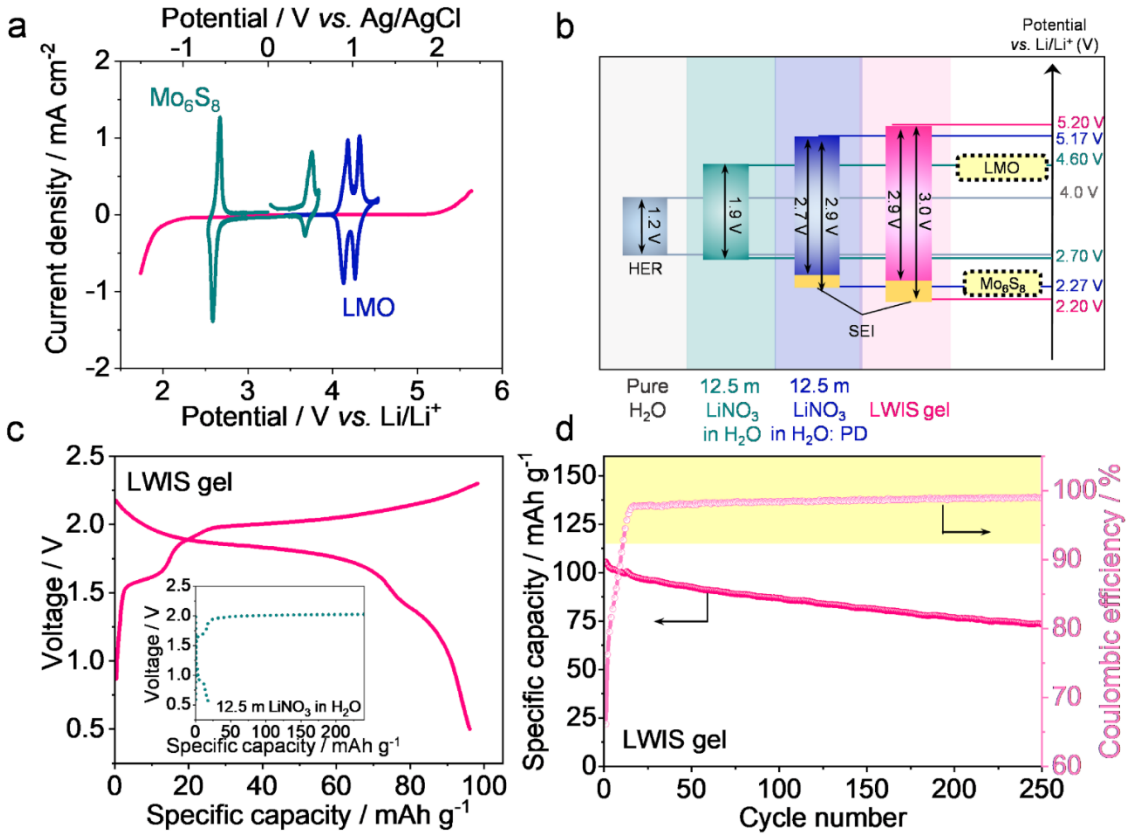

Figure 5.14. (**a**) CV curves of the Mo_6S_8 and LMO electrodes at 0.1 mV s^{-1} obtained with the LWIS gel electrolyte. The electrochemical window of LWIS gel electrolyte is presented for comparison. (**b**) Schematic of the electrochemical stability windows of different electrolytes and the redox voltages of Mo_6S_8 anode and LMO cathode. (**c**) Charge-discharge curves of Mo_6S_8||LMO full cells with 12.5 m $LiNO_3$ in H_2O electrolyte (inset) and LWIS gel electrolyte in

the 25th cycle at 1 C. (**d**) Cycling performance of Mo_6S_8|LWIS gel electrolyte|LMO full cell at 1 C.

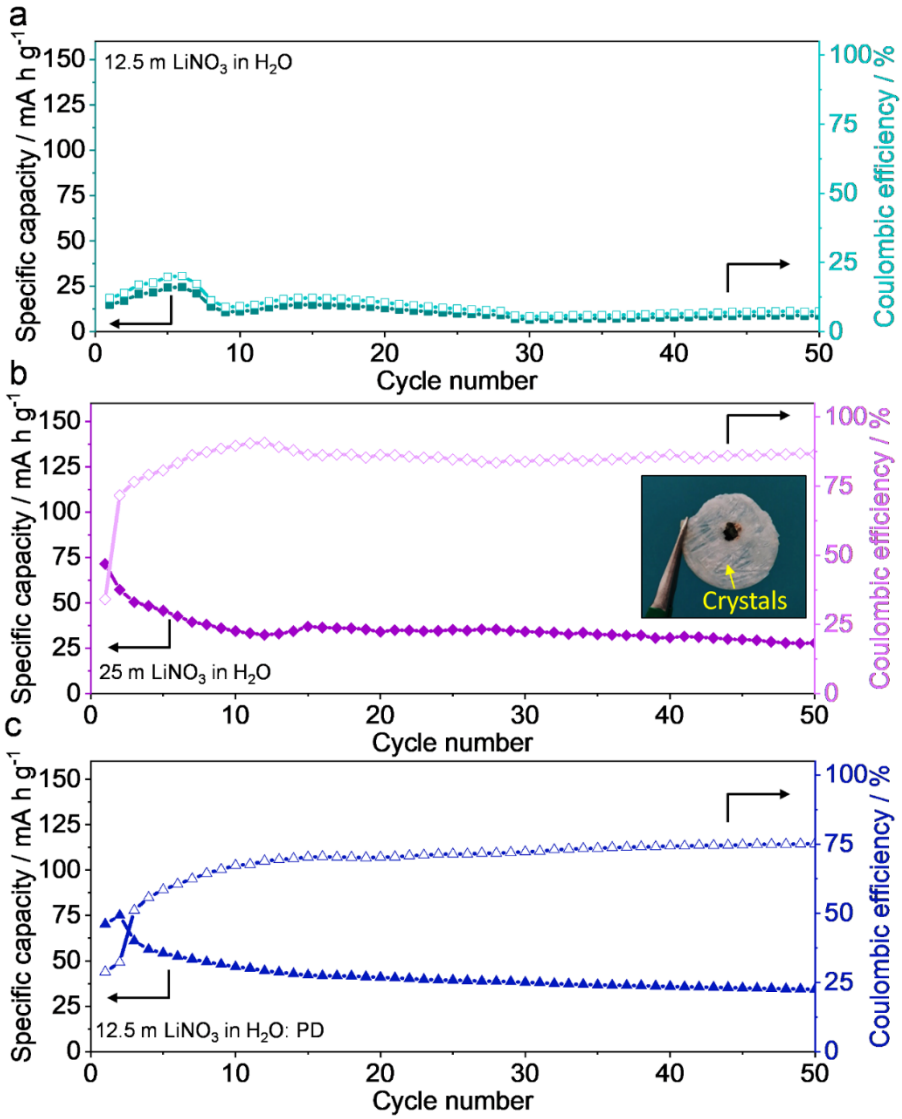

Figure 5.15. Cycling performances of Mo_6S_8||LMO full cell with (**a**) 12.5 m $LiNO_3$ in H_2O, (**b**) 25 m $LiNO_3$ in H_2O and (**c**) 12.5 m $LiNO_3$ in H_2O: PD electrolytes. Inset of **Figure 5.15**b: image of the separator after dismantling the cell after 50 cycles. Crystals can be observed on the separator.

The rate performance of the cell with LWIS gel electrolyte was presented in **Figure 5.16**. The specific discharge capacity reached 103, 87, 75 and 25 mAh g^{-1} at 0.5 C, 1 C, 2 C and 5 C, respectively (**Figure 5.16**b). It is seen that the Coulombic efficiency increased with the increase of current density due to the slower side reaction kinetics at high rates (**Figure 5.16**a).[218] Moreover, the capacity retention was 97 % of the initial value when the current

density was reversed back to 0.5 C (**Figure 5.16**a). Therefore, this aqueous battery configuration is highly reversible and robust. The excellent electrochemical performance of the LWIS gel electrolyte-based aqueous battery can be ascribed to the synergetic effect of PD diluent and TEGDA-based polymer matrix that efficiently reduces the water reactivity in HER/OER, and the formation of protective SEI layer on the anode that further inhibits the interfacial side reactions. However, when the current is increased to 5 C, the discharge capacity drops to about 25 mAh g^{-1}, which is not sufficient for practical application. The poorer cycling performances at high rate could be due to the slower reaction kinetic in the quasi-solid electrolytes.

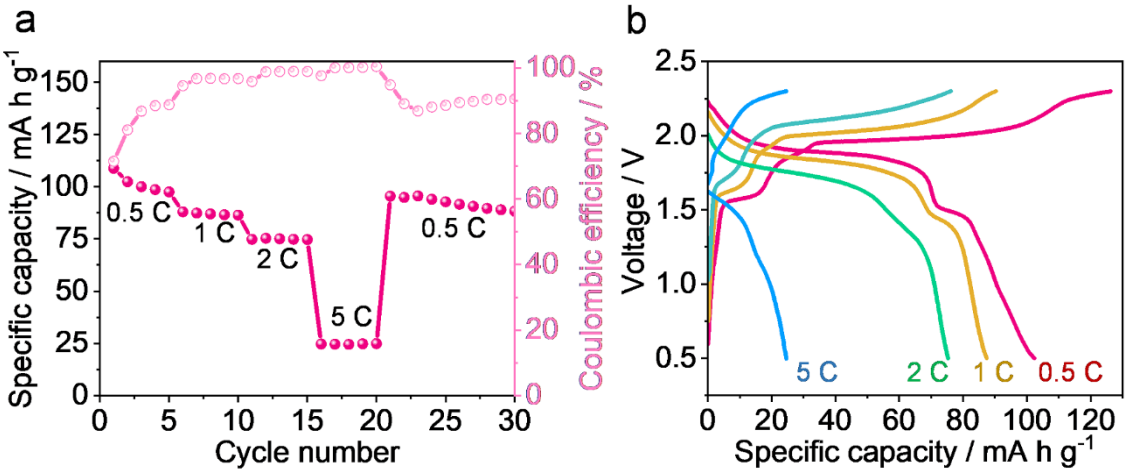

Figure 5.16. (**a**) Rate performance and (**b**) corresponding charge-discharge curves of Mo_6S_8|LWIS gel electrolyte|LMO full cell.

5.4.5 Formation of SEI on Mo_6S_8 anode surface in LWIS gel-electrolyte

Transmission electron microscopy (TEM) was employed to analyse the surface morphologies of Mo_6S_8 anodes after 20 cycles in different electrolytes. When the anode was cycled in 12.5 m and 25 m $LiNO_3$ in H_2O electrolyte, the Mo_6S_8 particles maintained fresh surfaces without SEI formation (**Figure 5.17**a and **Figure 5.18**a). By comparison, SEI layers with thicknesses of ≈4 nm and 7 nm were observed on the Mo_6S_8 surfaces after cycling in 12.5 m $LiNO_3$ in H_2O: PD electrolyte (**Figure 5.18**b) and LWIS gel electrolyte (**Figure 5.17**b), respectively. Moreover, these SEIs exhibited a structure consisting of Li_2O and Li_2CO_3 crystalline regions dispersed in an amorphous phase (**Figure 5.17**b).[219] The SEI composition was further investigated by X-ray photoelectron spectroscopy (XPS) depth profiling. For the anode cycled in LWIS gel

electrolyte, peaks at about 52.3, 54.5 and 57.2 eV in the Li 1s spectra are assigned to Li_2O, Li_2CO_3 and Li_3N/LiN_xO_y species, respectively (**Figure 5.17**e). Meanwhile, in the O 1s spectra, peaks at around 533.8, 532.2, 530.9 and 528.7 eV correspond to N_xO_y, Li_2CO_3, C-O and Li_2O, respectively (**Figure 5.17**g).[34] This SEI composition is well consistent with the results of C 1s and N 1s spectra (**Figure 5.19**).[220] Furthermore, the outer layer of the as-formed SEI is rich in Li_2O, Li_3N and LiN_xO_y while the inner layer mainly consists of Li_2CO_3 and organic species as schematically illustrated in as **Figure 5.17**c. Such an organic/inorganic hybrid SEI not only effectively suppresses HER, but also possesses high strength to maintain its structural integrity. Therefore, the SEI does not break upon cycling and does not expose unpassivated surfaces, thus suppressing the interfacial side reactions (*i.e.*, HER and OER).[172] The SEI constructed in 12.5 m $LiNO_3$ in H_2O: PD electrolyte (**Figure 5.20**) exhibited a similar composition compared with that in LWIS gel electrolyte. The inorganic species in SEI could be attributed to the trace of dissolved N_2, CO_2 and O_2 gases in PD diluent, since their solubilities in alcohols are much higher than those in water[221] and $LiNO_3$ cannot construct any robust decomposition product layer in aqueous media;[139] Meanwhile, the organic species in SEI may be related to the reduction of PD-involved solvation shell (see **Figure 5.5**b). For the Mo_6S_8 anode cycled in 12.5 m $LiNO_3$ in H_2O electrolyte, the Li 1s (**Figure 5.17**d) and O 1s (**Figure 5.17**f) XPS spectra displayed negligible peak intensities, confirming the SEI-free morphology on this anode. This is because the main SEI components (*e.g.* Li_2O, Li_3N, Li_2CO_3) would quickly dissolve or hydrolyse in the water media.[11] Therefore, these species can only stably exist as solid deposits on the anode surface in LWIS electrolytes with suppressed water reactivity in HER/OER. It should be noticed that recently researchers revealed that the SEI formed in aqueous electrolytes may be unstable during long cycling and storage for real-world battery application.[11, 202, 222] Developing electrolyte additives and/or anode surface coating would be an attractive approach to further improve the SEI stability in the future.

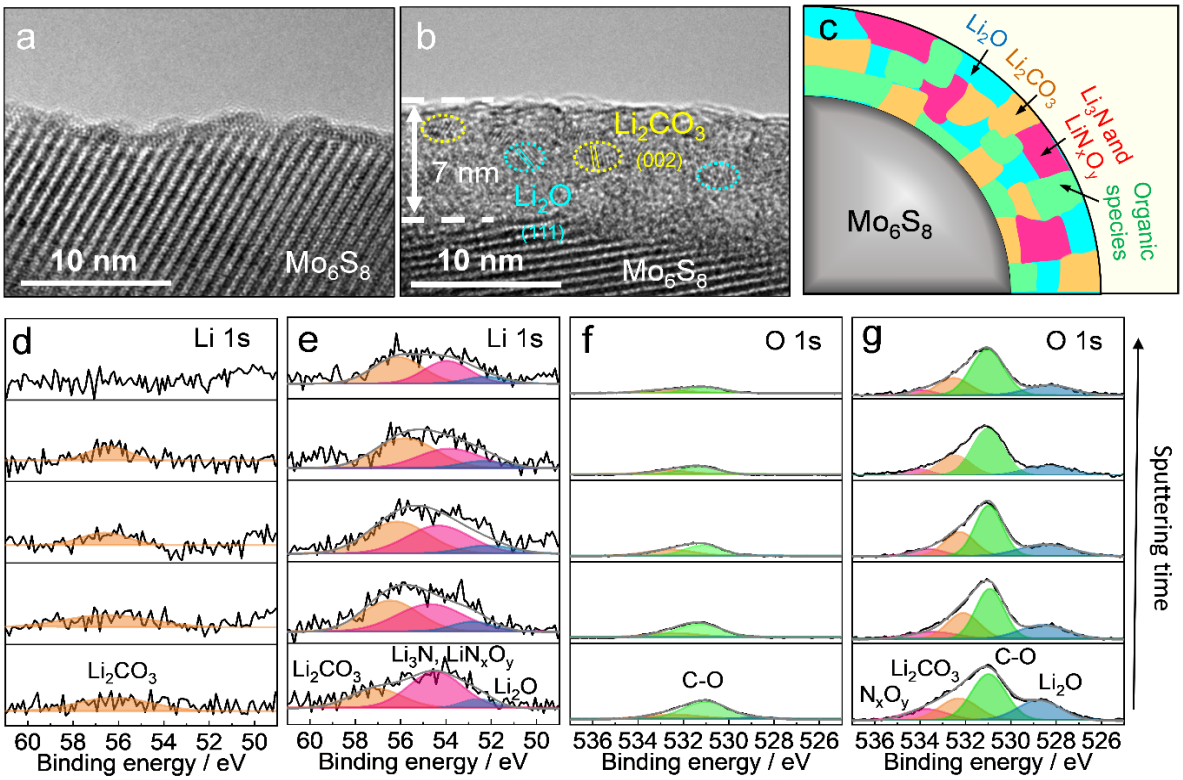

Figure 5.17. (**a, b**) TEM images of Mo_6S_8 anodes after 20 cycles in (**a**) 12.5 m $LiNO_3$ in H_2O and (**b**) LWIS gel electrolytes. (**c**) Schematic illustration of the SEI composition in the LWIS gel electrolyte. (**d, e**) Li 1s and (**f, g**) O 1s XPS spectra of Mo_6S_8 anode after 20 cycles in (**d, f**) 12.5 m $LiNO_3$ in H_2O and (**e, g**) LWIS gel electrolytes.

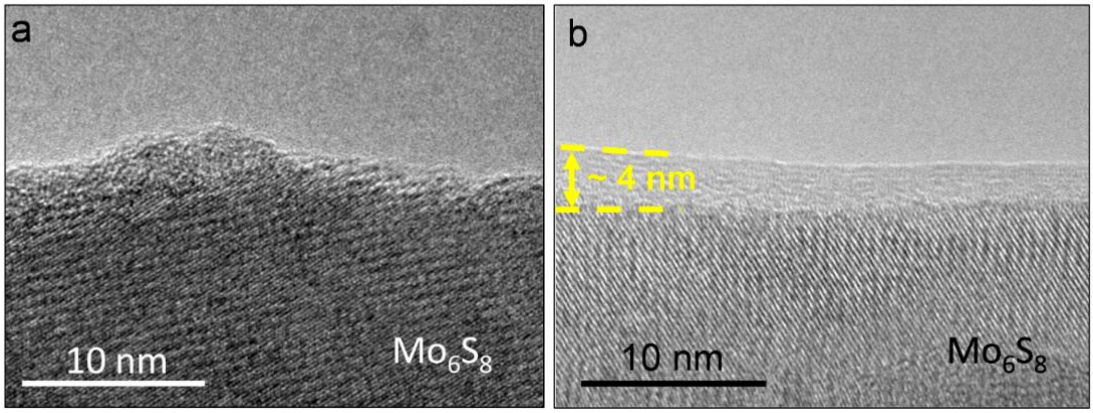

Figure 5.18. TEM images of Mo_6S_8 anode after 20 cycles in (**a**) 25 m $LiNO_3$ in H_2O and (**b**) 12.5 m $LiNO_3$ in H_2O: PD electrolytes.

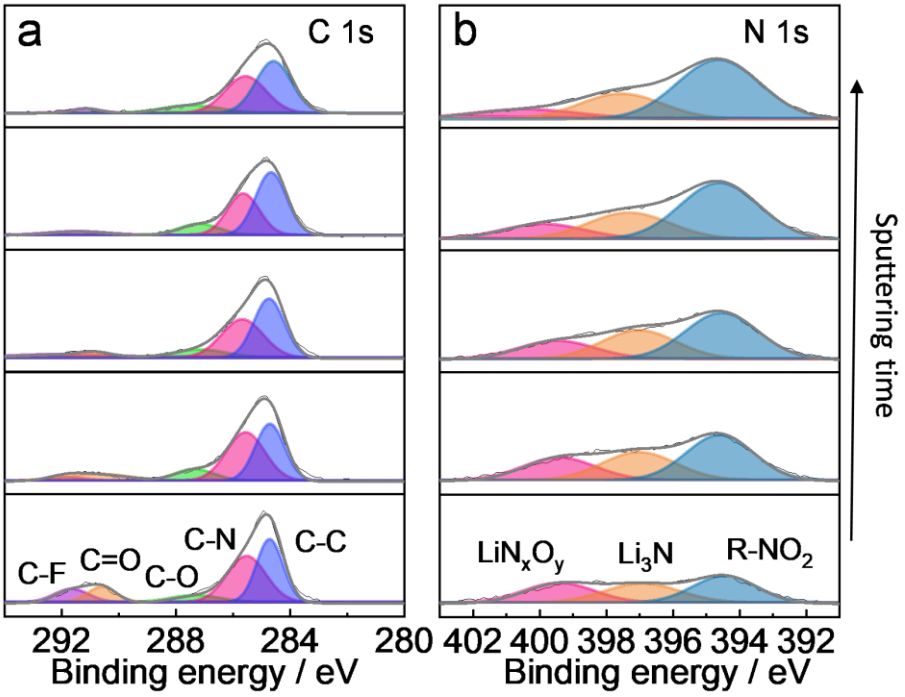

Figure 5.19. (**a**) C 1s and (**b**) N 1s XPS depth profiling spectra of a Mo_6S_8 anode after 20 cycles in LWIS gel electrolyte. C 1s spectrum: C-F: 291.8 eV; C=O: 290.5 eV; C-O 287 eV; C-N: 285.5 eV ; C-C: 284.5 eV,[14] N 1s spectrum: LiN_xO_y: 399 eV, Li_3N: 397 eV; R-NO_2: 394.5 eV.[34]

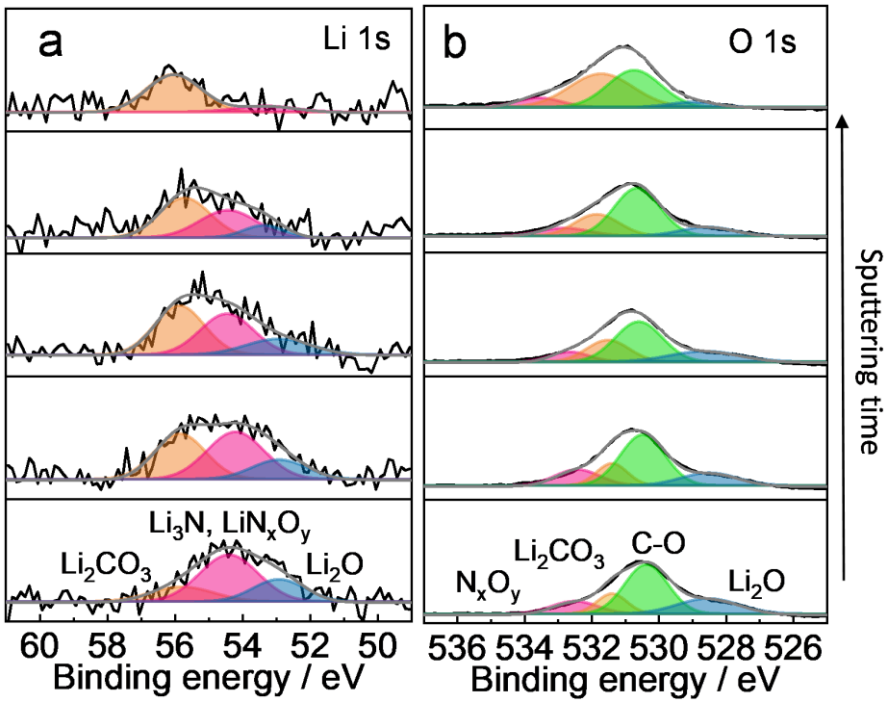

Figure 5.20. (**a**) Li 1s and (**b**) O 1s XPS depth profiling spectra of a Mo_6S_8 anode after 20 cycles in 12.5 m $LiNO_3$ in H_2O: PD electrolyte.

5.4 Conclusion

In summary, we reported a localized water-in-salt (LWIS) electrolyte with an electrochemical stability window of 2.9 V by using cheap inorganic $LiNO_3$ salt and 1,5-pentanediol (PD) diluent in aqueous electrolytes. The comprehensive characterizations and theoretical modelling reveal that the PD diluent not only creates a localized saturated solvation structure in the aqueous electrolyte, but also creates strong hydrogen-bonding interactions with water molecules and anions, thus significantly reducing the water reactivity in HER/OER. Furthermore, by *in-situ* gelling the electrolyte with TEGDA monomer to form a leak-free LWIS gel electrolyte, the electrochemical window was widened to 3.0 V due to further reduction of water reactivity in HER/OER and SEI formation, which is equivalent to that of the 21 m LiTFSI WIS aqueous electrolyte, but at much lower materials cost. The as-developed Mo_6S_8|LWIS gel electrolyte|LMO full cell delivered high cycling stability over 250 cycles with 98.53 % Coulombic efficiency at 1 C. The quasi-solid LWIS chemistry provides a new pathway for the development of cost-effective, safe and high-energy aqueous Li-ion batteries. Moreover, the design principles of the LWIS electrolytes can potentially be extended to a wide range of rechargeable alkali metal (*e.g.* sodium, potassium)-based and multivalent ion (*e.g.* zinc, magnesium)-based aqueous batteries for large-scale energy storage applications.

CHAPTER VI: Solvation Structure Design via Molecular Crowding Effect for High Voltage Zinc Batteries

6.1 Introduction

Li-ion batteries are largely dominating the portable energy storage market. However, their implementation for large-scale energy storage faces several challenges. Particularly, the safety concern due to the use of flammable organic electrolytes hinder their further development into reliable and sustainable battery systems.[48, 202] Accordingly, aqueous rechargeable batteries represent an attractive alternative, owing to their intrinsic safety, eco-friendliness, and inexpensive asset. For instance, rechargeable zinc-ion (Zn-ion) batteries have enticed extensive interest owing to the excellent compatibility of Zn metal with aqueous electrolytes. However, water-based electrolytes engender several shortcomings: (1) narrow electrochemical stability window (*i.e.*, 1.23 V), which is dictated by hydrogen evolution reaction (HER) and oxygen evolution reaction (OER); (2) corrosion reactions; and (3) dissolution of transition metal oxide in the aqueous electrolyte (*e.g.*, the dissolution of manganese (Mn) species from the widely used MnO_2 cathode material in Zn-ion batteries).[202, 223] Since the potential of the electrode couples must sit within the electrochemical stability window of the electrolyte, one major challenge to achieve high-voltage and high-energy-density Zn-based aqueous batteries resides in enlarging the electrochemical stability window of aqueous electrolytes.

For this purpose, various electrolyte design strategies have been investigated. In 2015, the pioneering work on "water-in-salt" electrolytes presented by Wang's group had spurred further research on aqueous systems.[130, 224] The "water-in-salt" electrolytes consist in introducing a large amount of metal salt into water. Increasing the salt to water ratio modifies the metal cation solvation structure due to the scarce availability of water molecules. The specific cation solvation structure, along with the restriction in the mobility of the water molecules, contributes to deferring the reduction and oxidation potential of water, thereby enlarging the electrochemical stability window of the electrolyte. This electrolyte design allowed the employment of high voltage cathode (*e.g.*, $LiMn_2O_4$ (LMO), $LiCoO_2$ (LCO), *etc.*) and limited side reactions (*e.g.*, water decomposition, metal transition dissolution, *etc.*). Inspired by this work, novel electrolyte formulations emerged simultaneously, including

hybrid aqueous electrolytes (*e.g.*, "water-in-bisalt" electrolyte [13, 134], "co-solvent-in-salt" electrolyte[150], *etc.*), "water-in-ionomer" electrolytes[140], localized highly concentrated aqueous electrolytes[20], and molecular crowding aqueous electrolytes[15].

Amongst these strategies, the solvation structure of molecular crowding electrolytes varies from other "water-in-salt" type electrolytes. Molecular crowding was first observed in biology. In living cells, the large amount of small hydrophilic molecules binds with water molecules, thereby restricting their mobility. Therefore, the intracellular water displays different properties than in a dilute environment.[137] Recently, Xie *et al.* adapted this approach to aqueous electrolytes for Li-ion batteries by employing low molecular weight poly(ethylene) glycol (PEG 400) as a molecular crowding agent. By introducing 96 wt% PEG in an aqueous 2 m LiTFSI electrolyte, the scarce water molecules were confined due to the abundant hydrogen bonds. As a comparison with "water-in-salt" electrolytes, adopting a molecular crowding strategy not only endows the aqueous electrolyte with a large electrochemical stability window but also reduces the cost, as a low concentration of metal salt is required.

Among different Zn-based batteries, Zn/Li hybrid aqueous batteries are particularly interesting as the coupling of a Zn metal anode with a lithium metal oxide cathode allows the battery to operate at a high working voltage without compromising safety. For instance, Li^+ intercalation LMO cathode operates at a much higher voltage than Zn^{2+} intercalation MnO_2 cathode in Zn/Li hybrid batteries. In the Zn||LMO hybrid battery, on the cathode side, Li^+ ions de-intercalate and intercalate from the LMO cathode during the charge and discharge processes. LMO cathode presents a high average working potential of ≈ 4.0 V *vs.* Li/Li^+, which can significantly increase the operating voltage of Zn/Li hybrid batteries. Optimising the electrolyte to ensure that LMO resides well-inside the electrochemical stability window of the aqueous electrolyte is necessary to avoid severe electrolysis of water molecules.[13, 130] Moreover, LMO cathode suffers from transition metal dissolution in the aqueous electrolyte, leading to severe capacity fading.[225] On the anode side, Zn^+ ions endure plating and stripping during the charge and discharge processes. Zn metal has long been regarded as an ideal metal anode for aqueous rechargeable batteries owing to its intrinsic safe operation in water as well as high specific capacity (819 mAh g^{-1}), high volumetric energy capacity (5850 mAh cm^{-3}), and low redox potential (-0.76 V *vs.* SHE). In addition, Zn is abundant in the earth's crust and

inexpensive.[126] However, Zn metal anode presents several weaknesses such as poor Zn plating/stripping reversibility, dendrite growth, corrosion and precipitation of zinc hydroxide ($Zn(OH)^{2-}$) species into non-conductive zinc oxide (ZnO) caused by the increase of local pH value due to HER.[224] Therefore, electrolyte optimisation is essential to develop high-voltage aqueous Zn/Li hybrid batteries.

We, herein, adopt a molecular crowding strategy by introducing N-methylformamide (NMF) into a hybrid Zn/Li aqueous electrolyte composed of 7.7 m lithium triflate (LiOTf), 1 m zinc triflate ($Zn(OTf)_2$) and water (the concentration is expressed in molality "m": mol $kg^{-1}_{solvent}$). The solvation structure of the molecular crowding electrolyte was experimentally and theoretically investigated to highlight the beneficial presence of NMF in the electrolyte. Not only NMF is found to be extremely stable against Zn metal anode, but also it reduces the water molecule movement by creating numerous hydrogen bonds.[226] The molecular crowding effect of NMF prevented HER and promoted the creation of a robust SEI, which in turn hampered dendrite growth on the Zn anode. Meanwhile, the dissolution of transition metal elements from the LMO cathode was also reduced (**Figure 6.1**). Furthermore, the as-synthesised electrolyte was less expensive compared to the highly concentrated electrolyte counterpart owing to the much smaller amount of LiOTf required. As a result, a Zn||LMO full cell successfully cycled for more than 400 cycles with a capacity retention of 82.3 % and an average high Coulombic efficiency of 99.6 % after 400 cycles. Finally, both anode and cathode were characterised with in-depth analysis such as *in-situ* XRD and XPS depth profiling informing on the electrochemical mechanism.

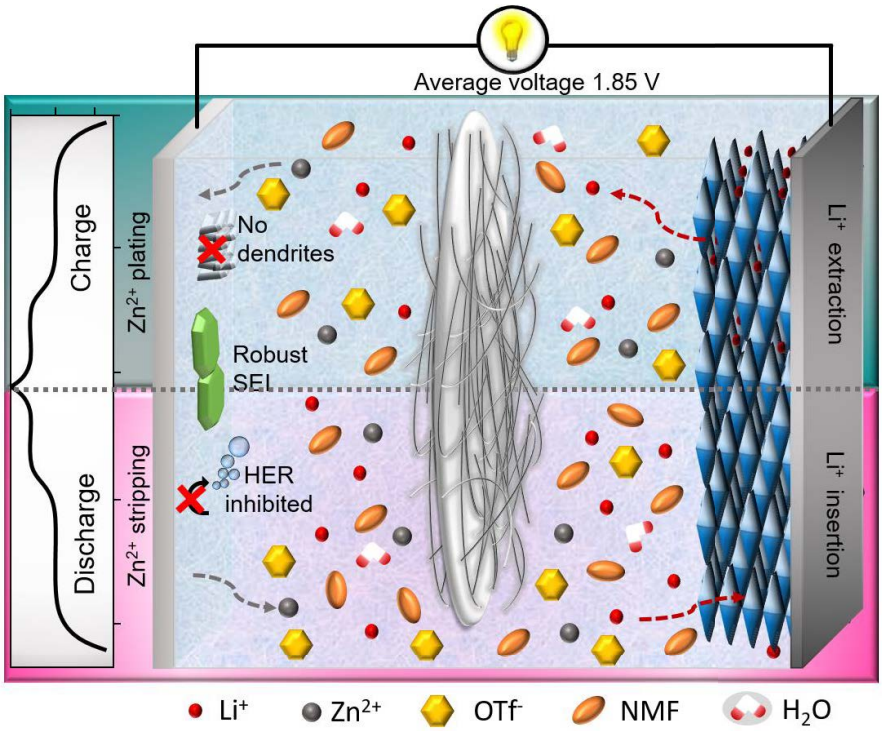

Figure 6.1. Schematic of the mechanism of Zn/Li hybrid battery during charge and discharge with 7.7 m LiOTf + 1 m $Zn(OTf)_2$ in H_2O: NMF molecular crowding electrolyte.

6.2 Experimental section

6.2.1 Electrolyte preparation.

Zinc trifluoromethanesulfonate ($Zn(OTf)_2$, 98%, Sigma Aldrich) and lithium trifluoromethanesulfonate (LiOTf, 99.995% trace metals basis, Sigma Aldrich) salts, and N-methylformamide (NMF, 99% Sigma Aldrich) solvent were used as received without further purification. The electrolytes were simply prepared by dissolving 1 m of $Zn(OTf)_2$ in water and then, adding a certain amount of LiOTf salt at 40 °C, where the unit "m" is molality (*i.e.*, mole of salts per kilo of solvent) and "M" correspond to molarity (*i.e.* mole of salts per litre of solvent).

6.2.2 Electrolyte characterizations

The pH of the electrolytes was measured with a FiveEasy Plus pH Meter FE28 (METTLER TOLEDO) at room temperature. The electrochemical stability window of the electrolytes was measured via linear sweep voltammetry (LSV) method using the VMP3 (Bio Logic Science Instruments) multichannel electrochemical station. In order to observe HER and OER

potential, the Zn species in the electrolyte were replaced by Li species, the anion mol number was conserved (*i.e.*, 1 m $Zn(OTf)_2$ was replaced with 2 m LiOTf). The testing cells were a three electrode system with a Pt wire as counter electrode, a Ti as working electrode and an Ag/AgCl as reference electrode. The voltage range was from the open circuit voltage (OCV) to 2.0 V vs. Ag/AgCl for the positive scan and from the OCV to -2.5 V vs. Ag/AgCl for the negative scan at the scan rate of 10 mV s^{-1}. A two electrodes system with Zn as counter and reference electrode and stainless-steel blocking electrode as working electrode was also employed to measure the Zn deposition potential. The voltage range was from the open circuit voltage (OCV) to 4.0 V *vs.* Zn/Zn^{2+} for the positive scan and from the OCV to -2.0 V *vs.* Zn/Zn^{2+} for the negative scan, and the scan rate was 10 mV s^{-1}. The ionic conductivity of the electrolytes was measured from 5 °C to 80 °C via electrochemical impedance spectroscopy (EIS) on the VMP3 electrochemical station from 100 kHz to 1 Hz with an alternating current amplitude of 5 mV. To ensure thermal equilibrium, the cells were kept at each testing temperature for at least 30 min before each EIS measurement. The Fourier transform infrared (FT-IR) spectra of the electrolytes were obtained with a Nicolet Magna 6700 spectrometer at room temperature. The Raman analyses were effectuated with a Renishaw Raman spectrometer system (Gloucestershire, UK). For the combustion test, 100 µL of electrolyte sample was dropped onto a glass fibre separator and exposed to a flame for 5 seconds. The weight losses of different electrolyte samples was measured by aging the samples at room temperature under atmospheric condition.

The static stability of the electrolyte toward Zn metal anode was qualitatively observed by introducing a piece of Zn metal into different electrolytes. After 49 days, FE-SEM images (Zeiss Supra 55VP) and XRD (Bruker D8 discover) measurement were effectuated.

6.2.3 Assembly and characterization of the aqueous full cells

Lithium manganese oxide ($LiMn_2O_4$, LMO) was purchase from Shanshan Co., Ltd. The cathodes were prepared by mixing the active material with carbon black and polyvinylidene fluoride (PVDF, Sigma Aldrich) binder with a mass ratio of 80: 10: 10 in anhydrous N-methyl-2-pyrrolidone (NMP, Sigma-Aldrich). The obtained slurry was coated onto a Ti foil current collector and dried in a vacuum oven overnight at 70 °C. The CVs of LMO electrodes were recorded in a two-electrode system with Zn as counter and reference electrode at 1 mV s^{-1}. The Zn||LMO aqueous full cells were assembled in coin cells with Zn foil as anode, LMO as

cathode with a mass loading of ≈2 mg cm^{-2}, and glass fibre (Whatman GF/A) as separator. The electrolyte: LMO ratio in each cell was set at ≈50 µL mg^{-1} uniformly. The electrochemical performances were recorded at 1 C for long cycling stability test and between 0.1 C to 5 C for rate performances based on the cathode mass (1 C = 148 mAh g^{-1}) between 1.0 and 2.1 V on a LAND 2001 A battery testing system at 30 °C. The corresponding EISs after 0, 15 and 100 cycles were recorded on the VMP3 electrochemical station in a frequency range of 10 mHz to 100 kHz with a disturbance amplitude of 5 mV. The Zn plating and stripping reversibility was investigated by galvanostatic cycling method. A symmetrical Zn||Zn coin cell was continually charged and discharged at 0.1 mA cm^{-2} with a cut-off capacity of 0.1 mAh cm^{-2}.

6.2.4 Material characterisations

Li insertion/disinsertion was observed with *in-situ* XRD analyses which were carried on a Bruker D8 discover diffractometer between 15° - 90° at room temperature. The electrodes were collected from the Zn||LMO cells after 5 and 25 cycles, washed with NMF and exposed to field emission scanning electron microscope imaging (FE-SEM, Zeiss Supra 55VP). Then, the surface composition of the electrodes (after 25 cycles) were investigated with XPS depth profiling analysis. The X-ray photoelectron spectroscopy (XPS) depth profiling spectra were obtained with a PHI 5000 VersaProbe II spectrometer using a monochromatic Al Kα X-ray source at 1486.6 eV. The amount of Mn ions dissolved in the electrolyte after cycling was determined by inductively coupled plasma mass spectroscopy (ICP-MS). The cells were disassembled after 25 cycles, and the Mn ions were eluted from the glass fibre separators via a sample digestion/extraction technique in a mix acid ($4HNO_3$-1HCl).

6.2.5 Numerical simulation

Molecular dynamics (MD) simulations were performed using NAMD.[167] The different electrolyte systems were set-up initially by using PACKMOL.[165] Periodic boxes of 20 Å were used. The properties of H_2O are assessed with SPC/E parameters. The force-fields parameters and partial charges of Zn^{2+}, Li^{+} and OTf^{-} were obtained from previous reports.[227] A Lennard–Jones (LJ) cut-off of 10 Å and a particle-particle particle-mesh solver for long-range Coulombic interactions were also employed. Velocity-Verlet algorithm was applied to integrate the equations of motion with a time step equalled to 0.5 fs. First, Langevin dynamics was performed at 500 K for 5 ns, and then NPT runs were performed at 298 K for 10 ns to ensure

that the equilibrium salt dissociation had been reached. Then, the NVT runs were 20 ns long at 298K. VMD was employed to visualise the last 1 ns trajectory which were used to obtain the structure of electrolyte.[168] The hydrogen bonds were calculated considering a distance cut-off of 3.5 Å and an angle cut-off of 30°.

6.3 Discussion

N-methylformamide (NMF) is an organic solvent which has been employed to synthesis solid-state electrolytes but, to the best of our knowledge, it hasn't be directly applied as electrolyte solvent nor additives in batteries.[228] NMF is miscible with water and have a suitable Li and Zn salts solvating capability. We selected Li and Zn salt based on OTf- anion owing to the capability of fluorinated anion to create robust SEI layer. As the solubility of Li salt is generally higher than that of Zn salt, the electrolytes were synthesised by introducing a maximal amount of Li salt into 1 m Zn salt solution. The solubility limit of LiOTf in several solvents containing 1 m $Zn(OTf)_2$ is displayed on **Figure 6.2**a. Although only 2.5 m of LiOTf can be dissolved at 25 ℃ in a solution of 1 m $Zn(OTf)_2$ in NMF (compared to 23 m at 25 ℃ in a solution of 1 m $Zn(OTf)_2$ in water), the mixture 1 m $Zn(OTf)_2$ in H_2O: NMF with a mass ratio of 1: 9 can dissolve 7.7 m LiOTf at room temperature. Therefore, a solution containing 7.7 m LiOTf + 1 m $Zn(OTf)_2$ in NMF crystallised (inset of **Figure 6.2**a, left picture) whereas the 7.7 m LiOTf + 1 m $Zn(OTf)_2$ in H_2O: NMF (7.7-H_2O: NMF) electrolyte remain liquid at room temperature (inset of **Figure 6.2**a, right picture). The presence of a small amount of water contributes to (1) increase the LiOTf solubility; (2) decrease the desolvation energy barrier which benefits smooth Zn plating[126]; and (3) provides non-flammability (**Figure 6.2**c). Meanwhile, the molecular crowding effect engendered by NMF molecules further promotes low volatility (**Figure 6.3**) and low cost. Furthermore, the 7.7-H_2O: NMF electrolyte is lighter than the analogue "water-in-salt" electrolyte (**Figure 6.2**b, inset). Therefore, for a similar battery assembly (*e.g.*, battery case, current collector, electrodes, separator and volume of electrolyte), the batteries with the crowding electrolyte will present a higher energy density.

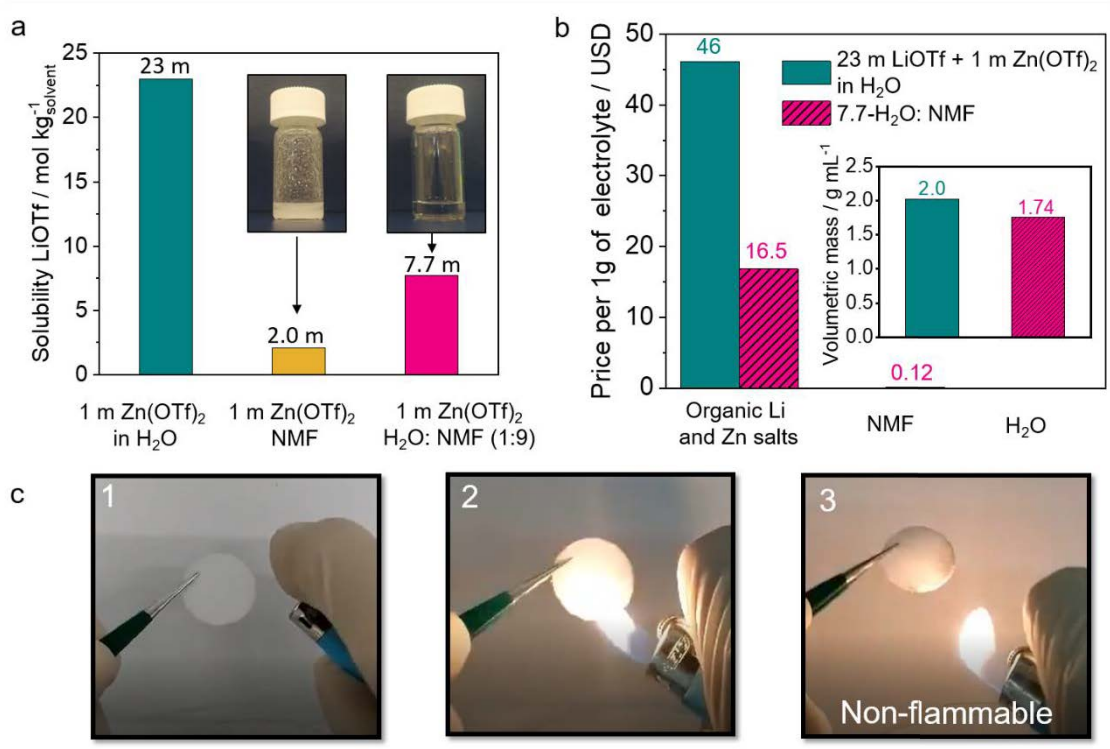

Figure 6.2. (**a**) Solubility limit of LiOTf in several solutions containing 1 m $Zn(OTf)_2$. Inset: Picture of 7.7 m LiOTf + 1 m $Zn(OTf)_2$ in NMF (left) and 7.7-H_2O: NMF (right). (**b**) Price comparison between the "water-in-salt" electrolyte (*i.e.*, 23 m LiOTf + 1 m $Zn(OTf)_2$ in H_2O) and the molecular crowding electrolyte (*i.e.*, 7.7-H_2O: NMF). Inset: Corresponding volumetric mass. (**c**) Flammability test of a glass fibre separator soaked with 7.7-H_2O: NMF electrolyte.

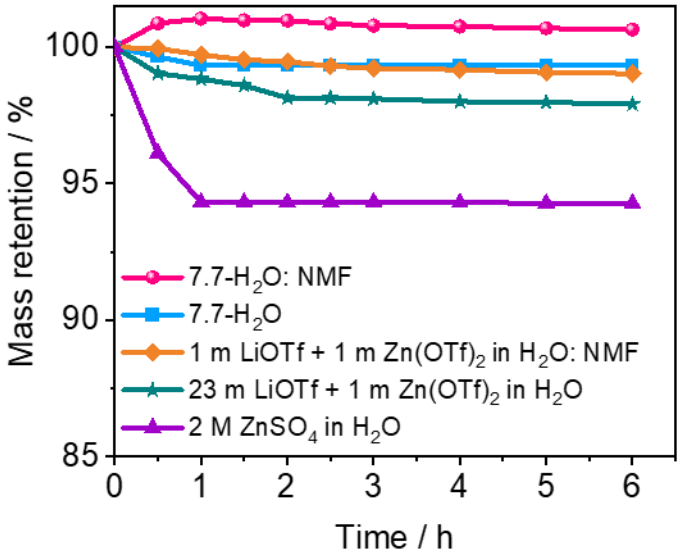

Figure 6.3. Mass loss of several electrolytes at room temperature and atmospheric conditions (7.7-H_2O electrolyte: 7.7 m LiOTf + 1 m $Zn(OTf)_2$ in H_2O).

6.3.1 N-methylformamide as molecular crowding agent

The evolution of the electrochemical stability window upon introduction of NMF in the electrolyte based on LiOTf only (*i.e.*, 9.7 m LiOTf in H_2O: NMF, mass ratio x: y) was investigated with linear sweep voltammetry (LSV) analysis (**Figure 6.4**a). In Zn-ion batteries, the Zn electroplating may partially conceal the decomposition of water molecules since both reactions occur at a similar potential. Therefore, to prevent Zn plating reaction during the LSV measurement, the amount of $Zn(OTf)_2$ in the electrolyte was equally replaced by LiOTf. The molecular crowding environment effectively delays the onset potentials of HER and OER. Besides, the introduction of NMF significantly reduces the plateau current from -1.01 mA cm^{-2} to -0.295 mA cm^{-2} after introducing NMF in the mass ratio H_2O: NMF (1: 9). (inset **Figure 6.4**a). When the mass percentage of NMF solvent in the electrolyte reaches 90 wt% (based on the total solvent mass), the HER is shifted to a lower potential (i.e., ≈-1.7 V vs. Ag/AgCl), meanwhile, the OER occurs at a higher potential (i.e., ≈1.55 V vs. Ag/AgCl) (**Figure 6.4**a). This phenomenon has been observed in electrolytes such as highly concentrated electrolytes, where the concentration of free water molecules is dramatically reduced, thereby modifying the cationic solvation shell.[130, 229] The electrochemical stability window of the electrolyte was enlarged to 3.25 V (*vs.* 2.35 V for the electrolyte without NMF), which is largely suitable for the application of high voltage cathode LMO. Furthermore, it is seen on **Figure 6.4**b that in the case of 7.7-H_2O electrolyte, the HER potential is ≈0 V vs. Zn/Zn^{2+} meanwhile the Zn plating potential is about -0.2 V vs. Zn/Zn^{2+}. Therefore, the Zn^{2+} reduction reaction competes with HER side reactions. As contrary, 7.7-H_2O: NMF electrolyte, the zinc deposition potential is much higher than that of HER.

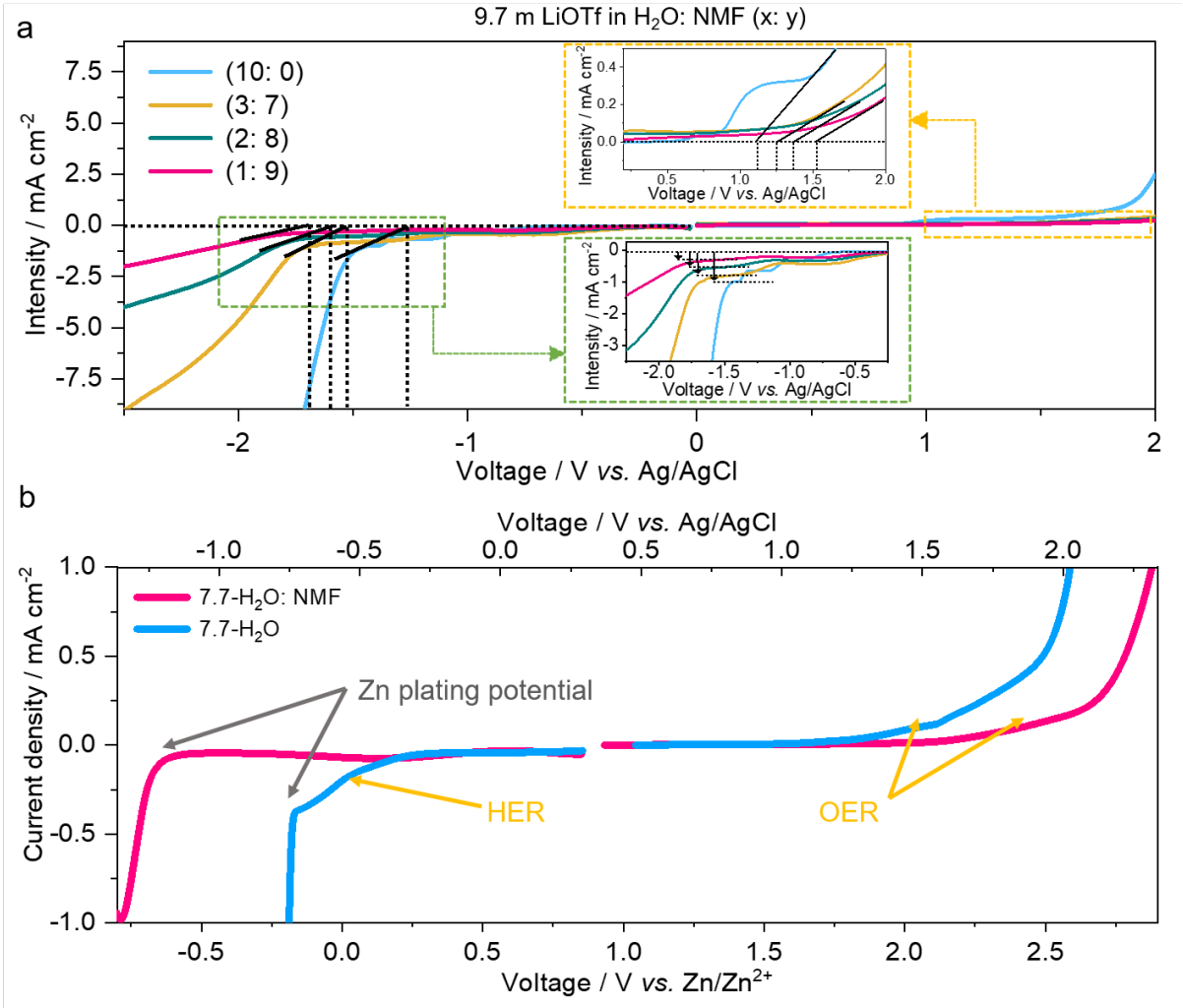

Figure 6.4. (**a**) Linear sweep voltammetry spectra of 9.7 m LiOTf in H_2O: NMF with various H_2O to NMF mass ratio (H_2O: NMF mass ratio = 10-0 to 1-9). To avoid Zn deposition, 1 m $Zn(OTf)_2$ was replaced by 2 m LiOTf. (**b**) Electrochemical stability window of 7.7-H_2O: NMF electrolyte and 7.7-H_2O electrolyte which evidenced the Zn potential deposition and water decomposition.

Raman spectroscopy and Fourier Transform Infra-Red (FTIR) spectroscopy were employed to illustrate the relation between the change in the solvation structure and NMF concentration. As seen on the Raman spectra, the intensity of the broad peak attributed to O-H stretching vibration mode of water molecules at 3000 – 3500 cm^{-1} considerably reduces and shifts to lower value when the concentration of NMF in the electrolyte increases. This change signifies the formation of NMF-H_2O complexes owing to the numerous hydrogen bonds formed between NMF and H_2O molecules (**Figure 6.5**a).[230] Accordingly, the FTIR spectra of the electrolytes confirms a decrease in the intensity of the characteristic peak of the H-O

stretching of water molecules (≈3500 cm^{-1}) when the concentration in NMF increases (**Figure 6.5**b). Interestingly, the peak corresponding to H-N stretching of NMF at ≈3300 cm^{-1} undergoes a shift toward lower wavelengths attesting that NMF molecules participate in hydrogen bonds with water molecules (**Figure 6.5**b). This is further verified on the additional bending peaks displayed on **Figure 6.5**c. Therefore, the addition of NMF solvent creates a molecular crowding environment, which contributes to improving the batteries' performances.

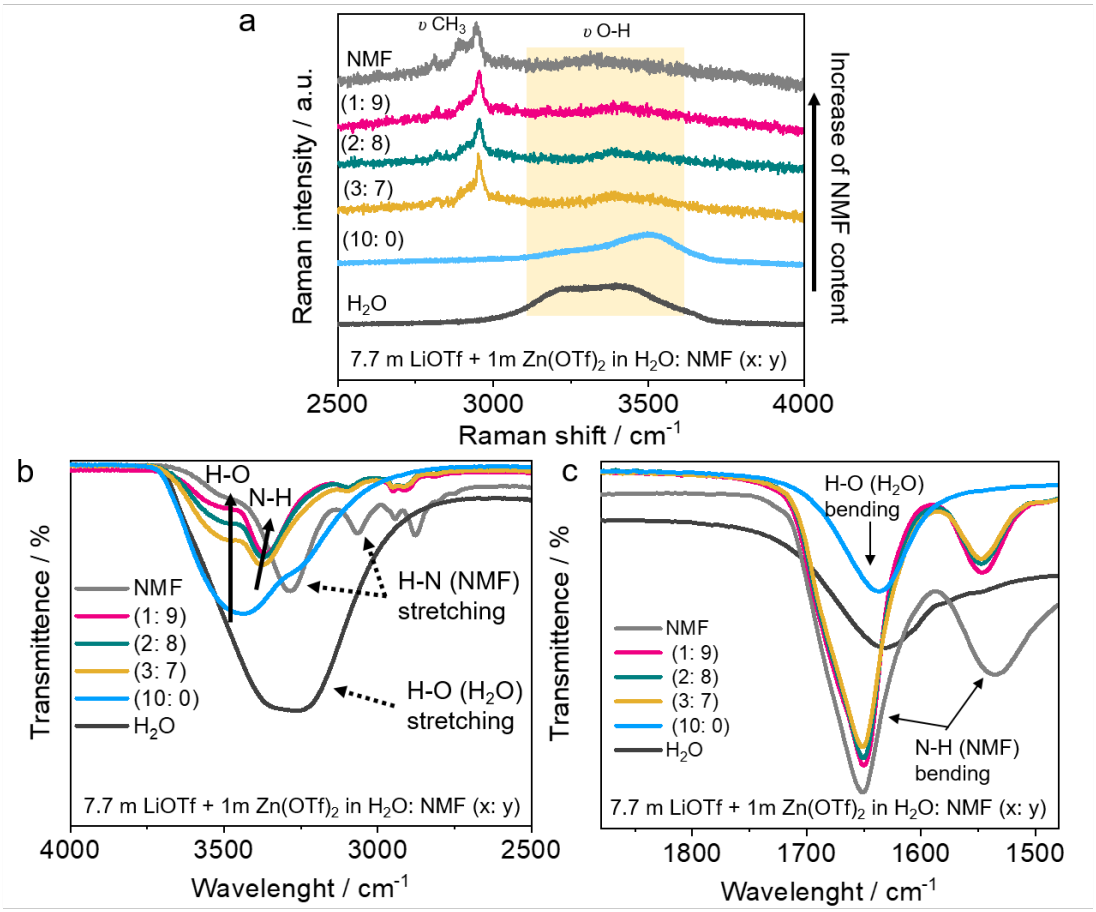

Figure 6.5. (**a**) Raman spectra and (**b-c**) FTIR spectra of the 7.7 m LiOTf + 1 m $Zn(OTf)_2$ in H_2O: NMF with various H_2O to NMF mass ratio (H_2O: NMF mass ratio of 10: 0 to 1: 9).

6.3.2 Solvation structure of the molecular crowding electrolyte

Molecular dynamic (MD) simulations were employed to theoretically investigate the solvation of Zn and Li ions in the electrolytes. **Figure 6.6**a displays the screenshots of the molecular arrangement in the electrolytes of 7.7-H_2O (left) and 7.7-H_2O: NMF (right) after 20 ns at 298

K. It is obvious that free water molecules are present in the electrolytes of 7.7-H_2O, whereas the water molecules in the electrolytes of 7.7-H_2O: NMF are surrounded and interact with NMF molecules, suggesting an efficient crowding effect of NMF.[15, 137] The addition of strong polar solvents in the aqueous electrolyte perturbs the solvation sheath of Zn^{2+} cations. The highly polar molecules can break the water clusters and preferentially solvate Zn^{2+}. Therefore, the introduction of NMF molecules totally changed both Li and Zn solvation sheaths as illustrated with the schematic evolution of the Zn^{2+} solvation sheath in **Figure 6.6**b. As shown by the radial distribution function (**Figure 6.6**c-d), $Zn(OTf)_2$ is preferentially coordinated to water molecules in the electrolytes of 7.7-H_2O ($Zn\text{-}O_{H2O}$ > $Zn\text{-}O_{OTF}$). However, in the electrolytes of 7.7-H_2O: NMF, Zn^{2+} cations are preferentially coordinated with OTf^- anions as less water molecules participate in the solvation sheath.[89] Similarly, OTf^- anions enter Li^+ solvation sheath, when NMF molecules are present in the electrolyte (**Figure 6.7**). Furthermore, NMF creates additional hydrogen bonds with water molecules, which further restrict their movements and contribute to expanding the electrochemical stability window of the 7.7-H_2O: NMF electrolyte (**Figure 6.6**e).[230b]

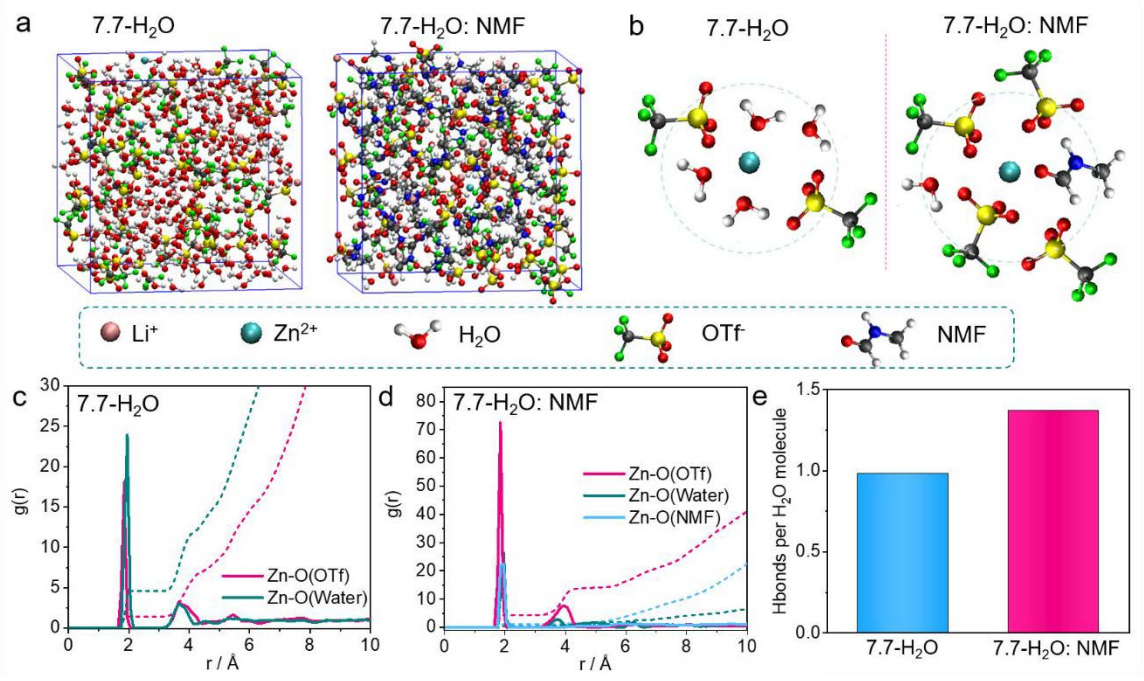

Figure 6.6. (**a**) Snapshots of the simulated cell with 7.7-H_2O (left) and 7.7-H_2O: NMF (right) after 20 ns at 298 K obtained with MD simulations. (**b**) Schematic representation of the solvation sheath of Zn cation in the corresponding electrolyte. The radial distribution function g(r) of Zn-O(OTf), Zn-O(H_2O) and Zn-O(NMF) pairs calculated from MD simulation trajectories

in (**c**) 7.7-H_2O and (**d**) 7.7-H_2O: NMF. (**e**) Number of hydrogen bonds formed in 7.7-H_2O and 7.7-H_2O: NMF systems at 20 ns.

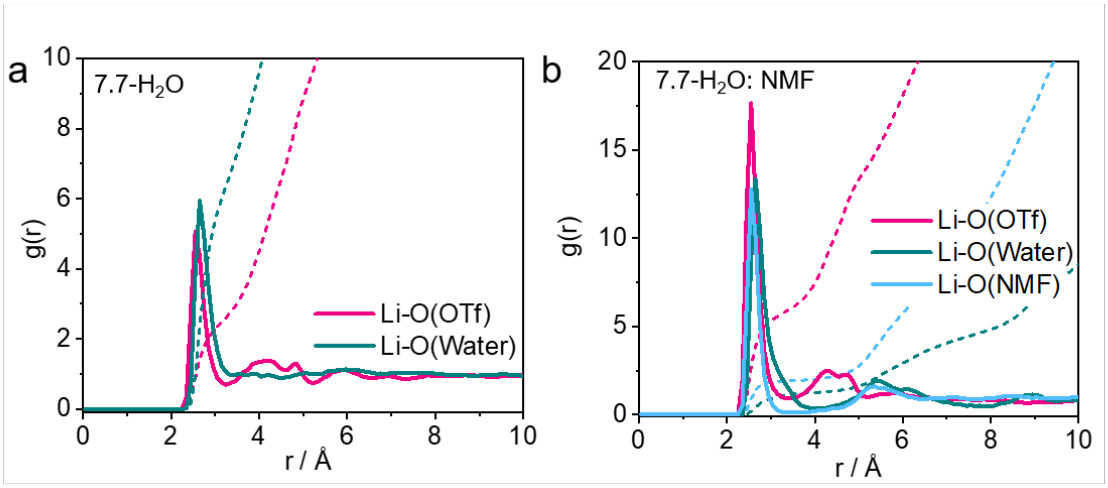

Figure 6.7. The radial distribution function g(r) of Li-O(OTf), Li-O(H_2O) and Li-O(NMF) pairs calculated from MD simulation trajectories in (**a**) 7.7-H_2O and (**b**) 7.7-H_2O: NMF.

6.3.3 Electrochemical performance of Zn||LMO full cells

The electrochemical performances of molecular crowding electrolytes were evaluated in Zn||LMO full cells between 1.0 V to 2.1 V. When the electrolytes of 7.7-H_2O was employed, the Zn||LMO cells exhibited a high specific capacity of 108 mAh g^{-1} during the first 50 cycles at 1 C (**Figure 6.8**a), owing to the higher ionic conductivity of the electrolyte (**Figure 6.9**). However, the specific capacity severely decreased after 60 cycles and dropped to only 10 mAh g^{-1} after 300 cycles (**Figure 6.8**a). As shown in the charge-discharge voltage profiles (**Figure 6.8**b), the cells with 7.7-H_2O electrolyte started decomposing at 2.06 V mostly due to OER, causing the drying of the cell and the decline in cycling performance.[231] In sharp contrast, upon introduction of NMF in the electrolyte, the cells with 7.7-H_2O: NMF electrolyte still delivered a capacity of 82 mAh g^{-1} after 400 cycles with a high Coulombic efficiency of 99.7 %, attesting of the excellent cycling stability. Additionally, the cells demonstrated no electrolyte decomposition even at a low current density of 0.1 C (**Figure 6.8**c). The rate performances of Zn||LMO cells with 7.7-H_2O electrolyte (blue line) and 7.7-H_2O: NMF (pink line) are shown on **Figure 6.8**d. A cut-off time was set equal to the theoretical charging time to prevent continuous water decomposition in the 7.7-H_2O electrolyte (*e.g.*, cut-off time = 10 h when the current density is 0.1 C; 5 h when the current density 0.2 C, *etc.*). Both cells successfully cycled for 10 cycles at 0.1 C delivering a specific capacity of about 110 mAh g^{-1}. However, it is obvious

that the cell with 7.7-H_2O electrolyte suffered from substantial side reactions as demonstrated by the low Coulombic efficiency of 70 % (*vs.* 96 % for the cell with 7.7-H_2O: NMF at 0.1 C). As the cycling rate was increased, the specific capacity obtained from the cells containing 7.7-H_2O electrolyte dropped sharply to almost 0 mAh g^{-1} at 1 C. This is a consequence of the severe electrolyte decomposition at low cycling rate, which dried the cell quickly and therefore degraded its cycling performance at higher rate.[232] As a comparison, the 7.7-H_2O: NMF electrolyte enabled the cells to deliver a stable specific capacity of 105 mAh g^{-1}, 101 mAh g^{-1}, 89 mAh g^{-1}, 61 mAh g^{-1} and 29 mAh g^{-1} at 0.2 C, 0.5 C, 1 C, 2 C and 5 C, respectively, with high Coulombic efficiencies close to 100 %. When the current density was returned to 0.2 C, the capacity retention of the Zn|7.7-H_2O: NMF|LMO cells reached 99.2 % of the specific capacity at 0.2 C (obtained in cycle 12). Furthermore, the Zn||LMO cell impedance was measured with EIS analysis before cycling, after 15 cycles and after 100 cycles (**Figure 6.10**). The EIS spectra were simulated via an equivalent circuit (inset **Figure 6.8**e) and the simulation results are organised in **Figure 6.8**e and **Table 6.1**. With the 7.7-H_2O electrolyte (**Figure 6.8**e, blue), the solid electrolyte interface resistance (R_f) sharply decreased between 0 and 15 cycles from 40979 to 678 Ω and then increased to 1881 Ω after 100 cycles, meanwhile the charge transfer resistance (R_{ct}) slightly decreased between 0 and 15 cycles from 1542 to 1258 Ω, and remarkably rose to 29 305 Ω after 100 cycles (**Table 6.1**). This phenomenon can be interpreted as an improvement in the interfacial contact reducing the cell impedance in the first cycles followed by a decline of the electrolyte amount in the cells due to its endless decomposition at the electrodes, thereby leading to the drying of the cell, which increased the internal resistance. For comparison, after adding NMF agent into the electrolyte (**Figure 6.8**e, pink), the values of R_f and R_{ct} continuously decreased from 9 891 to 1 208 (0 to 15 cycles), and to 443 Ω after 100 cycles, and from 11 087, to 6961 (0 to 15 cycles), and to 296 Ω after 100 cycles, respectively. The much smaller and sharply decreasing R_f in the first 15 cycles attests of the formation of a stable SEI while the steady diminishing R_{ct} value confirms the stability of the electrolyte.[233]

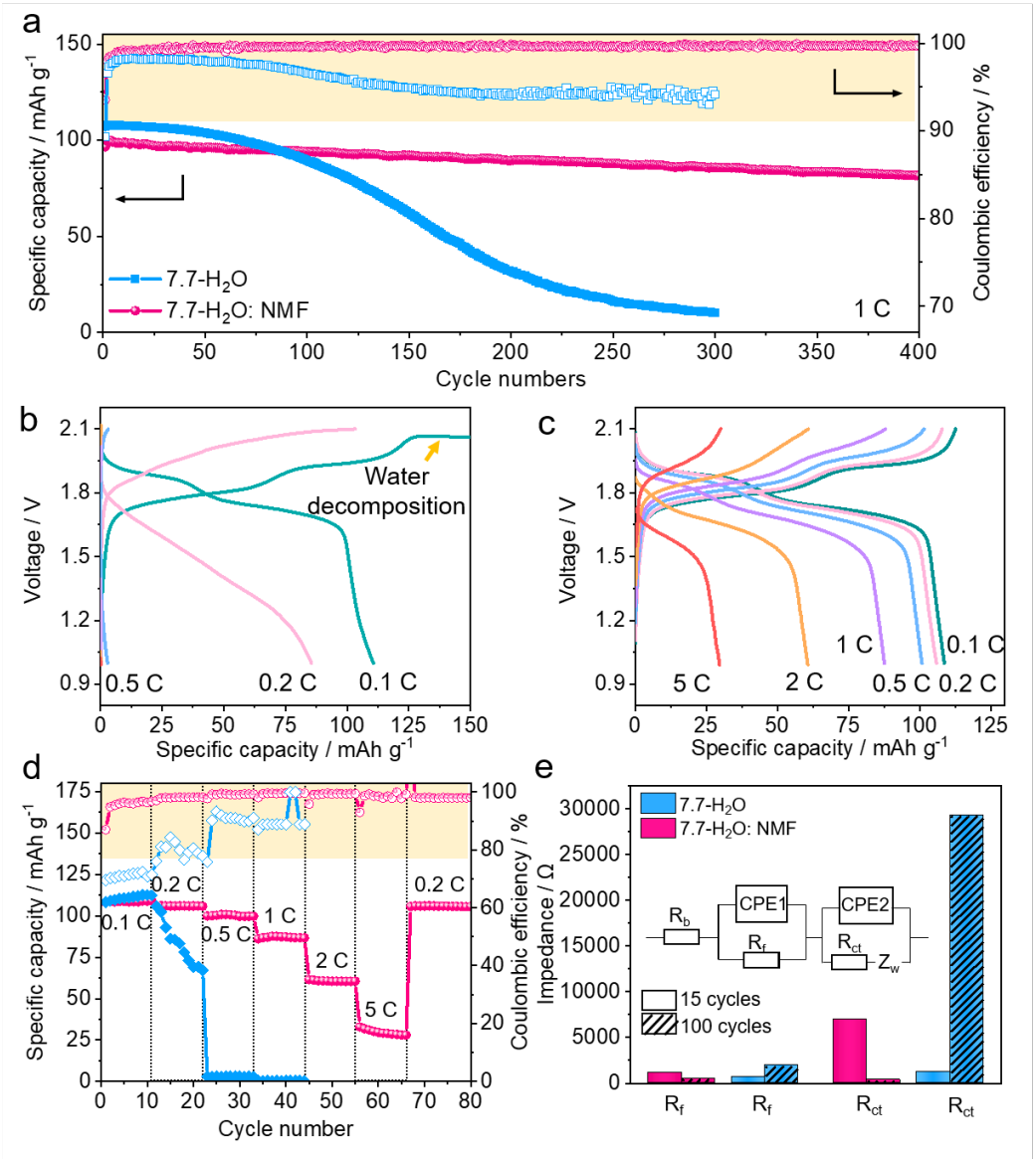

Figure 6.8. (**a**) Cycling performance of Zn||LMO full cells with 7.7-H_2O (blue line) and 7.7-H_2O: NMF (pink line) electrolytes at 1 C. Charge and discharge curves of (**b**) Zn| 7.7-H_2O| LMO batteries and (**c**) Zn| 7.7-H_2O: NMF|LMO batteries at various rate from 0.1 C to 5 C and, (**d**) corresponding rate performance of Zn||LMO full cells with 7.7-H_2O (blue line) and 7.7-H_2O: NMF (pink line) electrolytes. (**e**) The evolution of interfacial resistance of Zn||LMO batteries with 7.7-H_2O (blue) and 7.7-H_2O: NMF (pink) electrolytes at 15 and 100 cycles.

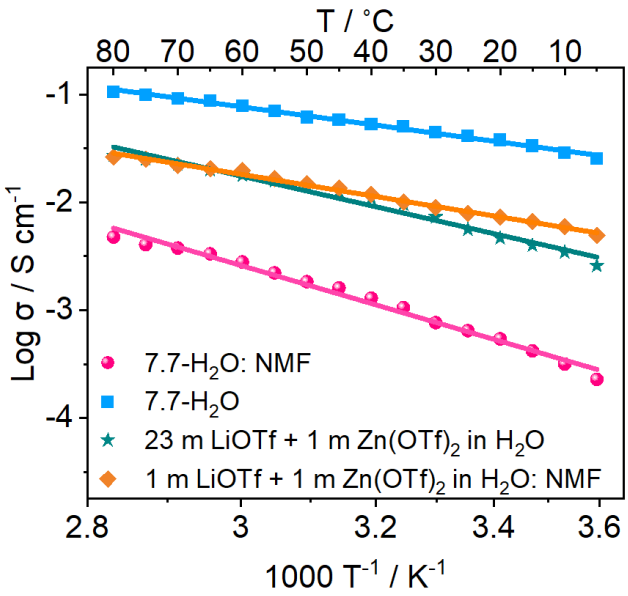

Figure 6.9. Ionic conductivity of various electrolytes. The experimental data is represented by the dots while the lines represent the Arrhenius fitting values.

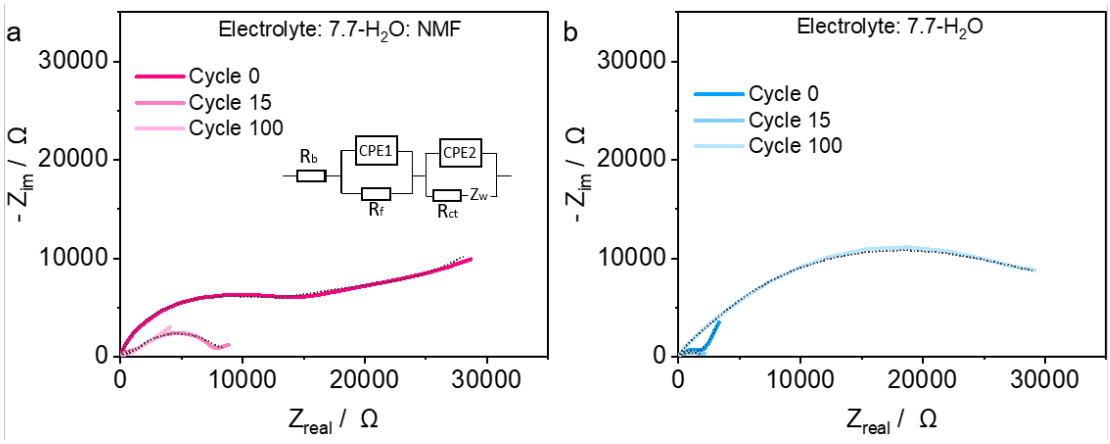

Figure 6.10. EIS spectra of the Zn||LMO cells with (**a**) 7.7-H_2O: NMF and (**b**) 7.7-H_2O electrolytes after 0, 15 and 100 cycles. The equivalent circuit is represented in the inset of **Figure 6.11**a. The dash lines represent the fitting values.

Table 6.1: The EIS simulation results of the Li||LMO cells in the two electrolyte samples.

	R_b (Ω)			R_f (Ω)			R_{ct} (Ω)		
Cycles	**0**	**15**	**100**	**0**	**15**	**100**	**0**	**15**	**100**
7.7-H_2O	1.336 ±0.009	3.614 ±0.013	3.473 ±0.011	41130 ±0.012	661.4 ±0.022	1899 ±0.016	1575 ±0.063	1217 ±0.022	29279 ±0.025
7.7-H_2O: NMF	31.47 ±0.012	0.973 ±0.016	10.43 ±0.013	9860 ±0.013	1146 ±0.021	502 ±0.015	11141 ±0.032	6975 ±0.027	337.4 ±0.018

To further demonstrate the advantages of molecular crowding electrolytes, the electrochemical performances of two different electrolytes were investigated: (1) the "water-in-salt" analogue electrolyte (*i.e.*, 23 m LiOTf + 1 m $Zn(OTf)_2$ in H_2O) where NMF molecules are absent; and (2) the dilute electrolyte (1 m LiOTf + 1 m $Zn(OTf)_2$ in H_2O: NMF) in which the concentration of LiOTf is reduced to 1 m, while the mass ratio of H_2O: NMF is kept equal to 1: 9. Although both Zn||LMO cells showed higher Coulombic efficiencies than that with 7.7 m LiOTf + 1 m $Zn(OTf)_2$ in H_2O electrolyte, the battery discharge capacity fades significantly (**Figures 6.11 and 6.12**). The poorer cycling performance are due to degradation of the electrolyte at high voltage due to the narrow electrochemical stability window of these electrolytes, and poor reversibility of the Zn plating and stripping caused by more free water molecules in the electrolyte. This observation suggests that the synergic contribution of relatively high LiOTf salt concentrations and NMF molecular crowding agents are essential to obtain optimal electrochemical performances.

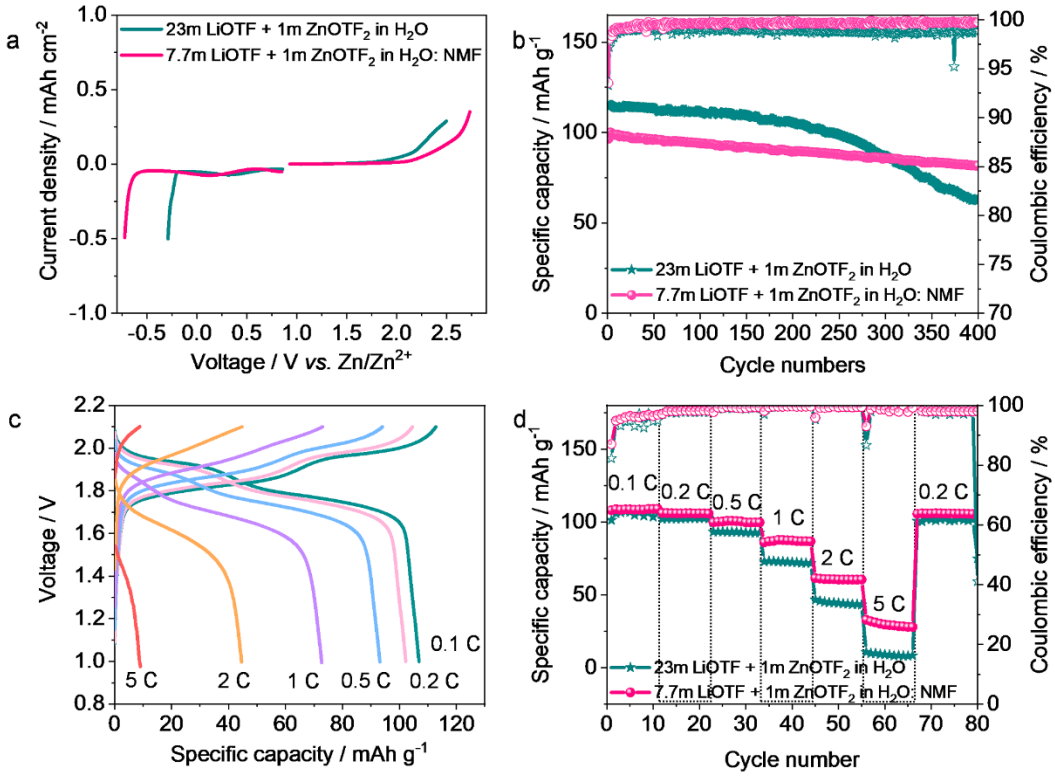

Figure 6.11. Electrochemical performance of the Zn||LMO cells with 23 m LiOTf + 1 m $Zn(OTf)_2$ in H_2O. (**a**) Electrochemical stability window of the 23 m LiOTf + 1 m $Zn(OTf)_2$ in H_2O and 7.7 m LiOTf + 1 m $Zn(OTf)_2$ in H_2O: NMF. (**b**) Long cycling performance of Zn||LMO batteries with 23 m LiOTf + 1 m $Zn(OTf)_2$ in H_2O and 7.7 m LiOTf + 1 m $Zn(OTf)_2$ in H_2O: NMF

electrolytes. (**c**) Charge-discharge profile of Zn||LMO batteries with 23 m LiOTf + 1 m $Zn(OTf)_2$ in H_2O electrolyte at different rate (0.1 C to 5 C). (**d**) Corresponding rate performances of Zn||LMO batteries with 23 m LiOTf + 1 m $Zn(OTf)_2$ in H_2O and 7.7 m LiOTf + 1 m $Zn(OTf)_2$ in H_2O: NMF electrolytes.

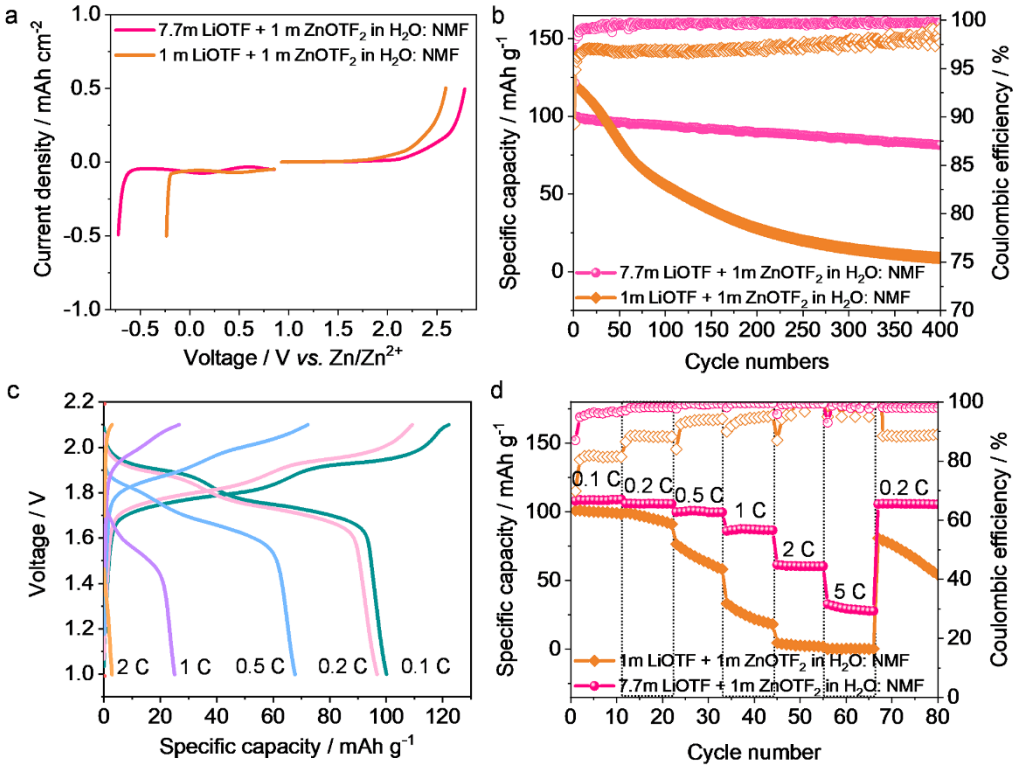

Figure 6.12. Electrochemical performance of the Zn||LMO cells with 1m LiOTf + 1 m $Zn(OTf)_2$ in H_2O: NMF. (**a**) Electrochemical stability window of the 1 m LiOTf + 1 m $Zn(OTf)_2$ in H_2O: NMF and 7.7 m LiOTf + 1 m $Zn(OTf)_2$ in H_2O: NMF. (**b**) Long cycling performance of Zn||LMO batteries with 1 m LiOTf + 1 m $Zn(OTf)_2$ in H_2O: NMF and 7.7 m LiOTf + 1 m $Zn(OTf)_2$ in H_2O: NMF electrolytes. (**c**) Charge-discharge profile of Zn||LMO batteries with 1 m LiOTf + 1 m $Zn(OTf)_2$ in H_2O: NMF electrolyte at different rate (0.1 C to 5 C). (**d**) Corresponding rate performances of Zn||LMO batteries with 1 m LiOTf + 1 m $Zn(OTf)_2$ in H_2O: NMF and 7.7 m LiOTf + 1 m $Zn(OTf)_2$ in H_2O: NMF electrolytes.

6.3.4 Characterization of zinc anodes

The compatibility of Zn anodes with different aqueous electrolytes was observed by field-emission scanning electron microscope (FE-SEM). Zn metal foils were submerged in 7.7-H_2O and 7.7-H_2O: NMF electrolytes, and in H_2O and NMF pure solvents for several days (**Figure 6.13**). After only 7 days, it is observed that H_2O rapidly corroded Zn metal and after 49 days,

the Zn metal was totally degraded with holes and protuberant white deposit. In contrast, the Zn metal in NMF remained mostly non-corroded. The Zn anode placed into 7.7-H_2O electrolyte exhibited, after 7 days, a white grey deposition on its surface, while after 49 days the white grey side product covered most of the Zn metal, attesting to the presence of free water molecules in the electrolyte, thus corroding Zn metal. In sharp contrast, the Zn metal in the molecular crowded electrolyte remained smooth and shiny even after 49 days. Furthermore, the surface morphologies of the Zn metal samples were observed by FE-SEM. The Zn metal, which remained 49 days in pure H_2O displayed crystalline spear-shaped morphologies. Although less obvious, similar morphologies were observed on the Zn sample that was submerged in 7.7-H_2O. As contrary, the Zn metal pieces, which were submerged in pure NMF solvent and 7.7-H_2O: NMF electrolyte exhibited smoother surface. As verified with XRD (**Figure 6.14**), the white crystalline deposit corresponds to zinc hydroxide zinc oxide (ZnO), as side product of the decomposition of water on Zn metal due to the more alkaline nature of these two solutions (**Figure 6.15**). Therefore, the corrosion of Zn anode in 7.7-H_2O: NMF electrolyte can be alleviated, owing to the scarcity of free water molecules in the electrolyte and the high stability of Zn in NMF solvent.[234]

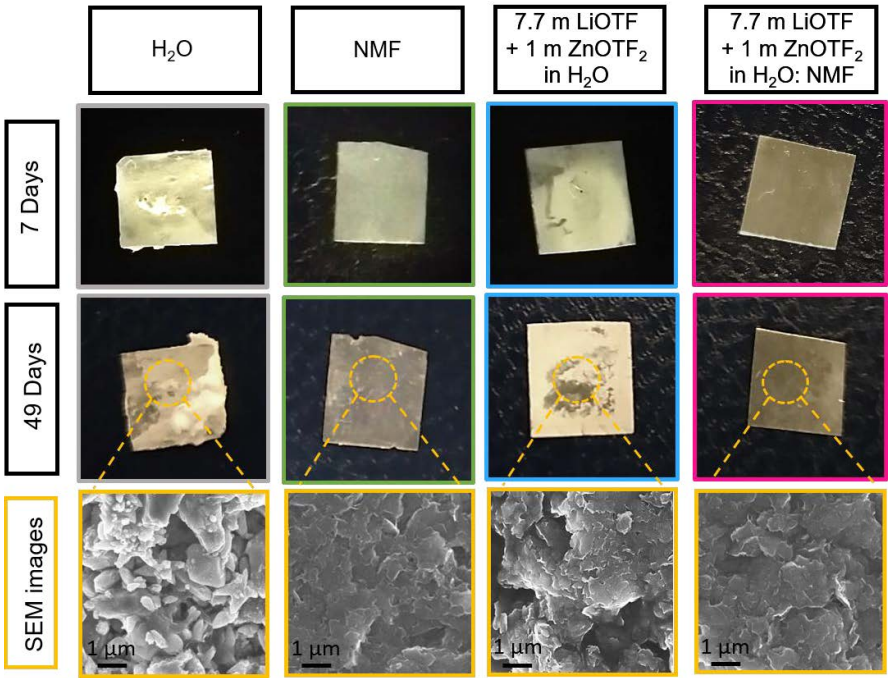

Figure 6.13. Static stability of zinc metal anode in pure H_2O (grey), pure NMF (green), 7.7-H_2O (blue) and 7.7-H_2O: NMF (pink) and the corresponding FE-SEM images.

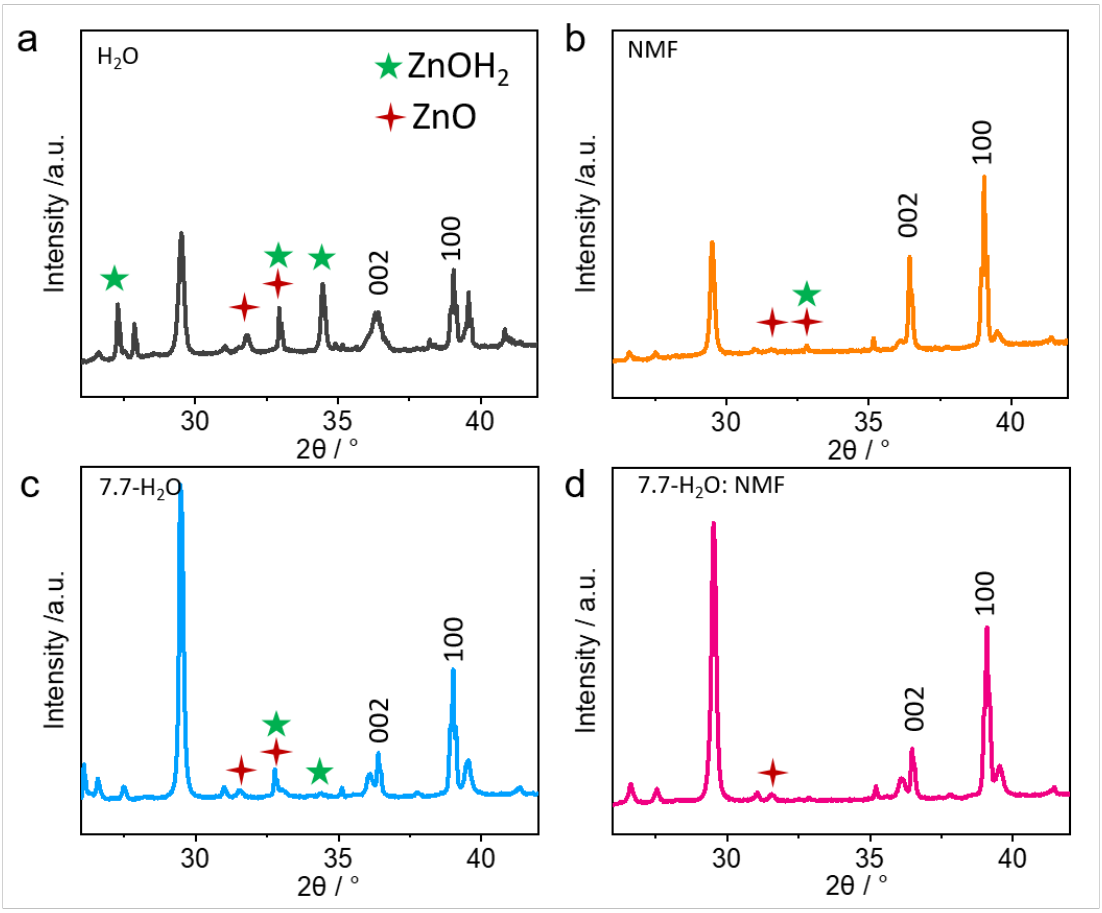

Figure 6.14. XRD profiles of the Zn metal after 49 days submerged in static stability of zinc metal anode in (a) pure H_2O, (b) pure NMF, (c) 7.7-H_2O and (d) 7.7-H_2O: NMF.

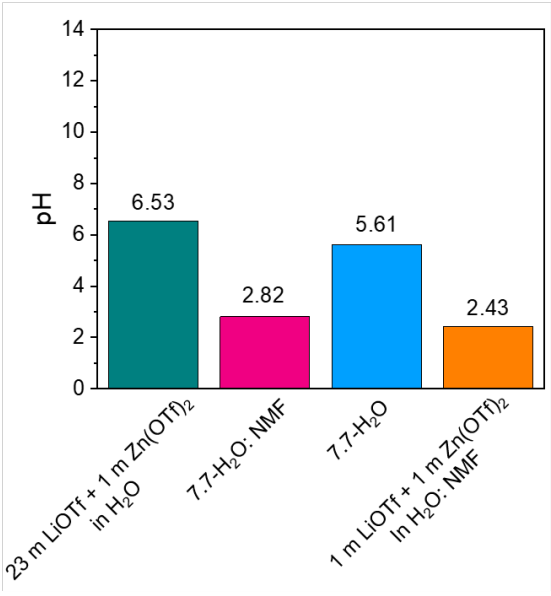

Figure 6.15. pH value of different electrolytes.

To investigate the plating and stripping efficiency of Zn anode in the 7.7-H_2O: NMF electrolyte, Zn||Zn symmetric cells were assembled with 7.7 m LiOTf + 1 m $Zn(OTf)_2$ in H_2O: NMF electrolyte. The symmetric cells successfully operated during more than 150 h at 0.1 mA cm^{-2} current density without short-circuiting (**Figure 6.16**). The insert of **Figure 6.16** displays a zoom-in of the plating and stripping process profile after 142 h, which remain steady attesting of the even Zn plating and stripping on the anode.[235] At different current densities ranging from 0.1 mA cm-2 to 2 mA cm-2, with a cut-off capacity of 0.1 mAh cm^{-2} to 2 mAh cm^{-2}, the overpotential remained constant for each current density, attesting of the reversible Zn plating and stripping (**Figure 6.17**). In the other hand, the oxidation and reduction peak obtained on the cyclic voltammetry (CV) spectrum demonstrated effective plating and stripping processes when 7.7 m LiOTf + 1 m $Zn(OTf)_2$ in H_2O: NMF was employed (**Figure 6.18**).

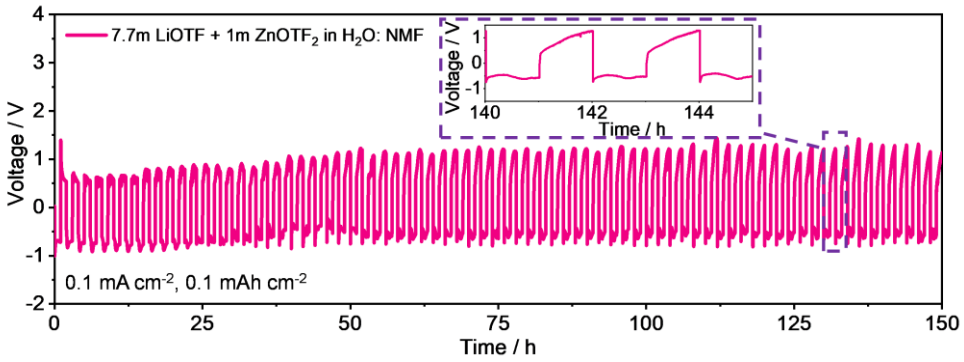

Figure 6.16. Symmetric Zn||Zn cell cycled with 7.7 m LiOTf + 1 m $Zn(OTf)_2$ in H_2O: NMF (1: 9). Inset: Zoom-in of the voltage profile after 140 h.

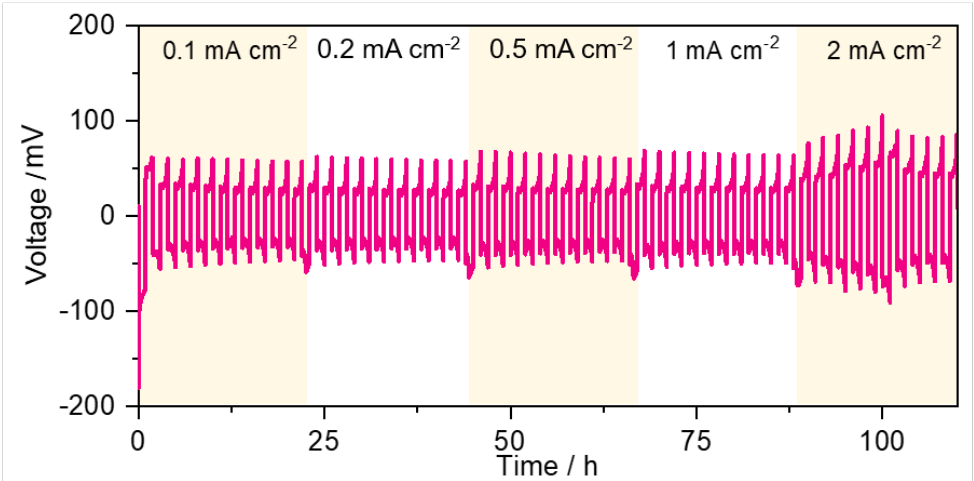

Figure 6.17. Voltage profile of Zn||Zn symmetric cells with the 7.7-H_2O: NMF electrolyte at different current density.

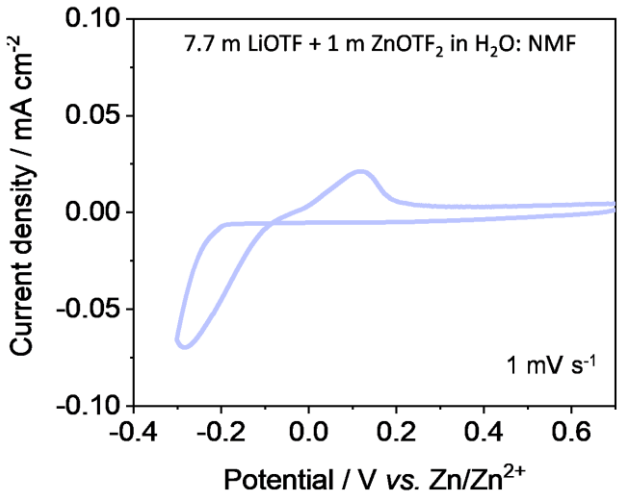

Figure 6.18. CV of the Zn||LMO cell with 7.7-H_2O: NMF.

The cycled Zn anodes were retrieved from Zn||LMO full cells after 5 and 25 cycles and were analysed by FE-SEM. The Zn deposition morphology when 7.7-H_2O electrolyte was employed presented sharp dendrites, already noticeable after 5 cycles (**Figure 6.19**a-c). As comparison, the Zn deposition on the Zn metal that had cycled in 7.7-H_2O: NMF demonstrated a smooth deposition without apparent dendrite growth (**Figure 6.19**b-d). The molecular crowding effect of NMF molecules induces a reduction in the Zn desolvation energy, thereby inhibiting dendrites growth.[126] Additionally, the Zn electrode retrieved after 25 cycles in 7.7-H_2O indicated the presence of ZnO by-products even after 90 s etching as confirm by the XPS depth profiling Zn 2p spectra with the large ZnO peak appearing at ≈1022.3 eV (**Figure 6.20**a). On the contrary, only an extremely small amount of ZnO species were apparent on the surface of Zn anode when cycled in 7.7-H_2O: NMF electrolyte (**Figure 6.20**b). The formation of ZnO suggests that H_2O molecules decomposed during cycling, thereby causing a local increase of the pH near the anode which triggered the formation of ZnO species.[234a, 236] The SEI formation is readily affected by H_2 evolution at the Zn metal surface. The absence of Zn oxide species on the Zn metal surface when NMF is present in the electrolyte indicate the suppression of HER, and therefore facilitate the formation of the SEI. Furthermore, F 1s, S 2p and C 1s XPS depth profiling spectra corresponding to the Zn anode in 7.7-H_2O mostly displayed species of organic nature (**Figure 6.20**a). As comparison, when the anode has cycled in 7.7-H_2O: NMF electrolyte (**Figure 6.20**b), an SEI layer composed of organic species and inorganic (*e.g.*, ZnF_2 and ZnS) is formed on the surface with the inorganic species mainly in the inner part and the inorganic species in the outer part of the SEI (*i.e.*, C 1s spectra: Zn-

$(C_2H_5)_2$, C-C, C-N, C-O, C=O at 283.4[237], 284.8[151], 286.2[152], 286.1[238], 287.8[151] eV, respectively; F 1s spectra: ZnF_2 and -CF_3 at 684.5 and 688.1 eV[238], respectively; S 2p spectra: ZnS and –SO_3 at 162.4 and 168.1[151] eV, respectively. According to the XPS analyses, a SEI is formed on the Zn anode during the first cycles. The SEI products cannot redissolve in the electrolyte due to the scarcity of available of free water molecules. Although the SEI formation mechanism in Zn battery systems remains partially un-understood, several electrolytes demonstrated similar SEI formation on Zn anode.[152, 239] Further investigation is needed to confirm the SEI formation mechanism.

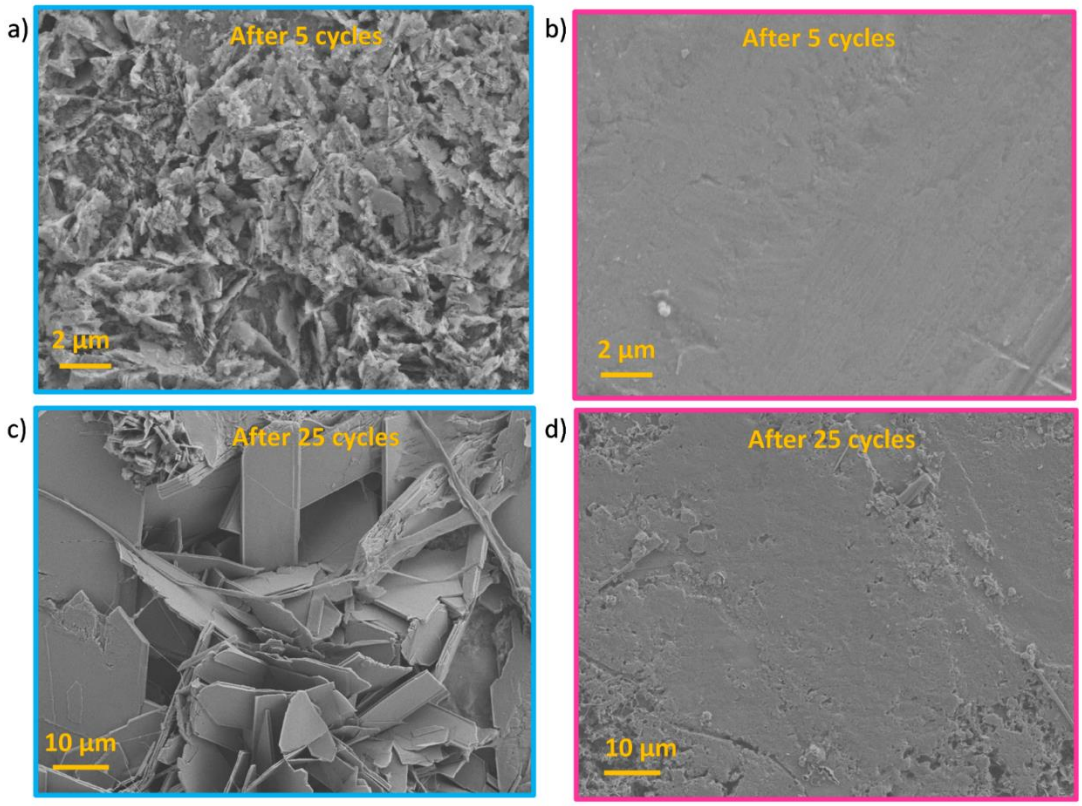

Figure 6.19. FE-SEM images of the Zn anode after 5 cycles (**a-b**) and 25 cycles (**c-d**) in (**a-c**) 7.7-H_2O, (**b-d**) 7.7-H_2O: NMF.

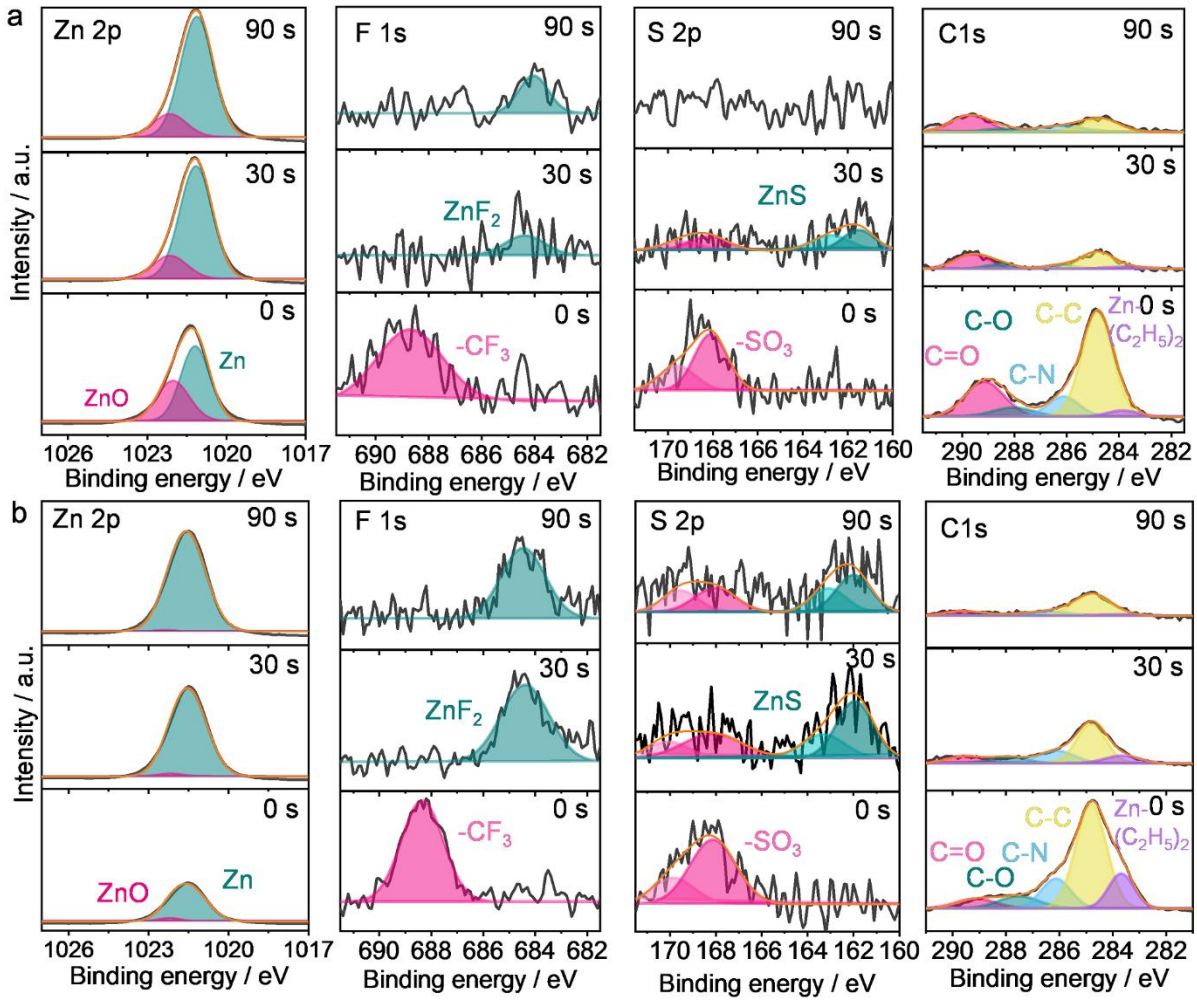

Figure 6.20. The Zn 2p, F 1s, S 2p and C 1s XPS depth profiling spectra of the Zn anode retrieved from Zn||LMO batteries after 25 cycles with (**a**) 7.7-H_2O and (**b**) 7.7-H_2O: NMF electrolytes.

6.3.5 Investigation on the LMO cathode

The electrochemical mechanism occurring at the cathode side was investigated to deepen our understanding of the Zn||LMO hybrid systems. The CVs of LMO cathode in the electrolyte with and without NMF exhibit two conventional oxidation peaks at ≈1.8 V and ≈2.0 V *vs.* Zn/Zn^{2+} and reduction peaks at ≈1.7 V and ≈1.9 V *vs.* Zn/Zn^{2+} corresponding to the intercalation and desintercalation of Li^+, respectively (**Figure 6.21**a).[240] *In-situ* XRD was employed to further investigate the Li insertion and disinsertion behaviour during cycling. **Figure 6.21**b displays the *in-situ* XRD patterns of the 5th cycle in the Zn|| LMO full cell without and with NMF at 0.2 C. During the charge process, there is an obvious shift toward higher angle attesting of the successful extraction of Li ions, whereas during the discharge process

the peak shifts back to its original position confirming the reversible Li ion insertion and extraction. One of the major drawbacks of spinel LMO cathodes reside in the continuous capacity fading caused by the disproportionation of trivalent manganese (Mn^{3+}) into divalent and tetravalent manganese (*i.e.*, Mn^{2+}, Mn^{4+}) species. Mn^{2+} is highly soluble in aqueous electrolytes, which engender irreversible crystallographic structural changes and dramatic capacity fading.[47, 138] After cycling, the separators were analysed by inductively coupled plasma mass spectroscopy (ICP-MS) in order to quantify the Mn^{2+} species present in different electrolytes (**Figure 6.21**c). Close to twice as much Mn^{2+} compounds were encountered in the 7.7-H_2O, signifying that the dissolution of Mn species from the cathode were quite significant when the crowding agent was absent (*i.e.*, 18 ppm mg^{-1}_{LMO} for 7.7-H_2O: NMF *vs.* 31 ppm mg^{-1}_{LMO} for 7.7-H_2O). Furthermore, LMO cathodes were analysed by XPS depth profiling which confirmed the excess of Mn^{2+} species soluble in the 7.7-H_2O (**Figure 6.21**d, left). As comparison, the XPS depth profiling spectra displayed large amount of Mn^{3+} species as well as reduced Mn^{2+} species in the LMO cathode which cycled in 7.7-H_2O: NMF (**Figure 6.21**d, right). The molecular crowding effect of NMF molecules largely obstructs the disproportionation of Mn^{3+} and the Mn^{2+} dissolution in the electrolyte, thereby resulting in high cycling performance of the Zn| 7.7-H_2O: NMF| LMO full cells.

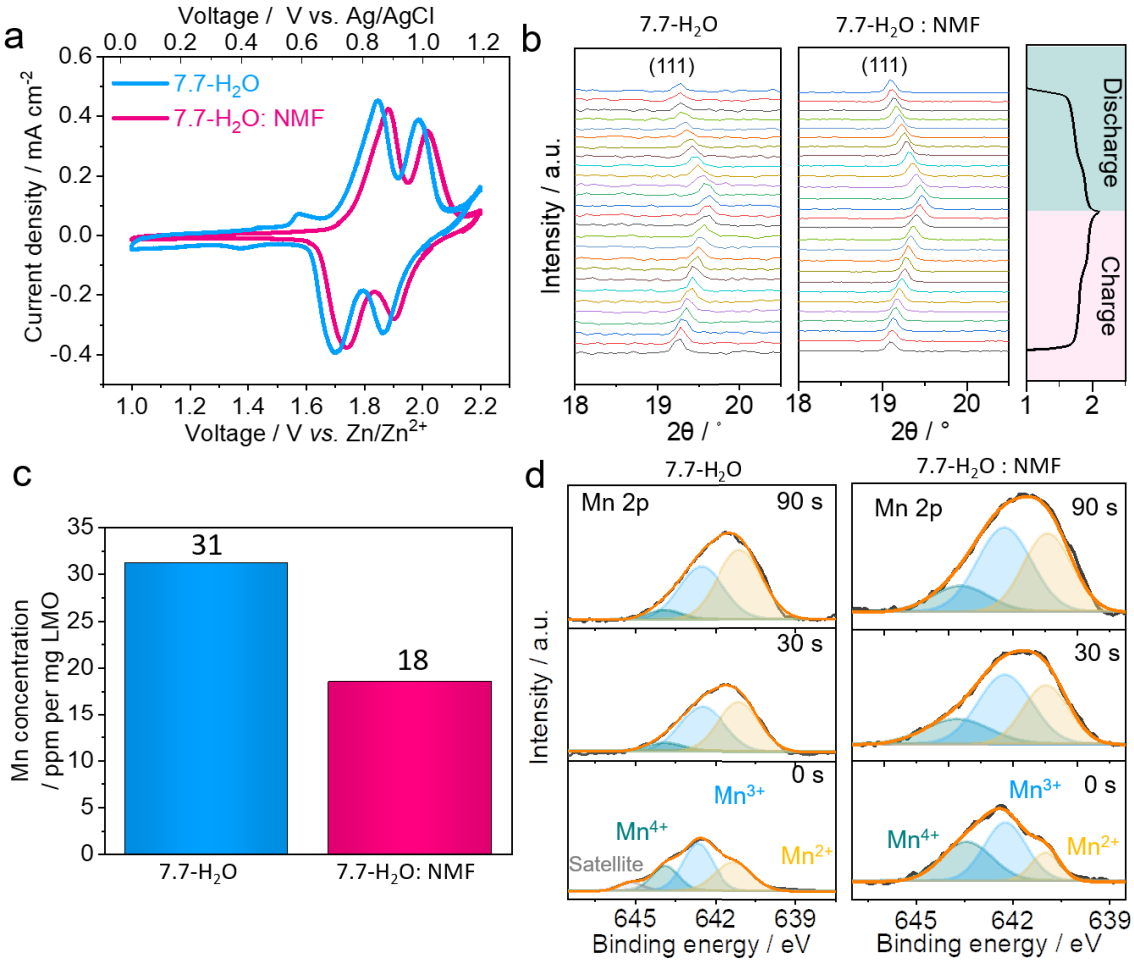

Figure 6.21. (**a**) Cyclic voltammograms of LMO cathode with 7.7-H_2O (blue line) and 7.7-H_2O: NMF (pink line) at 1 mV s^{-1}. (**b**) *In-situ* XRD patterns of LMO cathode during the 5th cycle in 7.7-H_2O (left) and 7.7-H_2O: NMF (right) at 0.2 C. (**c**) Mn amounts on the separators after cycling for 25 cycles in 7.7-H_2O (blue) and 7.7-H_2O: NMF (pink) obtained with ICP-MS analysis. (**d**) XPS depth profiling presenting the Mn 2p $_{3/2}$ spectra of LMO cathodes after 25 cycles with 7.7-H_2O (left) and 7.7-H_2O: NMF (right) electrolytes.

6.4 Conclusion

The molecular crowding strategy was adapted to Zn||LMO hybrid batteries by introducing N-methylformamide (NMF) into an aqueous electrolyte composed of 7.7 m LiOTf, 1 m $Zn(OTf)_2$ and water. It was found that NMF closely interacts with water molecules and disturb the Zn^{2+} cation sheath structure, which resulted in diverse benefits: (1) the electrochemical stability window was dramatically extended allowing the successful application of high voltage redox-couples such as LMO cathode. (2) The corrosion of Zn anode was alleviate due to the scarce

availability of free water molecules and high stability of NMF toward Zn metal. (3) The Zn plating and stripping processes were improved owing to the lower Zn desolvation energy barrier and a SEI was formed on the anode, which prevented dendrite growth. (4) The transition metal dissolution from LMO cathode into the electrolyte was reduced due to the small amount of free water molecules in the crowded electrolyte. Furthermore, the as-prepared electrolyte is non-flammable and less expensive than “water-in-salt” analogues. Finally, a Zn||LMO coin cell, which was assembled with the molecular crowding electrolyte, effectively cycled for more than 400 cycles with a high average Coulombic efficiency of 99.6 %.

CHAPTER VII: Conclusion and future perspectives

With the rapid transition to renewable electricity production, large-scale energy storage systems guaranteeing high safety, excellent reliability, and low manufacturing cost, needs to be developed. Lithium-ion batteries, which are largely dominating the battery market, still suffer from safety concerns due to the extremely flammable and toxic organic-based electrolytes employed in these batteries. The hazard issue is even more serious for high energy density batteries that rely on metal anodes such as lithium metal batteries. Recently, non-flammable electrolytes gained intensive attention. Here, we reviewed several types of non-flammable electrolytes for lithium and zinc –based secondary batteries (*i.e.*, non-flammable organic electrolytes, deep eutectic solvents, aqueous electrolytes and quasi-solid electrolytes). Subsequently, we engineered a deep eutectic solvent –based electrolyte for lithium metal batteries and aqueous –based electrolytes for lithium-ion batteries and Zn metal hybrid batteries.

Firstly, self-healing deep eutectic solvent polymer (DSP) electrolytes were synthesised by introducing a homemade self-healing polymer in an optimized deep eutectic solvent (*i.e.*, LiTFSI: NMAc (1: 4) + 10 wt% FEC). The *in-situ* polymerisation provided intimate electrode/electrolyte contact meanwhile, the organised polymer network formed ionic channels facilitating Li ion plating and stripping processes as demonstrated with numerical simulations, cryo-EM and electrochemical analyses. Furthermore, XPS depth profiling and FE-SEM images demonstrated that the FEC additive and the self-healing polymer not only contributed to the formation of a robust SEI layer rich in fluorinated compounds, but also efficiently inhibit dendrite growth. Finally yet importantly, the metal transition dissolution was reduced owing to the formation of a thin CEI layer on the LMO cathode. Therefore, the ultra-safe deep eutectic solvent self-healing polymer electrolytes enabled excellent cycling performance of Li||LMO batteries.

Secondly, we successfully synthesised a “localized water-in-salt” electrolyte for the first time. Since reducing the electrolyte manufacturing cost is primordial for large-scale energy storage applications, our electrolyte consisted in low-cost $LiNO_3$ inorganic lithium salt with 1,5-pentandiol diluent in water. The amount of Li salt in such electrolyte was divided by two in comparison with “water-in-salt” electrolytes (which are based on expensive LiTFSI salts). To enlarge further the voltage stability window and the safety properties of the aqueous

electrolyte, an acrylate monomer was *in-situ* polymerised into the localized water-in-salt electrolyte. The gelling of the electrolyte led to an increase in hydrogen bonds density, which diminished the reactivity of water molecules meanwhile leakage issue was suppressed. It was theoretically and experimentally demonstrated with molecular dynamic simulations and, FT-IR and Raman spectroscopy that the solvation structure of Li ions in "localized water-in-salt" electrolytes remained similar to that achieved in "water-in-salt" electrolytes. The as-prepared localized electrolytes exhibited a 3.0 V-wide electrochemical stability window, which allowed Mo_6S_8||LMO batteries to cycle for more than 250 cycles at 1 C. Furthermore, a stable SEI layer was discovered on the anode. We believe that the reduction of PD diluent and $LiNO_3$ in the first cycles resulted on the formation of a SEI layer.

Increasing the energy density of lithium ion aqueous batteries is challenging due to the lack of stable low potential anodes. Zinc metal benefit from good compatibility with aqueous electrolytes and high volumetric capacity. Accordingly, we developed a molecular crowding agent for zinc/lithium hybrid batteries by introducing 90 wt% of NMF into a mixture of LiOTf and $Zn(OTf)_2$ salts. NMF efficiently created numerous hydrogen bonds with water molecules, thereby enlarging the voltage stability window of the aqueous electrolyte. Owing to the delayed of HER and OER side reactions, the molecular crowding electrolyte could accommodate zinc metal as anode and LMO as cathode. Employing a high voltage lithium-based cathode permitted to increase the average operational voltage of the battery to 1.85 V. Zn||LMO coin cells demonstrated high reversibility with an average Coulombic efficiency superior to 99.6 %.

Although these works provided interesting pathways for developing non-flammable electrolytes for lithium and zinc –based rechargeable batteries. Several key challenges still need to be addressed:

(1) Improving the ionic conductivity and viscosity of deep eutectic solvents and super-concentrated electrolytes in order to improve high rate performance.
(2) Further understanding of the formation mechanism of SEI layers backed with advanced characterisations such as XPS depth profiling, TEM, *in-situ* analyses, *etc.* The formation mechanism of SEI layers in aqueous medium seems extremely complex and is still controversial in the research community.

(3) Continuous progress in anode engineering to prevent further water evolution reactions in aqueous systems and suppress dendrite growth in metal anode –based batteries.

(4) Approach commercial battery testing standards by including scalability, practical energy density and cost issues to design non-flammable batteries. For instance, developing pouch cells design, employing lean amount of electrolyte, and thin electrodes with high mass loading is necessary to achieve high energy density batteries.

APPENDICES

Appendix 1: Ionic conductivity of the DES, DES+FEC and GPE electrolyte. The experimental values are represented with dots meanwhile the lines are the Arrhenius fitting results.

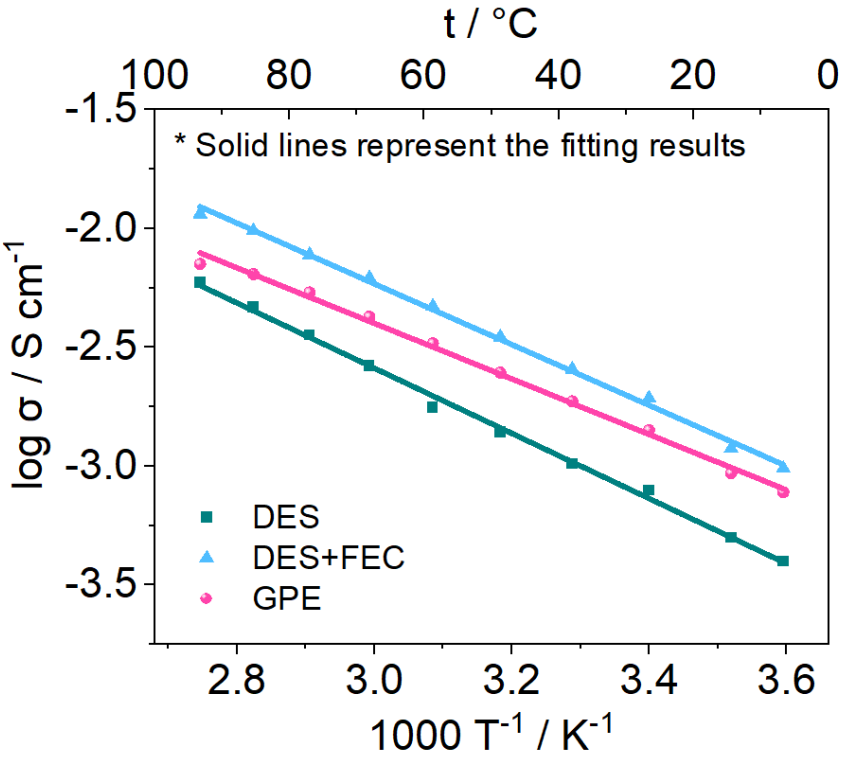

Appendix 2: Arrhenius fitting results corresponding to appendix 1.

Sample	σ at 25 °C (S cm^{-1})	σ_o (S cm^{-1} K$^{-1/2}$)	E_a (eV)
DES	8.91 x 10^{-4}	4.62 ± 0.084	1.18×10^{-1} ± 0.026
DES + FEC	2.24 x 10^{-3}	4.95 ± 0.084	1.10×10^{-1} ± 0.027
DSP	1.79 x 10^{-3}	3.03 ± 0.075	1.01×10^{-1} ± 0.024

Appendix 3: 2nd CV curves of (**a**) 10.5 m LiTFSI in H_2O and 10.5 m LiTFSI in H_2O: EC, (**b**) 12.5 m $LiNO_3$ in H_2O and 12.5 m $LiNO_3$ in H_2O: EC, (**c**) 12.5 m $LiNO_3$ in H_2O and 12.5 m $LiNO_3$ in H_2O: PD, and (**d**) 12.5 m $LiNO_3$ in H_2O: PD and LWIS gel electrolyte couples at 0.1 mV s^{-1}.

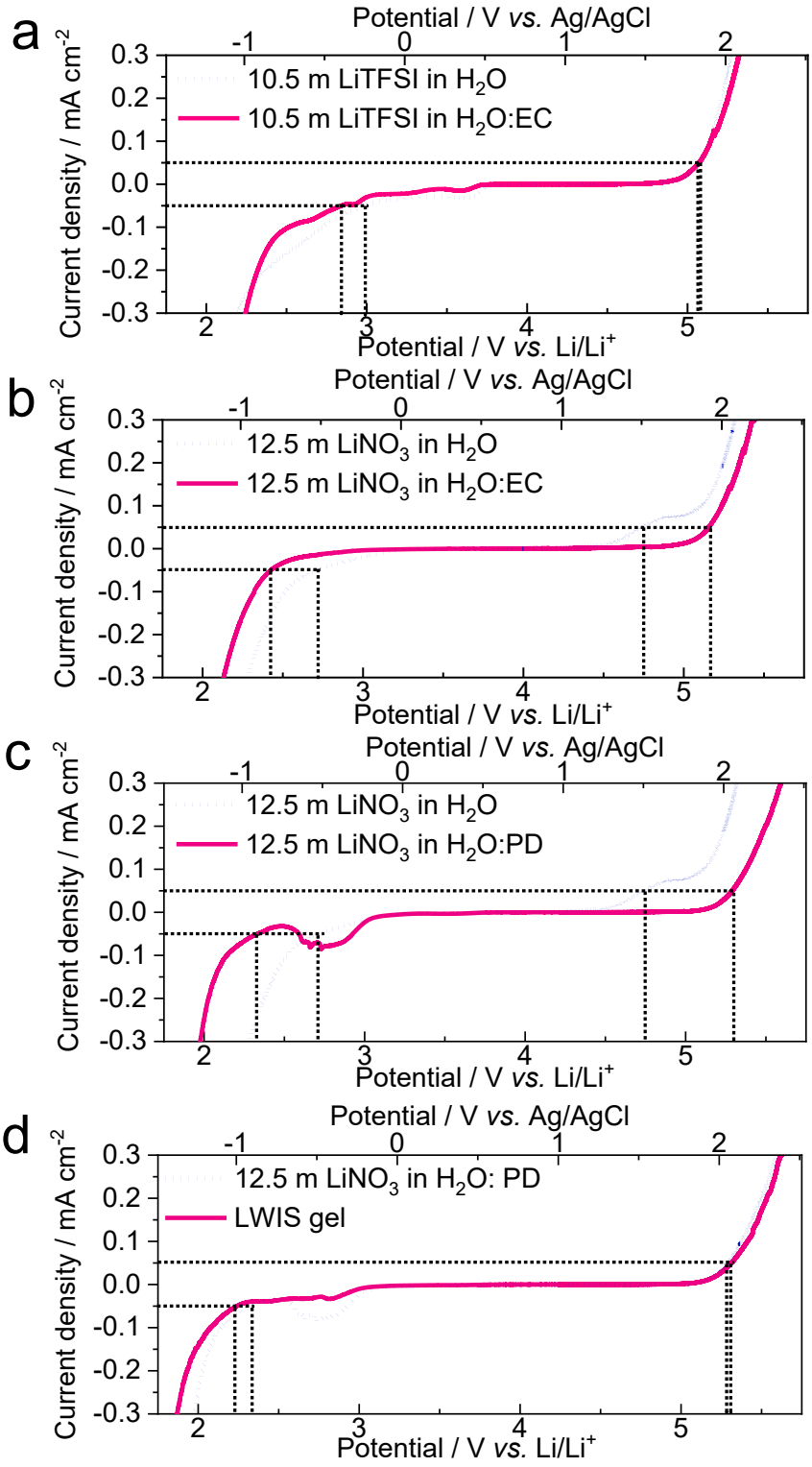
a
Potential / V vs. Ag/AgCl
Current density / mA cm-2
10.5 m LiTFSI in H2O
10.5 m LiTFSI in H2O:EC
Potential / V vs. Li/Li+
b
Potential / V vs. Ag/AgCl
Current density / mA cm-2
12.5 m LiNO3 in H2O
12.5 m LiNO3 in H2O:EC
Potential / V vs. Li/Li+
c
Potential / V vs. Ag/AgCl
Current density / mA cm-2
12.5 m LiNO3 in H2O
12.5 m LiNO3 in H2O:PD
Potential / V vs. Li/Li+
d
Potential / V vs. Ag/AgCl
Current density / mA cm-2
12.5 m LiNO3 in H2O: PD
LWIS gel
Potential / V vs. Li/Li+

Appendix 4: Ionic conductivity of different electrolytes. The experimental values are represented with dots meanwhile the lines are the Arrhenius fitting results.

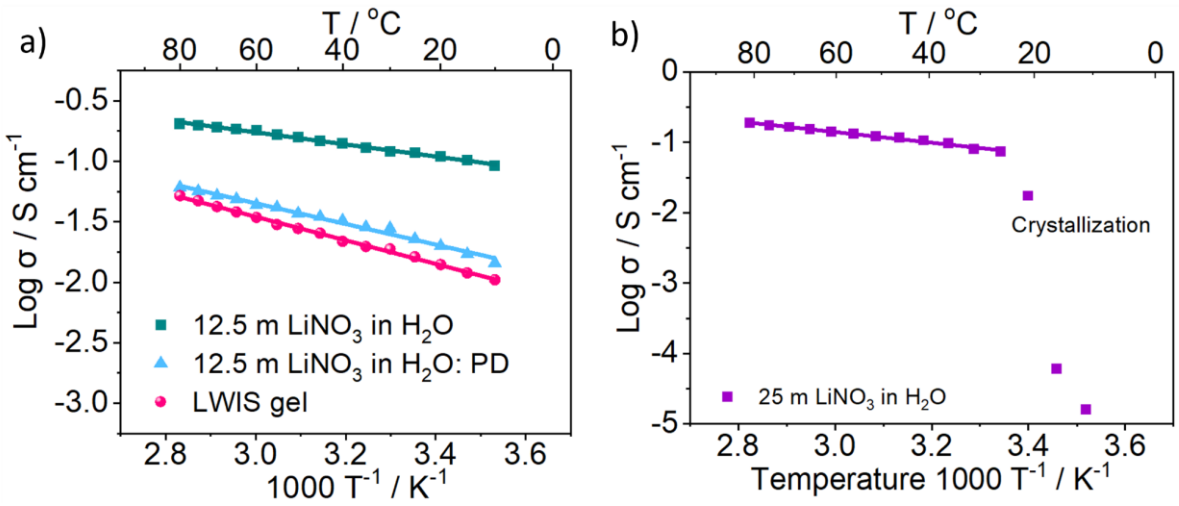

Appendix 5: Arrhenius fitting results corresponding to appendix 4.

Sample	σ at 25 °C (S cm^{-1})	σ_o (S cm^{-1} K$^{-1/2}$)	E_a (eV)
25 m $LiNO_3$ in H_2O	0.0738	4.10 ± 0.021	6.52×10^{-2} ± 0.073
12.5 m $LiNO_3$ in H_2O	0.116	2.09 ± 0.010	4.31×10^{-2} ± 0.033
12.5 m $LiNO_3$ in H_2O:PD	0.0228	3.37 ± 0.025	7.36×10^{-2} ± 0.079
LWIS gel	0.0162	4.32 ± 0.014	8.39×10^{-2} ± 0.044

Nomenclature

"Water-in-salt"	WIS
1,1,2,2-tetrafluoroethyl 2,2,3,3,-tetrafluoropropyl ether	HFE
1,1,2,2-tetrafluoroethyl-2,2,3,3-tetrafluoropropyl ether	TTE
1,5-pentanediol	PD
2-(3-(6-methyl-4-oxo-1,4-dihydropyrimidin-2-yl)ureido)ethyl methacrylate	UPyMA
2,2'-azobis(2-methylpropionitrile)	AIBN
2-hydroxyethyl acrylate	HEA
1-ethyl-3-methylimidazolium dicyanamide	C2mim-dca
1-butyl-1-methylpyrrolidinium trifluoromethylsulfonate	[Py1,4]TfO
1-vinyl-3-dodecylimidazolium bis(trifluoromethanesulfonyl) imide	VDIM-TFSI
1-butyl-1-methylpyrrolidinium bis(trifluoromethylsulfonyl)imide	BMPTFSI
Aluminium	Al
Bulk resistance	R_b
Cathode electrolyte interphase	CEI
Charge transfer resistance	R_{ct}
Chevrel phase molybdenum sulphide	Mo_6S_8
Copper	Cu
Cryo-electron microscopy	Cryo-EM
Cyclic voltammetry	CV
Deep eutectic solvent	DES
Deep Eutectic Solvent-Based Self-Healing Polymer	DSP
Diethylene carbonate	DEC
Difluoroethylene carbonate	DFEC
Dimethyl carbonate	DMC
Dimethyl sulfoxide	DMSO
Electrochemical impedance spectroscopy	EIS
Ethyl methyl carbonate	EMC
Ethylene carbonate	EC
Ethylene carbonate	EC
Eutectogel	ETG
Field emission scanning electron microscopy	FE-SEM
Fluoroethylene phosphate	FEC
Fourier transform infra-red	FT-IR
Glass fibre	GF
Hydrogen evolution reaction	HER
Inductively coupled plasma mass spectroscopy	ICP-MS
$Li_4Ti_5O_{12}$	LTO
$LiCoO_2$	LCO
$LiFePO_4$	LFP
$LiMn_2O_4$	LMO
Linear sweep voltammetry	LSV
$LiNi_{0.5}Mn_{1.5}O_4$	LNMO
$LiNi_xMn_yCo_zO_2$	NMC

Lithium	Li
Lithium acetate	$LiCH_3COO$ or LiAc
Lithium bis(fluorosulfonyl)amide	LiFSA
Lithium bis(fluorosulfonyl)imide	LiFSI
Lithium bis(perfluoroethanesulfonyl)imide	LiBETI
Lithium bis(trifluoromethanesulfonyl)imide	LiTFSI
Lithium carbonate	Li_2CO_3
Lithium difluoro(oxalate)borate	LiDFOB
Lithium fluoride	LiF
Lithium hexafluorophosphate	$LiPF_6$
Lithium nitrate	$LiNO_3$
Lithium oxide	Li_2O
Lithium perchlorate	$LiClO_4$
Lithium sulfate	Li_2SO_4
Lithium tetrafluoroborate	$LiBF_4$
Lithium triflate or lithium trifluoromethanesulfonate	LiOTf
Localized water-in-salt	LWIS
Manganese oxide	MnO_2
Mass percentage	wt%
Molecular dynamic	MD
N,N-dimethylacetamide	DMA
N-methyl-2-pyrrolidone	NMP
N-methylacetamide	NMAc
N-methylformamide	NMF
N-butyl-N-ethylpyrrolidinium bis (fluorosulfonyl)imide	$PYR_{24}FSI$
N-butyl-N-ethylpyrrolidinium-bis(trifluoromethanesulfonyl)imide	$PYR_{24}TFSI$
N-methyl-N-propyl-piperidinium bis(fluorosulfonyl)imide	$[PP_{13}][FSI]$
N-propyl-N-methylpyrrolidinium bis(fluorosulfonyl)imide	C_3mpyrFSI
N-butyl-N-methylpyrrolidinium dicyanamide	C_4mpyr-dca
Nuclear magnetic resonance	NMR
Oxygen evolution reaction	OER
Open circuit voltage	OCV
Pentaerythritol tetraacrylate	PETEA
Poly(vinyl alcohol)	PVA
Poly(vinylidene fluoride-hexafluoro propylene	PVDF-HFP
Polyaniline	PANI
Polyethylene glycol	PEG
Polyethylene glycol dimethyl ether	PEGDME
Polyethylene glycol methyl ether acrylate	MPEGA
Polyethylene oxide	PEO
Propylene carbonate	PC
Propylene carbonate	PC
Silica	SiO_2
Solid electrolyte interface resistance	R_f
Solid electrolyte interphase	SEI
Standard hydrogen electrode	SHE

Succinonitrile	SN
Tetraethylene dimethyl acrylate	TEGDME
Tetraethylene glycol dimethyl ether	TEGDME
Thermogravimetric analysis	TGA
Titanium disulfide	TiS_2
Titanium oxide	TiO_2
Transmission electron microscopy	TEM
Triethyl phosphate	TEP
Trimethyl phosphate	TMP
Tris(trifluoroethyl) phosphate	TFEP
Tris(trimethylsilyl)borate	TMSB
Vanadium disulfide	VS_2
Vanadium oxide	VO_2
Vinylene carbonate	VC
Vogel–Tamman– Fulcher	VTF
Volume (percentage)	vol (vol%)
X-ray diffraction	XRD
X-ray photoelectron spectroscopy	XPS
Zinc	Zn
Zinc acetate	$Zn(CH_3COO)_2$
Zinc bis(trifluoromethanesulfonyl)imide	$Zn(TFSI)_2$
Zinc chloride	$ZnCl_2$
Zinc dihydrogen phosphate	$Zn(H_2PO_4)_2$
Zinc hydroxide sulfate	$Zn_4SO_4(OH)_6{\cdot}nH_2O$
Zinc nitrate	$Zn(NO_3)_2$
Zinc oxide	ZnO
Zinc perchlorate	$Zn(ClO_4)_2$
Zinc sulfate	$ZnSO_4$
Zinc triflate or zinc trifluoromethanesulfonate	$Zn(OTf)_2$

References

[1] Q. Zheng, Y. Yamada, R. Shang, S. Ko, Y.-Y. Lee, K. Kim, E. Nakamura, A. Yamada, *Nat. Energy* **2020**, *5*, 291-298.

[2] C.-C. Su, M. He, J. Shi, R. Amine, Z. Yu, L. Cheng, J. Guo, K. Amine, *Energy Environ. Sci.* **2021**, *14*, 3029-3034.

[3] Q. Wu, X. Tang, Y. Qian, J. Duan, R. Wang, J. Teng, J. Li, *Appl. Energy Mater.* **2021**, *4*, 10234-10243.

[4] A. Boisset, S. Menne, J. Jacquemin, A. Balducci, M. Anouti, *Phys. Chem. Chem. Phys.* **2013**, *15*, 20054-20063.

[5] Z. Hu, F. Xian, Z. Guo, C. Lu, X. Du, X. Cheng, S. Zhang, S. Dong, G. Cui, L. Chen, *Chem. Mater.* **2020**, *32*, 3405-3413.

[6] W. Yang, X. Du, J. Zhao, Z. Chen, J. Li, J. Xie, Y. Zhang, Z. Cui, Q. Kong, Z. Zhao, C. Wang, Q. Zhang, G. Cui, *Joule* **2020**, *4*, 1557-1574.

[7] J. Zhao, J. Zhang, W. Yang, B. Chen, Z. Zhao, H. Qiu, S. Dong, X. Zhou, G. Cui, L. Chen, *Nano Energy* **2019**, *57*, 625-634.

[8] B. Joos, T. Vranken, W. Marchal, M. Safari, M. K. Van Bael, A. T. Hardy, *Chem. Mater.* **2018**, *30*, 655-662.

[9] M. W. Logan, S. Langevin, B. Tan, A. W. Freeman, C. Hoffman, D. B. Trigg, K. Gerasopoulos, *J. Mater. Chem. A* **2020**, *8*, 8485-8495.

[10] Z. Liu, Y. Huang, Y. Huang, Q. Yang, X. Li, Z. Huang, C. Zhi, *Chem. Soc. Rev.* **2020**, *49*, 180-232.

[11] N. Dubouis, P. Lemaire, B. Mirvaux, E. Salager, M. Deschamps, A. Grimaud, *Energy Environ. Sci.* **2018**, *11*, 3491-3499.

[12] L. Suo, D. Oh, Y. Lin, Z. Zhuo, O. Borodin, T. Gao, F. Wang, A. Kushima, Z. Wang, H.-C. Kim, *J. Am. Chem. Soc.* **2017**, *139*, 18670-18680.

[13] L. Chen, J. Zhang, Q. Li, J. Vatamanu, X. Ji, T. P. Pollard, C. Cui, S. Hou, J. Chen, C. Yang, L. Ma, M. S. Ding, M. Garaga, S. Greenbaum, H.-S. Lee, O. Borodin, K. Xu, C. Wang, *Energy Lett.* **2020**, *5*, 968-974.

[14] F. Wang, O. Borodin, M. S. Ding, M. Gobet, J. Vatamanu, X. Fan, T. Gao, N. Eidson, Y. Liang, W. Sun, *Joule* **2018**, *2*, 927-937.

[15] J. Xie, Z. Liang, Y.-C. Lu, *Nat. Mater.* **2020**, *19*, 1006-1011.

[16] D. Dong, J. Xie, Z. Liang, Y.-C. Lu, *Energy Lett.* **2021**, *7*, 123-130.

[17] C. Yang, J. Chen, T. Qing, X. Fan, W. Sun, A. von Cresce, M. S. Ding, O. Borodin, J. Vatamanu, M. A. Schroeder, *Joule* **2017**, *1*, 122-132.

[18] C. Yang, J. Chen, X. Ji, T. P. Pollard, X. Lü, C.-J. Sun, S. Hou, Q. Liu, C. Liu, T. Qing, *Nature* **2019**, *569*, 245-250.

[19] F. Wang, Y. Lin, L. Suo, X. Fan, T. Gao, C. Yang, F. Han, Y. Qi, K. Xu, C. Wang, *Energy Environ. Sci.* **2016**, *9*, 3666-3673.

[20] P. Jaumaux, X. Yang, B. Zhang, J. Safaei, X. Tang, D. Zhou, C. Wang, G. Wang, *Angew. Chem. Int. Ed.* **2021**, *60*, 19965-19973.

[21] L. Wang, Y. Zhang, H. Hu, H. Y. Shi, Y. Song, D. Guo, X. X. Liu, X. Sun, *Appl. Mater. Interfaces* **2019**, *11*, 42000-42005.

[22] C. Y. Chen, K. Matsumoto, K. Kubota, R. Hagiwara, Q. Xu, *Adv. Energy Mater.* **2019**, *9*, 1900196.

[23] X. Zeng, J. Mao, J. Hao, J. Liu, S. Liu, Z. Wang, Y. Wang, S. Zhang, T. Zheng, J. Liu, *Adv. Mater.* **2021**, *33*, 2007416.

[24] F. Wang, O. Borodin, T. Gao, X. Fan, W. Sun, F. Han, A. Faraone, J. A. Dura, K. Xu, C. Wang, *Nat. Mater.* **2018**, *17*, 543-549.

[25] Y. Jin, K. S. Han, Y. Shao, M. L. Sushko, J. Xiao, H. Pan, J. Liu, *Adv. Funct. Mater.* **2020**, *30*, 2003932.

[26] K. Leng, G. Li, J. Guo, X. Zhang, A. Wang, X. Liu, J. Luo, *Adv. Funct. Mater.* **2020**, *30*, 2001317.

[27] C. Yang, L. Suo, O. Borodin, F. Wang, W. Sun, T. Gao, X. Fan, S. Hou, Z. Ma, K. Amine, K. Xu, C.

Wang, *Proc. Natl. Acad. Sci.* **2017**, *114*, 6197-6202.
[28] J. Zhao, K. K. Sonigara, J. Li, J. Zhang, B. Chen, J. Zhang, S. S. Soni, X. Zhou, G. Cui, L. Chen, *Angew. Chem. Int. Ed.* **2017**, *56*, 7871-7875.
[29] J. Bae, Y. Qian, Y. Li, X. Zhou, J. B. Goodenough, G. Yu, *Energy Environ. Sci.* **2019**, *12*, 3319-3327.
[30] aP. Jiang, L. Chen, H. Shao, S. Huang, Q. Wang, Y. Su, X. Yan, X. Liang, J. Zhang, J. Feng, *Energy Lett.* **2019**, *4*, 1419-1426; bG. Fu, S. Buddhiranon, N. Kim, A. Seko, K. Adachi, Y. Tsukahara, T. Kyu, *Polymer* **2018**, *159*, 64-74.
[31] W. Kao-ian, R. Pornprasertsuk, P. Thamyongkit, T. Maiyalagan, S. Kheawhom, *J. Electrochem. Soc.* **2019**, *166*, A1063-A1069.
[32] J. Zheng, M. H. Engelhard, D. Mei, S. Jiao, B. J. Polzin, J.-G. Zhang, W. Xu, *Nat. Energy* **2017**, *2*, 17012.
[33] Y. Ma, Z. Zhou, C. Li, L. Wang, Y. Wang, X. Cheng, P. Zuo, C. Du, H. Huo, Y. Gao, *Energy Stor. Mater.* **2018**, *11*, 197-204.
[34] W. Zhang, Z. Shen, S. Li, L. Fan, X. Wang, F. Chen, X. Zang, T. Wu, F. Ma, Y. Lu, *Adv. Funct. Mater.* **2020**, *30*, 2003800.
[35] H. Mountford, D. Waskow, L. Gonzalez, C. Gajjar, N. Cogswell, M. Holt, T. Fransen, M. Bergen, R. Gerholdt, **2021**.
[36] M. V. Reddy, A. Mauger, C. M. Julien, A. Paolella, K. Zaghib, *Mater.* **2020**, *13*, 1884.
[37] T. Placke, R. Kloepsch, S. Dühnen, M. Winter, *J. Solid State Electrochem.* **2017**, *21*, 1939-1964.
[38] J. Liu, Z. Bao, Y. Cui, E. J. Dufek, J. B. Goodenough, P. Khalifah, Q. Li, B. Y. Liaw, P. Liu, A. Manthiram, Y. S. Meng, V. R. Subramanian, M. F. Toney, V. V. Viswanathan, M. S. Whittingham, J. Xiao, W. Xu, J. Yang, X.-Q. Yang, J.-G. Zhang, *Nat. Energy* **2019**, *4*, 180-186.
[39] S. S. Zhang, *Appl. Energy Mater.* **2018**, *1*, 910-920.
[40] W. Xu, J. Wang, F. Ding, X. Chen, E. Nasybulin, Y. Zhang, J.-G. Zhang, *Energy Environ. Sci.* **2014**, *7*, 513-537.
[41] R. Fong, U. Von Sacken, J. R. Dahn, *J. Electrochem. Soc.* **1990**, *137*, 2009.
[42] A. Hagopian, M.-L. Doublet, J.-S. Filhol, *Energy Environ. Sci.* **2020**, *13*, 5186-5197.
[43] K. Xu, *Chem. Rev.* **2014**, *114*, 11503-11618.
[44] J. Wang, Y. Yamada, K. Sodeyama, C. H. Chiang, Y. Tateyama, A. Yamada, *Nat. Commun.* **2016**, *7*, 12032.
[45] aX. Fan, X. Ji, L. Chen, J. Chen, T. Deng, F. Han, J. Yue, N. Piao, R. Wang, X. Zhou, X. Xiao, L. Chen, C. Wang, *Nat. Energy* **2019**, *4*, 882-890; bJ. Chen, A. Naveed, Y. Nuli, J. Yang, J. Wang, *Energy Stor. Mater.* **2020**, *31*, 382-400.
[46] J. Yu, Y.-Q. Lyu, J. Liu, M. B. Effat, S. C. Kwok, J. Wu, F. Ciucci, *J. Mater. Chem. A* **2019**, *7*, 17995-18002.
[47] P. Jaumaux, Q. Liu, D. Zhou, X. Xu, T. Wang, Y. Wang, F. Kang, B. Li, G. Wang, *Angew. Chem. Int. Ed.* **2020**, *59*, 9134-9142.
[48] P. Jaumaux, J. Wu, D. Shanmukaraj, Y. Wang, D. Zhou, B. Sun, F. Kang, B. Li, M. Armand, G. Wang, *Adv. Funct. Mater.* **2021**, *31*, 2008644.
[49] aX. Zhang, R. Lv, W. Tang, G. Li, A. Wang, A. Dong, X. Liu, J. Luo, *Adv. Funct. Mater.* **2020**, *30*, 2004187; bT. Shoji, M. Hishinuma, T. Yamamoto, *J. Appl. Electrochem.* **1988**, *18*, 521-526.
[50] C. Xu, B. Li, H. Du, F. Kang, *Angew. Chem. Int. Ed.* **2012**, *51*, 933-935.
[51] H. Kim, G. Jeong, Y. U. Kim, J. H. Kim, C. M. Park, H. J. Sohn, *Chem. Soc. Rev.* **2013**, *42*, 9011-9034.
[52] C. Zhao, X. Wang, C. Shao, G. Li, J. Wang, D. Liu, X. Dong, *Sust. Energy Fuels* **2021**, *5*, 332-350.
[53] Q. Li, G. Liu, H. Cheng, Q. Sun, J. Zhang, J. Ming, *Eur. J. Chem.* **2021**, *27*, 15842-15865.
[54] M. F. Lagadec, R. Zahn, V. Wood, *Nat. Energy* **2018**, *4*, 16-25.
[55] W. S. Harris, *Electrochemical studies in cyclic esters, Vol. 8381*, University of California, Lawrence Radiation Laboratory, **1958**.
[56] A. Mauger, C. M. Julien, J. B. Goodenough, K. Zaghib, *J. Electrochem. Soc.* **2020**, *167*, 070507.
[57] M. Armand, M. Duclot, *French Pat.* **1978**, filled on November 22,1978.

[58] B. Scrosati, *J. Solid State Electrochem.* **2011**, *15*, 1623-1630.
[59] J. Besenhard, G. Eichinger, *J. Electroanal. Chem. Interfacial Electrochem.* **1976**, *68*, 1-18.
[60] A. Yoshino, *Nat. Energy* **2021**, *6*, 449-449.
[61] K. Mizushima, P. Jones, P. Wiseman, J. B. Goodenough, *Mater. Res. Bull.* **1980**, *15*, 783-789.
[62] M. Thackeray, W. David, P. Bruce, J. Goodenough, *Mater. Res. Bull.* **1983**, *18*, 461-472.
[63] A. Manthiram, J. Goodenough, *J. Solid State Chem.* **1987**, *71*, 349-360.
[64] D. Guyomard, J. M. Tarascon, *J. Power Sources* **1995**, *54*, 92-98.
[65] K. Xu, *Chem. Rev.* **2004**, *104*, 4303-4417.
[66] J. Xie, Y. C. Lu, *Nat. Commun.* **2020**, *11*, 2499.
[67] J. Hou, L. Lu, L. Wang, A. Ohma, D. Ren, X. Feng, Y. Li, Y. Li, I. Ootani, X. Han, W. Ren, X. He, Y. Nitta, M. Ouyang, *Nat. Commun.* **2020**, *11*, 5100.
[68] X. Yan, L. Zhang, J. Lu, *Electrochim. Acta.* **2019**, *296*, 149-154.
[69] K. Xu, M. S. Ding, S. Zhang, J. L. Allen, T. R. Jow, *J. Electrochem. Soc.* **2002**, *149*, A622.
[70] Q.-K. Zhang, X.-Q. Zhang, H. Yuan, J.-Q. Huang, *Small* **2021**, *1*.
[71] P. Shi, H. Zheng, X. Liang, Y. Sun, S. Cheng, C. Chen, H. Xiang, *Chem. Commun.* **2018**, *54*, 4453-4456.
[72] L. Jiang, C. Liang, H. Li, Q. Wang, J. Sun, *Appl. Energy Mater.* **2020**, *3*, 1719-1729.
[73] K. Takada, Y. Yamada, A. Yamada, *Appl. Mater. Interfaces* **2019**, *11*, 35770-35776.
[74] Z. Zeng, V. Murugesan, K. S. Han, X. Jiang, Y. Cao, L. Xiao, X. Ai, H. Yang, J.-G. Zhang, M. L. Sushko, J. Liu, *Nat. Energy* **2018**, *3*, 674-681.
[75] J. G. Han, K. Kim, Y. Lee, N. S. Choi, *Adv. Mater.* **2019**, *31*, 1804822.
[76] T. Achiha, T. Nakajima, Y. Ohzawa, M. Koh, A. Yamauchi, M. Kagawa, H. Aoyama, *J. Electrochem. Soc.* **2010**, *157*, A707.
[77] N. von Aspern, G. V. Roschenthaler, M. Winter, I. Cekic-Laskovic, *Angew. Chem. Int. Ed.* **2019**, *58*, 15978-16000.
[78] X. Q. Zhang, X. B. Cheng, X. Chen, C. Yan, Q. Zhang, *Adv. Funct. Mater.* **2017**, *27*, 1605989.
[79] B. Han, Y. Zou, G. Xu, S. Hu, Y. Kang, Y. Qian, J. Wu, X. Ma, J. Yao, T. Li, *Energy Environ. Sci.* **2021**, *14*, 4882-4889.
[80] W. Huang, J. Wang, M. R. Braun, Z. Zhang, Y. Li, D. T. Boyle, P. C. McIntyre, Y. Cui, *Matters* **2019**, *1*, 1232-1245.
[81] I. Yoon, S. Jurng, D. P. Abraham, B. L. Lucht, P. R. Guduru, *Nano Lett.* **2018**, *18*, 5752-5759.
[82] T. M. Hagos, T. T. Hagos, H. K. Bezabh, G. B. Berhe, L. H. Abrha, S.-F. Chiu, C.-J. Huang, W.-N. Su, H. Dai, B. J. Hwang, *Appl. Energy Mater.* **2020**, *3*, 10722-10733.
[83] X. Fan, L. Chen, O. Borodin, X. Ji, J. Chen, S. Hou, T. Deng, J. Zheng, C. Yang, S.-C. Liou, *Nat. Nanotechnol.* **2018**, *13*, 715.
[84] D. Farhat, F. Ghamouss, J. Maibach, K. Edström, D. Lemordant, *Chem. Phys. Chem.* **2017**, *18*, 1333-1344.
[85] S. Das, *J. Electroanal. Chem* **2020**, *879*, 114794.
[86] J. Alvarado, M. A. Schroeder, M. Zhang, O. Borodin, E. Gobrogge, M. Olguin, M. S. Ding, M. Gobet, S. Greenbaum, Y. S. Meng, K. Xu, *Mater. Today* **2018**, *21*, 341-353.
[87] C.-C. Su, M. He, P. C. Redfern, L. A. Curtiss, I. A. Shkrob, Z. Zhang, *Energy Environ. Sci.* **2017**, *10*, 900-904.
[88] C.-C. Su, M. He, J. Shi, R. Amine, J. Zhang, J. Guo, K. Amine, *Nano Energy* **2021**, *89*, 106299.
[89] X. Ren, S. Chen, H. Lee, D. Mei, M. H. Engelhard, S. D. Burton, W. Zhao, J. Zheng, Q. Li, M. Ding, M. Schroeder, J. Alvarado, K. Xu, Y. S. Meng, J. Liu, J.-G. Zhang, W. Xu, *Chem* **2018**, *4*, 1877-1892.
[90] R. Amine, J. Liu, I. Acznik, T. Sheng, K. Lota, H. Sun, C. J. Sun, K. Fic, X. Zuo, Y. Ren, *Adv. Energy Mater.* **2020**, *10*, 2000901.
[91] S. Solchenbach, M. Metzger, M. Egawa, H. Beyer, H. A. Gasteiger, *J. Electrochem. Soc.* **2018**, *165*, A3022.
[92] J. Patra, H.-T. Huang, W. Xue, C. Wang, A. S. Helal, J. Li, J.-K. Chang, *Energy Stor. Mater.* **2019**,

16, 146-154.
[93] W. A. Henderson, *J. Phys. Chem. B* **2006**, *110*, 13177-13183.
[94] T. Tamura, T. Hachida, K. Yoshida, N. Tachikawa, K. Dokko, M. Watanabe, *J. Power Sources* **2010**, *195*, 6095-6100.
[95] aO. Borodin, J. Self, K. A. Persson, C. Wang, K. Xu, *Joule* **2020**, *4*, 69-100; bY. Yamada, *Electrochem.* **2017**, *85*, 559-565.
[96] T. Shiga, Y. Kato, H. Kondo, C.-a. Okuda, *J. Mater. Chem. A* **2017**, *5*, 5156-5162.
[97] N. Piao, X. Ji, H. Xu, X. Fan, L. Chen, S. Liu, M. N. Garaga, S. G. Greenbaum, L. Wang, C. Wang, *Adv. Energy Mater.* **2020**, *10*, 1903568.
[98] A. Bouibes, S. Saha, M. Nagaoka, *Sci. Rep.* **2020**, *10*, 1-10.
[99] M. Armand, F. Endres, D. R. MacFarlane, H. Ohno, B. Scrosati, *Nat. Mater.* **2009**, *8*, 621-629.
[100] X. Wang, M. Salari, D.-e. Jiang, J. Chapman Varela, B. Anasori, D. J. Wesolowski, S. Dai, M. W. Grinstaff, Y. Gogotsi, *Nat. Rev. Mater.* **2020**, *5*, 787-808.
[101] S. A. Forsyth, J. M. Pringle, D. R. MacFarlane, *Aust. J. Chem.* **2004**, *57*, 113-119.
[102] J. S. Moreno, Y. Deguchi, S. Panero, B. Scrosati, H. Ohno, E. Simonetti, G. B. Appetecchi, *Electrochim. Acta.* **2016**, *191*, 624-630.
[103] M. Hayyan, F. S. Mjalli, M. A. Hashim, I. M. AlNashef, T. X. Mei, *J. Ind. Eng. Chem.* **2013**, *19*, 106-112.
[104] N. Karimi, M. Zarrabeitia, A. Mariani, D. Gatti, A. Varzi, S. Passerini, *Adv. Energy Mater.* **2021**, *11*, 2003521.
[105] D. Rakov, M. Hasanpoor, A. Baskin, J. W. Lawson, F. Chen, P. V. Cherepanov, A. N. Simonov, P. C. Howlett, M. Forsyth, *Chem. Mater.* **2021**, *34*, 165-177.
[106] Z. Wang, F. Zhang, Y. Sun, L. Zheng, Y. Shen, D. Fu, W. Li, A. Pan, L. Wang, J. Xu, *Adv. Energy Mater.* **2021**, *11*, 2003752.
[107] U. Pal, D. Rakov, B. Lu, B. Sayahpour, F. Chen, B. Roy, D. R. MacFarlane, M. Armand, P. C. Howlett, Y. S. Meng, *Energy Environ. Sci.* **2022**, *15*, 1907-1919.
[108] H. Yoon, P. C. Howlett, A. S. Best, M. Forsyth, D. R. MacFarlane, *J. Electrochem. Soc.* **2013**, *160*, A1629-A1637.
[109] K. Periyapperuma, E. Arca, S. Harvey, T. Pathirana, C. Ban, A. Burrell, C. Pozo-Gonzalo, P. C. Howlett, *Appl. Mater. Interfaces* **2020**, *12*, 42236-42247.
[110] aE. Azaceta, R. Tena-Zaera, R. Marcilla, S. Fantini, J. Echeberria, J. A. Pomposo, H. Grande, D. Mecerreyes, *Electrochem. Commun.* **2009**, *11*, 2184-2186; bM. Xu, D. G. Ivey, W. Qu, Z. Xie, *J. Power Sources* **2015**, *274*, 1249-1253.
[111] M. Kar, B. Winther-Jensen, M. Armand, T. J. Simons, O. Winther-Jensen, M. Forsyth, D. R. MacFarlane, *Electrochim. Acta.* **2016**, *188*, 461-471.
[112] T. J. Simons, D. R. MacFarlane, M. Forsyth, P. C. Howlett, *Chem. Electro. Chem.* **2014**, *1*, 1688-1697.
[113] M. Kar, B. Winther-Jensen, M. Forsyth, D. R. MacFarlane, *Phys. Chem. Chem. Phys.* **2013**, *15*, 7191-7197.
[114] M. Xu, D. Ivey, W. Qu, Z. Xie, *J. Power Sources* **2014**, *252*, 327-332.
[115] Z. Liu, T. Cui, G. Pulletikurthi, A. Lahiri, T. Carstens, M. Olschewski, F. Endres, *Angew. Chem. Int. Ed.* **2016**, *55*, 2889-2893.
[116] Z. Liu, G. Li, T. Cui, A. Lahiri, A. Borodin, F. Endres, *Phys. Chem. Chem. Phys.* **2017**, *19*, 25989-25995.
[117] W. Zhou, M. Zhang, X. Kong, W. Huang, Q. Zhang, *Adv. Sci.* **2021**, *8*, 2004490.
[118] X. Wang, G. M. A. Girard, H. Zhu, R. Yunis, D. R. MacFarlane, D. Mecerreyes, A. J. Bhattacharyya, P. C. Howlett, M. Forsyth, *Appl. Energy Mater.* **2019**, *2*, 6237-6245.
[119] T. Huang, M.-C. Long, X.-L. Wang, G. Wu, Y.-Z. Wang, *Chem. Eng. J.* **2019**, *375*, 122062.
[120] D. Lee, H. I. Kim, W. Y. Kim, S. K. Cho, K. Baek, K. Jeong, D. B. Ahn, S. Park, S. J. Kang, S. Y. Lee, *Adv. Funct. Mater.* **2021**, *31*, 2103850.
[121] A. Nandy, J. Smiatek, *Phys. Chem. Chem. Phys.* **2019**, *21*, 12279-12287.

[122] F. M. Perna, P. Vitale, V. Capriati, *Curr. Opin. Green Sustain.* **2020**, *21*, 27-33.
[123] A. P. Abbott, G. Capper, D. L. Davies, R. K. Rasheed, V. Tambyrajah, *Chem. Commun.* **2003**, 70-71.
[124] T. T. A. Dinh, T. T. K. Huynh, L. T. M. Le, T. T. T. Truong, O. H. Nguyen, K. T. T. Tran, M. V. Tran, P. H. Tran, W. Kaveevivitchai, P. M. L. Le, *Omega* **2020**, *5*, 23843-23853.
[125] X. Zhang, J. Chen, Z. Xu, Q. Dong, H. Ao, Z. Hou, Y. Qian, *Energy Stor. Mater.* **2022**, *46*, 147-154.
[126] J. Shi, T. Sun, J. Bao, S. Zheng, H. Du, L. Li, X. Yuan, T. Ma, Z. Tao, *Adv. Funct. Mater.* **2021**, *31*, 2102035.
[127] S. Chen, P. Sun, J. Humphreys, P. Zou, M. Zhang, G. Jeerh, B. Sun, S. Tao, *Appl. Mater. Interfaces* **2021**, *13*, 46634-46643.
[128] J. Ruiz-Olles, P. Slavik, N. K. Whitelaw, D. K. Smith, *Angew. Chem. Int. Ed.* **2019**, *58*, 4173-4178.
[129] Z. Li, S. Zhang, Z. Jiang, D. Cai, C. Gu, J. Tu, *Mater. Chem. Phys.* **2021**, *267*, 124701.
[130] L. Suo, O. Borodin, T. Gao, M. Olguin, J. Ho, X. Fan, C. Luo, C. Wang, K. Xu, *Science* **2015**, *350*, 938-943.
[131] H. Zhang, D. Wang, C. Shen, *Appl. Surf. Sci.* **2020**, *507*, 145059.
[132] Y. Yamada, A. Yamada, *Chem. Lett.* **2017**, *46*, 1056-1064.
[133] W. Sun, L. Suo, F. Wang, N. Eidson, C. Yang, F. Han, Z. Ma, T. Gao, M. Zhu, C. Wang, *Electrochem. Commun.* **2017**, *82*, 71-74.
[134] L. Suo, O. Borodin, W. Sun, X. Fan, C. Yang, F. Wang, T. Gao, Z. Ma, M. Schroeder, A. von Cresce, S. M. Russell, M. Armand, A. Angell, K. Xu, C. Wang, *Angew. Chem. Int. Ed.* **2016**, *55*, 7136-7141.
[135] Y. Yamada, K. Usui, K. Sodeyama, S. Ko, Y. Tateyama, A. Yamada, *Nat. Energy* **2016**, *1*, 1-9.
[136] Y. Shang, N. Chen, Y. Li, S. Chen, J. Lai, Y. Huang, W. Qu, F. Wu, R. Chen, *Adv. Mater.* **2020**, *32*, 2004017.
[137] S. Nakano, D. Miyoshi, N. Sugimoto, *Chem. Rev.* **2014**, *114*, 2733-2758.
[138] T. Liu, A. Dai, J. Lu, Y. Yuan, Y. Xiao, L. Yu, M. Li, J. Gim, L. Ma, J. Liu, *Nat. Commun.* **2019**, *10*, 1-11.
[139] J. Zheng, G. Tan, P. Shan, T. Liu, J. Hu, Y. Feng, L. Yang, M. Zhang, Z. Chen, Y. Lin, *Chem* **2018**, *4*, 2872-2882.
[140] X. He, B. Yan, X. Zhang, Z. Liu, D. Bresser, J. Wang, R. Wang, X. Cao, Y. Su, H. Jia, C. P. Grey, H. Frielinghaus, D. G. Truhlar, M. Winter, J. Li, E. Paillard, *Nat. Commun.* **2018**, *9*, 5320.
[141] J. Hao, X. Li, X. Zeng, D. Li, J. Mao, Z. Guo, *Energy Environ. Sci.* **2020**, *13*, 3917-3949.
[142] Z. Ye, Z. Cao, M. O. L. Chee, P. Dong, P. M. Ajayan, J. Shen, M. Ye, *Energy Stor. Mater.* **2020**, *32*, 290-305.
[143] Y. Dong, M. Jia, Y. Wang, J. Xu, Y. Liu, L. Jiao, N. Zhang, *Appl. Energy Mater.* **2020**, *3*, 11183-11192.
[144] L. Zhang, I. A. Rodríguez-Pérez, H. Jiang, C. Zhang, D. P. Leonard, Q. Guo, W. Wang, S. Han, L. Wang, X. Ji, *Adv. Funct. Mater.* **2019**, *29*, 1902653.
[145] Q. Ni, H. Jiang, S. Sandstrom, Y. Bai, H. Ren, X. Wu, Q. Guo, D. Yu, C. Wu, X. Ji, *Adv. Funct. Mater.* **2020**, *30*, 2003511.
[146] Q. Zhang, Y. Ma, Y. Lu, L. Li, F. Wan, K. Zhang, J. Chen, *Nat. Commun.* **2020**, *11*, 4463.
[147] N. Patil, C. de la Cruz, D. Ciurduc, A. Mavrandonakis, J. Palma, R. Marcilla, *Adv. Energy Mater.* **2021**, *11*, 2100939.
[148] W. Kao-ian, M. T. Nguyen, T. Yonezawa, R. Pornprasertsuk, J. Qin, S. Siwamogsatham, S. Kheawhom, *Mater. Today Energy* **2021**, *21*, 100738.
[149] L. Ma, T. P. Pollard, Y. Zhang, M. A. Schroeder, M. S. Ding, A. V. Cresce, R. Sun, D. R. Baker, B. A. Helms, E. J. Maginn, C. Wang, O. Borodin, K. Xu, *Angew. Chem. Int. Ed.* **2021**, *60*, 12438-12445.
[150] X. Song, H. He, M. H. Aboonasr Shiraz, H. Zhu, A. Khosrozadeh, J. Liu, *Chem. Commun.* **2021**, *57*, 1246-1249.
[151] C. Huang, X. Zhao, S. Liu, Y. Hao, Q. Tang, A. Hu, Z. Liu, X. Chen, *Adv. Mater.* **2021**, *33*, 2100445.
[152] L. Cao, D. Li, T. Pollard, T. Deng, B. Zhang, C. Yang, L. Chen, J. Vatamanu, E. Hu, M. J. Hourwitz,

L. Ma, M. Ding, Q. Li, S. Hou, K. Gaskell, J. T. Fourkas, X. Q. Yang, K. Xu, O. Borodin, C. Wang, *Nat. Nanotechnol.* **2021**, *16*, 902-910.
[153] Z. Yu, L. Cao, H. Liu, D.-W. Wang, *Energy Stor. Mater.* **2021**, *43*, 158-164.
[154] J. Hao, J. Long, B. Li, X. Li, S. Zhang, F. Yang, X. Zeng, Z. Yang, W. K. Pang, Z. Guo, *Adv. Funct. Mater.* **2019**, *29*, 1903605.
[155] D. Zhou, Y. B. He, R. Liu, M. Liu, H. Du, B. Li, Q. Cai, Q. H. Yang, F. Kang, *Adv. Energy Mater.* **2015**, *5*, 1500353.
[156] Q. Wu, Y. Yang, C. Ma, Z. Chen, Q. Su, C. Zhu, Y. Gao, R. Ma, C. Li, *Sus. Chem. Eng.* **2021**, *9*, 5631-5641.
[157] W. Ling, F. Mo, J. Wang, Q. Liu, Y. Liu, Q. Yang, Y. Qiu, Y. Huang, *Mater. Today Phys.* **2021**, 100458.
[158] S. Huang, F. Wan, S. Bi, J. Zhu, Z. Niu, J. Chen, *Angew. Chem. Int. Ed.* **2019**, *58*, 4313-4317.
[159] Y. Chen, J. Zhao, Y. Wang, *Appl. Energy Mater.* **2020**, *3*, 9058-9065.
[160] aM. Chen, J. Chen, W. Zhou, X. Han, Y. Yao, C. P. Wong, *Adv. Mater.* **2021**, *33*, 2007559; bR. Chen, X. Xu, S. Peng, J. Chen, D. Yu, C. Xiao, Y. Li, Y. Chen, X. Hu, M. Liu, *Sus. Chem. Eng.* **2020**, *8*, 11501-11511.
[161] P. Yang, C. Feng, Y. Liu, T. Cheng, X. Yang, H. Liu, K. Liu, H. J. Fan, *Adv. Energy Mater.* **2020**, *10*, 2002898.
[162] Y. Tang, C. Liu, H. Zhu, X. Xie, J. Gao, C. Deng, M. Han, S. Liang, J. Zhou, *Energy Stor. Mater.* **2020**, *27*, 109-116.
[163] C. Y. Chan, Z. Wang, Y. Li, H. Yu, B. Fei, J. H. Xin, *Appl. Mater. Interfaces* **2021**, *13*, 30594-30602.
[164] J. Evans, C. A. Vincent, P. G. Bruce, *Polymer* **1987**, *28*, 2324-2328.
[165] L. Martinez, R. Andrade, E. G. Birgin, J. M. Martinez, *J. Comput. Chem.* **2009**, *30*, 2157-2164.
[166] S. Plimpton, *J. Comput. Phys.* **1995**, *117*, 1-19.
[167] J. C. Phillips, D. J. Hardy, J. D. C. Maia, J. E. Stone, J. V. Ribeiro, R. C. Bernardi, R. Buch, G. Fiorin, J. Henin, W. Jiang, R. McGreevy, M. C. R. Melo, B. K. Radak, R. D. Skeel, A. Singharoy, Y. Wang, B. Roux, A. Aksimentiev, Z. Luthey-Schulten, L. V. Kale, K. Schulten, C. Chipot, E. Tajkhorshid, *J. Chem. Phys.* **2020**, *153*, 044130.
[168] W. Humphrey, A. Dalke, K. Schulten, *J. Mol. Graph.* **1996**, *14*, 33-38.
[169] M. Armand, J.-M. Tarascon, *Nature* **2008**, *451*, 652-657.
[170] J. W. Choi, D. Aurbach, *Nat. Rev. Mater.* **2016**, *1*, 16013.
[171] D. Lin, Y. Liu, Y. Cui, *Nat. Nanotechnol.* **2017**, *12*, 194-206.
[172] X. Cao, X. Ren, L. Zou, M. H. Engelhard, W. Huang, H. Wang, B. E. Matthews, H. Lee, C. Niu, B. W. Arey, *Nat. Energy* **2019**, *4*, 796-805.
[173] X. Fan, X. Ji, F. Han, J. Yue, J. Chen, L. Chen, T. Deng, J. Jiang, C. Wang, *Sci. Adv.* **2018**, *4*, eaau9245.
[174] D. Zhou, R. Liu, Y. B. He, F. Li, M. Liu, B. Li, Q. H. Yang, Q. Cai, F. Kang, *Adv. Energy Mater.* **2016**, *6*, 1502214.
[175] D. Lin, Y. Liu, Z. Liang, H.-W. Lee, J. Sun, H. Wang, K. Yan, J. Xie, Y. Cui, *Nat. Nanotechnol.* **2016**, *11*, 626-632.
[176] X.-B. Cheng, R. Zhang, C.-Z. Zhao, Q. Zhang, *Chem. Rev.* **2017**, *117*, 10403-10473.
[177] D. Zhou, D. Shanmukaraj, A. Tkacheva, M. Armand, G. Wang, *Chem* **2019**, *5*, 2326-2352.
[178] N. W. Li, Y. X. Yin, J. Y. Li, C. H. Zhang, Y. G. Guo, *Adv. Sci.* **2017**, *4*, 1600400.
[179] Q. Zhang, K. De Oliveira Vigier, S. Royer, F. Jerome, *Chem. Soc. Rev.* **2012**, *41*, 7108-7146.
[180] E. L. Smith, A. P. Abbott, K. S. Ryder, *Chem. Rev.* **2014**, *114*, 11060-11082.
[181] Y. Hu, H. Li, X. Huang, L. Chen, *Electrochem. Commun.* **2004**, *6*, 28-32.
[182] B. Zhou, D. He, J. Hu, Y. Ye, H. Peng, X. Zhou, X. Xie, Z. Xue, *J. Mater. Chem. A* **2018**, *6*, 11725-11733.
[183] K. Abraham, Z. Jiang, B. Carroll, *Chem. Mater.* **1997**, *9*, 1978-1988.
[184] M. K. Tran, M.-T. F. Rodrigues, K. Kato, G. Babu, P. M. Ajayan, *Nat. Energy* **2019**, *4*, 339.
[185] P. Chandra Rath, C.-J. Wu, J. Patra, J. Li, T.-C. Lee, T.-J. Yeh, J. K. Chang, *J. Mater. Chem. A* **2019**,

7, 16516-16525.
[186] W. Zaidi, A. l. Boisset, J. Jacquemin, L. Timperman, M. r. m. Anouti, *J. Phys. Chem. C* **2014**, *118*, 4033-4042.
[187] T. Hou, G. Yang, N. N. Rajput, J. Self, S.-W. Park, J. Nanda, K. A. Persson, *Nano Energy* **2019**, *64*, 103881.
[188] N. Chen, Y. Dai, Y. Xing, L. Wang, C. Guo, R. Chen, S. Guo, F. Wu, *Energy Environ. Sci.* **2017**, *10*, 1660-1667.
[189] aK. Ahmed, N. Naga, H. Furukawa, *ECS Trans.* **2018**, *88*, 427-436; bM. A. Wisniewska, J. G. Seland, W. Wang, *J. Appl. Poly. Sci.* **2018**, *135*, 46695.
[190] aC. Chen, S. H. Lee, M. Cho, J. Kim, Y. Lee, *Appl. Mater. Interfaces* **2016**, *8*, 2658-2665; bT. Sun, Z. J. Li, H. G. Wang, D. Bao, F. L. Meng, X. B. Zhang, *Angew. Chem. Int. Ed.* **2016**, *55*, 10662-10666.
[191] M. Liu, D. Zhou, Y.-B. He, Y. Fu, X. Qin, C. Miao, H. Du, B. Li, Q.-H. Yang, Z. Lin, *Nano Energy* **2016**, *22*, 278-289.
[192] D. Zhou, A. Tkacheva, X. Tang, B. Sun, D. Shanmukaraj, P. Li, F. Zhang, M. Armand, G. Wang, *Angew. Chem. Int. Ed.* **2019**, *58*, 6001-6006.
[193] X. Xu, D. Zhou, X. Qin, K. Lin, F. Kang, B. Li, D. Shanmukaraj, T. Rojo, M. Armand, G. Wang, *Nat. Commun.* **2018**, *9*, 3870.
[194] S. Xia, J. Lopez, C. Liang, Z. Zhang, Z. Bao, Y. Cui, W. Liu, *Adv. Sci.* **2019**, *6*, 1802353.
[195] C. Ding, X. Fu, H. Li, J. Yang, J. L. Lan, Y. Yu, W. H. Zhong, X. Yang, *Adv. Funct. Mater.* **2019**, *29*, 1904547.
[196] X. Shen, H. Liu, X.-B. Cheng, C. Yan, J.-Q. Huang, *Energy Stor. Mater.* **2018**, *12*, 161-175.
[197] H. Shin, J. Park, S. Han, A. M. Sastry, W. Lu, *J. Power Sources* **2015**, *277*, 169-179.
[198] Y.-G. Cho, S.-H. Jung, S. H. Joo, Y. Jeon, M. Kim, K. M. Lee, S. Kim, J. M. Park, H. K. Noh, Y.-S. Kim, *J. Mater. Chem. A* **2018**, *6*, 22483-22488.
[199] Z. Lu, X. Lu, J. Ding, T. Zhou, T. Ge, G. Yang, F. Yin, M. Wu, *Appl. Surf. Sci.* **2017**, *426*, 19-28.
[200] aY. Yokoyama, T. Fukutsuka, K. Miyazaki, T. Abe, *J. Electrochem. Soc.* **2018**, *165*, A3299; bL. Coustan, K. Zaghib, D. Bélanger, *J. Power Sources* **2018**, *399*, 299-303.
[201] S. Ko, Y. Yamada, K. Miyazaki, T. Shimada, E. Watanabe, Y. Tateyama, T. Kamiya, T. Honda, J. Akikusa, A. Yamada, *Electrochem. Commun.* **2019**, *104*, 106488.
[202] L. Droguet, A. Grimaud, O. Fontaine, J. m. Tarascon, *Adv. Energy Mater.* **2020**, *10*, 2002440.
[203] S. Sikkanthar, S. Karthikeyan, S. Selvasekarapandian, D. Arunkumar, H. Nithya, K. Junichi, *Ionics* **2016**, *22*, 1085-1094.
[204] W. Xue, Z. Shi, L. Suo, C. Wang, Z. Wang, H. Wang, K. P. So, A. Maurano, D. Yu, Y. Chen, *Nat. Energy* **2019**, *4*, 374-382.
[205] N. Kumar, J. Seminario, *J. Phys. Chem. C* **2016**, *120*, 16322-16332.
[206] W. L. Jorgensen, D. S. Maxwell, J. Tirado-Rives, *J. Am. Chem. Soc.* **1996**, *118*, 11225-11236.
[207] R. W. Hockney, J. W. Eastwood, *Computer simulation using particles*, crc Press, **1988**.
[208] aI. V. Leontyev, A. A. Stuchebrukhov, *J. Chem. Phys.* **2009**, *130*, 085102; bE. E. Bruce, N. F. J. T. J. o. c. p. van der Vegt, *J. Chem. Phys.* **2018**, *148*, 222816.
[209] Y. Yamada, J. Wang, S. Ko, E. Watanabe, A. Yamada, *Nat. Energy* **2019**, *4*, 269-280.
[210] T. A. Barnes, J. W. Kaminski, O. Borodin, T. F. Miller III, *J. Phys. Chem. C* **2015**, *119*, 3865-3880.
[211] X. Cao, H. Jia, W. Xu, J.-G. Zhang, *J. Electrochem. Soc.* **2021**, *168*, 010522.
[212] T. Liang, R. Hou, Q. Dou, H. Zhang, X. Yan, *Adv. Funct. Mater.* **2021**, *31*, 2006749.
[213] C. Yan, Y. X. Yao, X. Chen, X. B. Cheng, X. Q. Zhang, J. Q. Huang, Q. Zhang, *Angew. Chem. Int. Ed.* **2018**, *57*, 14055-14059.
[214] aJ. Gliński, G. Chavepeyer, J.-K. Platten, *Colloids Surf. A* **2000**, *162*, 233-238; bX. Chen, Q. Zhang, *Acc. Chem. Res.* **2020**, *53*, 1992-2002.
[215] K. Xu, C. Wang, *Nat. Energy* **2016**, *1*, 1-2.
[216] H. Bi, X. Wang, H. Liu, Y. He, W. Wang, W. Deng, X. Ma, Y. Wang, W. Rao, Y. Chai, *Adv. Mater.* **2020**, *32*, 2000074.

[217] H.-G. Steinrück, C. Cao, G. M. Veith, M. F. Toney, *J. Chem. Phys.* **2020**, *152*, 084702.
[218] R.-S. Kühnel, D. Reber, C. Battaglia, *J. Electrochem. Soc.* **2020**, *167*, 070544.
[219] Y. Li, Y. Li, A. Pei, K. Yan, Y. Sun, C. L. Wu, L. M. Joubert, R. Chin, A. L. Koh, Y. Yu, J. Perrino, B. Butz, S. Chu, Y. Cui, *Science* **2017**, *358*, 506-510.
[220] W. Qi, L. Ben, H. Yu, W. Zhao, G. Zhao, X. Huang, *Prog. Nat. Sci.* **2020**, *30*, 321-327.
[221] J. J. J. o. C. Tokunaga, E. Data, **1975**, *20*, 41-46.
[222] R. Bouchal, Z. Li, C. Bongu, S. Le Vot, R. Berthelot, B. Rotenberg, F. Favier, S. A. Freunberger, M. Salanne, O. Fontaine, *Angew. Chem. Int. Ed.* **2020**, *59*, 15913-15917.
[223] G. Fang, J. Zhou, A. Pan, S. Liang, *Energy Lett.* **2018**, *3*, 2480-2501.
[224] X. Yuan, F. Ma, L. Zuo, J. Wang, N. Yu, Y. Chen, Y. Zhu, Q. Huang, R. Holze, Y. Wu, *Electrochem. Energy Rev.* **2021**, *4*, 1-34.
[225] D. H. Jang, Y. J. Shin, S. M. Oh, *J. Electrochem. Soc.* **1996**, *143*, 2204.
[226] A. Dey, F. E. Jenney, Jr., M. W. Adams, E. Babini, Y. Takahashi, K. Fukuyama, K. O. Hodgson, B. Hedman, E. I. Solomon, *Science* **2007**, *318*, 1464-1468.
[227] aT. Mendez-Morales, Z. Li, M. Salanne, *Batter. Supercaps* **2020**, *4*, 646-652; bA. Perez de la Luz, J. A. Aguilar-Pineda, J. G. Mendez-Bermudez, J. Alejandre, *J. Chem. Theo. Comput.* **2018**, *14*, 5949-5958; cS. Obst, H. Bradaczek, *J. Mol. Model.* **1997**, *3*, 224-232; dA. P. Sunda, A. Venkatnathan, *J. Comput. Chem.* **2011**, *32*, 3319-3328; eI. Skarmoutsos, J. Samios, *Chem. Phys. Lett.* **2004**, *384*, 108-113.
[228] A. Miura, N. C. Rosero-Navarro, A. Sakuda, K. Tadanaga, N. H. Phuc, A. Matsuda, N. Machida, A. Hayashi, M. Tatsumisago, *Nat. Rev. Chem.* **2019**, *3*, 189-198.
[229] K. Fujii, H. Wakamatsu, Y. Todorov, N. Yoshimoto, M. Morita, *J. Phys. Chem. C* **2016**, *120*, 17196-17204.
[230] aG. Maisano, P. Migliardo, M. P. Fontana, M. C. Bellissent-Funel, A. J. Dianoux, *J. Phys. C* **1985**, *18*, 1115-1133; bY. Wang, M. Guo, S. Wei, S. Yin, Y. Wang, Z. Song, M. R. Hoffmann, *Comput. Theo. Chem.* **2014**, *1049*, 28-34.
[231] Z. Hou, L. Zhang, J. Chen, Y. Xiong, X. Zhang, Y. Qian, *Mater. Chem. Front.* **2021**, *5*, 2749-2757.
[232] aR. Tian, S. H. Park, P. J. King, G. Cunningham, J. Coelho, V. Nicolosi, J. N. Coleman, *Nat. Commun.* **2019**, *10*, 1933; bH. Zhang, X. Liu, H. Li, I. Hasa, S. Passerini, *Angew. Chem. Int. Ed.* **2021**, *60*, 598-616.
[233] aT. Joshi, K. Eom, G. Yushin, T. F. Fuller, *J. Electrochem. Soc.* **2014**, *161*, A1915; bM. B. Pinson, M. Z. Bazant, *J. Electrochem. Soc.* **2012**, *160*, A243.
[234] aJ. Shin, J. Lee, Y. Park, J. W. Choi, *Chem. Sci.* **2020**, *11*, 2028-2044; bP. T. Gilbert, *J. Electrochem. Soc.* **1952**, *99*, 16.
[235] L. Cao, D. Li, E. Hu, J. Xu, T. Deng, L. Ma, Y. Wang, X. Q. Yang, C. Wang, *J. Am. Chem. Soc.* **2020**, *142*, 21404-21409.
[236] D. Li, L. Cao, T. Deng, S. Liu, C. Wang, *Angew. Chem. Int. Ed.* **2021**, *60*, 13035-13041.
[237] J. Vohs, M. Barteau, *J. Electron Spectros. Relat. Phenomena* **1989**, *49*, 87-96.
[238] S. Di, X. Nie, G. Ma, W. Yuan, Y. Wang, Y. Liu, S. Shen, N. Zhang, *Energy Stor. Mater.* **2021**, *43*, 375-382.
[239] H. Qiu, X. Du, J. Zhao, Y. Wang, J. Ju, Z. Chen, Z. Hu, D. Yan, X. Zhou, G. Cui, *Nat. Commun.* **2019**, *10*, 1-12.
[240] D. Weng, H. Duan, Y. Hou, J. Huo, L. Chen, F. Zhang, J. Wang, *Prog. Nat. Sci.* **2020**, *30*, 139-152.